Last glacial-deglacial variability in sea surface characteristics and ice sheet activities in the Labrador Sea/Baffin Bay

Kumulative Dissertation
zur Erlangung des akademischen Grades
eines Doktors der Naturwissenschaften

-Dr. rer. nat.-

am Fachbereich Geowissenschaften
der Universität Bremen

vorgelegt von
Defang You
Bremerhaven, 2023

Gutachter der Dissertation:
Prof. Dr. Ruediger Stein
Prof. Dr. Marit-Solveig Seidenkrantz

Ph.D. Colloquium

The history of deglacial meltwater discharge in the subpolar North Atlantic: Sedimentary records from the eastern Labrador Sea

January 18th, 2024

Versicherung an Eides Statt / Affirmation in lieu of an oath

**gem. § 5 Abs. 5 der Promotionsordnung vom 18.06.2018 /
according to § 5 (5) of the Doctoral Degree Rules and Regulations of 18 June, 2018**

Ich / I, Defang You, Am Alten Hafen 26, 27568 Bremerhaven, 6008780
_____

    (Vorname / First Name, Name / Name, Anschrift / Address, ggf. Matr.-Nr. / student
    ID no., if applicable)

versichere an Eides Statt durch meine Unterschrift, dass ich die vorliegende Dissertation selbständig und ohne fremde Hilfe angefertigt und alle Stellen, die ich wörtlich dem Sinne nach aus Veröffentlichungen entnommen habe, als solche kenntlich gemacht habe, mich auch keiner anderen als der angegebenen Literatur oder sonstiger Hilfsmittel bedient habe und die zu Prüfungszwecken beigelegte elektronische Version (PDF) der Dissertation mit der abgegebenen gedruckten Version identisch ist. / With my signature I affirm in lieu of an oath that I prepared the submitted dissertation independently and without illicit assistance from third parties, that I appropriately referenced any text or content from other sources, that I used only literature and resources listed in the dissertation, and that the electronic (PDF) and printed versions of the dissertation are identical.

Ich versichere an Eides Statt, dass ich die vorgenannten Angaben nach bestem Wissen und Gewissen gemacht habe und dass die Angaben der Wahrheit entsprechen und ich nichts verschwiegen habe. / I affirm in lieu of an oath that the information provided herein to the best of my knowledge is true and complete.

Die Strafbarkeit einer falschen eidesstattlichen Versicherung ist mir bekannt, namentlich die Strafandrohung gemäß § 156 StGB bis zu drei Jahren Freiheitsstrafe oder Geldstrafe bei vorsätzlicher Begehung der Tat bzw. gemäß § 161 Abs. 1 StGB bis zu einem Jahr Freiheitsstrafe oder Geldstrafe bei fahrlässiger Begehung. / I am aware that a false affidavit is a criminal offence which is punishable by law in accordance with § 156 of the German Criminal Code (StGB) with up to three years imprisonment or a fine in case of intention, or in accordance with § 161 (1) of the German Criminal Code with up to one year imprisonment or a fine in case of negligence.

Bremerhaven, October 10th 2023
_____   _____

Ort / Place, Datum / Date   Unterschrift / Signature

Table of Contents

Abbreviations

AMOC	Atlantic Meridional Overturning Circulation
AMS	Accelerator Mass Spectrometry
AO	Arctic Oscillation
B/A	Bølling/Allerød warm period
BC	Baffin Current
$C_{37:4}$	tetra-unsaturated alkenones
D/O	Dansgaard-Oeschger cycle
DSOW	Denmark Strait Overflow Water
DWBC	Deep Western Boundary Current
EGC	East Greenland Current
GrIS	Greenland Ice Sheet
HBI	highly branched isoprenoid alkane
HBI-III (Z)	tri-unsaturated HBI (Z-isomer)
HE	Heinrich Event
HS	Heinrich Stadial
HTM	Holocene Thermal Maximum
IC	Irminger Current
iGDGTs	isoprenoid glycerol dibiphytanyl glycerol tetraethers
IRD	ice-rafted debris
ISOW	Iceland-Scotland Overflow Water
LC	Labrador Current
LGM	Last Glacial Maximum
LIA	Little Ice Age
LIS	Laurentide Ice Sheet
LSW	Labrador Sea Water
MIS	marine isotope stage
MIZ	marginal ice zone
MPT	Mid-Pleistocene Transition
MS	magnetic susceptibility
MW	meltwater event
NAC	North Atlantic Current
NADW	North Atlantic Deep Water
NAO	North Atlantic Oscillation
PIP_{25}	phytoplankton-based IP_{25} values
SPG	subpolar gyre

SST	sea surface temperature
TC	total carbon
TEX$_{86}$	Tetraether index of tetraethers consisting of 86 carbon atoms
TOC	total organic carbon
U$_{37}^{K}$	alkenone unsaturation
WBD	wet bulk density
WGC	West Greenland Current
XRD	X-ray diffraction
XRF	X-ray fluorescence
YD	Younger Dryas cold event
δD$_{PA}$	stable hydrogen isotope compositions of palmitic acid
$\overline{SS}$	mean size of sortable silt
$\triangle$R	local reservoir age

Abstract

In the context of global warming, the accelerated melting of the Greenland Ice Sheet (GrIS) and Arctic sea ice in recent years has led to increased meltwater discharge and subsequent sea-level rise. The meltwater discharge may affect sea surface characteristics in the polar and subpolar regions and potentially yield significant influence on ocean circulation patterns. Additionally, the far-reaching implications of ocean forcings on ice sheet instability and sea ice retreat have also raised considerable attention. To enhance our understanding of influences of meltwater discharge on abrupt climatic changes and interactions among ice sheet instability, sea ice variability, and sea surface characteristics, it is essential to investigate sedimentary records on different timescales beyond modern observation. To achieve these objectives, we conducted detailed paleoenvironmental reconstructions from three sediment cores: one obtained from the eastern Labrador Sea (Core MSM12/2-05-01) and two others from southern Baffin Bay (Core SL170 and SL174).

The first study provides insights into deglacial abrupt climate changes caused by meltwater plumes in the Labrador Sea. Based on our well-dated and high-resolution sedimentary records representing the last 19 ka, four millennial-scale meltwater events have been identified between 14 ka BP and 8.2 ka BP based on independent biomarker proxies and X-ray fluorescence (XRF) scanning data. These events were characterized by increased sea ice formation, decreased sea surface temperatures (SSTs), and reduced primary production, which might have occurred within a few decades. We propose that these abrupt changes in sea surface characteristics were triggered by meltwater pulsing into the Labrador Sea periodically, resulting from the collapse of the Laurentide Ice Sheet (LIS) and GrIS caused by (sub-)surface ocean warming in the Labrador Sea. Furthermore, the increased meltwater discharges potentially promoted stratification of the upper ocean column in the Labrador Sea/subpolar area, thus preventing Atlantic Water inflow and disrupting the deglacial climate.

The second study addresses a comprehensive picture of interactions between ice sheet instability and sea surface characteristics in the Labrador Sea during the last 50 ka, spanning the last glacial-deglacial-Holocene period. The XRF scanning, biomarker, and planktic/benthic foraminifer data were used in this study, indicating the intensified warm Irminger Current inflow led to (sub-)surface warming in the Labrador Sea, which might have contributed to the disintegration of the surrounding LIS and GrIS, and subsequently increased meltwater discharge. The patterns of meltwater discharge and detrital material input were distinct during different phases: primarily characterized by iceberg discharge during the last glacial period, contrasting with the prevalence of meltwater plumes during the last deglaciation. Consistent with our first study, the increased meltwater discharge has caused surface freshening in the Labrador Sea, resulting in decreased SSTs, increased sea ice formation, and reduced open-water phytoplankton

productivity. Furthermore, our records provided proxy evidence that an offshore polynya probably occurred south of Greenland during the last glacial maximum.

The third study focuses on changes in sea surface characteristics during the last deglaciation in southern Baffin Bay, compared with those from the Labrador Sea. The biomarker-based reconstruction exhibited six significant sea ice retreats in southeastern Baffin Bay, and one prominent retreat was observed in southwestern Baffin Bay, spanning the last 16-10 ka. These sea ice retreats appear to be closely linked to enhanced Atlantic Water inflow. Notably, a major sea ice retreat occurred around 14.4 ka BP, coinciding with elevated detrital input from the GrIS and the LIS. Another significant transition happened in both Baffin Bay and the Labrador Sea during the middle Younger Dryas (YD). This transition aligns with a slight recovery of the Atlantic Meridional Overturning Circulation (AMOC) but predates the onset of Heinrich Event 0 (HE0). The enhanced Atlantic Water inflow might have played a role in the occurrence of HE0, contributing to the second decline in the AMOC during the late YD, thereby the persistence of a cold episode of YD.

In summary, this study provides new insights into variations in sea surface characteristics and their interactions with ice sheet activities in the Labrador Sea and Baffin Bay during the last glacial-deglacial-Holocene period. Meanwhile, our findings provide more information about the impact of freshwater forcing/ice sheet activities on abrupt climate changes. Furthermore, these findings highlight the significance of oceanic processes within the polar and subpolar regions and their contributions to paleoclimate changes.

Zusammenfassung

Im Zusammenhang mit der globalen Erwärmung hat das beschleunigte Abschmelzen des grönländischen Eisschilds (GrIS) und des arktischen Meereises in den letzten Jahren zu einem verstärkten Schmelzwasserabfluss und einem anschließenden Meeresspiegelanstieg geführt. Der Schmelzwasserabfluss kann sich auf die Eigenschaften der Meeresoberfläche in den polaren und subpolaren Regionen auswirken und möglicherweise einen erheblichen Einfluss auf die Ozeanzirkulationsmuster haben. Umgekehrt haben die weitreichenden Auswirkungen der ozeanischen Einflüsse auf die Instabilität der Eisschilde und den Rückzug des Meereises ebenfalls große Aufmerksamkeit erregt. Um die Einflüsse des Schmelzwasserabflusses auf abrupte klimatische Veränderungen und die Wechselwirkungen zwischen der Instabilität der Eisschilde, der Variabilität des Meereises und den Eigenschaften der Meeresoberfläche besser zu verstehen, ist es unerlässlich, die Sedimentaufzeichnungen auf verschiedenen Zeitskalen zu untersuchen, die über die modernen Beobachtungen hinausgehen. Um diese Ziele zu erreichen, haben wir detaillierte Paläoumweltrekonstruktionen aus drei Sedimentkernen durchgeführt: einem aus der östlichen Labradorsee (Kern MSM12/2-05-01) und zwei weiteren aus der südlichen Baffin Bay (Kern SL170 und SL174).

Die erste Studie bietet Einblicke in deglaziale abrupte Klimaänderungen, die durch Schmelzwasserfahnen in der Labradorsee verursacht wurden. Auf der Grundlage unserer gut datierten und hochauflösenden Sedimentaufzeichnungen, die die letzten 19000 Jahre repräsentieren, wurden vier Schmelzwasserereignisse von tausendjährigem Ausmaß zwischen 14000 Jahren vor Heute (= 14000 JvH) und 8200 JvH identifiziert, die auf unabhängigen Biomarker-Proxies und Röntgenfluoreszenz (XRF)-Scandaten basieren. Diese Ereignisse waren durch verstärkte Meereisbildung, sinkende Meeresoberflächentemperaturen (SST) und eine verringerte Primärproduktion gekennzeichnet, die innerhalb weniger Jahrzehnte stattgefunden haben könnten. Wir vermuten, dass diese abrupten Veränderungen der Meeresoberflächeneigenschaften durch Schmelzwasser ausgelöst wurden, das in regelmäßigen Abständen in die Labradorsee strömte und das Ergebnis des Zusammenbruchs des Laurentide Ice Sheet (LIS) und des GrIS war, der durch die Erwärmung des Ozeans in der Labradorsee verursacht wurde. Darüber hinaus förderten die verstärkten Schmelzwasserabflüsse möglicherweise die Schichtung der oberen Ozeansäule in der Labradorsee/im subpolaren Bereich, wodurch der Zufluss von Atlantikwasser verhindert und das deglaziale Klima gestört wurde.

Die zweite Studie liefert ein umfassendes Bild der Wechselwirkungen zwischen der Instabilität des Eisschildes und den Eigenschaften der Meeresoberfläche in der Labradorsee während der letzten 50000 Jahre, d. h. während des letzten Glazials, des Deglazials und des Holozäns. Die in dieser Studie verwendeten XRF-Scanner-, Biomarker- und planktischen/benthischen Foraminiferen-Daten deuten darauf hin, dass der verstärkte warme Irmingerstrom zu einer

(Unter-)Oberflächenerwärmung in der Labradorsee führte, die möglicherweise zum Zerfall des umgebenden LIS und GrIS und in der Folge zu einem erhöhten Schmelzwasserabfluss beitrug. Die Muster des Schmelzwasserabflusses und des Eintrags von detritischem Material waren in den verschiedenen Phasen unterschiedlich: während der letzten Eiszeit war der Abfluss von Eisbergen vorherrschend, während der letzten Deglazialzeit dagegen waren Schmelzwasserfahnen vorherrschend. In Übereinstimmung mit unserer ersten Studie hat der verstärkte Schmelzwasserabfluss zu einer Auffrischung der Oberfläche in der Labradorsee geführt, was zu einem Rückgang der SST, einer verstärkten Meereisbildung und einer geringeren Produktivität des Phytoplanktons im Freiwasser führte. Darüber hinaus lieferten unsere Aufzeichnungen Beweise dafür, dass während des letzten glazialen Maximums südlich von Grönland wahrscheinlich eine Offshore-Polynja entstand.

Die dritte Studie konzentriert sich auf Veränderungen der Oberflächenwassereigenschaften während des letzten Geglazials in der südlichen Baffin Bay im Vergleich zu denen in der Labradorsee. Die auf Biomarkern basierende Rekonstruktion zeigte sechs signifikante Meereisrückgänge in der südöstlichen Baffin Bay und einen auffälligen Rückzug in der südwestlichen Baffin Bay, der sich über die letzten 16000 bis 10000 Jahre erstrecken. Diese Meereisrückgänge scheinen eng mit dem verstärkten Zufluss von Atlantikwasser verbunden gewesen zu sein. Ein größerer Meereisrückgang fand um 14400 JvH statt und fiel mit einem erhöhten Detrituseintrag aus dem GrIS und dem LIS zusammen. Ein weiterer bedeutender Übergang fand sowohl in der Baffin Bay als auch in der Labradorsee während der mittleren Jüngeren Dryas (YD) statt. Dieser Übergang fällt mit einer leichten Erholung der atlantischen meridionalen Umwälzzirkulation (AMOC) zusammen, liegt aber vor dem Einsetzen des Heinrich-Ereignisses 0 (HE0). Der verstärkte Zufluss von Atlantikwasser könnte beim Auftreten von HE0 eine Rolle gespielt haben und zum zweiten Rückgang der AMOC während der späten YD beigetragen haben, wodurch eine kalte Episode der YD fortgesetzt wurde.

Zusammenfassend lässt sich sagen, dass diese Studie neue Einblicke in die Variationen der Oberflächenwassereigenschaften und ihre Wechselwirkungen mit den Eisschildaktivitäten in der Labradorsee und der Baffin Bay während des letzten Glazial-Deglazial-Holozän-Zeitraumes liefert. Gleichzeitig liefern unsere Ergebnisse weitere Informationen über die Auswirkungen von Süßwasserantrieben und Eisschildaktivitäten auf abrupte Klimaänderungen. Darüber hinaus unterstreichen diese Ergebnisse die Bedeutung ozeanischer Prozesse in den polaren und subpolaren Regionen und ihren Beitrag zu paläoklimatischen Veränderungen.

Acknowledgement

First of all, I would like to thank my supervisor Prof. Dr. Ruediger Stein. Thank you so much for offering me the opportunity to work with you. I still remember how excited I was when I received the decision that I could come to AWI to conduct my PhD project. I am appreciated it very much for all the supervision and teaching you have given me over the last four years. Thanks for your patience and support in letting me know how to perform scientific research and how to be a qualified researcher.

Many thanks to Prof. Dr. Marit-Solveig Seidenkrantz for reviewing this dissertation. I am grateful to have met and talked to you at EGU.

Special thanks to Dr. Kirsten Fahl. Thank you so much for your supervision of my lab work. You were always there to encourage me when I was confused and frustrated. Thank you for teaching me to have a positive attitude towards work and life.

Many thanks to Prof. Dr. Gesine Mollenhauer, Prof. Dr. Audrey Limoges, Prof. Dr. Dierk Hebbeln for being my TAC meeting members and scientific discussions. Great acknowledgment also to all the co-authors for your contributions to the manuscripts.

Special thanks to my Canadian supervisor Prof. Dr. Audrey Limoges. Thanks for your supervision and care when I had a research stay in Fredericton. Thanks also to Dr. Nicolas Van Nieuwenhove for the help during my research stay.

Many thanks to Walter Luttmer for your guidance in the lab, and I miss chatting with you so much, which lets me know more than just research. Thanks to Dr. Enno Schefuß and Dr. Ralph Kreutz for supporting my lab work at MARUM. Thanks also to Valea Schumacher, Susanne Wiebe, and Mandy Kuck for your technique support at AWI.

Great acknowledgment to all my colleagues at AWI. Special thanks to Dr. Junjie Wu for your encouragement and help. Thanks to Dr. Shuzhuang Wu, Dr. Elena Vorrath, Dr. Nicole Syring, Dr. Jeetendra Saini, Dr. Henrik Sadatzki, Dr. Weng-si Chao, Dr. Julia Hagemann, Ling Liu, Kevin Kussner, Nele Lamping, Wee Wei Khoo, Monika Mikler, Taina Pinho, Vincent Rigalleau, and Vivian Sinnen. Thanks also to ArcTrain PIs and students.

Last but not least, I would like to express particular gratitude to my parents and family for your support. I am also grateful to all my friends in Bremerhaven. Many thanks to Dr. Qiyun Ma for your encouragement in the last phase of my PhD study.

1 Introduction

1.1 Background

In recent years, the acceleration of decay and melting in the Greenland Ice Sheet (GrIS) and Antarctic Ice Sheet has raised concerns about the impact of ocean warming on ice sheet instability (Yang et al., 2016; Sévellec et al., 2017; Box et al., 2022). The significant reduction in Arctic sea ice extent during summer has also been observed under a sustained warming climate, leading to a pronounced Arctic Amplification. The increased meltwater discharge from the retreat of ice sheets and sea ice can also affect the surrounding ocean environment. To enhance our understanding of the interactions between ice sheet and ocean, it is essential to investigate the ice sheet instability and related changes in sea surface characteristics in the past within paleoclimate timescales.

Recent observations indicate a weakening of the Atlantic Meridional Overturning Circulation (AMOC) since the mid-twentieth century (Rahmstorf et al., 2015; Caesar et al., 2018), leading to reduced northward heat transport, decreased primary production in the subpolar regions, and also related to extreme weather events in Europe (Caesar et al., 2018; Osman et al., 2019). It has been proposed that the decline in the AMOC might be related to the perturbation of meltwater discharge into the polar and subpolar North Atlantic, where the North Atlantic Deep Water forms (Srokosz and Bryden, 2015; Rahmstorf et al., 2015; Osman et al., 2019). However, our comprehension of the impact of changes in sea surface characteristics within the North Atlantic regions on climate change remains limited.

The Labrador Sea and Baffin Bay are optimal areas for reconstructing the history of interactions between ice sheet activities and sea surface characteristics due to their proximity to the Laurentide Ice Sheet (LIS) and GrIS during the last glacial period. Paleoceanography and paleoclimate reconstructions from these areas offer valuable insights into the past variability in the subpolar/polar regions, shedding light on patterns of abrupt climate change. These reconstructions may improve data-model comparisons, and further enhance our understanding for past and future changes in ocean circulation and climate, particularly under sustained global warming.

1.2 Modern characteristics of the Labrador Sea/Baffin Bay

1.2.1 Geography and bathymetry

The Atlantic Ocean is the second-largest ocean in the world, covering approximately 20% of Earth's surface. It separates the continents of Europe and Africa to the east and the continents of North and South America to the west. Within the interconnected global ocean system, it is connected to the Arctic Ocean in the north, the Pacific Ocean in the southwest, the Indian Ocean in the southeast, and the Southern Ocean in the south. Further divided by the Equator, it forms the North and South Atlantic.

Based on geographic definition, the Arctic Circle (66°34′N) divides the North Atlantic into subpolar and polar regions (Elverhøi et al., 1998; Source: Wikipedia, link: https://en.wikipedia.org/wiki/Polar_regions_of_Earth). The subpolar North Atlantic is characterized by its distinct geography and environmental conditions. Spanning a substantial area between approximately 40°N and 66°34′N, this region encompasses the Labrador Sea, Irminger Sea, etc (Fig. 1.1). The geography of the subpolar North Atlantic is marked by a combination of continental shelves, deep-sea basins, and underwater ridges. It encompasses parts of the continental shelves of North America and Europe, including coastal areas off Newfoundland, Greenland, Iceland, the Faroe Islands, and the British Isles. Prominent geological formations such as the Greenland-Scotland Ridge, Reykjanes Ridge, and the Rockall Plateau, etc. contribute to its distinctive landscape (Source: Wikipedia, link: https://en.wikipedia.org/wiki/Atlantic_Ocean).

The Labrador Sea is the core area of the subpolar North Atlantic and it is also the focus area of this dissertation. The Labrador Sea is located in the western subpolar Atlantic between the Labrador Peninsula and Greenland, connecting to the north with Baffin Bay through the Davis Strait (Fig. 1.1). The Labrador Sea is a small oceanic basin that developed during the separation of the North American and Greenland tectonic plates (Chalmers and Pulvertaft, 2001). The movement of these two plates initiated around 60 million years ago (Paleocene) and stopped about 40 million years ago (Eocene). Concurrently, the onset of magmatic sea-floor spreading in the Davis Strait and Baffin Bay during the Paleocene was accompanied by volcanic activities (Chalmers and Pulvertaft, 2001).

Adjacent to the Labrador Sea, Baffin Bay serves as another focal point within this study, closely linked with environmental shifts in the Labrador Sea. Defined by its latitudinal location, Baffin Bay falls within the polar regions. It is located between Baffin Island and western Greenland, connecting to the Labrador Sea through Davis Strait and to the Arctic Ocean through Nares Strait (Fig. 1.1). The relatively shallow mantle depth observed in the central portion of Baffin Bay suggests that its crust likely has an oceanic origin, possibly arising from sea-floor spreading processes (Manchester and Clark, 1973). Additionally, the Nordic Seas—comprising the Iceland

Sea, Norwegian Sea, and Greenland Sea—share this polar classification, whereas they exhibit similarities in water mass characteristics with the subpolar North Atlantic. This likeness arises from factors such as the influence of warm and saline North Atlantic Water inflow, as well as the formation of deep waters.
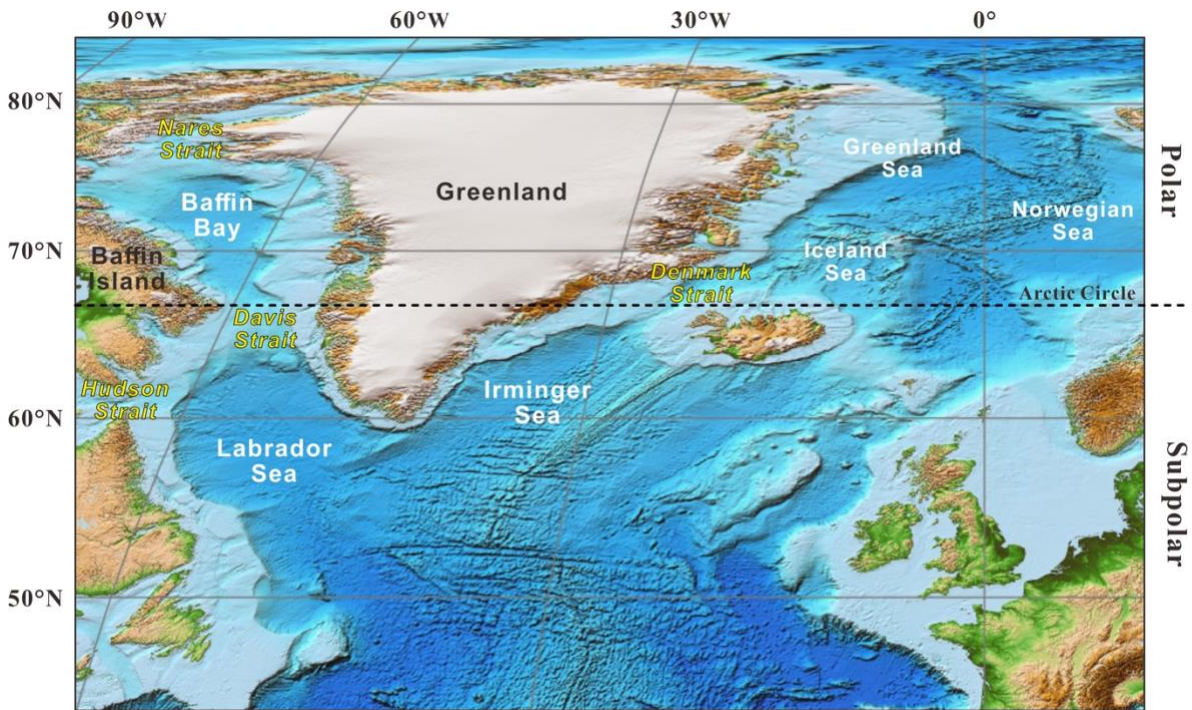
Fig. 1.1 Bathymetry map of the North Atlantic Ocean and geographical distribution of different sea areas. The map was taken from ETOPO1 (source: *https://www.ncei.noaa.gov*). Based on geographical definition, the North Atlantic is divided into polar and subpolar regions.

1.2.2 Hydrography

In the subpolar North Atlantic, the warm and saline Gulf Stream and North Atlantic Current (NAC) inflow are the dominant warm water inflow, which transports heat from the subtropical regions towards high-latitude subpolar regions (Fig. 1.2). The Irminger Current, derived from the NAC, flows westward off the southwest coast of Iceland and along Greenland into the Labrador Sea. The East Greenland Current along the eastern Greenland continental margin is one of the cold and low-salinity currents which flows from the Arctic Ocean. The Irminger Current and East Greenland Current mix in the southern tip of Greenland, forming a relatively warm West Greenland Current which flows northward along the western Greenland continental margin into the Baffin Bay (Drinkwater et al., 1996; Cuny et al., 2005; Stanford et al., 2011; Kieke and Yashayaev, 2015). West Greenland Current mixes with Arctic Water in northern Baffin Bay and forms the cold Baffin Current flowing southward along Baffin Island. After passing through the Davis Strait, the Baffin Current mixes with the branches of the Irminger Current, forming the Labrador Current (Fig. 1.2).
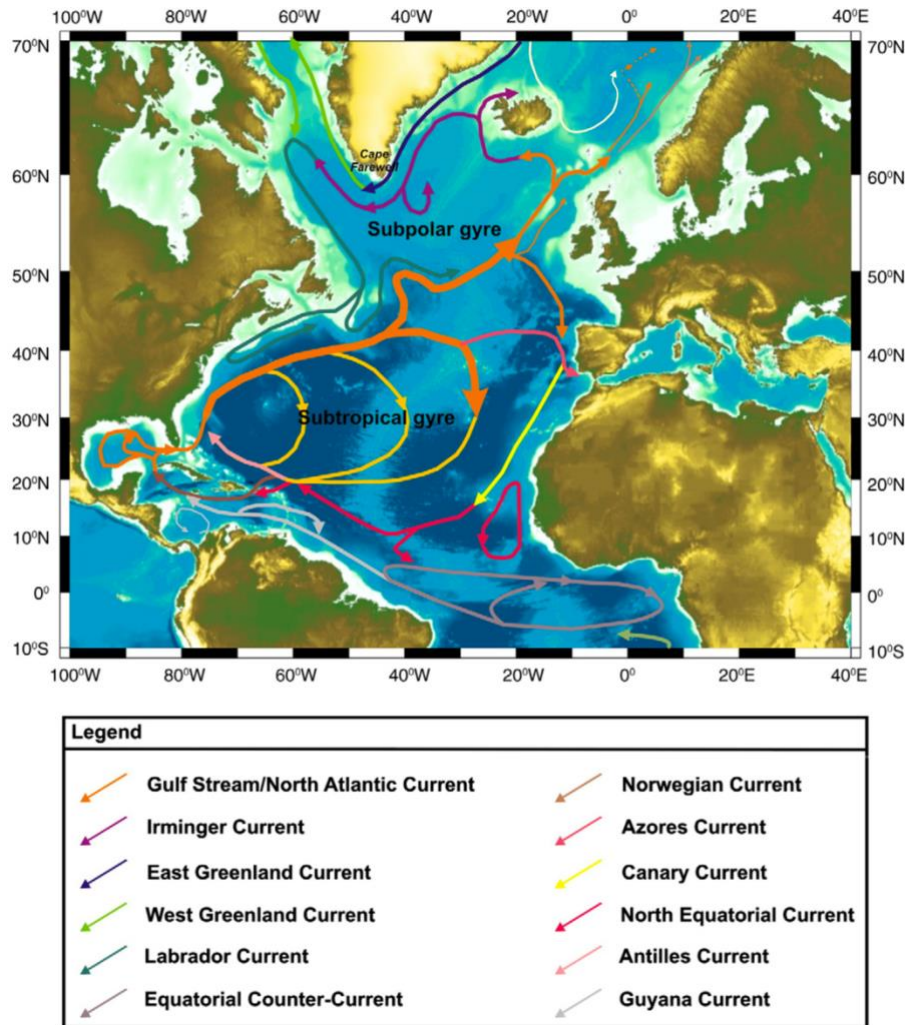
Fig. 1.2 Map of the North Atlantic region showing patterns of sea surface circulation (Modified from Stanford et al., 2011).

The subpolar/polar North Atlantic also serves as a crucial region where the distinctive intermediate and deep-water masses form (Fig. 1.3). Due to the heat loss from the ocean to the atmosphere, the density of the North Atlantic water mass increases as it flows towards high-latitude regions. The ongoing cooling process causes increased density in surface waters, leading to their eventual sink into the deep ocean in the Nordic Seas and Labrador Sea, i.e., the formation of North Atlantic Deep Water (NADW) (Rahmstorf, 2002; Stanford et al., 2011). As shown in Fig. 1.4, the NADW consists of three water masses: Denmark Strait Overflow Water (DSOW), Iceland Scotland Overflow Water (ISOW), and Labrador Sea Water (LSW). Depending on the differences in density, DSOW is the deepest component of NADW, whereas the LSW is the uppermost component (Hunter et al., 2007). The southward movement of NADW can be referred to as the Deep Western Boundary Current (DWBC). The northward transport of warm and saline Atlantic Water, coupled with the generation of deep waters in the subpolar North Atlantic,

constitutes the primary driving force behind the AMOC, which plays an important role in the Earth's climate system (cf., Rahmstorf, 2002; Caesar et al.,2018; Caesar et al., 2021).
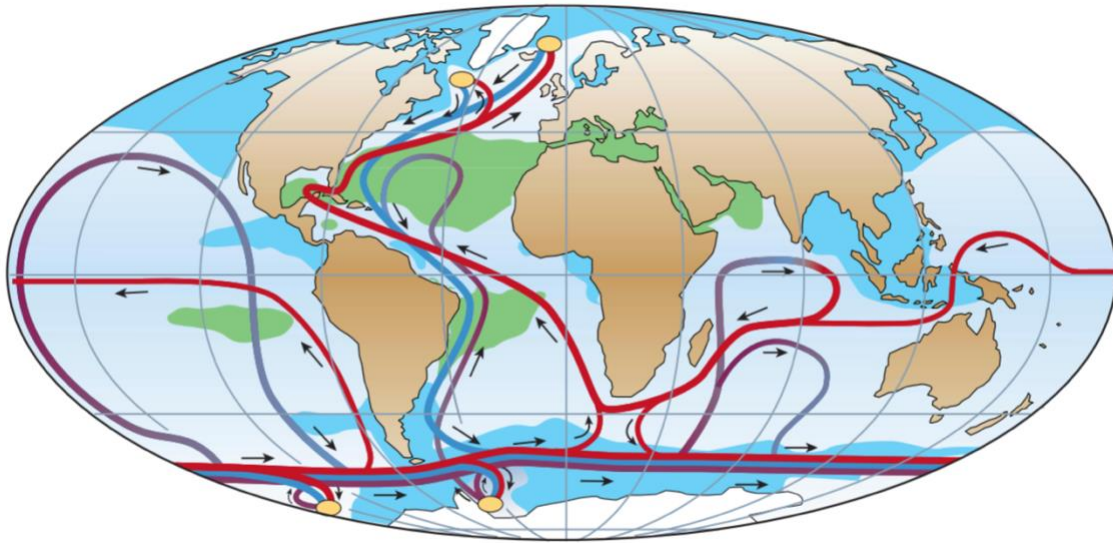
Fig. 1.3 The global ocean circulation (Figure from Rahmstorf, 2002). Yellow dots indicate locations where deep-water forms.
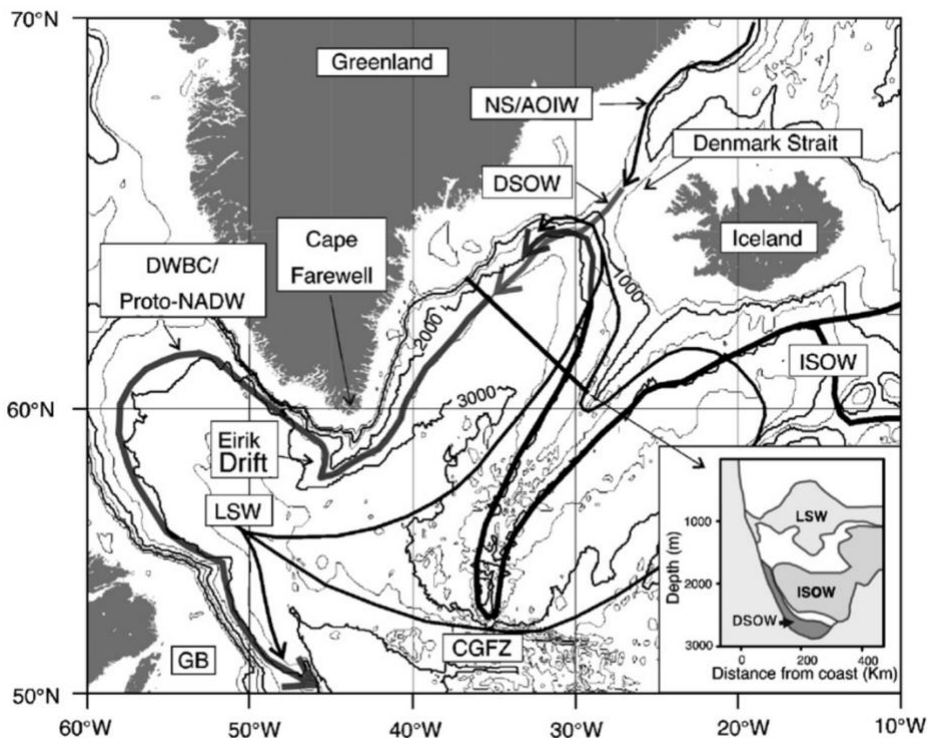
Fig. 1.4 Pathways of the main deep and intermediate water masses in the subpolar North Atlantic (Figure from Hunter et al., 2007). NS/AOIW, Norwegian Sea/Arctic Ocean Intermediate Water; DSOW, Denmark Strait Overflow Water; ISOW, Iceland Scotland Overflow Water; LSW, Labrador Sea Water. GB, Grand Banks; CGFZ, Charlie Gibbs Fracture Zone.

1.2.3 Sea ice

The modern sea ice distributions in the Northern Hemisphere are shown in Fig. 1.5. The satellite data shows the Labrador Sea maintains an ice-free condition throughout the entirety of the years, whereas Baffin Bay is covered by sea ice in winter but ice-free in summer. In addition, seasonal sea ice cover is prevalent in the eastern Greenland margin during the winter months, probably due to the impact of the East Greenland Current, whereas most of the Nordic Seas remain ice-free conditions all year round. Compared to the mean sea ice extent in 1981-2010, the summer sea ice extent shows a distinct retreat in the northeastern Greenland margin.
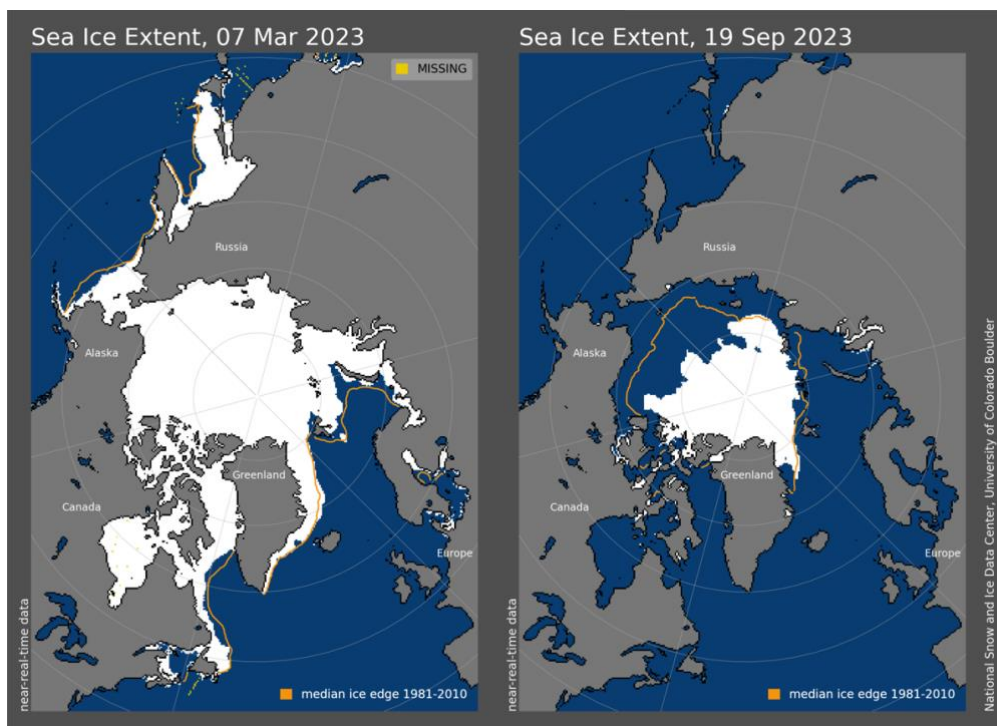
Fig. 1.5 Satellite-derived sea ice extent of the polar/subpolar regions in the Northern Hemisphere (Source: NSIDC, link: *https://nsidc.org*). The left panel shows the maximum sea ice extent in March 2023, and the right panel presents the minimum sea ice extent in September 2023. The orange lines indicate the median ice edge of 1981-2010.

1.2.4 Primary production and carbon flux

Phytoplankton contributes approximately half of global primary production (Tilstone et al., 2014) and primary production plays an important role in atmosphere-ocean carbon exchange and the export of carbon into the deep sea (Alkire et al., 2012). The dominant feature of primary production in the subpolar North Atlantic is the spring bloom. This phenomenon happens from April to June as the winter mixed-layer becomes shallower, thereby exposing surface layers with elevated nutrient concentrations to greater light availability and extended daylight hours (Tilstone et al., 2014). It has been proposed that sea ice plays a substantial role in influencing primary

production in the subpolar/polar regions. The seasonal melting of sea ice leads to shallowing of the mixed layer and eventually triggering the onset of the spring phytoplankton bloom (Frajka-Williams and Rhines, 2010; Chan et al., 2017; Wassmann et al., 2020). In the parts that are affected by melting of sea ice, the phytoplankton dynamics resemble those of the arctic shelf seas, and the bloom may take place as late as May (Sakshaug, 2004). As shown in Figure 1.6, the North Atlantic regions show high chlorophylⅡ concentrations in May, indicating that the subpolar and polar regions in the North Atlantic are predominant areas with high primary production in Spring.

Primary production produces large amounts of marine organic matter, subsequently sinking to the sea floor (Tilstone et al., 2014; Wassmann et al., 2020). Notably, annual primary production is around 100 g C m^{-2} in the Labrador Sea and around 60–120 g C m^{-2} in Baffin Bay (Sakshaug, 2004). The marine organic matter is an important component of ocean sediments in the Labrador Sea and Baffin Bay and is a prerequisite for biogeochemical studies. Given the strong lateral transport in the upstream regions of the subpolar North Atlantic, one major concern is whether marine organic matter is produced in the surrounding/local areas. Recent sea ice reconstruction based on biomarker proxies from surface sediments in the Labrador Sea and Baffin Bay shows a similar distribution to modern sea ice conditions (Kolling et al., 2020), indicating that organic matter predominantly comes from in suit sources. Additionally, radiocarbon age differences between biomarker (alkenones) and planktic foraminifera (in situ) in records from the Gardar Drift are negligible (Mollenhauer et al., 2011). This observation suggests that marine organic matter was deposited quite rapidly or only transported over a very short lateral distance, further supporting that marine organic matter in the subpolar North Atlantic primarily originates from the surrounding/local areas.
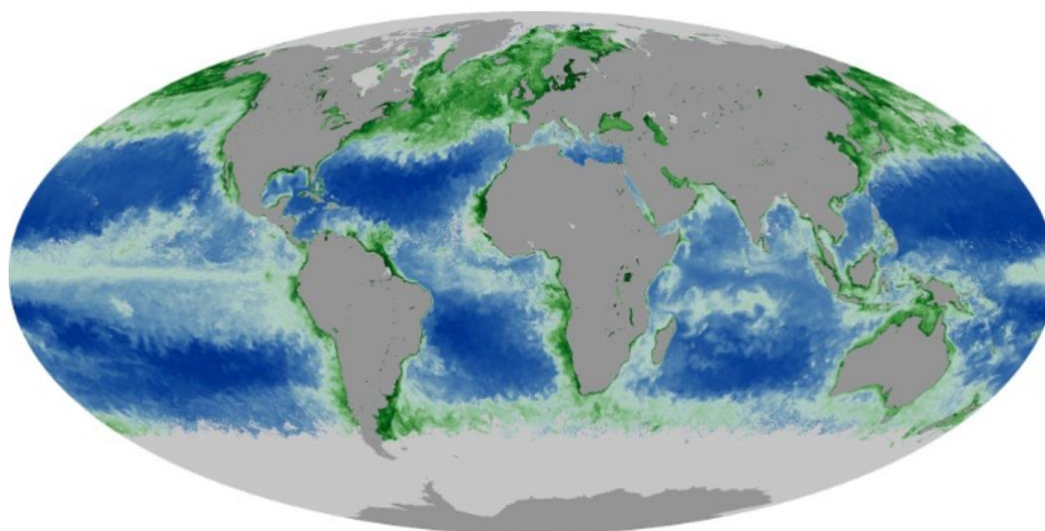
Fig. 1.6 Global distribution of chlorophyll concentrations in May.
(Source: NASA, link: *https://earthobservatory.nasa.gov/global-maps/MY1DMM_CHLORA*).

1.2.5 Detrital sediment sources and transport processes

Two prominent sources contribute to detrital sedimentation in the Labrador Sea. One source is fine-grained materials transported by ocean currents from upstream regions. The DWBC flows through the Irminger Sea and Labrador Sea in the subpolar regions and transports high-loading fine-grained materials from upstream regions due to high flow velocities and strong erosion (Elliot et al., 2002; Evans et al., 2007; Hunter et al., 2007). Notably, more oceanic basalts are eroded and transported from Greenland-Scotland Ridge by increased bottom currents, characterized by high titanium contents and magnetic susceptibility values (Kissel et al., 1999; Evans et al., 2007; Grützner and Higgins, 2010). The DWBC initially flows along the eastern edge of Greenland and later redirects at the southern Greenland margin to flow along the western edge. The shift in flow direction results in a decrease in flow velocities, thus leading to the rapid deposition of suspended material by bottom currents, forming an expanded sedimentary body called the Eirik Drift (Fig. 1.7; Hunter et al., 2007). The similar situations (i.e., high lateral transport from upstream regions) are also observed in the Reykjanes Ridge, forming Björn Drift and Gardar Drift in the Iceland Basin within the Northeastern Atlantic (Mollenhauer et al., 2011).
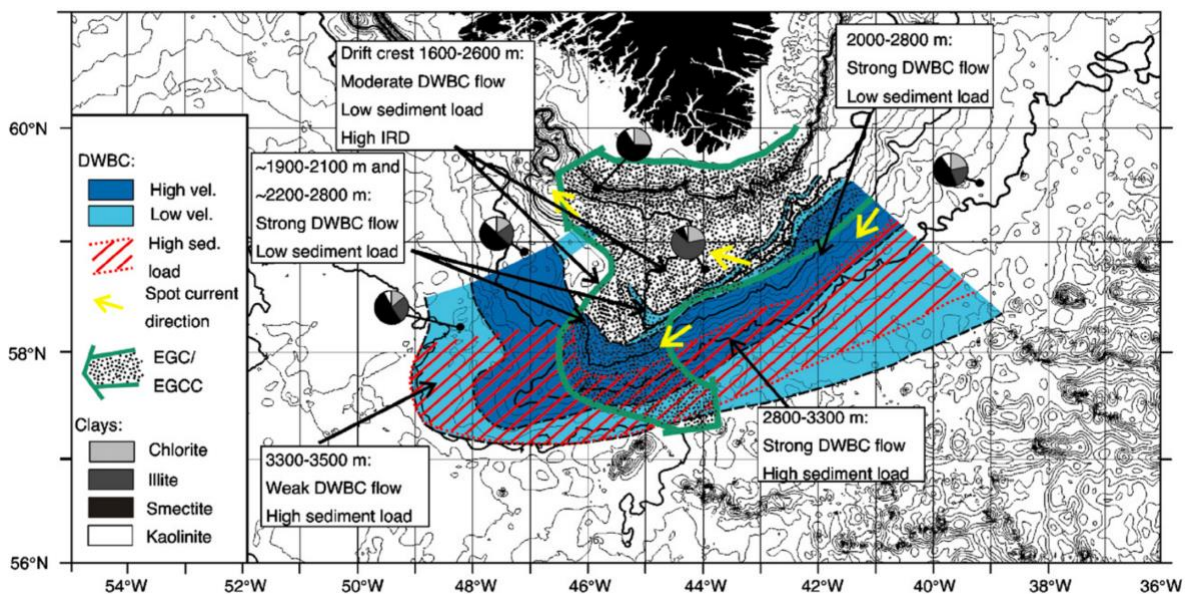
Fig. 1.7 Spatial distribution and distinct loading situation of Deep Western Boundary Current (DWBC) in the southern Greenland margin (Figure from Hunter et al., 2007). The yellow arrows show the direction of deep current flow, determined from spot current measurements, where the velocity exceeded 20 cm s^{-1}. The pie diagrams show the relative proportions of clay minerals in the surface sediment at various locations across the study area (Data from Fagel et al., 1996).

The influx of detrital material from Greenland is another important constituent of detrital sediment in the Labrador Sea and also Baffin Bay. Detrital material input becomes particularly pronounced under sustained warming conditions characterised by more meltwater and iceberg

discharge into the subpolar/polar regions due to the decay of the GrIS (Yang et al., 2016; Choi et al., 2021; Box et al., 2022). The meltwater discharge contributes fine-grained suspensions to the ocean, while iceberg discharge facilitates the transport of coarse fractions alongside fine materials (Weiser et al., 2021). Notably, the ocean-terminating glaciers are more easily influenced by changes in adjacent ocean conditions, thus producing more detrital materials into the ocean (Pattyn et al., 2018; King et al., 2020; Wood et al., 2021; Choi et al., 2021). For Baffin Bay, detrital contributions from Baffin Island and the Canadian Archipelago constitute other principal sources of detrital sediment (cf., Simon et al., 2016; Ownsworth et al., 2023; Okuman et al., 2023).

1.3 Recent climate changes in subpolar/polar regions

1.3.1 Modern observation and modelling research

Over the past three decades, the Arctic sea ice extent has exhibited significantly decreasing trends in summer, which has raised much concern (Fig. 1.8). Decrease in Arctic sea ice extent in summer has been unprecedented in the past 150 years as evidenced by historical reconstructions (Shukla et al., 2019). The reduced summer sea ice extent has led to expanded open water areas and prolonged ice-free conditions in the surrounding marginal seas and shelves of the Arctic Ocean (Serreze et al., 2007; Frey et al., 2015). Additionally, Arctic sea ice thickness has also diminished over the satellite observation period starting in 1979, and this trend remains consistent within the updated time series (Fig. 1.9; Masson-Delmotte et al., 2021; Sumata et al., 2023). Sustained observations show that the upper ocean temperature across the Arctic outflow with the East Greenland Current in the Fram Strait has increased significantly between 2003 and 2019, impacting winter sea ice thickness and extent downstream along the whole east coast of Greenland (de Steur et al., 2023). It's noteworthy that more than half of the observed decline in Arctic summer sea ice is attributed to higher concentrations of atmospheric greenhouse gases, while the remaining portion is linked to internal climate variability (Masson-Delmotte et al., 2021). Resulting from the shrinking sea ice extent, the ice-free regions absorb more solar energy during the summer months, resulting in heat accumulation in the upper ocean (Perovich et al., 2007). Consequently, this excess heat intensifies ice melting in the marginal ice zone during summer and delays the formation of new ice in the autumn (Stroeve et al., 2014). In addition, climate model projections suggest that more warm Atlantic Water may continue expanding to the Kara Sea and then to the Arctic Basin in a warming climate (i.e., Arctic Atlantification) (Shu et al., 2021). To enhance our understanding of natural factors for sea ice changes, more studies on sedimentary records from the subpolar/polar regions are needed.
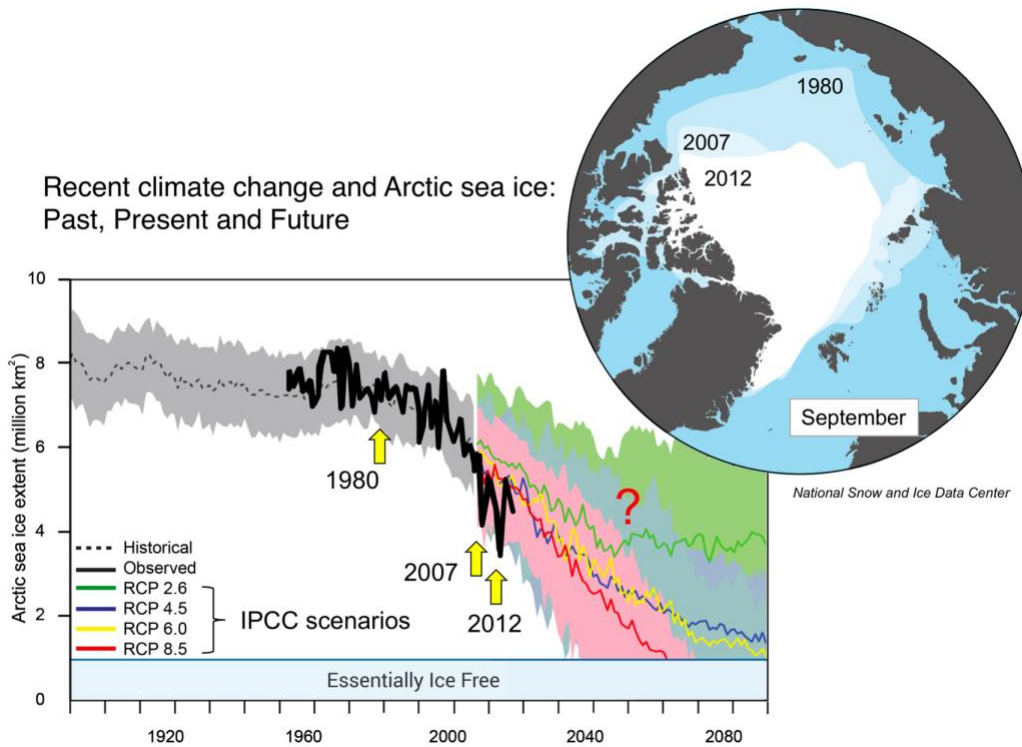
Fig. 1.8 September sea ice extent in the Arctic Ocean (1890–2090) based on historical data, direct observations/measurements, and projected by different climate models and different IPCC scenarios toward 2090 (Figure from Stein, 2019). RCP = Representative Concentration Pathways of greenhouse gases in relation to the probable radiative forcing in 2100. The shaded area represents the standard deviation (Stroeve et al., 2007; Stroeve et al., 2012; Stocker et al., 2013). Map shows September sea ice extent in 1980, 2007, and 2012 (Source: NSIDC, link: *https://nsidc.org*).
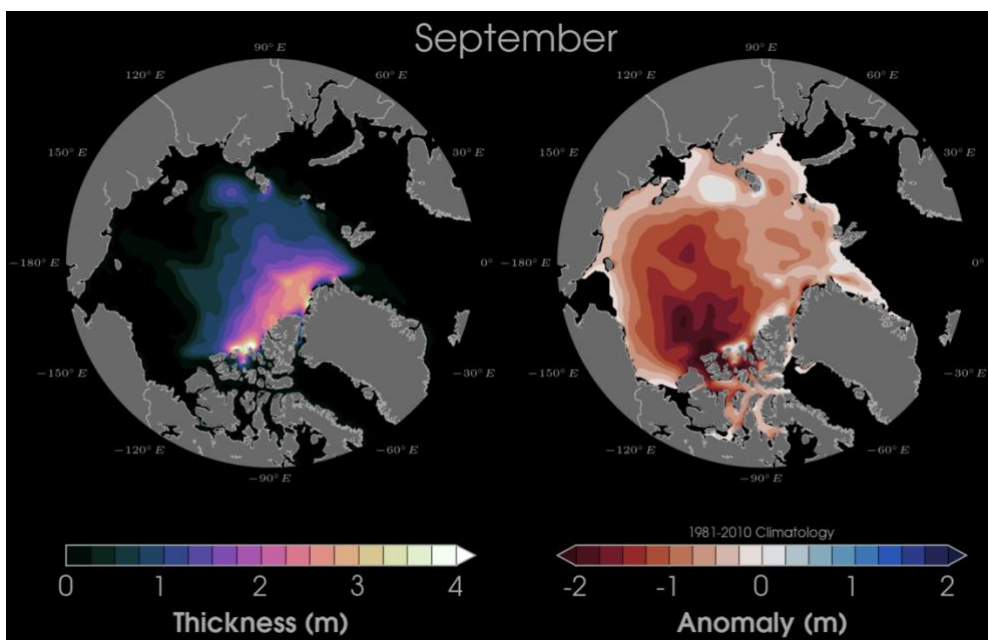
Fig. 1.9 Current simulated sea ice thickness and anomalies (1981-2010 baseline) updated for September 2023 (Source: Zachary Labe, link: *https://zacklabe.com/arctic-sea-ice-volumethickness/*).

Ice loss from the GrIS has also accelerated over the past decade and significant mass loss is observed in the southern and western Greenland regions (Fig. 1.10). Increased melting of the GrIS leads to increased meltwater discharge and rising sea levels (Yang et al., 2016; Flowers, 2018; Box et al., 2022; Hörhold et al., 2023). On the basis of estimates, Greenland lost 3.902 ± 342 billion tonnes of ice between 1992 and 2018, causing the mean sea level to rise by 10.8 ± 0.9 mm (Briner et al., 2020). Surface ablation and retreat of marine-terminating glaciers are the main processes of mass loss of ice sheets observed today (Fig. 1.11; Catania et al., 2019; Choi et al., 2021). Compared to inland ice sheet processes, increased glacier discharge is closely related to the retreat of glacier fronts (King et al., 2020; Wood et al.,2021). Notably, modelling research indicates that ice front retreat and ice flow acceleration are likely to account for 50% or more to meltwater discharge by the end of this century, with a significant contribution from northwest and central west Greenland (Choi et al., 2021). However, the retreat processes of marine-terminating glaciers and corresponding factors are still not fully understood.
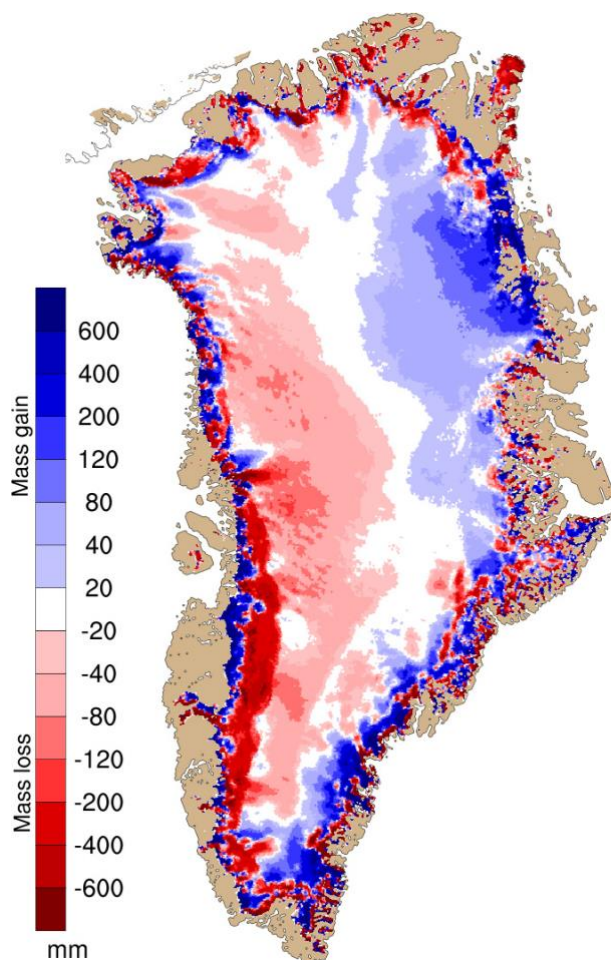
Fig. 1.10 Map shows the difference between the annual surface mass balance in 2019-2020 and the 1981-2010 (Source: CarbonBrief, link: *https://www.carbonbrief.org*). Blue shows more ice gain than average and red shows more ice loss than average.
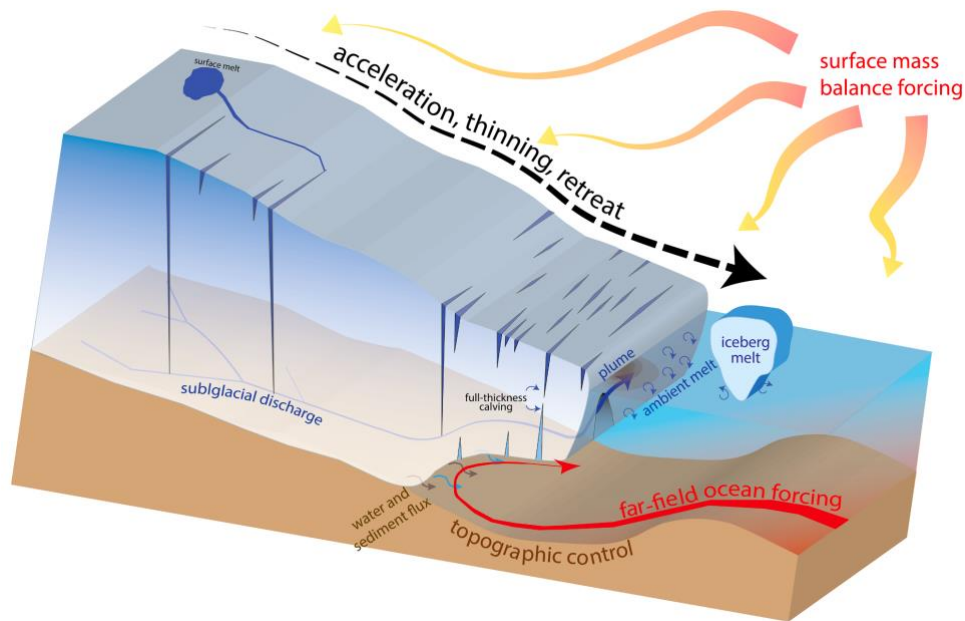
Fig. 1.11 Schematic illustration of outlet glacier processes involving the atmosphere, ice sheet, substrate, and ocean (Figure from Catania et al., 2019).

Observation and simulation of AMOC variability is another research hotspot, which may tell us how the ocean circulation responds to natural and anthropogenic changes. Modern measurements provide evidence for a weakening of the AMOC since the mid-twentieth century (Fig. 1.12; Srokosz and Bryden, 2015; Caesar et al., 2018; Jackson et al., 2022), possibly related to the melting of GrIS/meltwater discharge (Rahmstorf et al., 2015; Böning et al., 2016). Projections from recent research indicate that under the continued escalation of CO_2 emissions, the AMOC could potentially experience a collapse by the middle of this century (Ditlevsen and Ditlevsen, 2023). Many observations in the subpolar North Atlantic reflect that ocean overturning variability at subpolar latitudes is generated by the combined effects of wind stress and surface buoyancy anomalies (Kostov et al., 2021). On decadal timescales, freshwater flux anomalies in the subpolar North Atlantic may induce the most significant influence on the AMOC, while over multi-decadal timescales (exceeding 20 years), flux anomalies in the Arctic may play a more crucial role, e.g., Arctic sea ice decline contributes to the weakened AMOC, and subsequently reduced poleward heat transport (Sévellec et al., 2017).
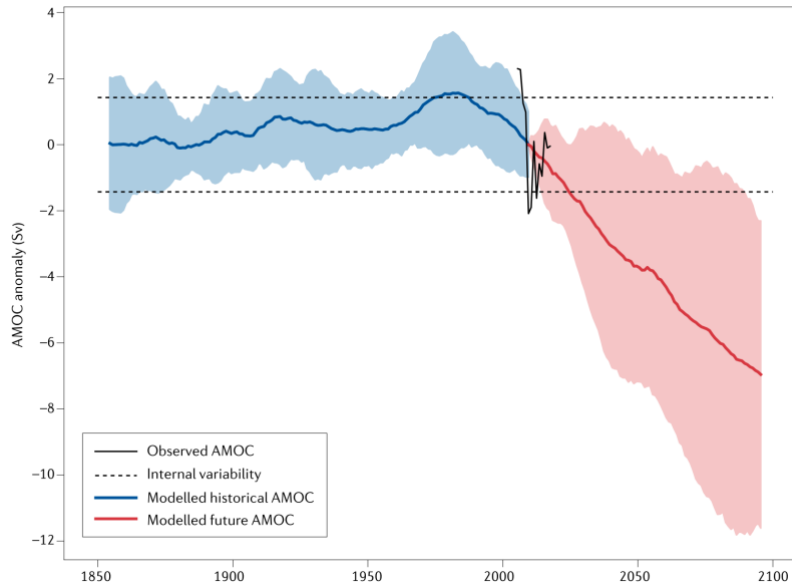
Fig. 1.12 Past and future AMOC changes from climate models (Figure from Jackson et al., 2022). Green line and red line indicate modelled historical and future AMOC anomaly, respectively. Annual mean observed AMOC anomalies from RAPID (black); the black horizontal lines indicate the internal variability of the AMOC; for modelled scenarios, the mean illustrates the forced response to changes in greenhouse gases and aerosols.

1.3.2 Significance of subpolar/polar regions in recent climate change

Sea ice plays a critical role in the polar system and is highly responsive to changes in various factors such as atmospheric circulation, incoming radiation, atmospheric and oceanic heat transfer, and the hydrological cycle (Fig. 1.13; Curry et al., 1995; Rudels et al., 1996; Thomas and Dieckmann, 2008). Sea ice significantly moderates the heat exchange between the ocean and atmosphere and has a profound impact on the polar's radiation budget due to its high albedo. Compared to open water with an albedo of 0.10, the albedo of ice ranges from 0.6 to 0.8 (Serreze and Barry, 2011). This higher albedo results in ice-covered surfaces reflecting as much as 8 times more incoming shortwave radiation. In turn, reduced sea ice cover leads to increased solar radiation penetrating the ocean, subsequently causing elevated sea surface temperatures and further amplifying Arctic warming, which is referred to as Arctic Amplification (Fig. 1.14; Serreze and Barry, 2011; Dai et al., 2019). In addition, reduced sea ice enables greater heat and moisture transfer from the ocean to the land, potentially leading to additional greenhouse gas emissions through the thawing of inland permafrost (Vaks et al., 2020). Moreover, the presence of sea ice strongly influences biological productivity. A more extended sea ice cover limits primary production by reducing light penetration. In the Arctic Ocean, sea ice also acts as a crucial agent for freshwater transportation. Increased sea ice export through the Fram Strait by the East Greenland Current may lead to decreased surface salinity in the Nordic Seas, subsequently affecting NADW formation (Sévellec et al., 2017). Beyond polar regions, a recent

simulation reveals that a decrease in Arctic sea ice extent may also trigger at least 37-48% of the increase of strong El Niño near the end of the 21st century (Liu et al., 2022). Therefore, to better predict future sea ice changes, studying the natural factors that influence sea ice variation is of special interest.
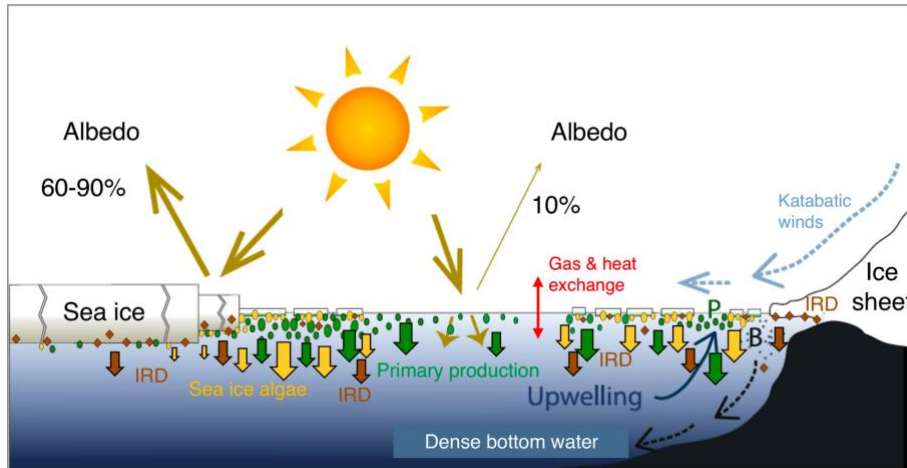
Fig. 1.13 Simplified scheme indicating the role of sea ice in the climate and ocean system (Figure from Stein, 2019 based on de Vernal et al., 2013, supplemented). The left part indicates the modern central and ice-edge Arctic area; the right part indicates the glacial Arctic situation with ice sheets reaching the shelf break, a situation similar to the modern circum-Antarctic situation. Letter B represents brine formation, and letter P indicates polynyas.
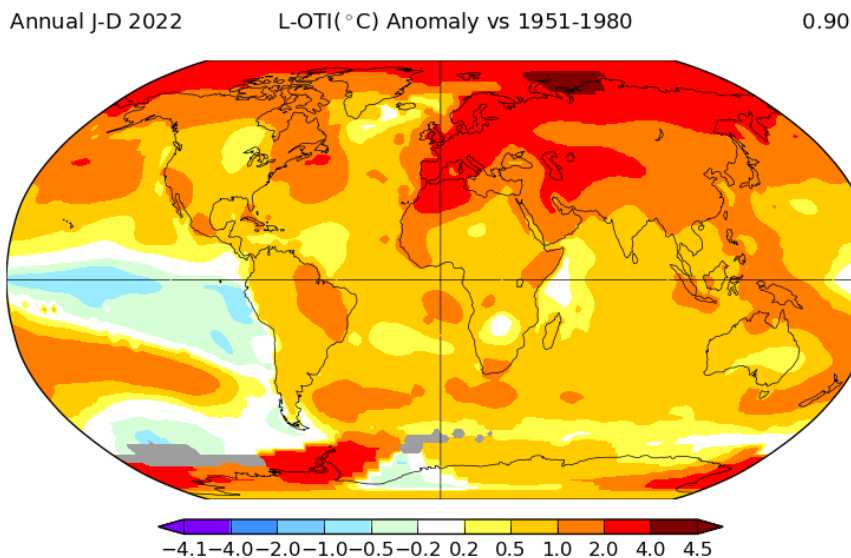
Fig. 1.14 Surface temperature anomaly in 2022 compared to the average temperature between 1951-1980 (Source: NASA, link: *https://data.giss.nasa.gov/gistemp/maps/index_v4.html*).

Fluctuations in atmospheric mass in the subpolar and polar regions, especially the Arctic Ocean, correlate with the Arctic Oscillation (AO) and the North Atlantic Oscillation (NAO), affecting climate changes in the continental area of the Arctic, Europe, and North America (Hurrell, 1995; Nakamura et al., 2015; Liu and He, 2020). Increased (reduced) Arctic sea ice cover in November may alter the wind patterns, leading to positive (negative) phases of the AO and NAO in winter (Darby et al., 2012; Nakamura et al., 2015). During a positive AO/NAO, the polar vortex remains strong, resulting in low atmospheric pressure in the Arctic and high atmospheric pressure over the subtropics (Fig. 1.15). The following northward shift of the Jet Stream leads to colder conditions around the North Pole, drier and warmer climates in the US, and milder and wetter conditions in Europe (Ambaum et al., 2001; Seager et al., 2020). During the negative phase of the AO/NAO, a weaker polar vortex and lower pressure in the Arctic induce a southward shift of the Jet Stream, allowing colder air masses and storms to move further southward, which affects weather in Europe and the US with harsher winter conditions (Stroeve et al., 2011).
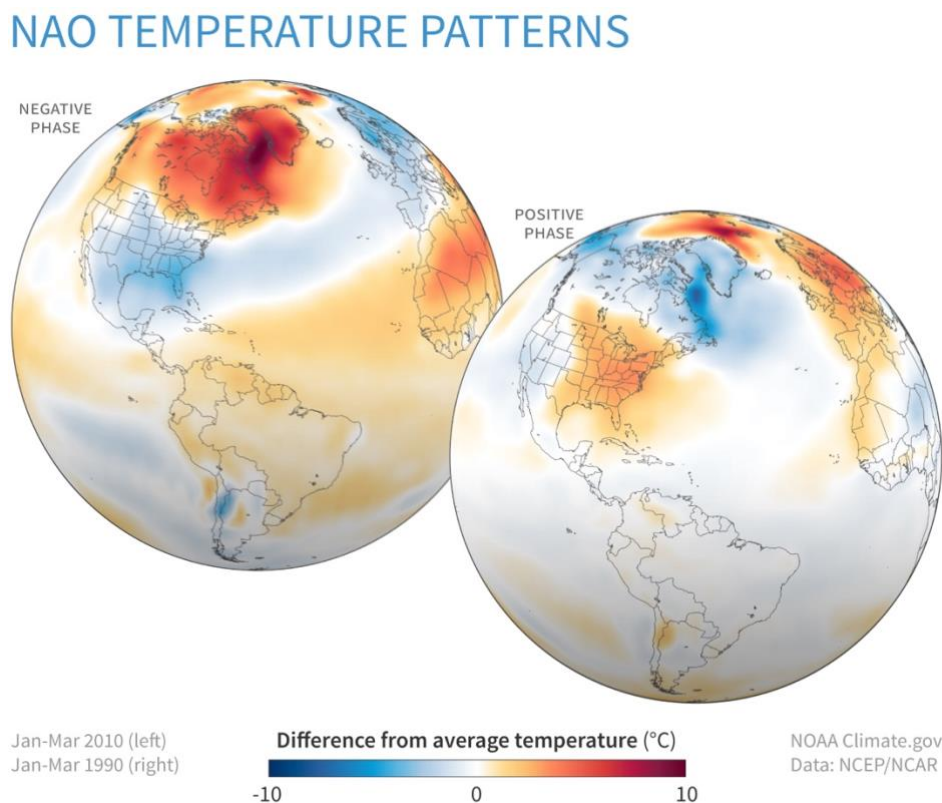
Fig. 1.15 Late winter temperature patterns compared to the 1981-2010 average under strongly negative (Jan-Mar 2010) and strongly positive (Jan-Mar 1990) North Atlantic Oscillation (NAO) (Source: NOAA, link: *https://www.climate.gov*).

The subpolar and polar oceans play an important role in global ocean circulation (Fig. 1.3). As an important component of the Earth System, the AMOC is a crucial mechanism responsible for redistributing heat across the Earth, contributing to approximately 20-30% of the total atmospheric and oceanic heat transport northwards. Therefore, the AMOC has a significant influence on climate change of the North Atlantic region and beyond, such as European air temperatures and precipitation, the frequency of Atlantic hurricanes and winter storms, spatial patterns of sea level and tropical monsoons, and the global carbon budget (McCarthy et al., 2015; Bellomo et al., 2021; Jackson et al., 2022). As introduced in section 1.2.2, the AMOC is closely related to the sinking of warm and saline Atlantic Water in the Nordic Seas and Labrador Sea, i.e., the NADW formation (Rahmstorf, 2002). Thus, changes in sea surface characteristics in the Nordic Seas and the Labrador Sea may affect the deep-water formation, subsequently disrupting AMOC/climate. The weakening AMOC observed in recent years has been suggested to be related to accelerated freshwater input from the Arctic Ocean and the GrIS (Srokosz and Bryden, 2015; Jackson et al., 2022). The sustained and increasing freshwater fluxes from Greenland could lead to a suppression of deep winter convection in the Labrador Sea with potential influence on the strength of AMOC (Rahmstorf et al., 2015), and such restricted ocean convection may enhance in the coming years (Böning et al., 2016). Furthermore, it has been proposed that the decline in net primary production in the subpolar Atlantic ($10 \pm 7\%$ decline over the last two centuries) closely coincides with Arctic surface warming and a weakened AMOC. Thus, if the AMOC continues to weaken as projected for the twenty-first century, it could lead to further declines in productivity across this globally relevant region (Osman et al., 2019).

1.4 Climate change during the late Quaternary

The Quaternary, a geological epoch dating back to 2.58 Ma, consists of the Pleistocene and Holocene. The most prominent feature of the Quaternary climate evolution is glacial-interglacial cycles caused by latitudinal and seasonal variations in solar radiation, which are controlled by orbital parameter cycles, known as Milankovitch cycles. These orbital parameters comprise eccentricity, obliquity, and precession, which have 400 kyr/100 kyr, 41 kyr, and 23 kyr cyclicities, respectively (Milankovitch, 1941; Imbrie et al., 1992). Eccentricity mainly modulates the total amount of radiation reaching the Earth. Obliquity primarily controls the latitudinal distribution of solar radiation and has a significant effect at high-latitude regions. Precession mainly controls the seasonal distribution, amplifying seasonality shifts in one hemisphere while reducing them in the other. During the Mid-Pleistocene Transition (MPT, spanning from 1200 to 800 ka), the dominant cycles changed from 41 kyr to 100 kyr, i.e., a shift in the periodicity of glaciations (Clark et al., 2006; McClymont et al., 2013). This transition resulted in more extensive and longer-lasting ice sheets in the Northern Hemisphere (Chalk et al., 2017; Batchelor et al., 2019; Barker et al., 2021). Following the MPT (i.e., during the late Quaternary), glacial cycles varied between 80 kyr and 120 kyr in length with an average recurrence interval of about 100 kyr (Denton et al., 2010).

1.4.1 The last glacial period

The last glaciation is the last glacial period during the late Quaternary, happening during the marine isotope stage (MIS) 4 to MIS 2 (around 71-11.7 ka) (Lisiecki and Raymo, 2005). This period is marked by a sequence of abrupt millennial-scale climate shifts alternating between cold (stadial) and warm (interstadial) conditions, closely linked to fluctuations in the strength of the AMOC (Fig. 1.16; Sirocko et al., 2021; Barker and Knorr, 2021). Notable examples of these shifts include the Dansgaard-Oeschger (D/O) cycles observed during MIS 3 and the Heinrich Events (HEs).

The Greenland Ice Core records reveal the presence D/O cycles, recurring every 1-2 kyr (Dansgaard et al., 1993; Dokken et al., 2013). D/O cycles exhibit a distinctive pattern characterized by an abrupt temperature increase of approximately $10 \pm 5°C$ from a cold stadial phase to a warm interstadial phase, followed by a gradual cooling (Dokken et al., 2013). However, the mechanisms responsible for D/O cycles remain not fully understood. Recent modelling studies suggest that the occurrence of such abrupt events was related to intermediate states of the Earth system, including the strength of AMOC, CO_2 level, and freshwater discharge in the North Atlantic regions (Menviel et al., 2020; Barker and Knorr, 2021) or direct astronomical influence (Zhang et al., 2021). Sea ice reconstructions in the Nordic Seas indicate that rapid sea ice

reductions occurred at the onset of D/O events and preceded the recovery of deep-water formation in the Nordic Seas, i.e., sea ice retreat in the subpolar regions triggered or amplified the abrupt heat release from the ocean to the atmosphere in the North Atlantic regions, leading to abrupt increases in air temperatures (Bakke et al., 2009; Hoff et al., 2016; Sadatzki et al., 2019, 2020). The sea ice retreat might have been induced by a northward-shifted jet and subsequently vigorous subpolar gyre (Li and Born, 2019) or enhanced warm water inflow due to salinity exceeding the threshold (Vettoretti and Peltier, 2016; Jensen et al., 2016).
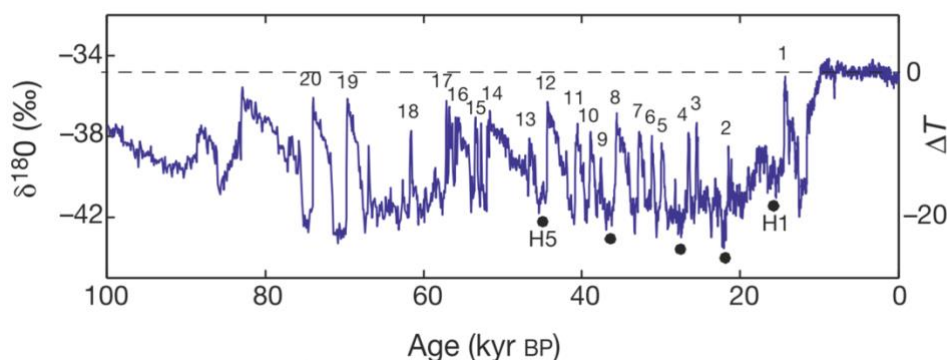
Fig. 1.16 Abrupt climate changes in Greenland Ice Core data during the last 100 ka (Figure from Ganopolski and Rahmstorf, 2001). Record of $\delta^{18}O$ from the GRIP core (Grootes et al., 1993) and estimated atmospheric temperature (in °C) over Greenland (Dahl-Jensen et al., 1998). The glacial climate is punctuated by Dansgaard-Oeschger (D/O) warm events (numbered). The timing of Heinrich events H1-H5 is marked by black dots.

The HEs are characterized by the anomalous occurrence of ice-rafted debris (IRD) in the subpolar North Atlantic spanning a broad area between 46°N and 50°N, often referred to as the IRD belt (Fig. 1.17; Ruddiman, 1977; Hemming, 2004). These events have been proposed to be caused by massive iceberg discharge into the subpolar North Atlantic, identified by IRD layers in the sediment as well as low concentrations of foraminifera (Fig. 1.18; Hemming, 2004; Hodell et al., 2008; Andrews and Voelker, 2018). The HEs are also characterized by the presence of detrital carbonate from the Hudson Strait, especially during HE5, HE4, HE2, and HE1 (Hemming, 2004; Hodell et al., 2008, 2017; Channell et al., 2012). Additionally, detrital input during HE0 might also be tracked back to the iceberg discharge from the Hudson Strait caused by the decay of the LIS (Andrews et al., 1995; You et al., 2023). However, for HE6 and HE3, the LIS might have not been the primary contributor to detrital input, and the involvement of other circum-Atlantic ice sheets should be taken into account (Hemmings, 2004; Naafs et al., 2013; Zhou et al., 2021). The occurrence of HEs has been proposed to be triggered by subsurface warming in the Labrador Sea/subpolar North Atlantic which has caused enhanced basal melting (cf., Alvarez-Solas et al., 2010; Marcott et al., 2011; Hodell et al., 2017; Max et al., 2022). Massive iceberg discharge during HEs might have caused surface freshening in the subpolar regions, preventing

deep-water formation in the North Atlantic, which led to a weakened AMOC and ultimately disrupted the climate (Praetorius et al., 2008; Lippold et al., 2012; Bohm et al., 2015; Thornalley et al., 2015; Henry et al., 2016; Lohmann et al., 2020). It is worth noting that Henrich Stadials (HS) did not correspond to HEs. HSs refer to the cold intervals documented in Greenland Ice Core records, whereas HEs indicate the periods with a large amount of detrital material from the LIS (Andrews and Voelker, 2018).
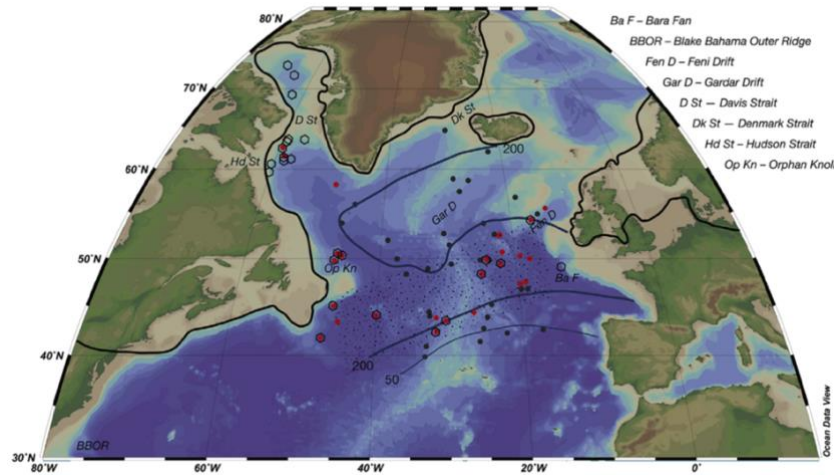
Fig. 1.17 Core sites of the initial Heinrich layer/event studies (red dots; published between 1988 and 1999) and sites with a detrital carbonate signal during Heinrich events (polygons) (Figure from Andrews and Voelker, 2018). Dark gray dots: core sites studied by Ruddiman (1977); the stippled area: the region referred to as the "IRD belt"; dark blue lines: IRD flux (mg cm^{-2} kyr^{-1}) from Ruddiman (1977) for the period from 40 to 25 ka, with numbers 200 and 50 indicating IRD flux; black lines: ice sheet extents during the LGM.
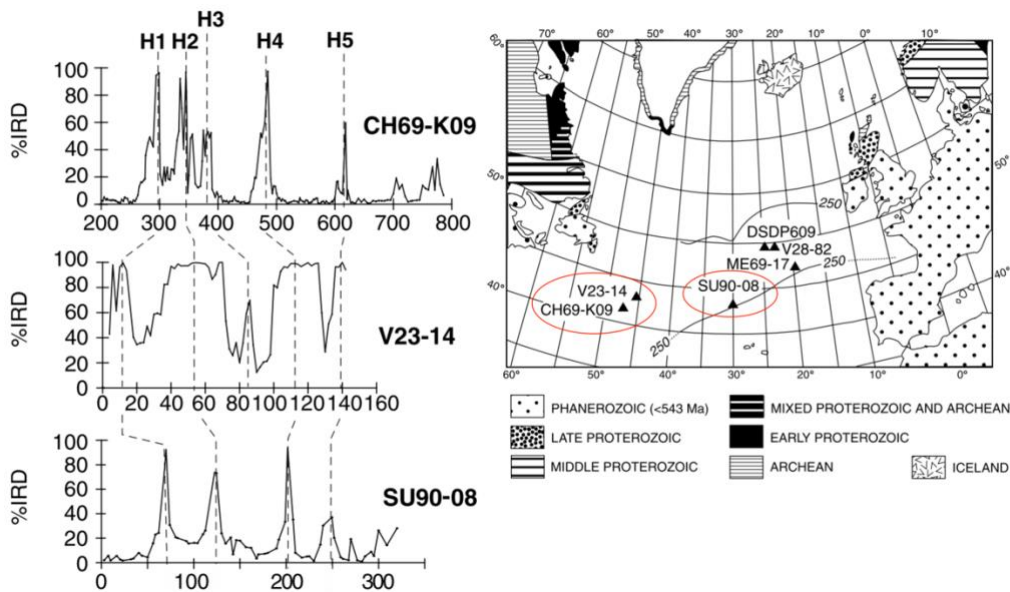
Fig. 1.18 Ice-rafted debris (IRD) concentrations for North Atlantic sediment cores with Heinrich layers (Modified from Hemming, 2004). The left panel only shows the records from Core CH69-K09 (Labeyrie et al., 1999), V23-14 (Hemming and Hajdas, 2003), and SU90-08 (Grousset et al., 1993). Refer to Hemming, (2004) for full records. Black lines are 250 mg cm^{-2} kyr^{-1} IRD flux lines for the period from 25 to 13 ka.

The last glacial maximum (LGM) is the interval when the global ice sheets and mountain glaciers reached their maximum extents in response to decreased northern summer insolation (Fig. 1.19; Clark et al., 2009; Patton et al., 2016; Margold et al., 2018; Batchelor et al., 2019). The sea level fell around 120 meters during the LGM and began to rise around 19 ka BP (i.e., the onset of the last deglaciation) due to the retreat of the ice sheets in the Northern Hemisphere (Clark et al., 2009). Different from weakened deep-water formation during HEs, a large-scale reorganization of deep-water formation in the Nordic Seas occurred during the LGM (Larkin et al., 2022). The active convection in the North Atlantic regions during the LGM might have been improved by the huge volumes of Northern-Hemisphere ice sheets, potentially altering the coupled atmosphere-ocean system (Zhang et al., 2014). Furthermore, such active ventilation in the North Atlantic might have induced higher carbon pump efficiency compared to the Holocene and enhanced CO_2 absorption contributing to lower CO_2 levels (Yu et al., 2019).
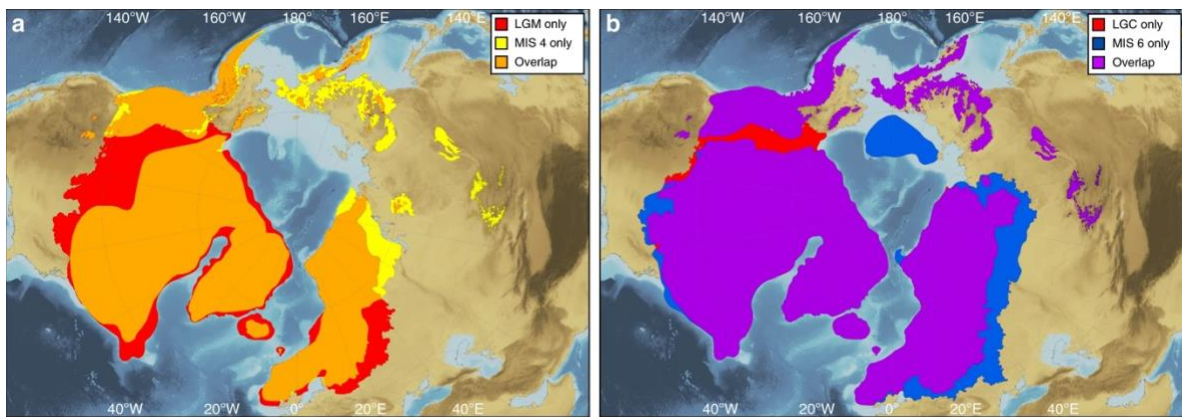
Fig. 1.19 Comparison of North Hemisphere ice-sheet extent during the last glacial cycle and MIS 6 (Figure from Batchelor et al., 2019). (a) comparison of the reconstructed ice-sheet extent during the LGM and MIS 4. (b) comparison of the reconstructed ice-sheet extent during the last glacial cycle (LGC, MIS 5d–2) and MIS 6.

1.4.2 The last deglaciation

The last deglaciation is a transition period from the LGM to the Holocene, with significant decay of the Northern Hemisphere ice sheets, rising sea level, and increased CO_2 levels (Denton et al., 2010; Lambeck et al., 2014; Yu et al., 2022). As an unstable transition characterized by millennial-scale abrupt climate changes, the last deglaciation contains several outstanding abrupt events such as HE1, Bølling/Allerød warm period (B/A), Younger Dryas cold event (YD) (Fig. 1.20; Svensson et al., 2008). Modelling research suggests that the occurrence of these abrupt events was related to variations in the AMOC, which has been linked to direct external forcing (i.e., astronomical influence) as well as internal feedback from the Earth system, including changes in Northern Hemisphere ice sheet heights, freshwater perturbations, and CO_2 levels (cf., Denton et al., 2010; Thornalley et al., 2010; Barker and Knorr, 2021; Zhang et al., 2021; Sun et

al., 2022; Pöppelmeier et al., 2023). However, the mechanisms of deglacial abrupt climate changes are still not fully understood.

Compared to extremely cold intervals (i.e., HS1 and YD), the Bølling/Allerød interval (14.7-12.9 ka BP) was a relatively warm period shown in the Greenland Ice Core records (Fig. 1.20; Rasmussen et al., 2006; Svensson et al., 2008). During the Bølling warm period, air temperatures in the Northern Hemisphere abruptly increased (Svensson et al., 2008), resulting in the melting of ice sheets and subsequent sea-level rise. The most rapid global sea-level rise event (MWP-1A) occurred around 14.65 ka BP (Fig. 1.21; Deschamps et al., 2012; Lambeck et al., 2014; Gregoire et al., 2016; Lin et al., 2021). Considerable uncertainty remains regarding the sources of meltwater discharge during MWP-1A. Model simulations suggest that meltwater from the LIS contributed the most to global sea-level rise (12 m), followed by the Eurasian Ice Sheet (4.6 m) and the Antarctic Ice Sheet (1.3 m) (Ivanovic et al., 2017; Lin et al., 2021). However, proxy records from the Norwegian Sea indicate that the Eurasian Ice Sheet might be the major source of MWP-1A (Brendryen et al., 2020). The occurrence of the Bølling warm period has been proposed to be caused by a sudden termination of freshwater discharge to the North Atlantic, resulting in a rapid recovery of the AMOC as a transient response (Liu et al., 2009). In contrast, recent simulations suggest that despite persistent deglacial meltwater influxes during this time interval, increasing CO_2 levels may have triggered the AMOC recovery, in combination with changes in the magnitude or routing of meltwater discharge (Zhang et al., 2017; Sun et al., 2022). Notably, the onset of rapid increases in atmospheric CO_2 was observed at 17.5 ka BP and increased by ~75ppm during the last deglaciation (Fig. 1.22; Monnin et al., 2001; Schmitt et al., 2012). In contrast to the Bølling warm period, the Allerød period was a relatively cold interval (Rasmussen et al., 2006), including two major meltwater-related cold phases (the Older Dryas stadial and Intra-Allerød Cold period) (Fig. 1.20; Yu et al., 1998; Thornalley et al., 2010). The primary source of these two meltwater events is still not clear, probably related to meltwater discharges from the LIS (Thornalley et al., 2010).
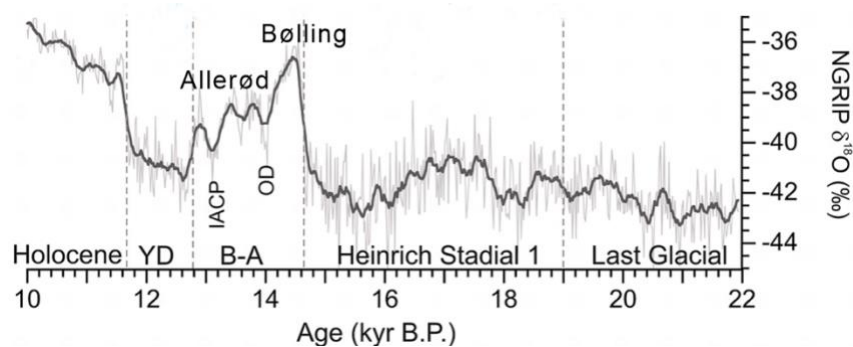
Fig. 1.20 Greenland Ice Core record (NGRIP-δ^{18}O) during the last 22-10 ka (Modified from Thornalley et al., 2011, based on Rasmussen et al., 2006). B-A: the Bølling-Allerød warm period, YD: the Younger Dryas cold event, OD: the Older Dryas cold event, IACP: the Intra-Allerød Cold period.
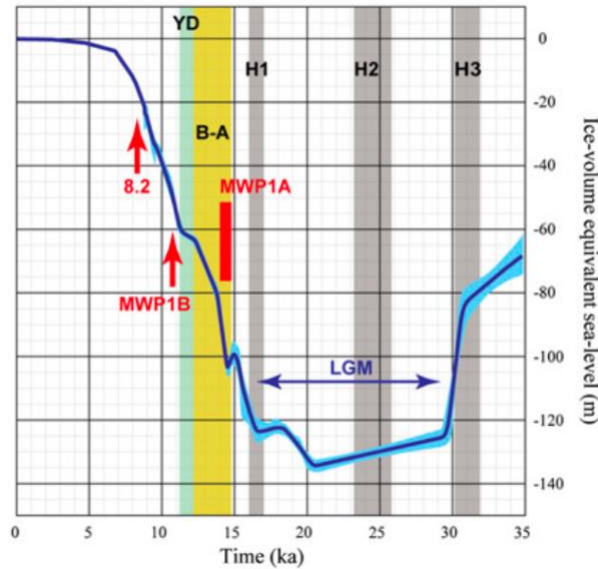
Fig. 1.21 Ice-sheet equivalent sea-level (m) estimates since the last 35 ka (Figure from Lambeck et al., 2014). Major climate events are shown: the Last Glacial Maximum (LGM), Heinrich events H1 to H3, the Bølling-Allerød warm period (B-A), and the Younger Dryas cold event (YD) as well as the timing of meltwater pulse (MWP)-1A, MWP-1B, and the 8.2 ka BP cold event.
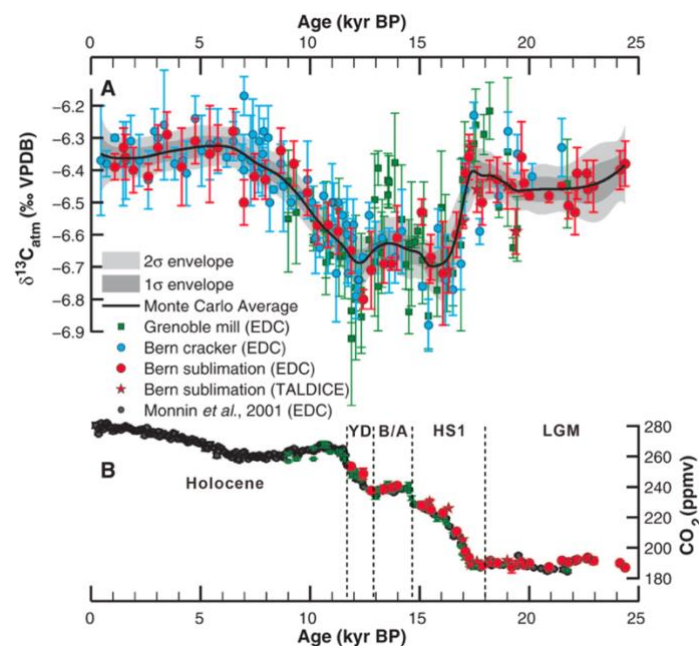
Fig. 1.22 Ice core reconstructions of atmospheric $\delta^{13}C$ and CO_2 concentration during the past 24 ka (Modified from Schmitt et al., 2012). (A) $\delta^{13}C_{atm}$ of atmospheric CO_2 measured with three different methods on two different ice cores. Error bars represent SD of replicate measurements where available and the mean SD for single measurements. The black line is the result of 4000 Monte Carlo simulations representing an error-weighted average of the different $\delta^{13}C_{atm}$ datasets. (B) CO_2 concentration. Black circles represent earlier measurements on EPICA Dome C (EDC) (Monnin et al., 2001); other symbols are the same as in (A). All ice core records are plotted on a synchronized age scale (Lemieux-Dudon et al., 2010). The last glacial maximum (LGM), Heinrich Stadial 1 (HS1), the Bølling-Allerød warm period (B/A), and the Younger Dryas cold event (YD).

The YD is the cold interval following the B/A warm period, resulting from a slowdown of the AMOC (McManus et al., 2004; Svensson et al., 2008; Muschitiello et al., 2019). Despite abrupt changes in the AMOC really being a characteristic feature of glacial terminations, the abrupt transition during YD seems to be a rare occurrence, i.e., transitioning from a period of significant deglacial warming to nearly glacial conditions (Barker and Knorr, 2021). The occurrence of YD has been proposed to be caused by a combination of the weakened AMOC, moderate negative radiative forcing, and altered atmospheric circulation (Renssen et al., 2015), whereas freshwater discharge into the subpolar North Atlantic has usually been considered as a primary trigger, which led to surface freshening in the Nordic Seas, and subsequently preventing deep-water formation (Broecker, 2006; Condron and Winsor, 2012; Muschitiello et al., 2019; Cheng et al., 2020). Other studies provide evidence that the outburst of Lake Agassiz via Mackenzie River into the Arctic Ocean around 12.9 ka BP might have been the major source of meltwater discharge into the Nordic Seas (Fig. 1.23; Peltier et al., 2006; Murton et al., 2010; Fahl and Stein, 2012; Keigwin et al., 2018; Sachs et al., 2018; Wu et al., 2020; Süfke et al., 2022). This meltwater event has triggered surface freshening in the Nordic Seas and suppressed deep-water formation/weakened AMOC, ultimately driving the onset of YD. Another hypothesis proposed that the occurrence of the YD might be related to a volcanic event (Laacher See eruption) in Germany (Berger, 1990; Baldini et al., 2018). However, a recent revised chronology of this volcanic event rules out any direct impact of the volcanic eruption on the occurrence of the YD (Reinig et al., 2021). In contrast to the stable and colder conditions during the early YD, the freshwater forcing was losing strength during the late YD, causing alternative sea ice cover and Atlantic Water influx in the Nordic Seas (Bakke et al., 2009). Thus, it has raised a question whether a hundred-year-scale flooding event could sustain a thousand-year-long cold period. Modelling simulation suggests that the export of Arctic sea ice into the Nordic Seas may have played a role in maintaining a weakened AMOC (Condron et al., 2020). Additionally, the presence of detrital carbonate input in the Labrador Sea indicates the occurrence of HE0 during the late YD (Andrews et al., 1995; You et al., 2023), probably contributing to a weakened AMOC during the late phase of the YD.

1.4.3 The Holocene

The Holocene began after the termination of the YD around 11.7 ka BP, characterized by abrupt increases in air temperatures reflected by Greenland Ice Core records (Svensson et al., 2008), rising sea levels (Lambeck et al., 2014), and the enhanced AMOC (McManus et al., 2004; Lippold et al., 2019). In contrast to the last deglaciation characterized by millennial-scale abrupt climate changes, the Holocene is marked by a relatively warmer climate with low-magnitude
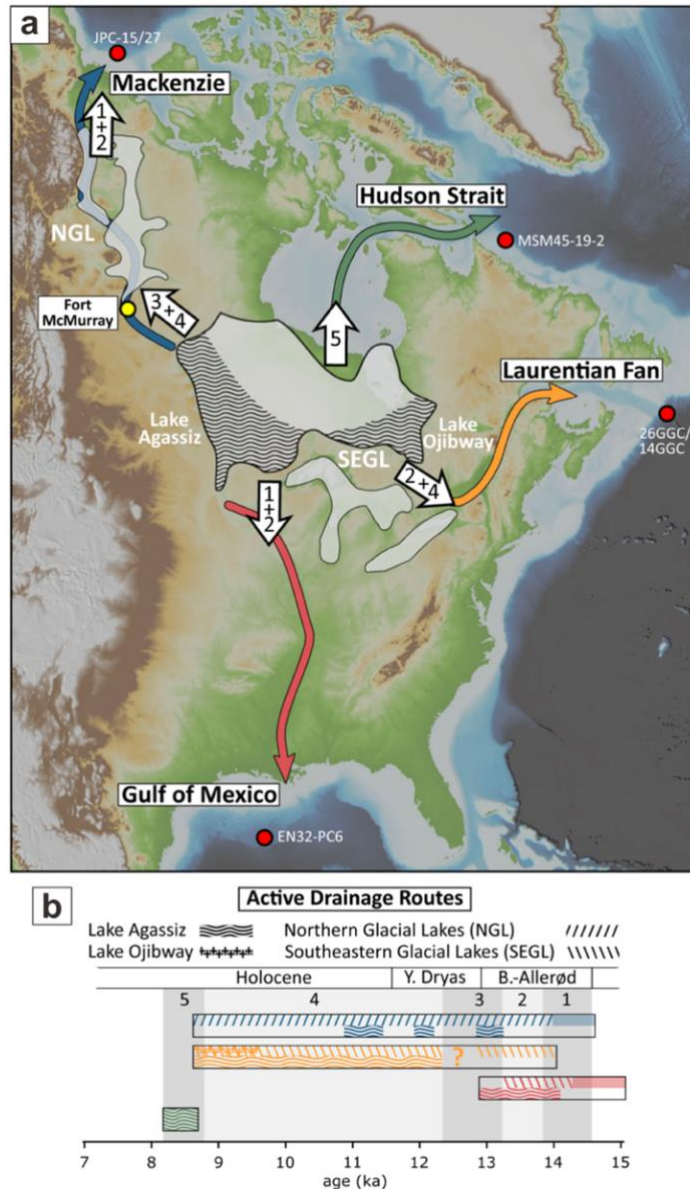
Fig. 1.23 Active drainage routes of meltwater from the Laurentide Ice Sheet during the last deglaciation and early Holocene (Figure from Süfke et al., 2022 based on Broecker, 2006). **a** Colored arrows mark the main drainage routes. Numbers in white arrows correspond to phases of different drainage route activation independent from prominent climate periods. Wavy areas correspond to the main areas of Lake Agassiz and Lake Ojibway during the Bølling-Allerød and the Younger Dryas before merging. **b** The major active drainage routes and their potential freshwater source. Northern glacial lakes (NGL) are Lake Mackenzie and Lake McConnell; Southeastern Glacial Lakes (SEGL) represent former glacial lakes in the Great Lakes area as well as glacial Lake Ojibway. Core MSM45-19-2 referred to Lochte et al., (2019); Core 26GGC/14GGC referred to Keigwin et al., (2005), Kurzweil et al., (2010); Core EN32-PC6 referred to Leventer et al., (1982), Flower et al., (2004).

climate fluctuations. In particular, the Holocene can be divided into three periods: the early Holocene (11.7-9 ka BP), including "Preboreal" and "Boreal" chronozones, the middle Holocene (9-5 ka BP) coeval with "Atlantic" chronozone, and the late Holocene coinciding with "Subboreal" and "Subatlantic" chronozones (Fig. 1.24; Wanner et al., 2008). A rapid sea-level rise has been

identified during the early Holocene (~11.3 ka BP), referred to as MWP-1B (Fig. 1.21). Additionally, the highest summer insolation occurred during the early Holocene (~9 ka BP) (Laskar et al., 2004), leading to a warmer period known as the (early to middle) Holocene Thermal Maximum (HTM) (Marcott et al., 2013). Despite lacking the globally synchronous HTM (Cartapanis et al., 2022), pollen records covering the Northern Hemisphere landmass indicate that both summer and winter temperatures were warmer during the HTM (Zhang et al., 2022). However, climate models suggest continuous warming during the whole Holocene (Liu et al., 2014). This discrepancy between proxy-based reconstructions and model stimulations is still under discussion (Kaufman and Broadman, 2023). Following a decreasing insolation, proxy-based reconstructions show a gradual cooling in air temperatures during the middle to late Holocene (Marcott et al., 2013; Zhang et al., 2022), referred to as Neoglacial cooling that culminated during the Little Ice Age (LIA) (Fig. 1.24; Nesje et al., 2001; Nesje and Dahl, 2003; Jones and Mann, 2004; Wanner et al., 2008). Notably, glacier advances were observed in Greenland, Svalbard, and Scandinavia during the Neoglacial cooling (Werner, 1993; Svendsen and Mangerud, 1997; Nesje, 2009; Lecavalier et al., 2014; Levy et al., 2017). Independent to the glacial-interglacial cycles during the late Pleistocene, IRD events with a 1500-year cycle were also identified in the subpolar North Atlantic during the Holocene, termed "Bond events" (Bond et al., 1997). The occurrence of Bond events is thought to have been caused by the retreat of ice sheets from eastern Greenland and Svalbard, likely in response to changes in insolation patterns (Bond et al., 2001).
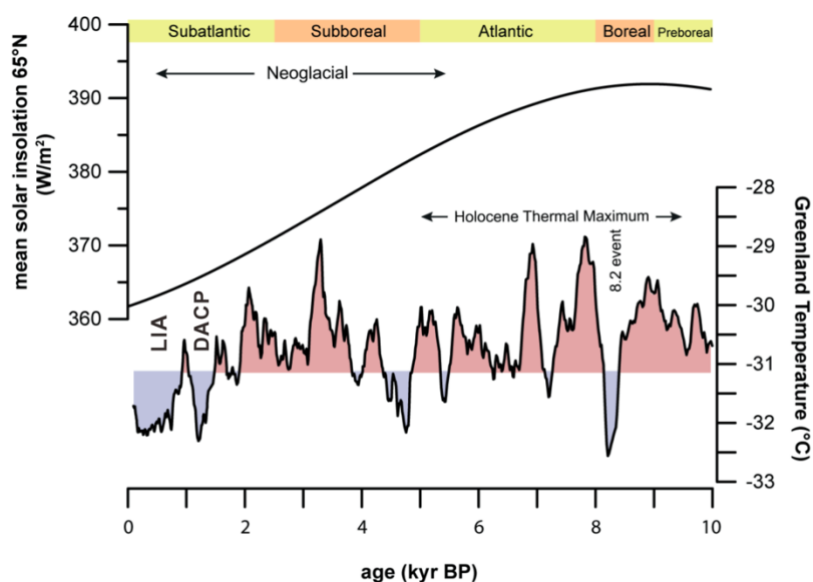
Fig. 1.24 Overview of Holocene Greenland temperatures (in °C) and the North Hemisphere solar insolation (Figure from Kolling, 2017). Temperature reconstruction based on $\delta^{18}O$ data of the GISP Ice Core (Alley et al., 2010). The solar insolation at 65°N referred to Laskar et al. (2004). LIA: Little Ice Age; DACP: Dark Ages Cold Period; 8.2 event: 8.2 ka BP cold event.

The 8.2 ka cold event interrupted the warm climate during the Holocene, which has been proposed to be caused by the catastrophic drainage of proglacial Lake Agassiz (Barber et al., 1999; Kleiven et al., 2008; Svensson et al., 2008). Lochte et al. (2019) proposed that the collapse of the Hudson Bay Ice Saddle around 8.5 ka BP might have a more substantial influence on surface freshening in the Labrador Sea compared to the lake outburst, thereby resulting in the occurrence of the 8.2 ka BP cold event (Fig. 1.23). As the LIS and Eurasian Ice Sheet gradually melted without causing significant freshwater perturbations (Peltier et al., 2015), the ocean circulation in the North Atlantic maintained a relatively stable state (Lippold et al., 2019). However, the input of Arctic sea ice may have perturbed the strength of the subpolar gyre, affecting the formation of the LSW and the northward movement of the NAC, subsequently disrupting the European climate (Fig. 1.25; Thornalley et al., 2009; Moffa-Sánchez and Hall, 2017).
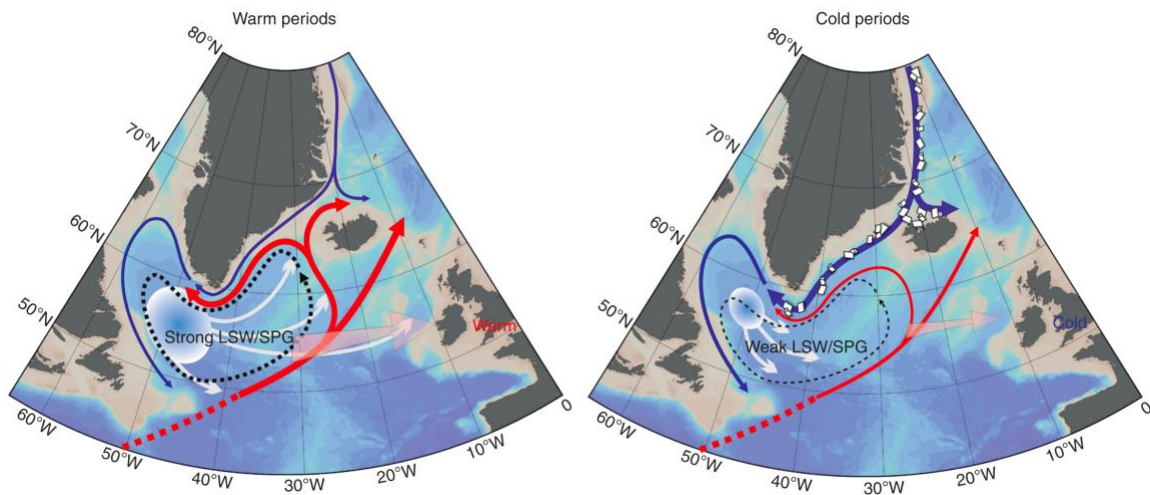
Fig. 1.25 Schematic of the ocean circulation patterns during centennial warm and cold periods in the subpolar North Atlantic (Figure from Moffa-Sánchez and Hall, 2017). The Atlantic water inflow and Polar water inflow are represented in red and blue arrows, respectively. The black dotted lines indicate the subpolar gyre (SPG), and the white circle and the arrows indicate the formation and spreading of Labrador Sea Water (LSW). The faded pink arrow represents the heat transport towards Europe in each scenario.

1.5 Approaches and proxies for paleoenvironmental reconstructions

The paleoenvironmental reconstruction based on sediment cores is the direct way to understand the environmental changes in the past beyond modern observations. Different approaches and proxies can be used to reconstruct various environmental parameters. For example, geochemistry, micropaleontology, and sedimentology proxies can be applied to directly or indirectly reconstruct sea surface characteristics (e.g., sea ice cover, meltwater discharge, SST, and open-water phytoplankton productivity, etc.) and ice sheet activities (e.g., the collapse of ice sheets). In this dissertation, the following proxies were used for paleoenvironmental reconstructions.

1.5.1 Sea ice

Grain-size distribution is a first-order proxy to identify ice transport in marine sediments. The presence of IRD can originate from icebergs and/or sea ice and is observed throughout glacial and interglacial periods. For distinguishing different ice transport between iceberg and sea ice, it is widely acknowledged that very coarse-grained materials (>250 μm), i.e., coarse-sand-, gravel-, and pebble-sized particles, are attributed to iceberg transport (e.g., Clark and Hanson, 1983; Hebbeln et al., 1998; Spielhagen et al., 2004; Stein, 2008). Furthermore, Spielhagen et al. (2004) determined a positive correlation between >63 μm fraction and iceberg-rafted >250 μm fraction in the Arctic Ocean, suggesting icebergs are the predominant transport agent for coarse fraction (>63 μm). In contrast to iceberg deposition, sea-ice deposition generally contains high contents of fine silt and clay (Fig. 1.26; Clark and Hanson, 1983). However, other processes might influence grain-size distributions and thus affect the analysis of sea-ice transport, such as winnowing caused by bottom currents, debris flows, river discharge, etc. (Anderson and Andrews, 1999; Evans et al., 2002; Dethleff, 2005; Stein, 2008).

Assemblages of different microfossils (i.e., diatoms, foraminifera, dinoflagellate cysts, and ostracods) are often-used proxies for sea ice reconstruction based on the ecological preference of specific species (de Vernal et al., 2013). Based on specific species directly related to sea ice, diatom assemblages can be used for quantitative reconstruction of sea ice (e.g., Ren et al., 2014, 2020, 2021). However, diatom data may be biased by opal dissolution related to changing opal export rates and related preservation efficiency, especially in the North Atlantic and Arctic areas (Crosta et al., 1998; Gersonde and Zielinski, 2000). Changes in benthic foraminiferal assemblages can indicate variations in sea ice cover, whereas they are not direct proxies for sea ice reconstruction (Scott et al., 2009; Seidenkrantz, 2013; Polyak et al., 2013; Lazar and Polyak, 2016). It should be noted that foraminifera probably respond to the surplus of food supply often available at sea ice edges (Seidenkrantz, 2013). In addition, the dominance of agglutinated foraminifera may reflect a corrosive bottom-water condition related to seasonal sea ice cover

(Cronin et al., 2008; Seidenkrantz, 2013). Also, the preservation of calcareous foraminifera is problematic particularly under the lysocline. In contrast to diatoms and foraminifera, dinoflagellate cysts have good preservation, and a large database is available for quantitative reconstruction for sea ice, while it is also not a direct proxy for sea ice and numbers of specimens may be low in distal offshore settings (de Vernal and Hillaire-Marcel, 2000; de Vernal et al., 2001, 2006; Matthiessen et al., 2005). For ostracods, only one species is used as a proxy for multi-year sea ice cover, whereas the low abundance and poor reservation limit its application (Cronin et al., 2010; Cronin et al., 2014; Gemery et al., 2017).
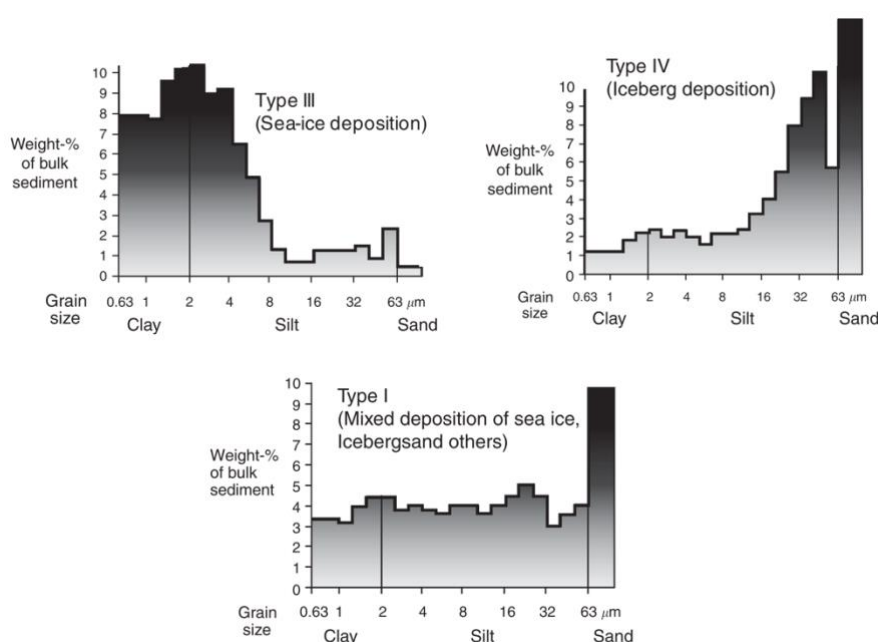
Fig. 1.26 Different sediment-size types in central Arctic Ocean sediments based on Coulter counter analysis of the silt and clay fractions, and interpretation in terms of transport processes (Figure from Stein, 2008 based on Clark and Hanson, 1983, redrawn by R. Spielhagen).

The abundance, distribution, and/or isotope composition of source-specific organic molecules-termed biomarkers provide more direct paleoenvironmental information (Fig. 1.27). Notably, the biomarker proxy (IP$_{25}$) was used in this dissertation to reconstruct sea ice cover. This sea ice biomarker is C$_{25}$ mono-unsaturated highly branched isoprenoid alkane (HBI), which was first detected and described by Belt et al. (2007) in their study from the Canadian Arctic. This compound (IP$_{25}$) is believed to be biosynthesized by diatoms living in the sea ice, including *Pleurosigma stuxbergii var. rhomboides*, *Haslea kjellmanii*, *H. crucigeroides*, and/or *H. spicula* (Belt et al., 2007; Brown et al., 2014). Thus, it serves as a specific, sensitive, and stable proxy for sea ice reconstruction and has been applied in many studies in the polar/subpolar regions (Fig. 1.28; e.g., Müller et al., 2009; Fahl and Stein, 2012; Müller and Stein, 2014; Belt, 2018; Sadatzki

et al., 2019; Wu et al., 2020). Based on the comparison by spatial distribution between biomarker data and satellite observations, IP$_{25}$ appears to represent spring or autumn (seasonal) sea ice conditions (Müller et al., 2011; Kolling et al., 2020). Furthermore, the tri-unsaturated HBI usually consists of two isomers (Z- and E-isomers), and the Z-isomer of triene (referred to as HBI-III (Z)) is commonly observed in open-water conditions. Particularly, high concentrations of HBI-III (Z) are found in the open-water regions adjacent to sea ice (i.e., the marginal ice zone, MIZ) (Belt et al., 2015; Smik et al., 2016, Belt, 2018).
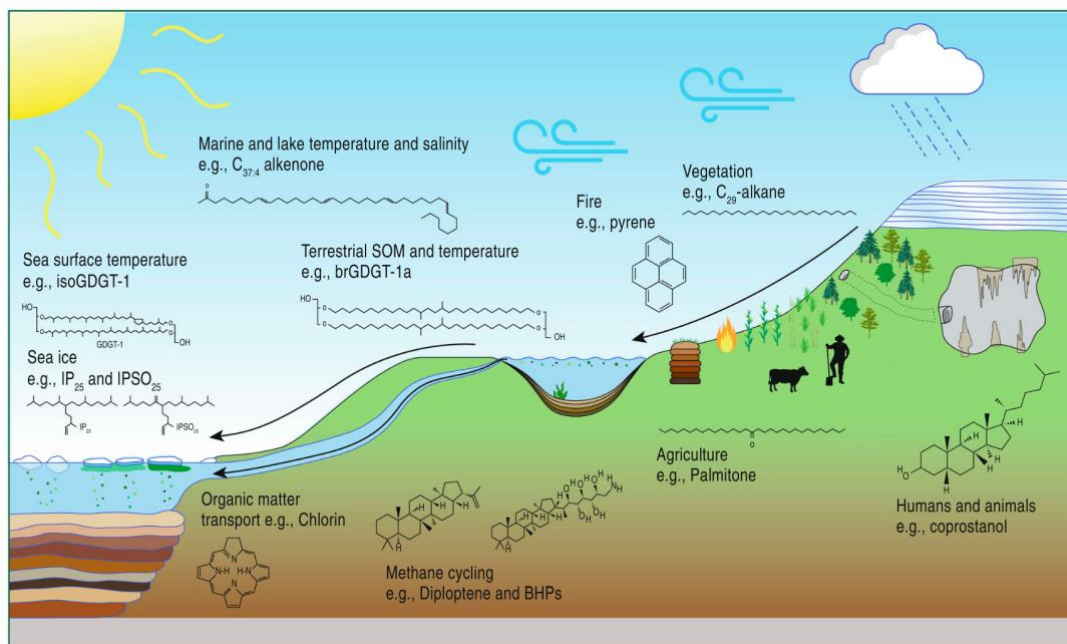
Fig. 1.27 Using different biomarkers to reconstruct environmental parameters (Figure from McClymont et al., 2023).
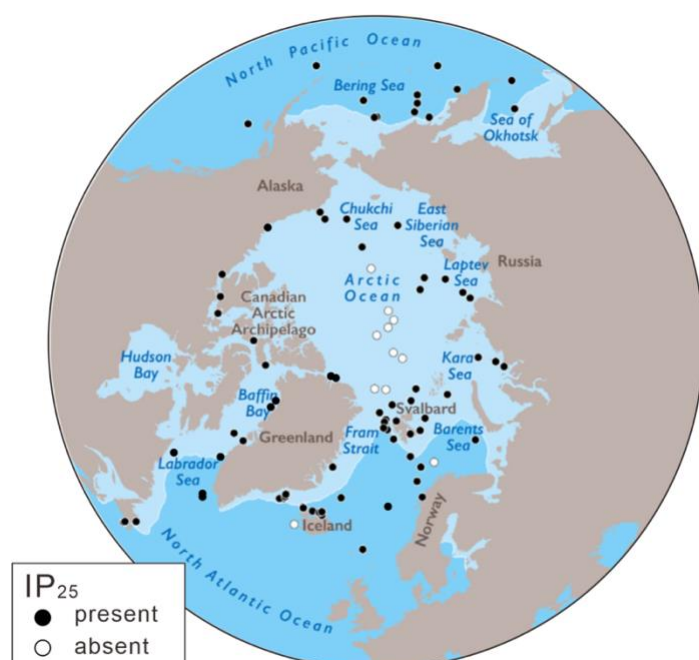
Fig. 1.28 Summary map of locations where IP$_{25}$ has been investigated in sediment cores from polar/subpolar regions in the Northern Hemisphere (Modified from Belt, 2018). Black dots indicate the presence of IP$_{25}$ in the paleo records, whereas white dots show locations without IP$_{25}$.

The production of IP_{25} is related to sea ice algae productivity. IP_{25} is absent under permanent sea ice cover and ice-free (i.e., open-water) conditions due to the absence of sea ice algae. In order to distinguish these two extreme scenarios, a semi-quantitative index (PIP_{25}) has been proposed by Müller et al. (2011), which combines IP_{25} with open-water phytoplankton biomarkers (e.g., dinosterol, brassicasterol, HBI-III (Z)). In the context without IP_{25} or with very low concentrations of IP_{25}, high concentrations of open-water phytoplankton biomarkers suggest ice-free conditions, whereas low to absent concentrations of phytoplankton biomarkers probably imply a permanent sea ice cover (Fig. 1.29). The following equation (1) shows the calibration of PIP_{25} values.

$$PIP_{25} = [IP_{25}] / ([IP_{25}] + [\text{Phytoplankton biomarker}] \times c) \qquad (1)$$

The balance factor c corresponds to the ratio of the mean concentration of IP_{25} and phytoplankton biomarkers. Based on the comparison between PIP_{25} values and satellite data, high PIP_{25} values (>0.75) indicate extended sea ice cover, whereas intermediate values (0.5-0.75), low values (0.1-0.5), and very low values (<0.1) reflect marginal sea ice, less sea ice, and ice-free conditions, respectively (Müller et al., 2011). The PIP_{25} values are often set to 1 if it is considered permanent sea ice cover (e.g., Müller and Stein, 2014; Hoff et al., 2016; Syring et al., 2020). Figure 1.30 shows PIP_{25} values based on different open-water phytoplankton biomarkers from Core MSM12/2-05-01 (this study), which demonstrates comparable variations in sea ice cover during the last glacial-deglaciation-Holocene period (for more details, see Chapter 3).
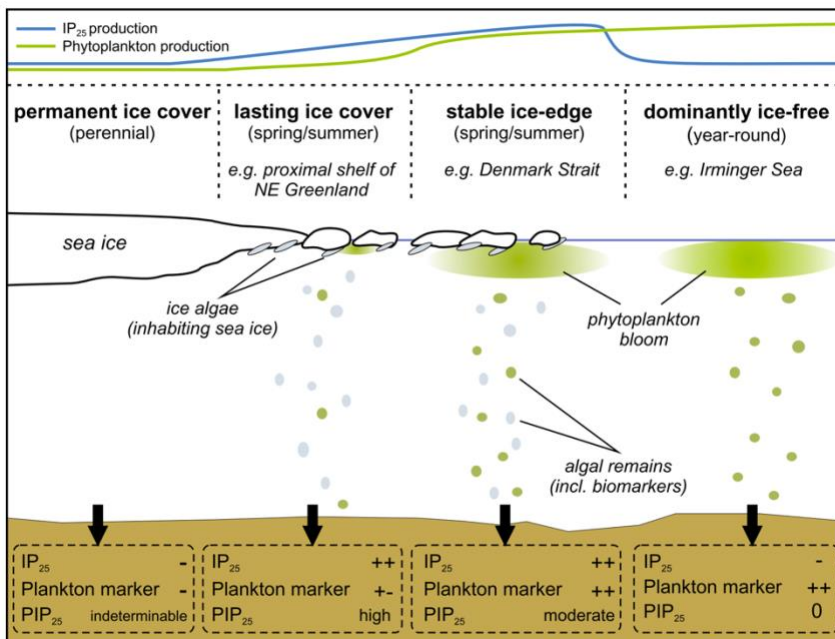
Fig. 1.29 Schematic illustration for distinct sea surface conditions and respective productivities of sea ice algae and phytoplankton (Figure from Müller et al., 2011). Overview contents of IP_{25} and the phytoplankton-derived biomarkers and corresponding PIP_{25} indices are shown for each setting.
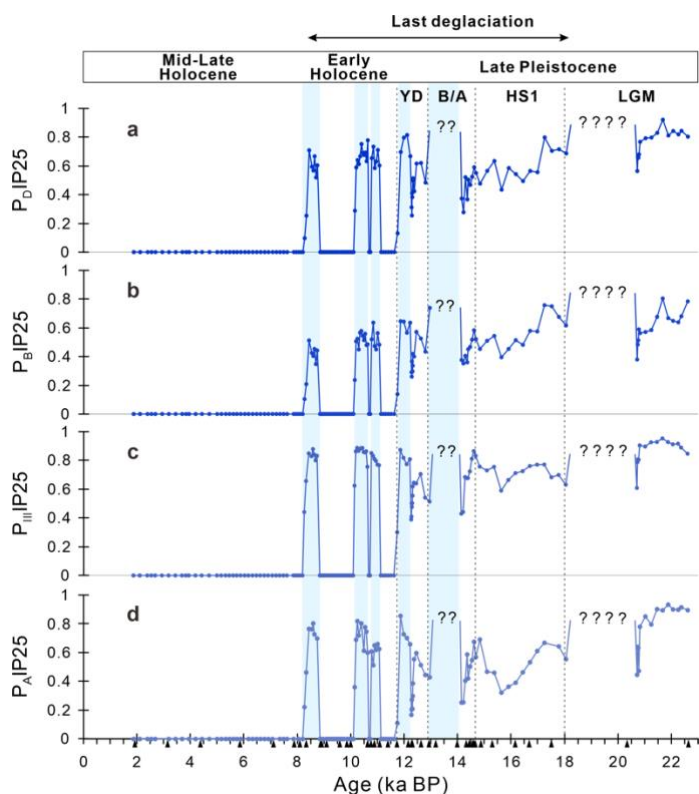
Fig. 1.30 PIP$_{25}$ values based on different open-water phytoplankton biomarkers from Core MSM12/2-05-01, the Labrador Sea. (a) P$_D$IP$_{25}$ based on dinosterol; **(b)** P$_B$IP$_{25}$ based on brassicasterol; **(c)** P$_{III}$IP$_{25}$ based on HBI-III (Z); **(d)** P$_A$IP$_{25}$ based on alkenones. For the intervals characterized by zero or minimum concentrations of IP$_{25}$ and phytoplankton biomarkers, PIP$_{25}$ values cannot be calculated (highlighted by question marks; cf., Müller et al., 2011; for details see Chapter 3). Light blue shadings highlight the intervals of strong meltwater discharge during the last deglaciation. Vertical stippled lines mark the intervals: Last Glacial Maximum (LGM), Heinrich Stadial 1 (HS1), the Younger Dryas (YD), and the Bølling/Allerød (B/A). Black triangles mark available AMS^{14}C dates.

Sedimentary ancient DNA is another novel tool that unlocks and exploits the genetic biodiversity preserved in marine sediments specifically for past sea ice reconstructions (Schepper et al., 2019; Zimmermann et al., 2023). Furthermore, bromine and iodine enrichment in ice cores has been suggested to indicate the extent of newly formed sea ice areas, comparable to IP$_{25}$-based sea ice reconstruction (Maffezzoli et al., 2019; Vallelonga et al., 2021; Corella et al., 2022; Scoto et al., 2022).

1.5.2 Sea surface temperature

SST is one of the major parameters of water mass characteristics. Often-used proxies include U$_{37}^K$, TEX$_{86}$, RI-OH', and transfer function of foraminifera/diatom/dinoflagellate cyst assemblages, etc. In this dissertation, the biomarker proxy (alkenones) was used to reconstruct SST. Alkenones, long-chain unsaturated ketones with 37 carbon atoms, are produced by predominated coccolithophorid species *Emiliania huxleyi* and its close relative *Gephyrocapsa oceanica* (Marlowe et al., 1984; Prahl et al., 1988). This compound comprises di-unsaturated (C$_{37:2}$), tri-unsaturated (C$_{37:3}$), and tetra-unsaturated (C$_{37:4}$) methyl alkenones. The concentrations of C$_{37:2}$ and C$_{37:3}$ are normally higher than that of C$_{37:4}$ in marine sediments (Marlowe et al., 1984; Prahl et al., 1988). Insights from culture experiments have revealed that *Emiliania huxleyi* synthesizes C$_{37:4}$ at low temperatures but not under warmer conditions (Fig. 1.31; Prahl and Wakeham, 1987; Rosell-Melé, 1998). Brassell et al. (1986) proposed that alkenone unsaturation (U$_{37}^K$) was related

to SST variations, which can be used as a proxy for paleotemperature reconstruction (see following equation 2).

$$U_{37}^{K}=(C_{37:2}-C_{37:4})/(C_{37:2}+C_{37:3}+C_{37:4}) \qquad (2)$$
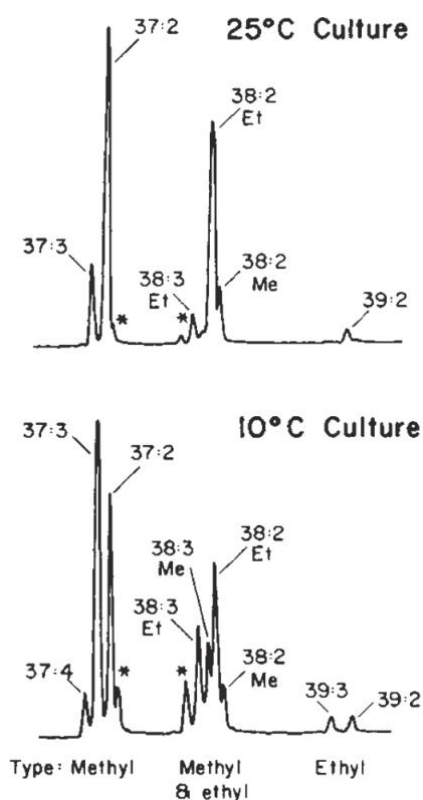
Fig. 1.31 Gas chromatograms of the long-chain, unsaturated ketone compositions measured in cultures of *Emiliania huxleyi* grown at 10 °C and 25 °C (Figure from Prahl and Wakeham, 1987). The presence of $C_{37:4}$ alkenone under 10°C whereas the absence of $C_{37:4}$ alkenone under 25°C.

Further culture experiments with *Emiliania huxleyi* confirmed the positive correlation between U_{37}^{K} and SST, i.e., higher SST coinciding with higher U_{37}^{K} (Prahl and Wakeham, 1987; Prahl et al., 1988). Additionally, the correlation between U_{37}^{K} analysis from surface sediments and modern observed SSTs further supports that SST was the main factor affecting alkenone unsaturation (Rosell-Melé et al., 1995). Given the rare detection of $C_{37:4}$ in marine sediments where SST > 15 °C, a simplified version of alkenone unsaturation ($U_{37}^{K'}$) has been proposed omitting $C_{37:4}$ (Prahl and Wakeham, 1987) (equation 3). Further, a global SST calibration equation based on $U_{37}^{K'}$ has been established by Müller et al. (1998), which was derived from alkenones analysis on global core-top sediments (equation 4). In particular, the best linear correlation between $U_{37}^{K'}$ and SST was obtained using the annual mean SSTs from 0 to 10 m water depth range.

$$U_{37}^{K'}=(C_{37:2})/(C_{37:2}+C_{37:3}) \qquad (3)$$

$$U_{37}^{K'}=0.033T + 0.044 \qquad (4)$$

$U^K_{37}{}'$ -based SST reconstructions in the northern high-latitude oceans exhibits significant warm bias, often accompanied by relatively higher $C_{37:4}$ concentrations (cf., Filippova et al., 2016; Wang et al., 2021). However, despite probably not only being affected by SSTs, the regional U^K_{37} values (including $C_{37:4}$) show a high positive correlation with SSTs in the North Atlantic, particularly under cold conditions (SSTs < 10°C) (Rosell-Melé et al., 1995; Filippova et al., 2016). Therefore, U^K_{37}-based SST reconstructions tend to better reflect SST in the high-latitude North Atlantic regions (Filippova et al., 2016). Notably, the better linear correlation between U^K_{37} and SST was obtained using spring or summer temperatures rather than the annual mean SST, probably related to the blooming season of coccolithophorids in the high-latitude regions. A new regional calibration for SST reconstruction in the subpolar/polar North Atlantic has been proposed by Filippova et al. (2016) (equation 5). Figure 1.32 shows comparisons of SST reconstruction based on different equations of Core MSM12/2-05-01 (this study).

$$U^K_{37} = 0.021T + 0.243 \qquad\qquad (5)$$
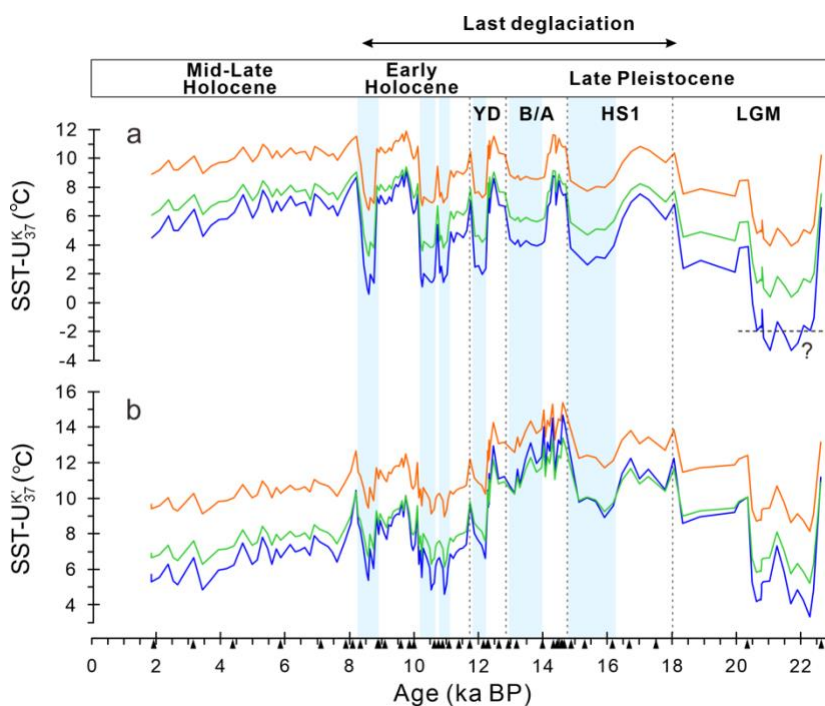
Fig. 1.32 SST reconstruction based on different equations from Core MSM12/2-05-01, the Labrador Sea. (a) SST calibration based on U^K_{37}; (b) SST calibration based on $U^K_{37}{}'$. The orange, green and blue curves were calibrated according to the equations from Müller et al. (1998), Rosell-Mele et al. (1995), Filippova et al. (2016), respectively. The temperatures below dashed line (-2 °C) are unrealistic. Light blue shadings highlight the intervals with increased meltwater discharge during the last deglaciation (refer to Chapter 3).

In addition to U^K_{37}, TEX_{86} index (Tetraether index of tetraethers consisting of 86 carbon atoms) is also often-used biomarker proxy for SST reconstruction calculated from the relative abundance of isoprenoid glycerol dibiphytanyl glycerol tetraethers (iGDGTs) (Schouten et al., 2003). iGDGTs can be produced by marine Archaea Thaumarchaeota, which play an important role in pelagic ammonia oxidation in marine environments and tend to maximize in abundance at

subsurface depths of less than 200 m (Schouten et al., 2003; Schouten et al., 2013). For a more precise estimate, Kim et al. (2010) have proposed modified versions $\text{TEX}_{86}^{\text{H}}$ and $\text{TEX}_{86}^{\text{L}}$ to reconstruct SST in low (below 15°C) and high-temperature conditions (above 30°C), respectively. It should be noted that the TEX_{86}-based SST calibration might be influenced by non-marine-sourced iGDGTs when a large amount of terrigenous material was input into study areas (Blaga et al., 2009; Inglis et al., 2022).

Mg/Ca ratios of planktic/benthic foraminifera are also proxies for reconstructing upper/bottom ocean temperatures in the past (e.g., Peck et al., 2008; Marcott et al., 2011; Lochte et al., 2019; Max et al., 2022). This is due to the temperature-related variations in magnesium uptake within foraminiferal calcite, leading to elevated Mg/Ca ratios in foraminifera with higher growth temperatures (Nurnberg, 1995; Anand et al., 2003). In particular, different transfer functions are used for different foraminifera species (Elderfield and Ganssen, 2000). In this study, Mg/Ca ratios of planktic foraminifera were determined from Core MSM12/02-05-01. Temperatures were further calculated using species-specific *N. pachyderma* (sin.) calibration equation (Elderfield et al., 2000) (equation 6). Furthermore, different transfer functions based on foraminifera/diatom/dinoflagellate cyst assemblages have been proposed for SST reconstruction (cf., Imbrie and Kipp, 1971; De Seve, 1999; de Vernal and Hillaire-Marcel, 2000).

$$\text{Mg/Ca} = 0.5 \exp(0.1\ T) \qquad (6)$$

1.5.3 Sea surface salinity

The biomarker proxy, the percentage of tetra-unsaturated alkenones ($\%C_{37:4}$) was used in this study to reconstruct meltwater discharge. $C_{37:4}$ has been identified in many surface sediments from polar/subpolar North Atlantic regions, whereas less or no $C_{37:4}$ has been found in low or middle-latitude regions (Rosell-Melé, 1998; Müller et al., 1998; Filippova et al., 2016). Culture experiments have revealed that *Emiliania huxleyi* synthesizes $C_{37:4}$ at low temperatures but not under warmer conditions (Fig. 1.31; Prahl and Wakeham, 1987; Rosell-Melé, 1998). In addition, previous research suggests that other alkenone producers adapted to low-salinity water can also produce $C_{37:4}$ (Bard et al., 2000; Rosell-Melé, 1998; Bendle et al., 2005). Therefore, increased $\%C_{37:4}$ values (see following equation 7) can be attributed to low-temperature and/or low-salinity conditions, often associated with meltwater discharge (Bard et al., 2000; Martrat et al., 2007; McClymont et al., 2023).

$$\%C_{37:4} = C_{37:4} / (C_{37:2} + C_{37:3} + C_{37:4}) \times 100 \qquad (7)$$

More recently, Lochte et al. (2020) and Wang et al. (2021) have proposed that $\%C_{37:4}$ might be an index for sea ice cover. According to culture experiments, it has been observed that $C_{37:4}$ can

be produced by a newly found lineage of coccolithophorids living in sea ice, yielding $\%C_{37:4}$ values reaching around 80% (Wang et al., 2021). However, this new finding does not indicate that all presence of $C_{37:4}$ in the polar/subpolar regions are synthesized by this new sea ice species. The low contents of $C_{37:4}$ in sediments (i.e., much less than 80%) probably indicate that open-water algae (e.g., *Emiliania huxleyi*) production influenced by meltwater is the primary source of alkenones.

Lighter hydrogen (^1H) and oxygen isotopes (^{16}O) are enriched in ice sheets due to fractionation (Sessions et al., 1999; Ravelo and Hillaire-Marcel, 2007). Therefore, meltwater discharge from ice sheets can lighten the stable compositions of hydrogen isotope (δ^2H) and oxygen isotope ($\delta^{18}O$) of seawater in surrounding areas, consistent with decreased sea-surface salinity. The fluctuations in stable hydrogen and oxygen isotope compositions of seawater can be documented in organic matters and calcium shells produced by phytoplankton and foraminifera, respectively. The $\delta^{18}O$ of planktic foraminifera is often-used proxy for meltwater discharge in polar and subpolar regions (e.g., Duplessy et al., 1992; Thornalley et al., 2010; Seidenkrantz et al., 2013, Keigwin et al., 2018). However, it should be noted that besides the $\delta^{18}O$ of seawater, calcification temperature and brine rejection also affect $\delta^{18}O$ values of planktic foraminifera (Ravelo and Hillaire-Marcel, 2007). Furthermore, the absence/dissolution of calcareous foraminifera during some periods may limit the use of the $\delta^{18}O$ of planktic foraminifera as a proxy for meltwater discharge.

Compared to microfossils, biomarkers have good preservation in sediments and compound-specific hydrogen isotope analysis may provide direct and continuous reconstruction for meltwater discharge. The δ^2H of palmitic acid (δD_{PA}) has been used in many studies to reflect salinity variations indicating meltwater discharge (e.g., Häggi et al., 2015; Sachs et al., 2018; Crivellari et al., 2018), which was also applied in this study. Despite being synthesized by a wide range of marine and terrestrial organisms, Sachs et al. (2018) provides compelling evidence indicating that marine phytoplankton are the primary contributors of palmitic acid in Arctic Ocean sediments. Their investigation of surface sediments spanning significant salinity gradients from 11 to 32 demonstrates a correlation between δD_{PA} values and surface water salinity, i.e., lower (higher) δD_{PA} values correspond to lower (higher) salinity sea-surface conditions (Fig. 1.33).
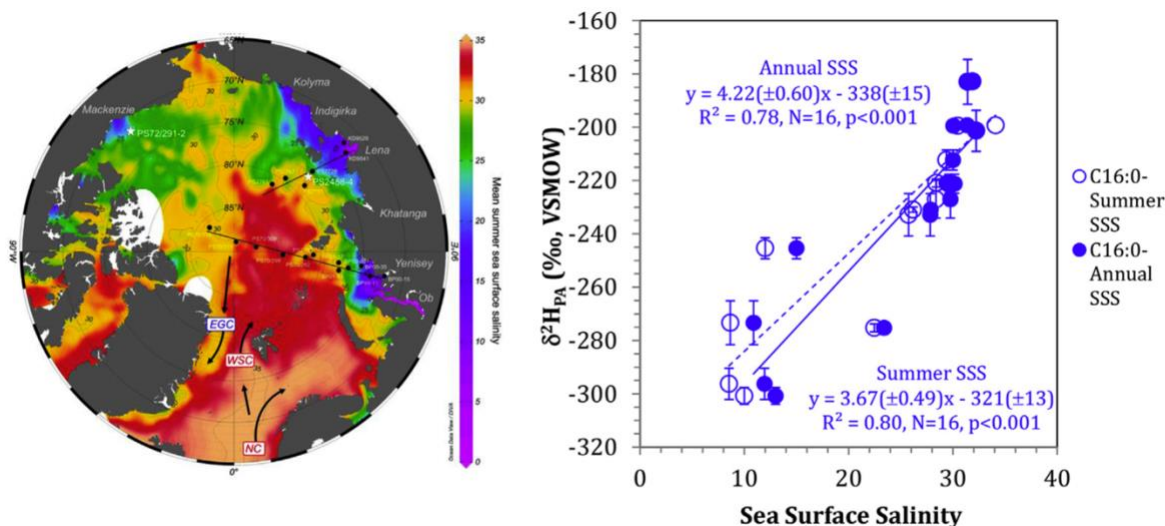
Fig. 1.33 Map of summer sea surface salinity in Arctic Ocean and correlations between sea surface salinity and stable hydrogen isotope compositions of palmitic acid (δD$_{PA}$, C$_{16:0}$) in the selected surface sediments (Modified from Sachs et al., 2018). The locations of surface sediment samples along two transects in the Kara and Laptev Seas are indicated by black dots. Salinity data is from the World Ocean Atlas 2013 (Source: *https://odv.awi.de/data/ocean/world-ocean-atlas-2013/*). SSS: sea surface salinity.

1.5.4 Primary production

Primary production is another major parameter of water mass/sea surface characteristics. Multiple biomarker proxies were used in this dissertation to reconstruct primary production. The open-water phytoplankton biomarkers dinosterol and brassicasterol are produced by a variety of phytoplankton genera such as dinoflagellates, diatoms, and haptophytes, indicating open-water phytoplankton productivity (Volkman, 1986; Fahl and Stein, 1999). Brassicasterol can originate from both marine and riverine/lacustrine algae, whereas dinosterol is primarily biosynthesized by dinoflagellates (Volkman, 1986; Rampen et al., 2010). Therefore, interpretations based on brassicasterol need more caution (Xiao et al., 2015). HBI-III (Z) has also been used as a proxy for open-water phytoplankton and particularly, it has been proposed to be somehow related to the MIZ (Belt et al., 2015; Smik et al., 2016; Belt, 2018). Furthermore, alkenones, mainly produced by coccolithophorid species *Emiliania huxleyi* are also a commonly-used proxy for open-water phytoplankton productivity (Marlowe et al., 1984; Prahl et al., 1988).

Microfossils are also important approaches to reconstruct primary production. Diatom and dinoflagellate cysts are primary contributors to organic carbon synthesis; thus, the total abundance of diatom and dinoflagellate cysts are direct proxies for primary production (cf., Nelson et al., 1995; Devillers and de Vernal, 2000; Crosta and Koç, 2007; de Vernal and Marret, 2007). Further, increased total abundance of planktic/benthic foraminifera can also be used to indicate increased primary production due to sufficient food supply to foraminifera caused by phytoplankton blooms (Kucera, 2007, Jorissen et al., 2007). Although food supply is a major

factor affecting foraminiferal abundance and their assemblages, other water mass properties (e.g., temperature and salinity), sediment properties (e.g., organic flux and oxygen conditions) may also influence the presence of planktic/benthic foraminifera (cf., Jennings and Helgadottir, 1994; Jorissen et al., 1995; Morey et al., 2005; Kucera, 2007; Jorissen et al., 2007). Therefore, foraminiferal assemblages may reflect a comprehensive signal of the water mass rather than one single environmental parameter. In this study, planktic and benthic foraminiferal assemblage analyses were applied to indicate variations in water mass characteristics, combined with biomarker proxies.

According to different ecological preferences, different water masses are characterised by different dominant or characteristic foraminiferal species, indicating distinct productivity conditions/water mass characteristics. Therefore, changes in the concentrations of specific foraminifer species within sedimentary records provide valuable information about water mass variations. Figure 1.34 shows modern distributions of three dominate planktic foraminifera in the North Atlantic regions. *Neogloboquadrina pachyderma* (sinistral) is dominant planktic species in the Labrador Sea and the Nordic Seas, indicating cold polar water mass (e.g., Carstens et al., 1997; Pflaumann et al., 2003; Kucera, 2007; Hoff et al., 2016). *Globigerina bulloides* shows high concentrations in the southern Labrador Sea, indicating warm subpolar water mass with increased productivity (e.g., Johannessen et al., 1994; Kucera, 2007; Consolaro et al., 2018). Increased concentrations of *Turborotalita quinqueloba* are found in the frontal locations suggesting warm subpolar water mass with higher primary production (e.g., Carstens et al., 1997; Rasmussen and Thomsen, 2008; Seidenkrantz et al., 2021). In addition, often-observed benthic foraminifera in the subpolar/polar regions includes *Cassidulina neoteretis* indicating Atlantic Water, *Cassidulina reniforme* indicating polar water, *Epistominella exigua* suggesting high food supply, *Cibicidoides wuellerstorfi* suggesting high bottom-water oxygenation, etc. (cf., Seidenkrantz,1995; Rasmussen and Thomsen, 2017; Jennings et al., 2017; Bartels et al., 2017; Consolaro et al., 2018; Seidenkrantz et al., 2021; Cage et al., 2021).
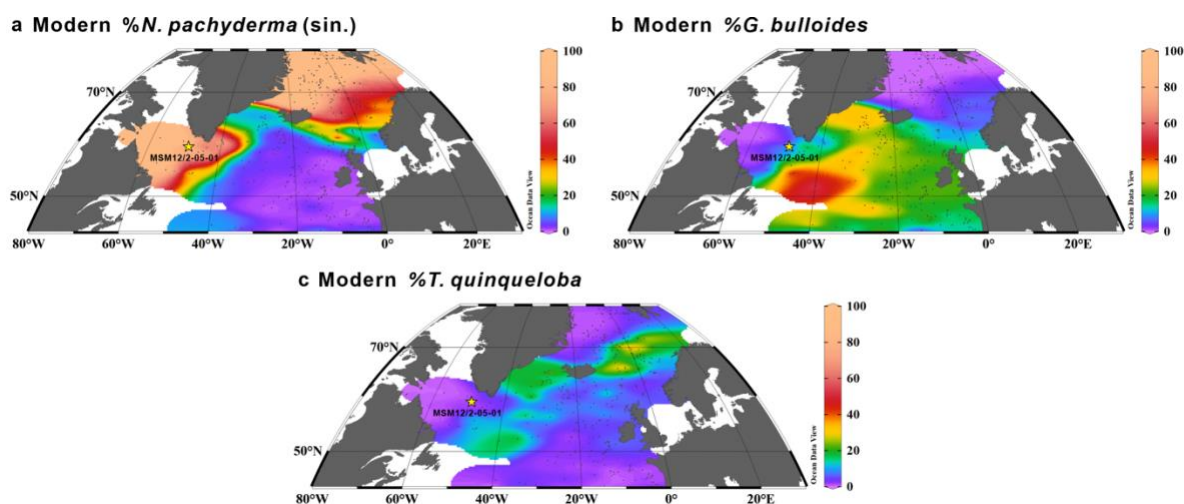
Fig. 1.34 Morden distribution of the dominant planktic foraminifera in the North Atlantic.
(**a**) Distribution patterns of %*Neogloboquadrina pachyderma* (sinistral); (**b**) Distribution patterns of %*Globigerina bulloides*; (**c**) Distribution patterns of %*Turborotalita quinqueloba*. Planktic foraminifer data from the MARGO dataset (Kucera et al., 2005). The yellow star shows the location of study Core MSM12/2-05-01 in the Labrador Sea.

1.5.5 Ice sheet activities

In this study, IRD abundance, specific element ratios of X-ray fluorescence (XRF) scanning, and mineral compositions of X-ray diffraction (XRD) measurement were used to indicate detrital material input/the decay of ice sheets. IRD deposition in glacial-marine sediments is an important sedimentological parameter, providing valuable insights into aspects such as iceberg distribution and the collapse of ice sheets (Ruddiman, 1977; Grobe, 1987). The IRD contents may give information about iceberg input and magnitude of ice sheet retreat (Ruddiman, 1977; Grobe, 1987; Heinrich, 1988). Notably, the sediments from the subpolar North Atlantic were characterized by the presence of IRD during the glacial period. This region is recognized as a significant zone for iceberg discharge and melt in the past, referred to as "IRD belt" (Ruddiman, 1977) (Fig. 1.17, 1.18). Sedimentary layers characterized by a large amount of IRD deposition in the North Atlantic have been proposed to be closely linked with the disintegration of the LIS, referred to as HEs (Heinrich. 1988; Alley and MacAyeal, 1994, Hemming, 2004). In addition to the LIS, the GrIS might have also contributed to the IRD deposition in the North Atlantic (cf., Bond et al., 1995).

In addition to increases in lithic debris content, the Heinrich layers in the North Atlantic exhibit a distinctive abundance of detrital carbonate. The predominant presence of Paleozoic Carbonate bedrock in the Hudson Bay and Hudson Strait regions suggest the influx of detrital carbonate from icebergs primarily originated from the Hudson Strait, a significant outlet of the LIS (cf., Hemming, 2004; Hodell et al., 2008; Simon et al., 2014). A commonly employed method to

assess detrital carbonate input is the analysis of Ca/Sr ratios through XRF scanning (Hodell et al., 2008; Channell et al., 2012; Max et al., 2022). Additionally, calcite and dolomite contents quantitated by XRD measurement, as well as specific organic biomarker proxies like petrogenic compounds, can offer further insight into the decay of the LIS (Naafs and Stein, 2013; Hodell et al., 2017; Jennings et al., 2017; Hefter et al., 2017). Moreover, the increased contents of other detrital elements such as Si, Ti, and Fe, also serve as indicators of amplified detrital material from the decay of the LIS and GrIS (cf., Carlson et al., 2008; Weiser et al., 2021).

1.6 Rationale and key questions of this dissertation

Sea ice is a critical component in the Earth's system and is highly responsive to various environmental factors such as insolation and heat transfer between ocean and atmosphere, etc. (Thomas and Dieckmann, 2008). Over the past few decades, the loss of summer Arctic sea ice has accelerated due to anthropogenic effects, leading to increased solar radiation penetration into the polar regions and causing the Arctic Amplification (Serreze and Barry, 2011; Shukla et al., 2019). Climate modelling projection suggests that more warm Atlantic Water is expected to continue expanding into the Arctic Basin in a warming climate, further amplifying Arctic warming (i.e., Arctic Atlantification) (Shu et al., 2021). Under these circumstances, understanding the dynamical mechanisms of rapid sea ice variations have gained much attention.

In addition to sea ice, ice sheets are another important component in Earth's system. In the context of global warming, the decay of the GrIS has accelerated in recent years, leading to increased meltwater discharge and rising sea levels (Yang et al., 2016; Pattyn et al., 2018; Hugonnet et al., 2021). Meltwater discharge into the polar/subpolar regions may affect sea surface characteristics in the adjacent oceans and potentially have significant perturbations in ocean circulation patterns (Rahmstorf et al., 2015; Böning et al., 2016). Furthermore, ocean forcing (e.g., warm water incursion) has been proposed to be one of the main drivers of ice sheet retreat (cf., Straneo and Heimbach, 2013; Wood et al., 2021). Thus, it has raised concerns about the past interactions between ocean and ice sheets, which helps us enhance understanding of the evolution of ice sheets in a changing climate and improve predictions of global ocean circulation and sea level change.

As an unstable period in the Earth system, the last glacial termination is an ideal interval to investigate non-linear feedback in the climate system (Barker and Knorr, 2021). The last glacial termination is characterized by significant decay of North Hemisphere ice sheets with meltwater discharge into the North Atlantic, which was closely linked with abrupt climate changes. However, the role of ice sheet activity/meltwater discharge in abrupt climate changes is still not fully understood.

This dissertation aims to investigating factors affecting sea ice variability, the impact of meltwater discharge on abrupt climate changes, and interactions between sea surface characteristics and ice sheet instability during the last glacial-deglacial-Holocene period. The Labrador Sea and Baffin Bay are optimal study areas to answer these issues given their proximity to the LIS and the GrIS during the last glacial period, where sedimentation records document the history of ice sheet activities and meltwater discharge. Furthermore, high sedimentation rates from these regions allow detailed studies and comparisons about abrupt climate changes during the last deglaciation. Firstly, we studied the high-resolution records from the eastern Labrador Sea, spanning the last 19 ka BP, to reconstructed the history of variations in sea surface

characteristics (i.e., sea ice cover, meltwater discharge, etc.) and their pivotal roles in deglacial abrupt climate changes. Secondly, to get a comprehensive picture of interactions between ice sheet instability and sea surface characteristics, we extended the records from the Labrador Sea back to 50 ka BP, in combination with more proxy records. Finally, to know whether abrupt changes in sea surface characteristics in southern Baffin Bay were comparable to those in the Labrador Sea during the last deglaciation, sedimentary records from two additional cores from southern Baffin Bay were included in our study.

Specifically, the key questions are as follows:

1) **What was the history of sea surface characteristics in the eastern Labrador Sea during the last 19 ka? What role did meltwater discharge play during the last deglaciation characterized by abrupt climate changes?**

Freshwater perturbations in the subpolar North Atlantic are often thought to be associated with abrupt climate changes during the last deglaciation, while many uncertainties remain regarding the timing, pattern, and influence of meltwater release. The high-resolution and well-dated records from the eastern Labrador Sea provide more information about the history of sea surface characteristics/meltwater discharge in the subpolar North Atlantic, improving our understanding of deglacial abrupt climate changes. Multiple biomarker proxies were used to reconstruct sea ice cover, meltwater discharge, SST, and open-water phytoplankton productivity. XRF scanning data, XRD data, and coarse fraction records were applied to indicate the decay of the surrounding ice sheets.

2) **How did ice sheet activities affect sea surface characteristics in the eastern Labrador Sea during the last 50 ka? Were patterns of meltwater discharge different during the last glacial period versus the last deglaciation? How did ocean forcings affect the instability of LIS and GrIS?**

The decay of ice sheets may affect the surrounding ocean environment, and changes in sea surface conditions can, in turn, affect the ice sheet stability. Current observations show that the circulation of the adjacent oceans is strongly coupled with the decay of ice sheets through physical processes occurring at the ice-ocean interfaces. However, related palaeoceanographic records are still scarce. Multiple biomarker proxies, planktic and benthic foraminiferal assemblages, XRF scanning, and coarse fraction data, etc., were used to study the interactions between ocean and ice sheets in the Labrador Sea during the last 50 ka.

3) What was the history of sea surface characteristics in southern Baffin Bay during the last deglaciation? If sea ice variations in southern Baffin Bay were comparable to those in the Labrador Sea? Was there any implication for the last deglacial abrupt climate changes?

Changes in sea surface characteristics, especially sea ice distribution, in the Labrador Sea-Baffin Bay transect during the last deglaciation are still not clear. Multiple biomarker proxies were used to reconstruct sea surface characteristics, and specific planktic and benthic foraminifera species were applied to indicate water mass changes. Combined with previously published records, a comprehensive picture of sea ice distribution along the Labrador Sea-Baffin Bay transect during the last deglaciation can be established. Abrupt sea ice retreat may provide insights into warm water incursions, which were closely related to the deglacial abrupt climate changes.

1.7 Outline of this dissertation and declaration of author's contribution

This dissertation consists of six main chapters outlined as follows,

Chapter 1 introduces the study background, modern characteristics of the Labrador Sea and Baffin Bay, recent climate changes in the polar/subpolar regions, past climate changes during the late Quaternary, used approaches and proxies for paleoenvironmental reconstructions, and key questions addressed in this dissertation.

Chapter 2 describes locations of sediment cores, study materials, chronology, and specific experimental procedures.

Chapter 3 (paper I) addresses the key question 1. It presents reconstructions of sea surface characteristics in the eastern Labrador Sea and the surrounding ice sheet activities during the last 19 ka based on high-resolution records of multiple biomarker proxies, and XRF scanning data, etc. Four millennial-scale meltwater events have been identified, characterized by increased sea ice formation and decreased sea surface temperatures. These abrupt changes that probably occurred within a few decades might have been triggered by meltwater pulsing into the Labrador Sea periodically, resulting from the collapse of the LIS and GrIS, and were closely linked with deglacial abrupt climate changes.

Chapter 4 (paper II) addresses the key question 2. It presents reconstructions of sea surface characteristics in the eastern Labrador Sea and the surrounding ice sheet activities during the last 50 ka based on multiple biomarker proxies, planktic and benthic foraminifera data, and XRF scanning data, etc. Enhanced warm Irminger Current inflow might have caused (sub-)surface warming in the Labrador Sea, subsequently contributing to the retreat of the LIS and GrIS. Notably, the patterns of meltwater discharge varied across different phases, with iceberg discharge prevailing during the last glacial period versus meltwater plumes during the last deglaciation. Furthermore, our findings shed light on the occurrence of an offshore polynya south of Greenland during the Last Glacial Maximum.

Chapter 5 (paper III) addresses the key question 3. It presents biomarker-based reconstructions of sea surface characteristics in southern Baffin Bay spanning the last 16-10 ka. Combined with published records, deglacial sea ice distributions in the Labrador Sea-Baffin Bay transect were obtained. Six significant sea ice retreats were identified in southeastern Baffin Bay and one prominent sea ice retreat was observed in southwestern Baffin Bay, probably related to strong Atlantic Water incursions. One abrupt transition happened in both Baffin Bay and the Labrador Sea during the mid-YD, coinciding with enhanced Atlantic Water inflow and a slight recovery of the AMOC, which might have triggered the occurrence of HE0 and probably resulted in the second decrease in AMOC during the late YD and the persistence of a cold episode of YD.

Chapter 6 gives conclusions of all findings and addresses the key questions in this dissertation. Furthermore, it includes an outlook for future research.

This cumulative PhD dissertation is composed of three joint-authorship manuscripts that have been or will be published in peer-reviewed journals. The author's contributions to each work are outlined as follows:

Paper I: Last deglacial abrupt climate changes caused by meltwater pulses in the Labrador Sea

Authors: Defang You, Ruediger Stein, Kirsten Fahl, Maricel C. Williams, Daniela N. Schmidt, Ian Nicholas McCave, Stephen Barker, Enno Schefuß, Lu Niu, Gerhard Kuhn, Frank Niessen

Publication state: This manuscript was published in the journal *Communications Earth & Environment* on 17 March 2023 (*https://doi.org/10.1038/s43247-023-00743-3*).

Author contributions: R. Stein designed this study. D. You and M. Williams prepared foraminifer samples for radiocarbon measurement. D. You carried out biomarker analyses and evaluations (i.e., HBIs, sterols, alkenones, and stable hydrogen isotope compositions of fatty acid). K. Fahl and E. Schefuß conducted evaluation and quality controls of biomarker data. D. You carried out bulk parameters and coarse fraction analyses. F. Niessen and G. Kuhn performed MSCL logging and XRF scanning, respectively. M. Williams, D. Schmidt, I. McCave, and S. Barker generated and evaluated sortable silt and Mg/Ca ratios of foraminifera. R. Stein provided XRD data. D. You wrote the first version of the manuscript with strong input from R. Stein. D. Schmidt, I. McCave, S. Barker, and L. Niu contributed to the first version of this manuscript. All the co-authors contributed to the data interpretation and the final version of the paper.

Paper II: Interaction between ice sheet instability and sea surface characteristics in the Labrador Sea during the last 50 ka

Authors: Defang You, Ruediger Stein, Kirsten Fahl, Audrey Limoges, Enno Schefuß

Publication state: This manuscript was submitted to the journal *Earth and Planetary Science Letters* on 19 July 2023 and is under review now.

Author contributions: D. You and R. Stein designed this study. D. You carried out biomarker analyses and evaluations (i.e., HBIs, sterols, alkenones, and stable hydrogen isotope compositions of fatty acid). K. Fahl and E. Schefuß conducted evaluation and quality controls of biomarker data. D. You conducted planktic and benthic foraminiferal assemblages' analysis, bulk parameters measurements, and coarse fraction analyses. R. Stein provided XRF scanning data and XRD data. D. You wrote the first version of the manuscript with input from R. Stein and A. Limoges. All the co-authors contributed to the data interpretation and the final version of the paper.

Paper III: Deglacial sea surface characteristics in the Labrador Sea-Baffin Bay and implication for abrupt transition during the mid-Younger Dryas

Authors: Defang You, Ruediger Stein, Kirsten Fahl, Rebecca Jackson

Publication state: Preliminary and in preparation.

Author contributions: D. You and R. Stein designed this study. D. You carried out biomarker analyses and evaluations (i.e., HBIs and sterols). K. Fahl conducted evaluation and quality controls of biomarker data. R. Jackson provided benthic foraminifera data. D. You conducted bulk parameter measurements. D. You wrote the first version of the manuscript with input from R. Stein and some additional comments by R. Jackson. All the co-authors contributed to the data interpretation and the final version of the paper.

2 Materials and methods

2.1 Locations of sediment cores

The study area of this dissertation is the west Greenland marginal seas, including the Labrador Sea and Baffin Bay. The Labrador Sea is located in the western subpolar Atlantic between the Labrador Peninsula and Greenland, connecting to the north with Baffin Bay through the Davis Strait. Baffin Bay is located between Baffin Island and western Greenland, connecting to the Labrador Sea through Davis Strait and to the Arctic Ocean through Nares Strait (Fig. 2.1). Three sediment cores were used in this dissertation. The first sediment core (MSM12/2-05-01) is located on the Eirik Drift, the eastern Labrador Sea, which contains an expanded sedimentary section with the sedimentation rates over 30 cm/kyr (Hunter et al., 2007). Another two sedimentary cores are from the southern Baffin Bay. Core SL170 is on southeastern Baffin Bay, proximate to the Disko Bugt and the Uummannaq Trough. Core SL174 is situated in the southwestern side of Baffin Bay, in close proximity to Baffin Island.
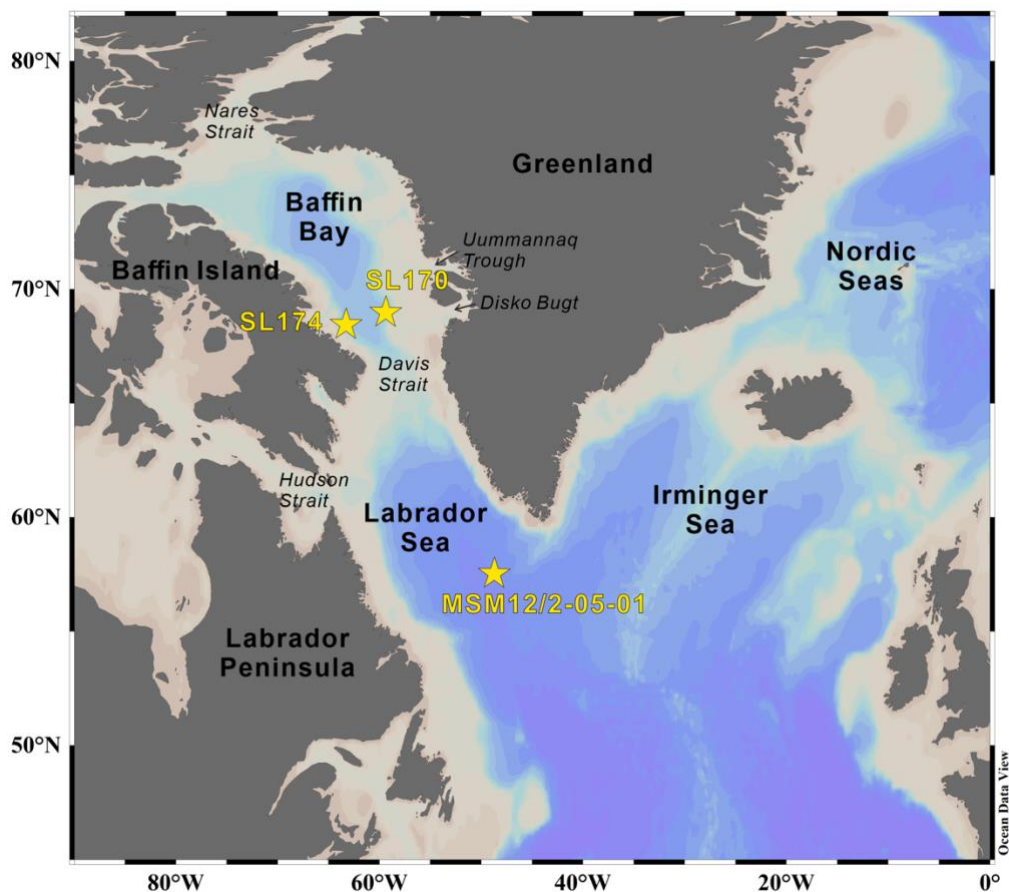
Fig. 2.1 Map of study area and the locations of study cores.

2.2 Materials

2.2.1 Sediment core from the eastern Labrador Sea

The 15 m long gravity core MSM12/2-05-01 (MSM12/647-1) was retrieved on the Eirik Drift (57° 32.31′ N, 48° 44.32′ W; water depth of 3491 m) from the eastern Labrador Sea during the R/V *Maria S. Merian* cruise MSM12/2 in 2009 (Uenzelmann-Neben, 2009) (Fig. 2.2). The lithology of this core is dominated by silty clay with some layers characterized by sandy silty clay and dropstones (1293-1313 cm, 1355-1377 cm, 1384-1391 cm, 1423-1446 cm). Notably, the presence of laminated silty clay/clayey silt deposits and the absence of coarse-grained materials is dominated in the depth of 460-1080 cm (for more details see Stein et al., 2009a).
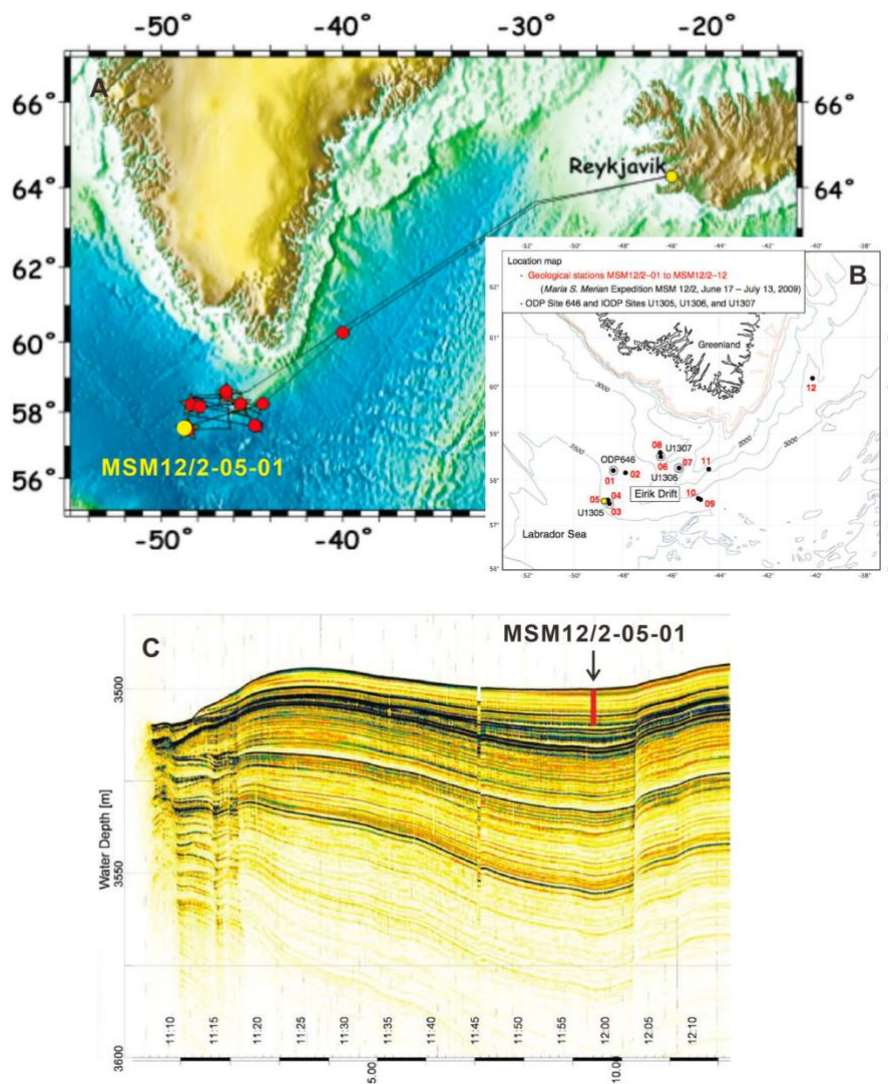
Fig. 2.2 Ship track of RV *Maria S. Merian* cruise MSM12-2 in the Labrador Sea with locations of seismic profiles (black lines) and geological stations (red dots in A, black dots in B) and PARASOUND profile with location of Core MSM12/2-05-01 (Modified from Uenzelmann-Neben, 2009). The location of study core MSM12/2-05-01 is highlighted in yellow (A). Horizontal scales are time UTC (upper) and kilometer (lower numbers and bars) (C).

2.2.2 Sediment cores from southern Baffin Bay

The 683 cm long sediment core SL170 (MSM09/02-0455/13, 68°58.15′ N, 59°23.58′ W) and the 777.5 cm long sediment core SL174 (MSM09/ 02-0467/3, 68°31.88′ N, 63°19.82′ W) were recovered from southern Baffin Bay during the *Maria S. Merian* cruise MSM09/02 (Kucera et al., 2014) (Fig. 2.3). The water depths of Core SL170 and Core SL174 is 1078 m and 1559 m, respectively. In this dissertation, samples within depths 0-677 cm of Core SL170 and within depths 2-296 cm of Core SL174 were used for measurements, which intervals have radiocarbon age controls.
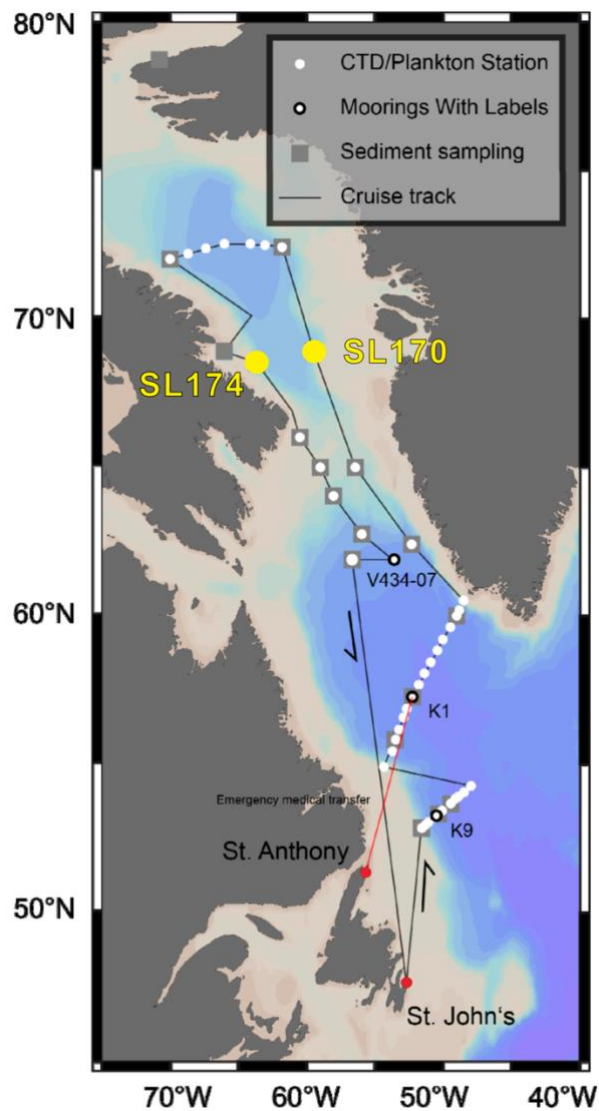
Fig. 2.3 Ship track of RV *Maria S. Merian* cruise MSM09/02 in the Labrador Sea and Baffin Bay with locations of CTD/plankton stations, moorings, and sediment stations (Modified from Kucera et al., 2014). The locations of study cores SL170 and SL174 in Baffin Bay are highlighted in yellow.

2.3 Chronology

2.3.1 Chronology of Core MSM12/2-05-01

The age model of Core MSM12/2-05-01 is constrained by 44 Accelerator Mass Spectrometry (AMS) ^{14}C dates of planktic foraminifera *Neogloboquadrina pachyderma* (sinistral). All the AMS ^{14}C dates were calibrated to calendar years (cal. ka BP) based on the Marine 13 and Marine 20 calibration curve, respectively (Reimer et al., 2013; Heaton et al., 2020). Since the local reservoir age may be changing over time and proxy data do not yet provide available reservoir age reconstruction in the study area, a global mean reservoir age was used for calibration to keep consistency with most studies in the open North Atlantic regions (Fig. 2.4; Table 2.1). Furthermore, due to the uncertainty of the local reservoir age ($\triangle$R), a $\triangle$R of 0 ± 200 years was applied to account for the reservoir age variations, which is in line with other studies in the North Atlantic (cf., Oppo et al., 2015; Andrews et al., 2018). In the first paper (Chapter 3), we used the Marine 13 calibration curve to keep consistency with other published records. In addition, we also tested the calibration with the Marine 20 calibration curve, and the results are similar (i.e., the whole records become around 200 years younger) and do not influence our interpretations (Table 2.2; for more details, see Supplementary Fig. 8 from Chapter 3). Heaton et al. (2023) proposed that despite some uncertainty in the high-latitude regions, the Marine 20 calibration curve is recommended to use for age calibrations in the polar regions. Thus, the age model of the second manuscript was developed based on the Marine 20 calibration curve (Chapter 4). The final age-depth models were established based on the Bayesian age-modelling (Bacon) approach (Blaauw and Christen, 2011). Figure 2.5 shows the age-depth models of Core MSM12/02-05-01 based on Marine 13 and Marine 20 calibration curve, respectively.

Additionally, Heaton et al. (2023) suggested that modelled reservoir ages during the glacial period (i.e., before the Holocene) might be useful for calibrations in high-latitude regions. Thus, besides using a $\triangle$R of 0 ± 200 years, we also tried to use modelled reservoir ages in our study and compared the records based on different age models (Outlook; Appendix A).
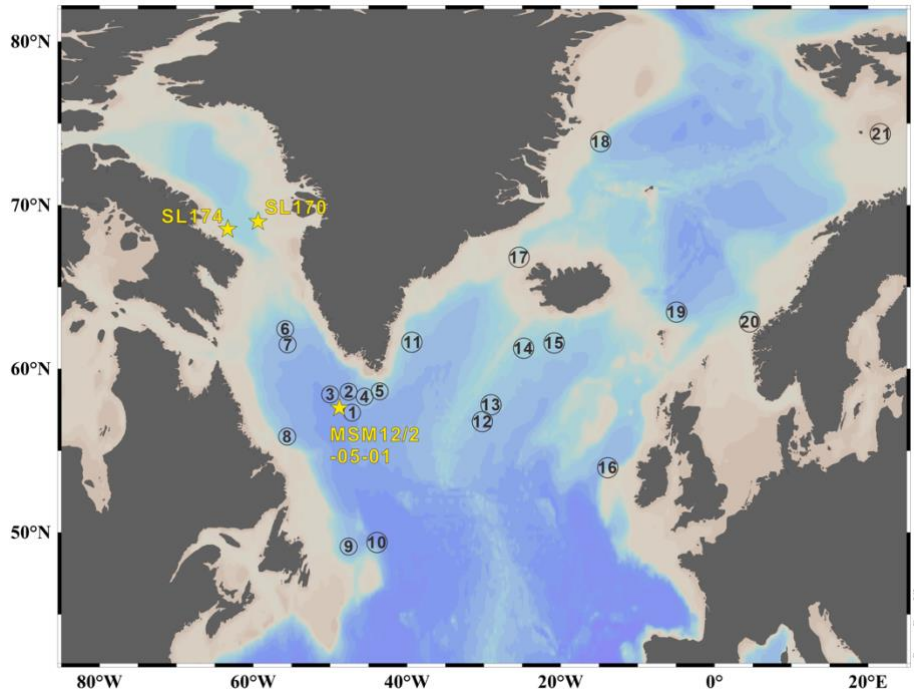
Fig. 2.4 Map showing the locations of study cores (yellow stars) and reference cores in the North Atlantic regions used for local reservoir age (△R) comparison (numbered).

Table 2.1 Pre-Holocene local reservoir ages (△R) used in sediment cores from the North Atlantic regions before the Marine 20 calibration curve was proposed.

Number	Region	Core	△R (year)	Reference
1	Labrador Sea	MD99-2227	0	Colville et al., 2011
2		HU-090-013-013	0	de Vernal and Hillaire-Marcel, 2000
3		GS16-204-22CC-A	0	Griem et al., 2019
4		TTR-451	YD: 437; HS1: 801 and 499	Stanford et al., 2006
5		IODP-U1306	0	Channell et al., 2012
6		DA04-31P	LGM-YD: 200; HS1: 600	Knutz et al., 2011
7		DA04-31P; HU87033-008	LGM-YD: 200	Winsor et al., 2015a
8		MD99-2236	50 ± 50	Jennings et al., 2015
9		KN158-4-27 GGC	0	Hoffmann et al., 2019
10		cold-water coral	YD: 200; B/A: 0	Cao et al., 2007
11	Irminger Sea	SU90-24	0	Elliot et al., 1998
12	Iceland Basin	MD99-2254	0	Solignac et al., 2004
13		KN166-14 11JPC/3GGC	0	Elmore et al. ,2015
14		ODP-984	0	Praetorius et al., 2008
15		EW9302-24/25/26GGC	YD: 350; HS1: 700	Oppo et al., 2015
16	Rockall Trough	ODP-980	YD: 400; HS1: 1100-1600	Benway et al., 2010
17	Nordic Seas	PS2644; MD99-2260/2323	0	Andrews et al., 2017
18		PS1878; PS1910	0	Telesinski et al., 2014
19		JM-FI-19PC	0	Ezat et al., 2017
20		marine shells vs. terrestrial plant	YD: 250	Bondevik et al., 2006
21		GC14-190-01PC	0	Knies et al., 2018
n/a	Baffin Bay	SL170; SL174; JR175-VC29, etc.	140 ± 35	e.g., Lloyd et al., 2011; Jackson et al., 2017; Oksman et al., 2017; Jennings et al., 2017

Table 2.2 AMS ^{14}C dates of Core MSM12/2-05-01.

Lab ID	Depth (cm)	Species	AMS ^{14}C age (yr.)	△R	Calib. age (yr. BP) ***	Model age (yr. BP) ***	Calib. age (yr. BP) ****	Model age (yr. BP) ****
SUERC-45889*	4.75	planktic	2082±35	0±200	1669	1899	1504	1745
SUERC-47577	108.5	planktic	3450±38	0±200	3314	3281	3148	3109
SUERC-45890	200.5	planktic	4227±37	0±200	4319	4420	4131	4225
SUERC-47579	300.5	planktic	5473±39	0±200	5857	5875	5660	5678
SUERC-47579	390.5	planktic	6737±37	0±200	7236	7208	7027	6999
AWI-6946.1.1**	440.5	planktic	7520±85	0±200	7986	7860	7806	7659
AWI-6947.1.1	470.5	planktic	7933±86	0±200	8420	8123	8231	7925
AWI-6948.1.1	500.5	planktic	8115±84	0±200	8641	8334	8445	8133
AWI-6949.1.1	600.5	planktic	8134±84	0±200	8664	8852	8468	8654
AWI-6950.1.1	620.5	planktic	8298±83	0±200	8849	8962	8666	8767
SUERC-45891	650.5	planktic	8449±38	0±200	9038	9154	8842	8960
SUERC-47582	720.5	planktic	9049±40	0±200	9793	9625	9609	9449
AWI-5788.1.1	749.5	planktic	9096±122	0±200	9847	9802	9671	9622
AWI-5789.1.1	799.5	planktic	9585±117	0±200	10464	10099	10305	9920
AWI-5793.1.1	919.5	planktic	9831±127	0±200	10767	10680	10644	10538
AWI-5794.1.1	929.5	planktic	9606±120	0±200	10490	10729	10335	10586
AWI-5795.1.1	952.5	planktic	9641±119	0±200	10534	10855	10384	10715
AWI-5798.1.1	999.5	planktic	9860±119	0±200	10802	11131	10683	11023
AWI-5799.1.1	1029.5	planktic	10029±125	0±200	11008	11409	10903	11264
AWI-5800.1.1	1059.5	planktic	10428±128	0±200	11627	11744	11492	11571
AWI-5803.1.1	1108.5	planktic	10543±129	0±200	11788	12275	11653	12093
AWI-6484.1.1	1114.5	planktic	10621±100	0±200	11908	12308	11764	12124
AWI-6485.1.1	1118.5	planktic	11130±101	0±200	12611	12332	12430	12147
AWI-6486.1.1	1123.5	planktic	11141±94	0±200	12626	12635	12445	12469
AWI-6487.1.1	1127.5	planktic	11752±95	0±200	13213	12969	13080	12829
AWI-5952.1.1	1130.5	planktic	11854±131	0±200	13320	13217	13186	13097
SUERC-47583	1140.5	planktic	12379±43	0±200	13869	14027	13777	13965
SUERC-51888	1150.5	planktic	12975±44	0±200	14794	14374	14650	14253
AWI-6488.1.1	1153.5	planktic	12942±102	0±200	14742	14483	14601	14342
AWI-6489.1.1	1155.5	planktic	12671±102	0±200	14356	14555	14212	14401
AWI-6490.1.1	1157.5	planktic	12518±106	0±200	14086	14629	13978	14459
AWI-6491.1.1	1159.5	planktic	12721±106	0±200	14434	14699	14288	14515
AWI-5954.1.1	1160.5	planktic	12544±120	0±200	14135	14851	14020	14656
AWI-6492.1.1	1162.5	planktic	12972±105	0±200	14789	15387	14643	15169
AWI-5955.1.1	1165.5	planktic	13965±135	0±200	16361	16192	16035	15943
AWI-5956.1.1	1167.5	planktic	14937±147	0±200	17683	16731	17265	16458
SUERC-47584	1170.5	planktic	15386±51	0±200	18212	17542	17797	17232
SUERC-51887	1190.5	planktic	17007±57	0±200	20031	20358	19631	19943
SUERC-47585	1300.5	planktic	19096±67	0±200	22576	22647	22171	22219
SUERC-51889	1312.5	planktic	22063±90	0±200	25923	25923	25445	25163
SUERC-45892	1350.5	planktic	29502±316	0±200	33225	33012	33064	32659
SUERC-51890	1385.5	planktic	33049±305	0±200	36661	37134	36739	36828
SUERC-47586	1400.5	planktic	37491±521	0±200	41569	41163	41254	40775
SUERC-47587	1490.5	planktic	46458±1576	0±200	48598	50110	48401	49695

* AMS ^{14}C dates were carried out at the NERC Radiocarbon Laboratory at SUERC (Scottish Universities Environment Research Centre, the University of Glasgow). They were recalculated from the unpublished data of Williams, (2015). ** AMS ^{14}C dates were measured at the Alfred Wegener Institute, Bremerhaven. *** Calibrations based on the Marine 13 calibration curve (Reimer et al., 2013). **** Calibrations based on the Marine 20 calibration curve (Heaton et al., 2020).
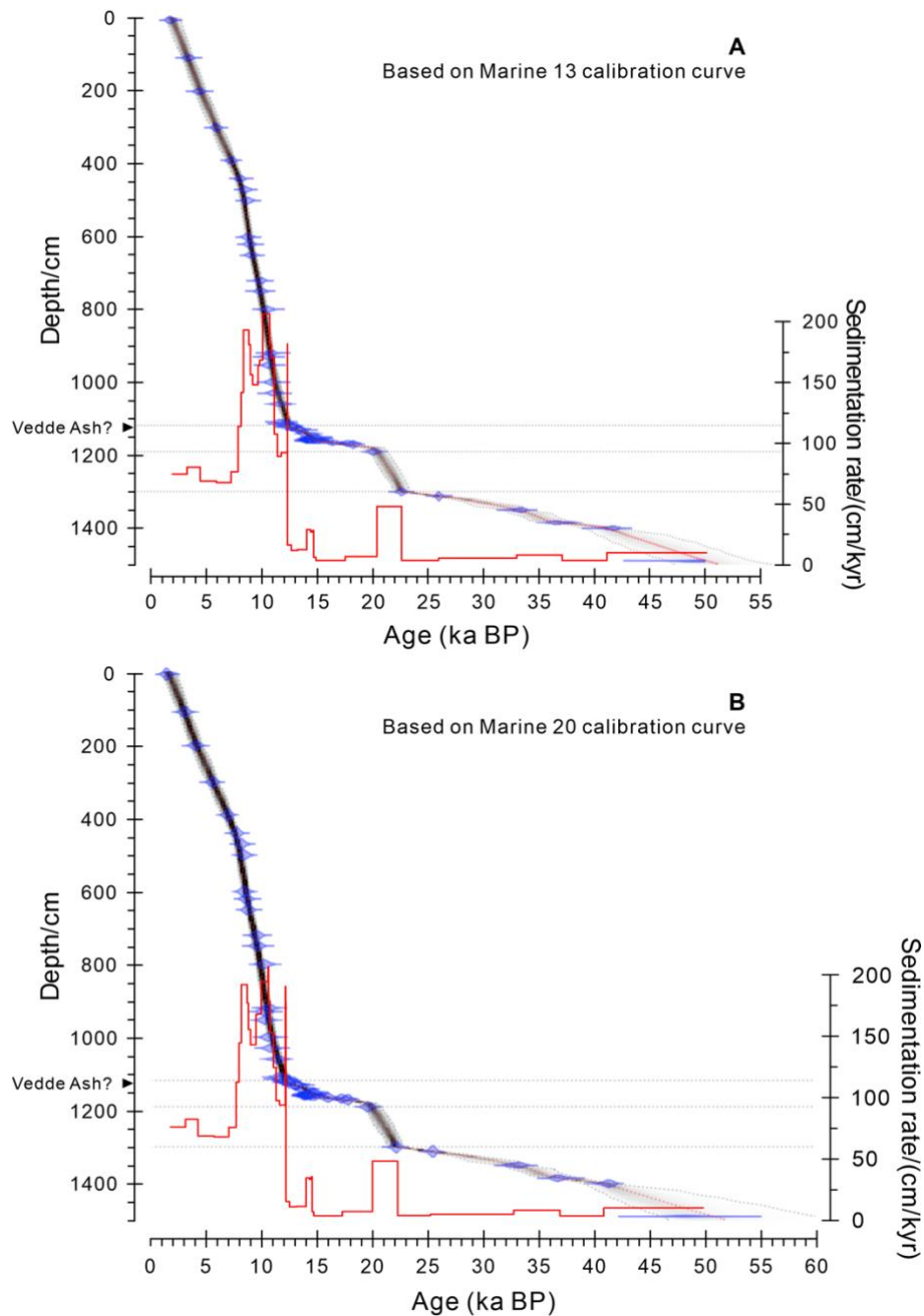
Fig. 2.5 Age-depth models and linear sedimentation rates (LSR) of Core MSM12/2-05-01 based on the Marine 13 and Marine 20 calibration curve, respectively. Bayesian age-depth models were established based on 44 AMS ^{14}C dates (see Table 2.2) using the Bacon program (Blaauw and Christen, 2011). The horizontal dashed lines indicate sediment depths where sedimentation rates change significantly. Grey stippled lines indicate 95% confidence intervals of calibration age. The red lines show LSR based on the calibrated age control points; The black triangles mark the depth of a prominent tephra layer that probably represents the Vedde Ash layer (Abbott and Davies, 2012). For more details about the differences between age models based on different calibration curves, please refers to Chapter 3.5 and 3.6.

2.3.2 Chronology of Core SL170 and SL174

The original age models of Core SL170 and Core SL174 were established based on AMS ^{14}C dates from Jackson et al. (2017). The local reservoir age ($\triangle$R=140$\pm$35) was used for calibration based on published studies from surrounding areas (Table 2.1). In this study, the Marine 20 calibration curve was applied to recalculate the AMS ^{14}C dates. The final age-depth models were established by the Bacon program (Blaauw and Christen, 2011). Core SL170 and Core SL174 are constrained by 13 and 9 AMS ^{14}C dates, respectively (Table 2.3; Table 2.4). This study focuses on the interval from the last deglaciation to the early Holocene, ensuring well age controls on both cores (i.e., 0-677 cm of Core SL174; 95-296 cm of Core SL174). Figure 2.6 shows the age-depth models of Core SL170 and Core SL174 based on the Marine 20 calibration curve.

Table 2.3 AMS ^{14}C dates of Core SL170.

Lab ID	Depth (cm)	Species	AMS ^{14}C age (yr.) *	$\triangle$R	Calib. age median (yr. BP) **	Model age median (yr. BP) **
ETH-55678	24-27	mixed benthic	9668$\pm$112	140$\pm$35	10227	10055
ETH-55679	35-37	mixed benthic	9460$\pm$80	140$\pm$35	9945	10149
ETH-55680	55-57	mixed benthic	9833$\pm$83	140$\pm$35	10432	10371
ETH-55681	74-76	planktic	9901$\pm$82	140$\pm$35	10525	10578
ETH-55683.1	98-100	mixed benthic	10243$\pm$80	140$\pm$35	11014	10846
ETH-55685	116-118	mixed benthic	10274$\pm$86	140$\pm$35	11058	11033
ETH-58351	159-160	mollusc fragments	10755$\pm$85	140$\pm$35	11744	11430
ETH-58353	180-181	mixed benthic	10671$\pm$85	140$\pm$35	11809	11603
ETH-55687	266-269	mixed benthic	11267$\pm$100	140$\pm$35	12486	12305
ETH-58354	288-290	mixed benthic	11150$\pm$75	140$\pm$35	12345	12462
ETH-55688	399-402	planktic	11597$\pm$104	140$\pm$35	12799	13365
KIA 40766	484-488	planktic	12730$\pm$60	140$\pm$35	14024	14240
ETH-58355	636-637	planktic	14640$\pm$130	140$\pm$35	16722	16131

* AMS ^{14}C dates were referred to Jackson et al. (2017). ** Calibrations based on the Marine 20 calibration curve (Heaton et al., 2020).

Table 2.4 AMS ^{14}C dates of Core SL174.

Lab ID	Depth (cm)	Species	AMS ^{14}C age (yr.) *	$\triangle$R	Calib. age median (yr. BP) **	Model age median (yr. BP) **
ETH-55690	97-100	planktic and mixed benthic	9793$\pm$120	140$\pm$35	10390	10304
Beta-344508	122-125	planktic and mixed benthic	10390$\pm$40	140$\pm$35	11212	11184
ETH-55691	142-145	mixed benthic	10997$\pm$110	140$\pm$35	12129	11710
ETH-58356	169-170	mixed benthic	11010$\pm$85	140$\pm$35	12152	12187
Beta - 344505	196-199	planktic	11410$\pm$50	140$\pm$35	12630	12692
KIA 40767	215-219	planktic	12000$\pm$80	140$\pm$35	13184	13238
Beta - 344507	233-236	planktic	12580$\pm$60	140$\pm$35	13832	13888
ETH-58357	278-279	planktic	14510$\pm$120	140$\pm$35	16562	16489
ETH-58358	294-295	planktic	15060$\pm$110	140$\pm$35	17228	17228

* AMS ^{14}C dates were referred to Jackson et al. (2017). ** Calibrations based on the Marine 20 calibration curve (Heaton et al., 2020).
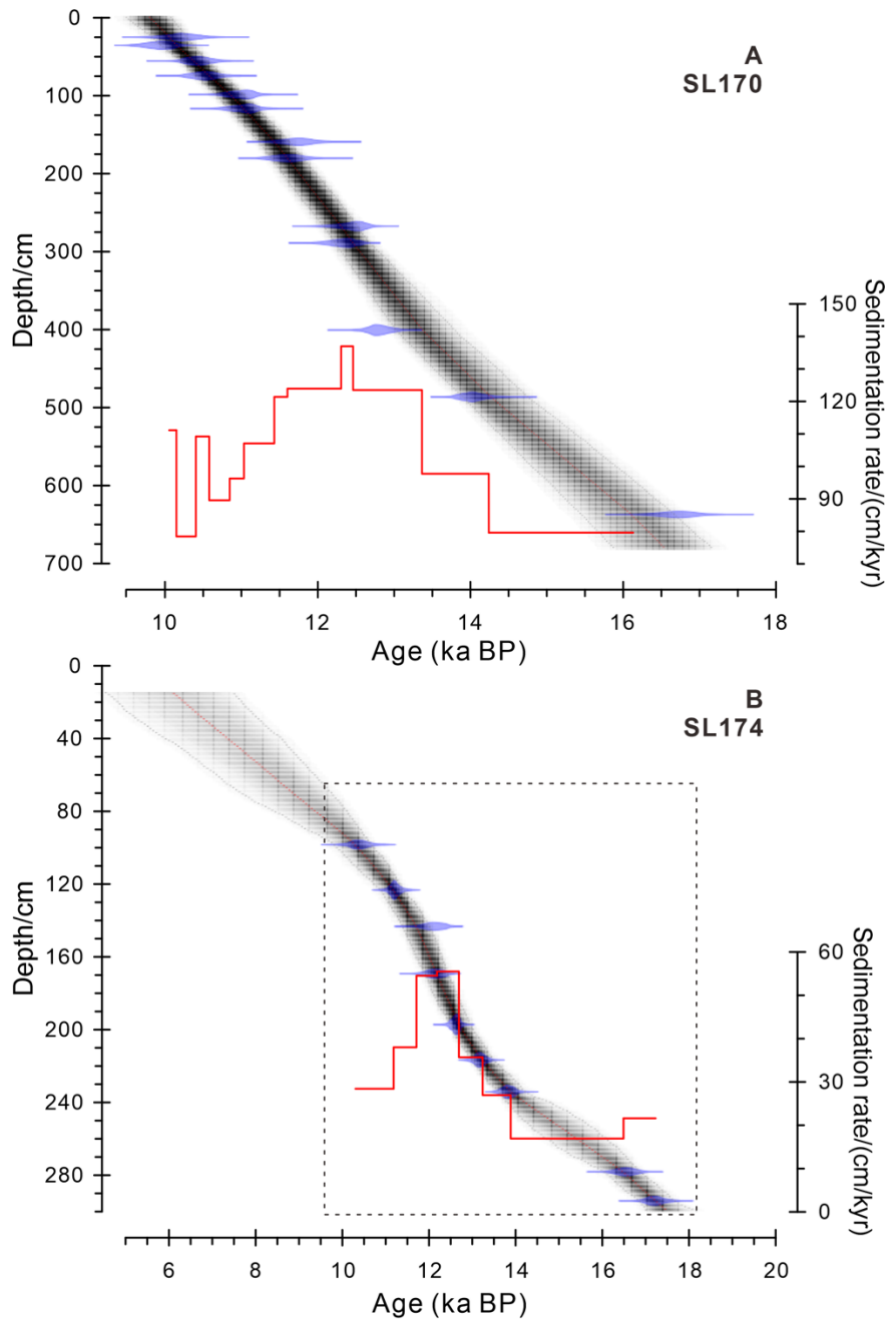
Fig. 2.6 Age-depth models and linear sedimentation rates (LSR) of Core SL170 (A) and Core SL174 (B) based on the Marine 20 calibration curve. Bayesian age-depth models were established based on AMS ^{14}C dates (see Table 2.3, 2.4) using the Bacon program (Blaauw and Christen, 2011). Grey stippled lines indicate 95% confidence intervals of calibration age. The red lines show LSR based on the calibrated age control points. The rectangle in plot B indicates the interval we focus on.

2.4 Methods

This subchapter details the methodology of experiments that I completed myself (Subchapter 2.4.1-2.4.3). Other methods of experiments done by collaborators are only briefly described (Subchapter 2.4.2). All samples were freeze-dried and stored at -20 ℃ before the experiments. The materials for geochemical measurements were homogenized by grinding. Figure 2.7 shows schematic illustration of the laboratory procedures.
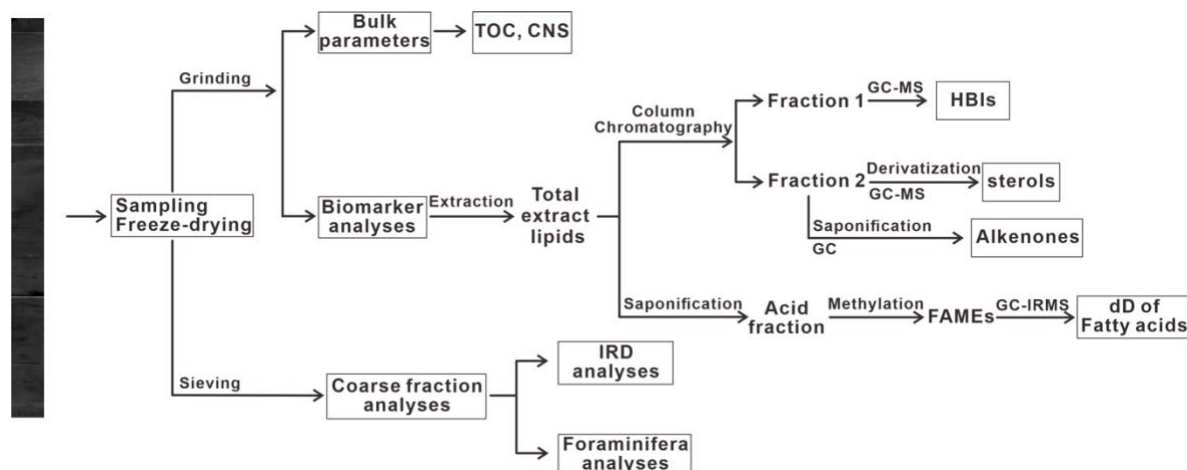
Fig. 2.7 The simplified laboratory procedures involved in this study. The X-ray photography from Core MSM12/2-05-01 within depths 550-700 cm.

2.4.1 Bulk parameter measurements

Bulk parameter measurements were carried out on three sediment cores. Freeze-dried and homogenized sediments were used for geochemical bulk parameter measurements. Total organic carbon (TOC) contents were measured by Carbon-Sulfur Analyser (CS-125, Leco) after removing carbonate with hydrochloric acid. Total carbon (TC) and total nitrogen contents were measured using the Carbon-Nitrogen-Sulfur Analyser (Elementar III, Vario). Inorganic carbon contents were calculated by subtracting TOC from TC values. Assuming that calcite is the predominant carbonate mineral ($CaCO_3$), the contents were calculated by the equation 8.

$$CaCO_3 = (TC-TOC) \times 8.333 \text{ (the stoichiometric calculation factor)} \qquad (8)$$

2.4.2 Biomarker analyses

HBIs, sterols, alkenones, and δD_{PA} analyses were conducted on samples from Core MSM12/02-05-01. Additionally, HBIs and sterols analyses were carried out on samples from Core SL170 and Core SL174. Figure 2.8 shows chemical structures of multiple biomarkers used in this study.
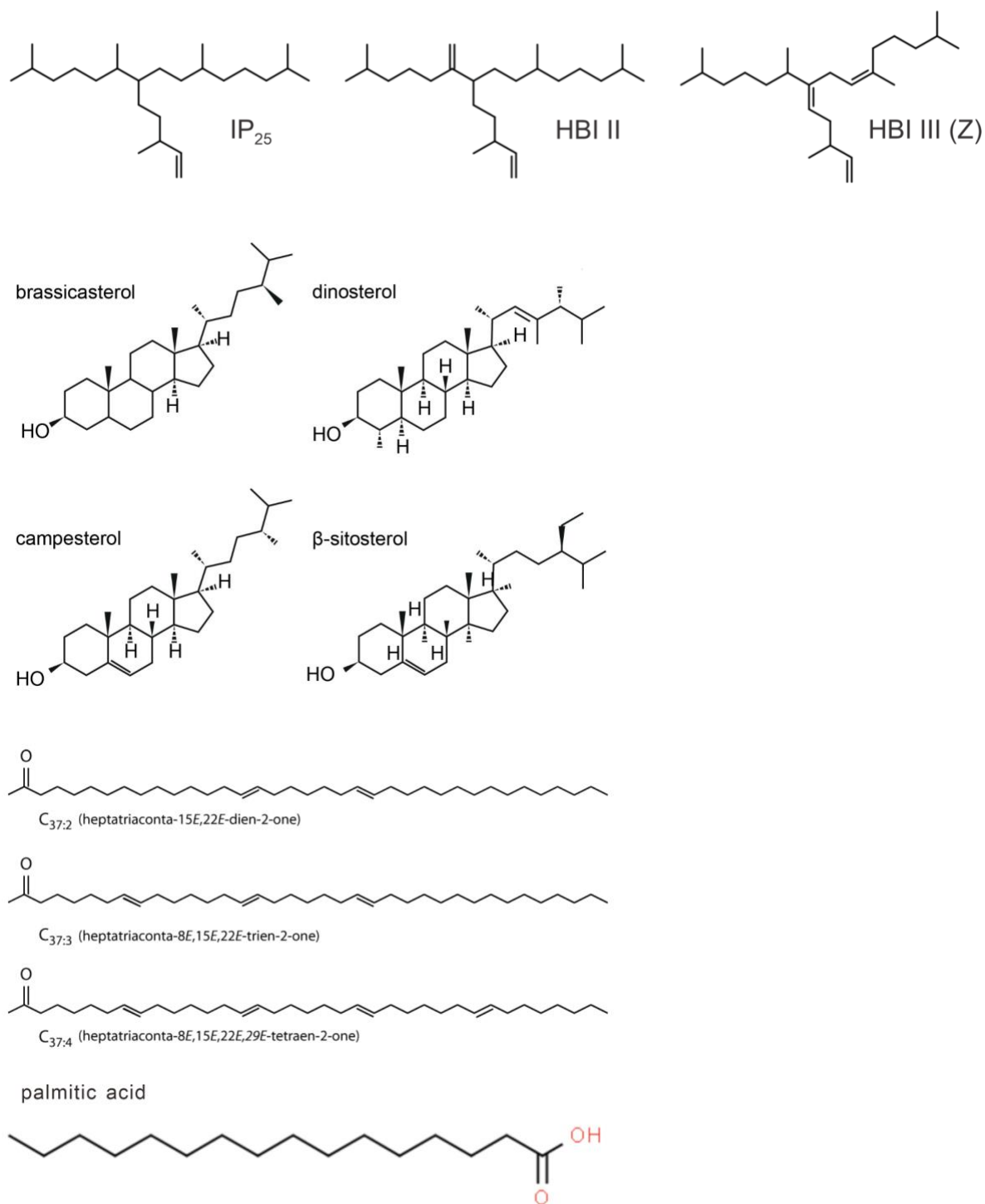
Fig. 2.8 Chemical structures of biomarkers used in this study. Figures of highly branched isoprenoids (HBIs) and specific sterols from Belt et al., 2019; figure of alkenones from Badger, 2021; figure of palmitic acid from ChemSpider (link: *http://www.chemspider.com/Chemical-Structure.960.html*).

1) lipid extraction and purification for HBIs, sterols, and alkenones

5 g of freeze-dried and homogenized sediments were extracted with 30 ml dichloromethane/ methanol (DCM/MeOH, 2:1 v/v) as solvent. Prior to extraction, the internal standards 7-hexylnonadecane (7- HND, 0.076 μg for HBIs), 9-octylheptadec-8-ene (9-OHD, 0.1 μg for

routine methodical checks), 5α-androstan-3β-ol (androstanol, 10.8 μg for sterols), and squalane (3.2 μg for alkane) were added to each sample. Samples were extracted by ultrasonication for 15 min followed by centrifugation (2000rpm, 4 mins). This procedure was repeated three times. The total lipid extracts were concentrated to around 5 ml by rotary evaporation (42 °C) and were transferred to glass vials and MeOH was added. The extracts were further extracted by *n*-hexane as a cleaning step. Furthermore, the extracts were separated into hydrocarbon and sterol fractions by open silica gel column chromatography using 5 ml *n*-hexane and 9 ml ethylacetate/*n*-hexane, respectively. As an extra cleaning step for analysing alkenones, saponification was applied to alkenone fractions using 1 ml 0.1 mol/l KOH (50°C, 12h). Additionally, open silica gel column chromatography was performed using DCM, and internal standard *n*-hexatriacontane (C_{36}, 2.1435 μg) was added to each sample before alkenones determination.

2) lipid extraction and purification for fatty acid

6g of freeze-dried and homogenized sediments were extracted by ultrasonication (15 mins, three times) with 30 ml dichloromethane/methanol (DCM/MeOH, 9:1 v/v). The internal standard $C_{19:0}$ fatty acid (50.5 μg) was added to each sample prior to the extraction. The dry extracts were saponified using 500 ul 0.1 mol/l KOH in MeOH (50 °C, 12h). For yielding neutral and acid fractions, *n*-hexane and *n*-hexane/DCM (4:1 v/v) were added to the extracts, respectively. The acid fractions were methylated with MeOH of known isotopic composition and concentrated HCl (2 ml MeOH(iso) and two drops of 37% HCl) (50°C, 12h), yielding the corresponding fatty acid methyl esters (FAMEs). The FAME fractions were cleaned by open pipet columns (4 cm silica gel with 0.5 cm Na_2SO_4) using DCM.

3) Instrumental determination

HBIs and sterols were analysed using two different gas chromatography-mass selective detector systems. The hydrocarbon fractions were analyses by GC Agilent 7890B (30m DB-1MS column, 0.25 mm i.d., 0.25 μm film thickness) coupled to an Agilent 5977A MSD (70 eV constant ionization potential, Scan 50–550 m/z, 1 scan/s, ion source temperature 230°C, Performance Turbo Pump). The temperature program as follows: 60°C for 3 min, a ramp of 15°C/min to 150°C, another ramp of 10 °C/min to 320°C, then 320°C isothermal for 15 min.

Sterol fractions were derivatized with 200 μl bis-trimethylsilyl-trifluoracet-amid (BSTFA) (60°C, 2h) before determination. The sterols were measured by GC Agilent 6850B coupled to MS Agilent 5975A MSD (same configurations as hydrocarbon measurement) with the temperature program as follows: 60°C for 2 min, a ramp of 15°C/min to 150°C, another ramp of 3°C/min to 320°C, then 320°C isothermal for 20 min.

Alkenones were analysed by GC Agilent 6890A FID (60m DB-1MS column, 0.32 mm i.d., 0.25 µm film thickness) with the temperature program as follows: 60 °C for 3 min, a ramp of 20°C/min to 150°C, another ramp of 6°C/min to 320°C, then 320°C isothermal for 40 min.

Stable hydrogen isotope composition of fatty acid was carried out on a Thermo Fisher Scientific MAT 253 Isotope Ratio Mass Spectrometer coupled via a GC IsoLink (GC-IRMS) operated at 1420 °C to a Thermo Fisher Scientific TRACE GC equipped with a Rxi-5ms column (30 m x 0.25 mm x 0.5 µm). Isotope values were measured against calibrated H_2 gas, and δD values were reported in permil against VSMOW. Measurement accuracy was controlled by *n*-alkane standards of known isotopic composition every six measurements. The long-term mean absolute deviation based on the external *n*-alkane standard mixture was 3.0‰. Daily determination of the H_3^+ factor using H_2 as reference gas gave 5.6–5.7, while the precision of the internal standard was 2‰.

4) Identification and quantification

HBIs were identified in the selected ion monitoring (SIM) mode and with a detection window between 17-19 minutes, whereas sterols were identified in the full scan (SCAN) mode. Specific compound identification was based on a comparison of GC retention times with reference compounds and published fragmentation patterns in mass spectra. HBIs were quantified based on their molecular ions (Fig. 2.9; m/z 350 for IP_{25}, m/z 348 for HBI-II, and m/z 346 for both HBI-III isomers) in relation to the fragment ion m/z 266 of 7-HND. Brassicasterol (24-methylcholesta-5,22E-dien-3β-ol), campesterol (24-methylcholest-5-en-3β-ol), sitosterol (24-ethylcholest-5-en-3β-ol), and dinosterol (4a-23,24-trimethyl-5a-cholest-22E-en-3β-ol) were quantified as trimethylsilyl ethers (Fig. 2.11). Their molecular ions m/z 470, m/z 472, m/z 486, and m/z 500 were used in relation to the molecular ion m/z 348 of androstanol. External calibration curves were applied and specific response factors were applied to balance the different responses of molecular ions of the analytes and the molecular/fragment ions of the internal standards. For more details, please refer to Fahl and Stein (2012). The identification of alkenones ($C_{37:4}$, $C_{37:3}$, and $C_{37:2}$) and specific fatty acids (i.e., palmitic acid) was based on retention times with reference compounds and the comparison with external standards (Fig. 2.10). The quantification of alkenones and palmitic acid was carried out in relation to internal standards C_{36} and $C_{19:0}$ fatty acid, respectively. For more analytical details and further reference about stable hydrogen isotope compositions of palmitic acid, see Häggi et al. (2015) and Sachs et al. (2018). It should be noted that alkenone fractions from Core SL170 and Core SL174 cannot be quantified from chromatograms due to interference by other compounds.
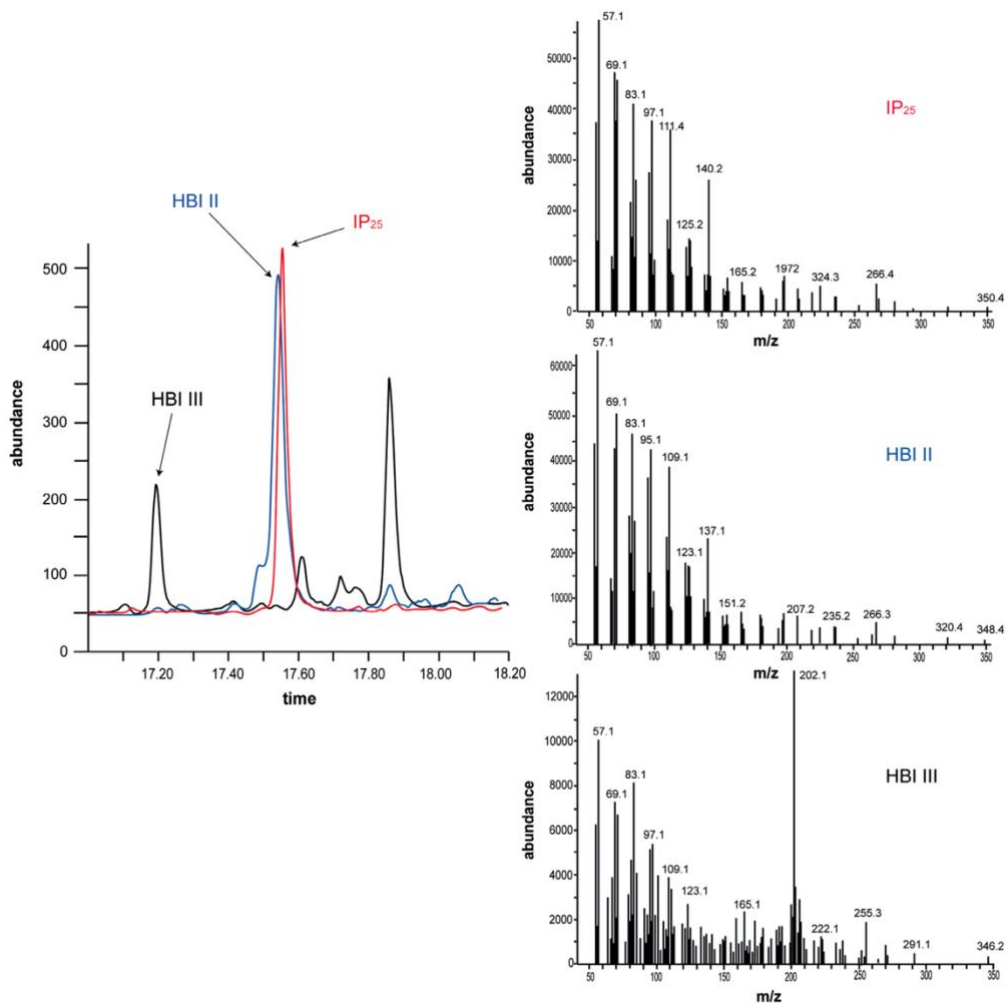
Fig. 2.9 The gas chromatogram of highly branched isoprenoids (HBIs) and their mass spectra (Figure from Kolling, 2017).

1: Heptatriaconta-8E,15E,22E,29E-tetraen-2-one ($C_{37:4}$)
2: Heptatriaconta-8E,15E,22E-trien-2-one ($C_{37:3}$)
3: Methylhexatriaconta-7E,14E,21E-trienoate ($C_{36:3}$OMe)
4: Heptatriaconta-15E,22E-dien-2-one ($C_{37:2}$)
5: Methylhexatriaconta-14E,21E-dienoate ($C_{36:2}$OMe)
6: Ethylhexatriaconta-14E,21E-dienoate ($C_{36:2}$OEt)
7: Octatrian-9E,16E,23E-trien-3-one ($C_{38:3}$Et)
8: Octatrian-9E,16E,23E-trien-2-one ($C_{38:3}$Me)
9: Octatrian-16E,23E-dien-3-one ($C_{38:3}$Et)
10: Octatrian-16E,23E-dien-2-one ($C_{38:3}$Me)

Fig. 2.10 The gas chromatogram of alkenones (Modified from Moossen, 2012). The zoomed-in section shows the C_{37} and C_{38} alkenones, and the C_{36} methyl esters. C_{37} alkenones are highlighted in red.
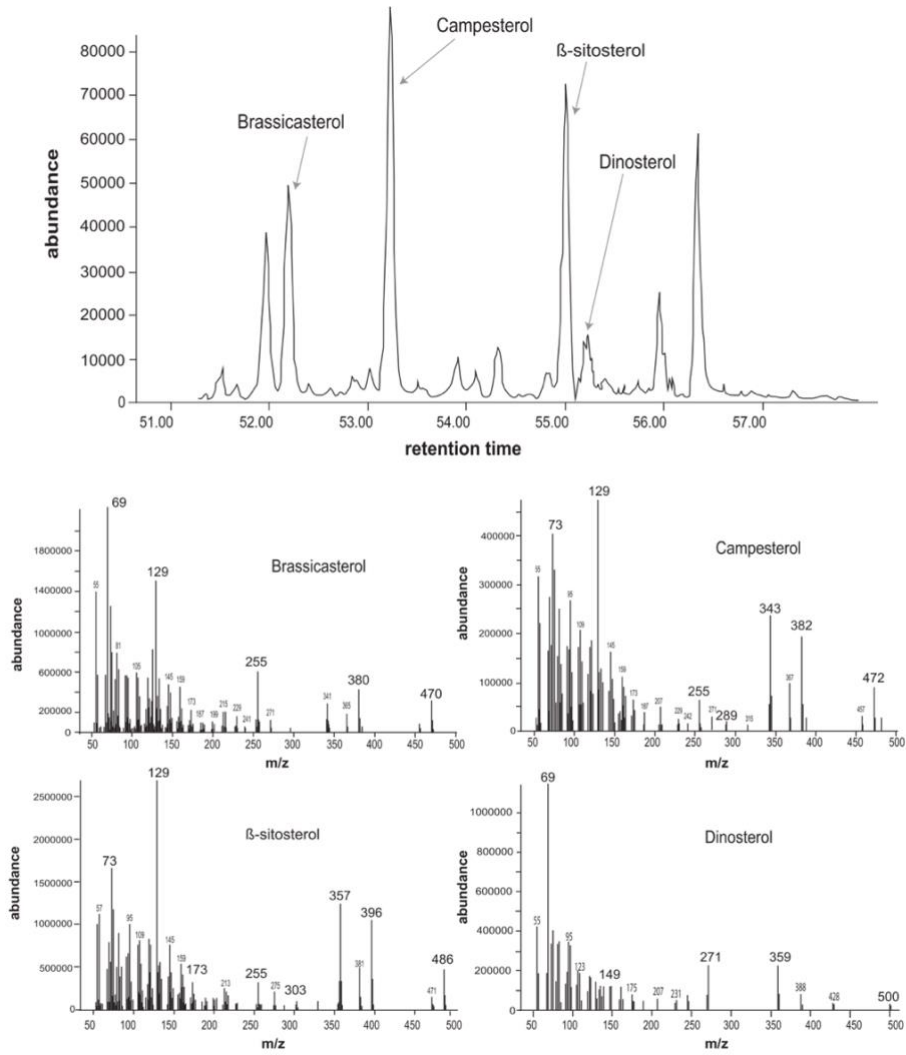
Fig. 2.11 The gas chromatogram of specific sterols and their mass spectra (Figure from Kolling, 2017).

5) Calculation of concentrations and accumulation rates

All biomarker concentrations were corrected to the amount of extracted sediment and normalized to the TOC contents of the samples. For the calculation of stable hydrogen isotope compositions of palmitic acid (δD_{PA}), δD_{PA} values were corrected for the methyl group added during methylation (For more details, see Häggi et al., 2015; Sachs et al., 2018). Accumulation rates of bulk parameters and biomarkers were calculated according to the following equations:

$$BAR = SR \times (WBD\text{-}1.026 \times PO/100) \qquad (9)$$
$$MAR = BAR \times BM \ (or \ TOC/100) \qquad (10)$$

BAR: bulk sediment accumulation rate (g cm^{-2} kyr^{-1}); SR: sedimentation rate (cm kyr^{-1}); WBD: wet bulk density (g cm^{-3}); PO: porosity (%); MAR: mass accumulation rate (g cm^{-2} kyr^{-1} or µg cm^{-2} kyr^{-1}); BM: biomarker concentration (µg g^{-1}Sed).

2.4.3 Coarse fraction analysis: IRD and foraminiferal assemblage analysis

Coarse fraction analysis was carried out on samples from Core MSM12/02-05-01. In addition, foraminifera data of Core SL170 was provided by Rebecca Jackson.

1) Identification and quantification

Around 10-15 grams of un-grinded bulk sediments were washed through a 63 μm sieve. Coarse fractions were dried and sieved through 125 μm and 250 μm meshes, respectively. IRD numbers were counted from coarse fractions above 250 μm excluding tephra particles in each sample. Planktic/benthic foraminiferal assemblage analysis was carried out on the two fractions 125-250 μm and >250 μm, respectively. The number of specimens per species from the two fractions was summed up. For samples with very large planktic foraminiferal specimens in total, a splitter was used to divide the samples equally into two, four, up to eight. For counting of benthic foraminifera, a splitter was not used. Figure 2.12 shows some SEM or digital micrographs of the main species of foraminifera used in this study.
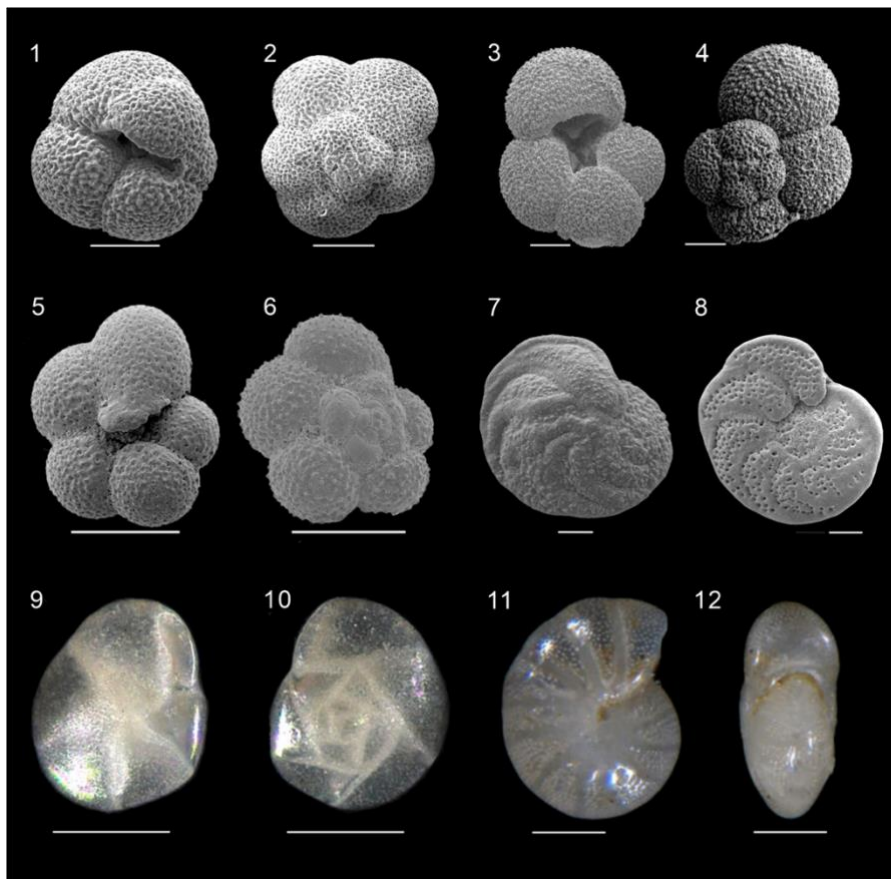
Fig. 2.12 SEM or digital micrographs of the main species of foraminifera used in this study (Chapter 4). 1,2 *Neogloboquadrina pachyderma* (sin.) (Photography from You, 2019); 3,4 *Globigerina bulloides* (Photography from Lam and Leckie, 2020); 5,6 *Turborotalita quinqueloba* (Photography from Sahoo et al., 2022); 7,8 *Cibicidoides wuellerstorfi* (Photography from You, 2019); 9,10 *Epistominella exigua* (Digital photo from Rodrigues et al., 2018); 11,12 *Melonis barleeanus* (Digital photo from Kireenko et al., 2022). Scale bar: 100 μm.

2) Calculation of abundance and accumulation rates

The number of IRD per gram (n/g) were used to indicate IRD absolute abundance. The total number of planktic/benthic foraminifera per gram (specimens/g) were applied to indicate absolute abundance of planktic/benthic foraminifera. Only samples with more than 300 planktic specimens were used for the relative abundance calculation of specific planktic species. For the relative abundance calculation of benthic foraminifera, it has been suggested that the total number of benthic specimens should be greater than 40 (cf., Seidenkrantz et al., 2021). However, due to the low abundance of benthic foraminifera in our samples, we lowered the minimum limit of the total specimens, and samples with more than 30 benthic specimens were used here for relative abundance calculation. Furthermore, accumulation rates of planktic and benthic foraminifera were calculated based on the bulk sediment accumulation rates and the absolute abundance of planktic/benthic foraminifera (equation 11).

$$\text{ARPF (or ARBF)} = \text{BAR} \times \text{PFN (or BFN)} \tag{11}$$

ARPF: accumulation rate of planktic foraminifera (specimens cm^{-2} kyr^{-1});
ARBF: accumulation rate of benthic foraminifera (specimens cm^{-2} kyr^{-1});
BAR: bulk sediment accumulation rate (g cm^{-2} kyr^{-1}) (equation 9);
PFN: planktic foraminifera number (per gram dry sediment) (specimens g^{-1});
BFN: benthic foraminifera number (per gram dry sediment) (specimens g^{-1})

2.4.4 Other methods

The following analysis was performed on Core MSM12/2-05-01 by collaborators. XRF scanning and XRD data of Core SL170 and Core SL174 are available from Jackson et al. (2017).
1) Core MSCL logging and XRF scanning

During Expedition MSM12/2, hole-core physical property measurements were conducted in the ship laboratory. These measurements include non-destructive, continuous determinations of core geometry (diameter), wet bulk density (WBD), P-wave velocity (Vp), and loop sensor magnetic susceptibility (MS) at 10 mm intervals. A standard Multi Sensor Core Logger (MSCL)-S track (GEOTEK Ltd., UK, Ser. No. 25) was used to measure temperature, core diameter, P-wave travel time, gamma-ray attenuation, and MS. A more explanation of the core logging process can be found in the "Multi-Sensor Core Logging" manual by GEOTEK, which is available for download from their website (link: *http://www.geotek.co.uk*). For further details, we refer to the Cruise Report (Uenzelmann-Neben, 2009).

The AWI Avaatech XRF Core Scanner was used for rapid and non-destructive determination of the chemical composition of sediment sections of Core MSM12/2-05-01. Split core surfaces

were scanned during a 10 kV, 30 kV, and 50 kV run to obtain reliable intensities (counts per second) of specific major elements. For documentation and analytical details, we refer to the Avaatech Manual (*https://epic.awi.de/id/eprint/37355/4/XRFCore-Scanner_user-manualV2.pdf*).

2) Grainsize analysis: Sortable Silt

The mean size of the non-cohesive sortable silt ($\overline{SS}$) fraction (10-63 μm) was measured from Core MSM12/2-05-01. 2-4 grams of sediments were added with 250 ml of 2 M acetic acid to remove carbonate. Subsequently, sediments were added with 150 ml 2 M sodium carbonate and heated at 85 °C for 5 hours to remove biogenic silica. The sample grainsize was measured using a Beckman Coulter Multisizer III with a 200 μm aperture. $\overline{SS}$ mean size measurement errors are ±2 % at sortable silt concentrations >5 %. For details, we refer to McCave et al. (1995, 2006).

3) Mg/Ca analysis of planktic foraminifera

80 to 200 individuals of *N. pachyderma* (sin.) were picked from the size fraction 150 - 212 μm for Mg/Ca analysis. Samples were cleaned before the measurement. The majority of the Mg/Ca determinations were carried out on the ICP-MS at Cardiff University with an analytical precision for Mg/Ca of ± 2 % relative standard deviation (RSD) and the remaining samples on the ICP-OES at the Bjerknes Centre for Climate Research with an analytical precision of ±1.4 % RSD. Temperatures were calculated based on following equation 11 for species-specific *N. pachyderma* (sin.) calibration (Elderfield et al., 2000). For analytical details and further references see Williams, (2015).

$$Mg/Ca = 0.5 \exp (0.1 \, T) \tag{12}$$

4) XRD measurements

A split of 1-2 grams of ground bulk sediment was measured continuously using a Phillips PW3020 diffractometer equipped with cobalt ka radiation, automatic divergence slit, graphite monochromator, and automatic sample changer, and measuring the spectrum from 20 to 40° 2Theta. Relative XRD intensities of quartz (4.26 Å), plagioclase (3.19 Å), k-feldspar (3.23 Å), dolomite (2.89 Å), and calcite (3.04 Å) were determined (Sommerfeldt, 2012). The inorganic carbon was divided into its calcite and dolomite proportions using the relative intensity (r.i.) values of the calcite (3.04 Å) and dolomite (2.89 Å) XRD peaks and assuming that calcite plus dolomite equals to the total carbonate content. Dolomite contents were calculated based on the following equation 13. For details and approach, we refer to Stein et al. (2009b, 2010).

$$\text{Dolomite (\%)} = \frac{\text{Dolomite 2.89 Å r.i.}}{(\text{Calcite 3.04 Å r.i.} + \text{Dolomite 2.89 Å r.i.})} \times \text{IC} \times 7.67 \tag{13}$$

3 Last deglacial abrupt climate changes caused by meltwater pulses in the Labrador Sea

Defang You[1*], Ruediger Stein[1,2,3], Kirsten Fahl[1], Maricel C. Williams[4], Daniela N. Schmidt[4], Ian Nicholas McCave[5], Stephen Barker[6], Enno Schefuß[2], Lu Niu[1], Gerhard Kuhn[1], Frank Niessen[1]

[1]Alfred Wegener Institute Helmholtz Centre for Polar and Marine Research, Bremerhaven 27568, Germany.

[2]MARUM-Center for Marine Environmental Sciences and Faculty of Geosciences, University of Bremen, Bremen 28359, Germany.

[3]Frontiers Science Center for Deep Ocean Multispheres and Earth System, Key Laboratory of Marine Chemistry Theory and Technology, Ocean University of China, Qingdao 266100, China.

[4]School of Earth Sciences, University of Bristol, Bristol BS8 1RJ, UK.

[5]Godwin Laboratory for Palaeoclimate Research, Department of Earth Sciences, University of Cambridge, Cambridge CB2 3EQ, UK.

[6]School of Earth and Environmental Sciences, Cardiff University, Cardiff CF10 3AT, UK.

*Corresponding author (Email: defang.you@awi.de)

3.1 Abstract

Freshwater perturbations are often thought to be associated with abrupt climate changes during the last deglaciation, while many uncertainties remain regarding the exact timing, pathway, mechanism, and influence of meltwater release. Here, we present very well-dated and high-resolution records from the eastern Labrador Sea representing the last 19.000 years, which demonstrate abrupt changes in sea surface characteristics. Four millennial-scale meltwater events have been identified between the last 14.000 and 8.200 years based on independent biomarker proxies and X-ray fluorescence scanning data. These events are characterized by increased sea ice formation and decreased sea surface temperatures which might have occurred within a few decades. We propose these abrupt changes were triggered by meltwater pulsing into the Labrador Sea periodically, resulting from collapse of the Laurentide-Greenland Ice Sheets caused by (sub-)surface ocean warming in the Labrador Sea. Our findings provide more precise information about impact of freshwater forcing on abrupt climate changes, which may help to improve simulations for past and future changes in ocean circulation and climate.

3.2 Introduction

Greenland Ice Cores preserve signals of atmospheric temperature fluctuations and reveal millennial-scale abrupt climate changes during the last glacial cycle (NGRIP members, 2004). These abrupt changes (known as Dansgarrd-Oeschger, D-O cycles (Dansgaard et al., 1993; Dokken et al., 2013)) were pronounced during Marine Isotope Stage 3 and also occurred during the last deglaciation (NGRIP members, 2004; Svensson et al., 2008). Modelling results suggest that these abrupt changes were related to intermediate or transitional climate states and closely associated with variations in the Atlantic Meridional Overturning Circulation (AMOC) (Barker et al., 2021). Previous research has linked AMOC variations to direct external forcing (i.e., astronomical influence) (Zhang et al., 2021) as well as internal feedback from the earth system, including changes in northern hemisphere ice sheet height, freshwater perturbations, and CO_2 levels, which can be related to variations in insolation caused by orbital changes (Denton et al., 2010; Thornalley et al., 2010; Barker et al., 2021).

As an unstable transition characterized by abrupt climate changes, the last deglaciation contains several outstanding stadial stages such as Heinrich Stadial 1 (HS1), the Younger Dryas (YD) cold event, and the 8.2 ka BP cold event (NGRIP members, 2004; Svensson et al., 2008). The occurrence of these cold episodes was often implicated with iceberg/meltwater discharge from the Laurentide Ice Sheet (LIS) (Hemming et al., 2004; Kleiven et al., 2008; Keigwin et al., 2018; Lochte et al., 2019). As one of the major outlets of the LIS ice streams (Margold et al., 2018), large numbers of iceberg/meltwater were transported through the Hudson Strait into the Labrador Sea during the last deglaciation (Jennings et al., 2015). Furthermore, the retreat of the Greenland Ice Sheet (GrIS) could also contribute to meltwater discharge into the Labrador Sea (Carlson et al., 2008; Winsor et al., 2015b; Levy et al., 2020; Funder et al., 2021). The freshwater from melted icebergs and land ice could have led to surface freshening not only in the Labrador Sea (de Vernal et al., 2000; Gibb et al., 2014) but may have extended over the wider North Atlantic subpolar area, as indicated from ice-rafted debris (IRD) records (Ruddiman et al., 1977; Hemming et al., 2004) (Fig. 3.1). This freshening may have caused reduced deep-water formation and limited ventilation in the North Atlantic (Denton et al., 2010; Thornalley et al., 2015; Muschitiello et al., 2019). However, many uncertainties remain regarding the exact timing, pathway, mechanism, and influence of meltwater discharge during the last deglaciation.

The Labrador Sea is an optimal area for reconstructing the history of meltwater discharge due to its proximity to the LIS and the GrIS. Furthermore, the sedimentation rates over Eirik Drift (in the eastern Labrador Sea) are high (average over 30 cm/kyr) (Hunter et al., 2007) allowing high-resolution proxy-based reconstructions of meltwater discharge, and sea ice cover, etc. Compared to upstream areas under intense winnowing (Elliot et al., 2002), this area might also preserve a continuous record of the strength of bottom currents, which could be related to Denmark Strait

Overflow Water (DSOW), the deepest component of North Atlantic Deep Water (Hunter et al., 2007) (Supplementary Fig. 3.1).
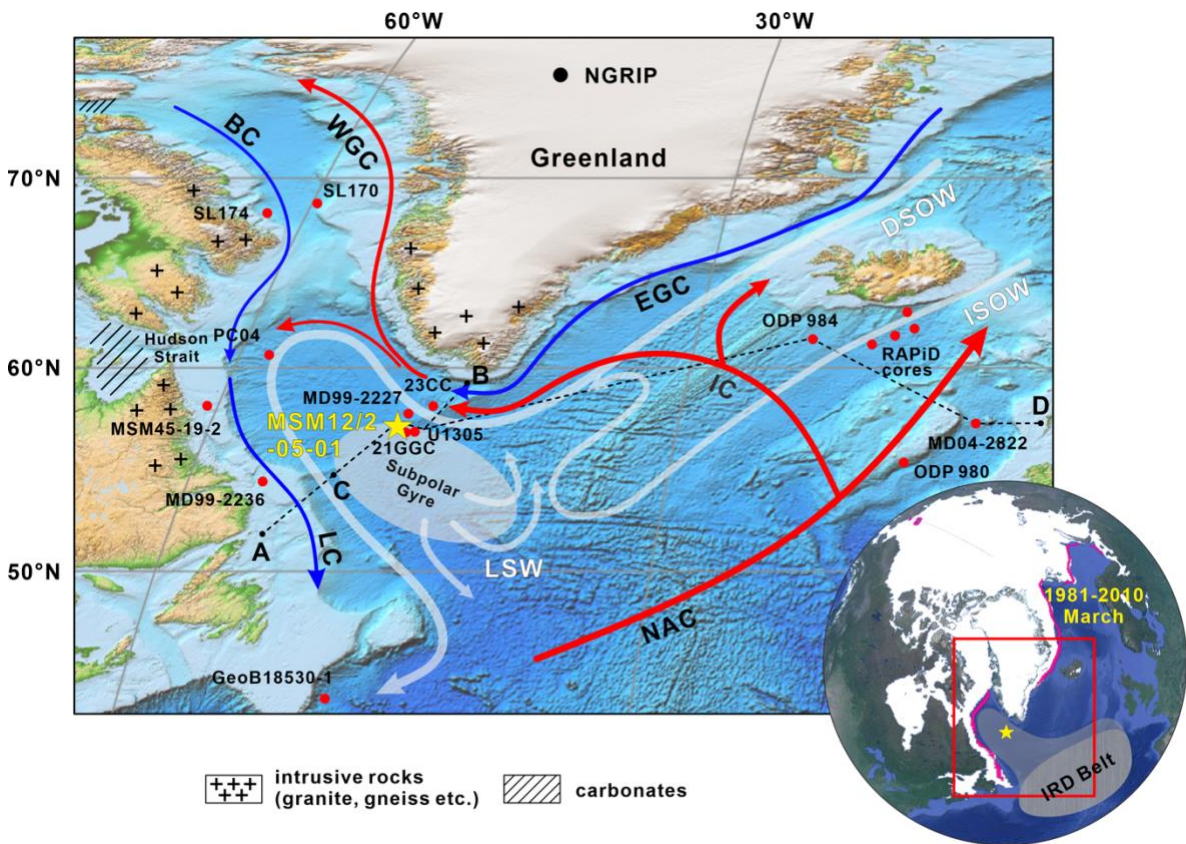
Fig. 3.1 Core sites and regional context of the study area.
Main map with core sites and modern ocean circulation pattern. Yellow star: Core MSM12/2-05-01; red dots: other cores referred to; red arrows: warm surface currents; blue arrows: cold surface currents; white arrows: deep and intermediate currents. NAC=North Atlantic Current; IC=Irminger Current; WGC=West Greenland Current; EGC=East Greenland Current; BC=Baffin Current; LC=Labrador Current; DSOW=Denmark Strait Overflow Water; ISOW=Iceland-Scotland Strait Overflow Water; LSW=Labrador Sea Water. Black stippled lines A to B and C to D show location of hydrographic transects presented in Supplementary Fig. 3.1. Simplified bedrock geology based on Simon et al. (2014). Map was taken from ETOPO1 (source: https://www.ngdc.noaa.gov/mgg/global/). Small overview map (right lower corner) with average sea ice extent of 1981-2010 March (image modified from Google Earth, data source: https://nsidc.org/), IRD belt (dark grey shading) (Ruddiman et al., 1977), distribution range of cores with IRD signal around the Labrador Sea (light grey shading) (Andrews and Voelker, 2018), and the study area (red box).

Here, we have investigated a very well-dated and high-resolution sediment core from the Eirik Drift (Fig. 3.1), representing an interval from the last deglaciation to Holocene, i.e., the last 19 ka. During the last deglaciation, four meltwater events have been identified by abrupt changes in sea surface characteristics, which are based on independent multiple biomarker proxies (i.e., IP_{25} and P_DIP_{25} for sea ice cover (Belt et al., 2007; Müller et al., 2011), specific sterols and alkenones for open-water phytoplankton productivity (Prahl et al., 1987; Belt et al., 2007; Müller et al.,

2011), the alkenone unsaturation index U_{37}^{K} for sea surface temperature (SST) (Prahl et al., 1987), the percentage of tetra-unsaturated alkenones (%$C_{37:4}$) and stable hydrogen isotope composition of palmitic acid (δD_{PA}) for meltwater discharge (Bard et al., 2000; Sachs et al., 2018), for details see Methods) and X-ray fluorescence (XRF) scanning data. Furthermore, sortable silt mean size has been used to reflect changes in bottom current intensity. In overall, enhanced Atlantic Water inflow may induce the (sub-)surface ocean warming and trigger collapse of the ice sheets surrounding the Labrador Sea. The following meltwater discharge potentially increased sea ice formation and promoted stratification of the upper ocean column in the Labrador Sea/subpolar area, preventing Atlantic Water inflow, and consequently disrupting the climate.

3.3 Results

3.3.1 Lithology, chronology and sedimentation rates.

During Expedition MSM12/2 of R/V *Maria S. Merian*, a 15m long Core MSM12/2-05-01 was recovered from the Eirik Drift at 57° 32.31′ N, 48° 44.32′ W in a water depth of 3491m (Uenzelmann-Neben, 2009). Here, we concentrate on the well-dated upper ~ 12 m of this core, representing the last 19 ka. The sediments are mainly composed of silty clay with intercalated grain-size related laminated intervals between 1103 and 1070 cm (12.2 to 11.8 ka BP), 992 and 940 cm (11 to 10.7 ka BP), 914 and 820 cm (10.6 to 10.2 ka BP), and 590 and 507 cm (8.7 to 8.3 ka BP), respectively (Supplementary Fig. 3.2 and X-ray photographs in Supplementary Fig. 3.3). A prominent maxima of tephra shards was found in the coarse fraction (>63 μm) in 1123 cm core depth (corresponding to 12.6 ka BP according to our age model; Fig. 3.2) that may represent the Vedde Ash dated to 12.12 ka BP (Abbott and Davies, 2012). We have not used this date for the development of our age model (see Methods for details).

Based on our age model, the mean sedimentation rate is 106.7 cm/kyr in the upper 1118 cm and 10 cm/kyr in the lower 60 cm. Three intervals with peak sedimentation rates occur at 12.4 to 12.1 ka BP (181 cm/kyr), 10.7 to 10.1 ka BP (206 cm/kyr), and 8.9 to 8.3 ka BP (193 cm/kyr), respectively (Fig. 3.2). One other interval with higher sedimentation rates occurs at 14.8 to 13.9 ka BP (28 cm/kyr). This well-dated sedimentary sequence of Core MSM12/2-05-01 allows a detailed proxy-based reconstruction of the environmental evolution in the Labrador Sea and its significance for (global) climate change during the last deglaciation.
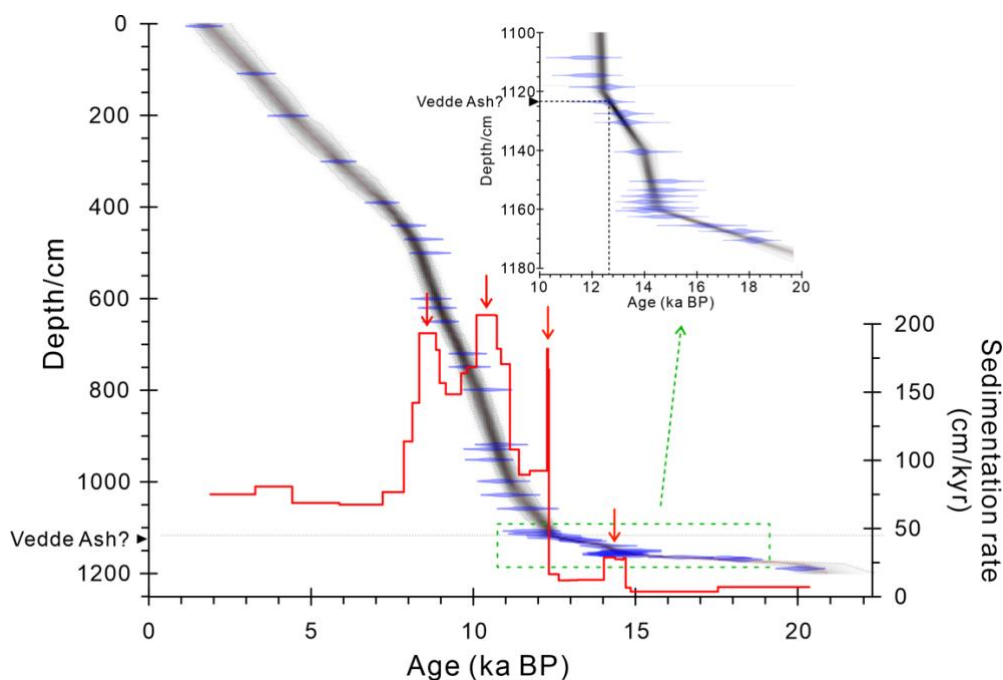
Fig. 3.2 Age model of Core MSM12/2-05-01.
Bayesian age-depth model was established based on 38 radiocarbon dates (see Supplementary Table 3.1) using the Bacon program (Blaauw and Christen, 2011). The horizontal dashed lines indicate sediment depths where sedimentation rates change significantly. Grey stippled lines indicate 95% confidence intervals of calibration age. The red line shows linear sedimentation rates (LSR) based on the calibrated age control points; red arrows highlight the intervals of maximum LSR. The black triangles mark the depth of a prominent tephra layer that probably represents the Vedde Ash layer (Abbott and Davies, 2012).

3.3.2 Changes in sea ice, sea surface temperature, and productivity.

The results of biomarker-based reconstruction of sea ice, SSTs, and primary productivity are shown in Figure 3.3. Following Mollenhauer et al. (2011), radiocarbon age differences between biomarker (alkenones) and planktic foraminifera in records from the Gardar Drift (close to Eirik Drift) are negligible, suggesting that marine organic matter has been deposited quiet rapidly or only transported over very short lateral distance. Therefore, we interpret our biomarker records to reflect predominantly surrounding environmental conditions. Furthermore, we base our argumentation on the similarity of the alkenone-based SSTs with those derived from Mg/Ca ratios of planktic foraminifera (more likely to be *in situ*) (Fig. 3.3c), suggesting that the more-easily transported biomarker records are not affected by long-distance allochthonous transport. Finally, biomarker-based reconstructions from surface sediments in the Baffin Bay and the Labrador Sea mirror modern surface water and sea ice conditions very well (Filippova et al., 2016; Kolling et al., 2020), therefore supporting our interpretation.

Several abrupt changes in surface characteristics occur during the last deglaciation. Around 18.4 ka BP, the sea ice extent decreased rapidly as shown by decreased values of sea ice proxy P_DIP_{25}, coinciding with the abrupt increase in SSTs. Temperatures based on both alkenones and

planktic foraminiferal Mg/Ca show relatively high values (warmer than the modern annual average) during the early HS1 (Fig. 3.3c) During the late HS1, the P_DIP_{25} values are around 0.5, indicating marginal ice zone conditions ($0.5<P_DIP_{25}<0.7$). Simultaneously increased concentrations of IP_{25} and open-water phytoplankton biomarkers (Fig. 3.3a, e, f) could be explained by polynya formation along the GrIS margin, caused by strong offshore katabatic winds at the edge of the extended ice sheets (cf., Syring et al., 2020). The maximum occurrence of HBI-III (Z) concentration may also support a marginal ice zone situation (cf., Belt et al., 2015). In addition to the late HS1, four prominent meltwater events have been identified (for details see below). These events are marked by abrupt increase in P_DIP_{25} values, decrease in the concentrations and accumulation rates of open-water phytoplankton indicators, decrease in SSTs, and low planktic foraminifera abundance, reflecting abruptly increased sea ice formation, reduced primary productivity, and strong meltwater discharge (cf., Fig. 3.4c). According to Müller et al. (2011), low concentrations of both IP_{25} and open-water phytoplankton biomarkers might point to permanent sea ice cover, prohibiting the growth of ice algae and open-water phytoplankton due to limited light and nutrient supply (Supplementary Fig. 3.4). However, SST values well above 0 ℃ in our record contradict this interpretation. Instead, oligotrophic conditions due to massive meltwater input seem to be a more realistic explanation of the reduced surface-water production in this case (cf., Fig. 3.4c).

During the middle to late Holocene (i.e., the last about 8 ka), the sea ice biomarker IP_{25} and the ice-edge related biomarker HBI-III (Z) are absent, but high contents of open-water phytoplankton biomarkers dinosterol and C_{37} alkenones are found, indicating an ice-free ($P_DIP_{25}=0$) and elevated surface-water productivity environment. The complete absence of HBI-III (Z) throughout this time interval characterized by the absence of any sea ice, is supporting that HBI-III (Z) is somehow related to sea ice (the marginal ice zone, see above) as proposed by Belt et al. (2015). The decreasing Holocene SST values reflected by both alkenones and Mg/Ca records, are probably driven by reduced summer insolation (Fig. 3.4a, e).

3.3.3 Changes in meltwater discharge.

We used the percentage of tetra-unsaturated alkenones (%$C_{37:4}$) as proxy for low temperature and/or low salinity conditions (i.e., meltwater input) (e.g., Bard et al., 2000). According to Prahl and Wakeham (1987), $C_{37:4}$ is synthesized by *Emiliania huxleyi* (a dominant coccolithophorid species in seawater) at low temperatures but also other alkenone producers adapted to low salinity water (Rosell-Melé, 1998; Bard et al., 2000; Bendle et al., 2005). More recently, Lochte et al. (2020) and Wang et al. (2021) have proposed that %$C_{37:4}$ might be an index for sea ice cover. Based on culture experiments (Wang et al., 2021), this alkenones can also be produced by a newly
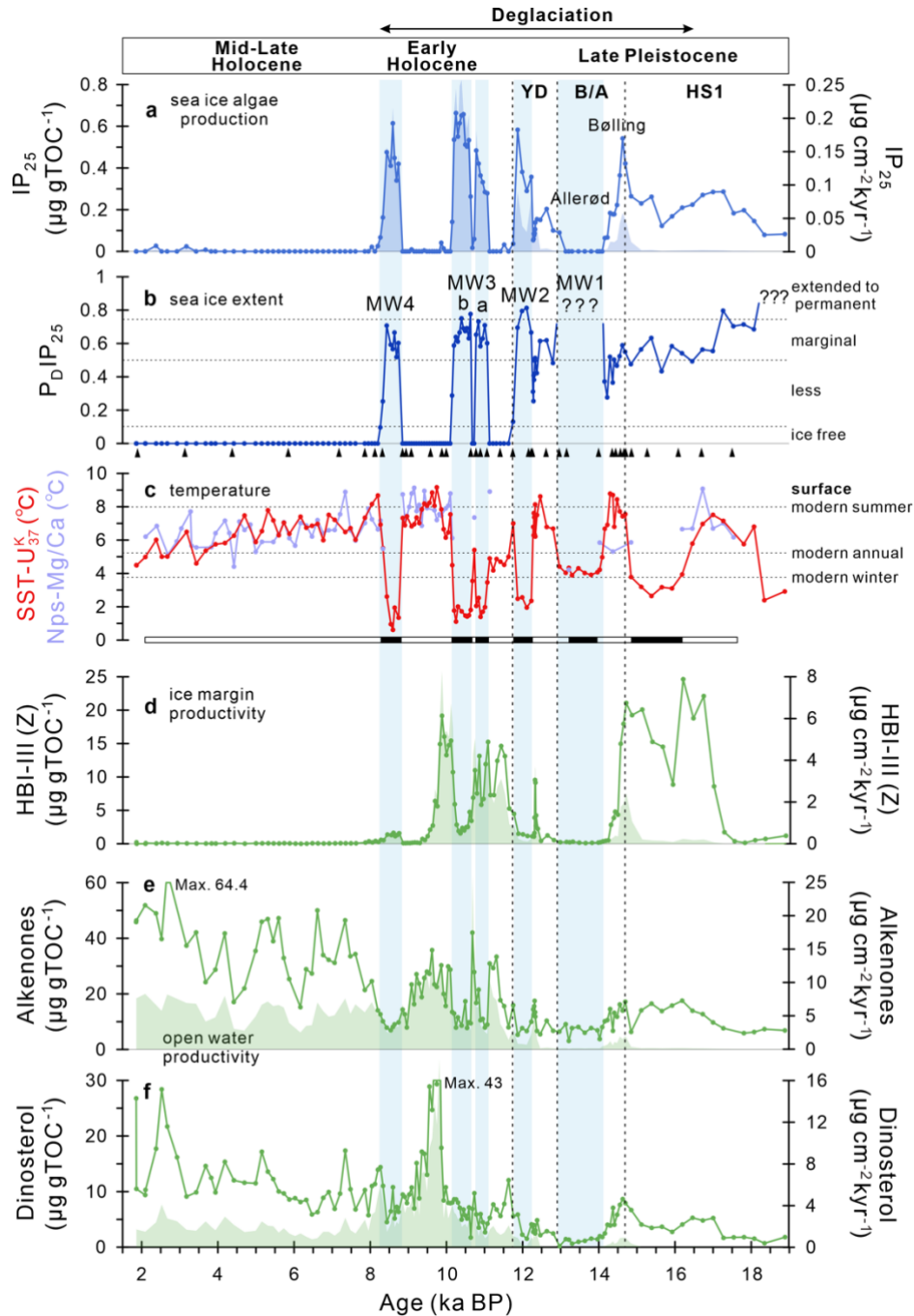
Fig. 3.3 Proxy records for sea surface characteristics (Core MSM12/2-05-01).
(**a**) Concentration (line) and accumulation rate (shading) of IP$_{25}$; (**b**) P$_D$IP$_{25}$ based on dinosterol. For the intervals characterized by zero or minimum concentrations of IP$_{25}$ and phytoplankton biomarkers, P$_D$IP$_{25}$ values cannot be calculated (highlighted by question marks; cf., Müller et al., 2011); for details see text and Supplementary Fig. 3.4; (**c**) Sea surface temperature (SST) based on U$_{37}^K$ and *N. pachyderma* (sin.) (Nps)-Mg/Ca values. Black and white bar represents the abundance of planktic foraminifera, with black bars indicating intervals of absence or low abundance of planktic foraminifera (thus no Mg/Ca temperatures and AMS[14]C could be determined), probably related to too low salinity due to strong meltwater discharge (cf., Fig. 3.4c); (**d**) HBI-III (Z); (**e**) Alkenones; (**f**) Dinosterol. Light blue shadings highlight the intervals of strong meltwater discharge. Vertical stippled lines mark the intervals: Heinrich Stadial 1 (HS1), the Younger Dryas (YD), and the Bølling/Allerød (B/A). Black triangles mark available AMS[14]C dates.

found lineage of coccolithophorids living in sea ice, reaching %$C_{37:4}$ values around 80%. However, $C_{37:4}$ is not the dominant alkenones in our record (i.e., less than 12%) (Fig. 3.4c), suggesting that open-water algae production influenced by meltwater is probably the primary source of alkenones here. In order to further support our argumentation that %$C_{37:4}$ is related to meltwater discharge, stable hydrogen isotope compositions of palmitic acid (δD_{PA}) have been measured in selected samples. Although palmitic acid is produced by most marine and terrestrial organisms, Sachs et al. (2018) presented multiple lines of evidence that support marine phytoplankton being its primary source to Arctic Ocean sediments. In their study of surface sediments along transects representing large salinity gradients from 11 to 32, these authors demonstrate the correlation between the δD_{PA} values and surface water salinity, with low (high) δD_{PA} values indicating low (high) salinity sea surface environments. Thus, the good correlation between %$C_{37:4}$ and δD_{PA} values supports our interpretation as meltwater signal (Fig. 3.5a).

%$C_{37:4}$ values are highly variable during the last deglaciation. Following the late HS1 interval with %$C_{37:4}$ values that gradually increased, four meltwater events have been identified that display abrupt and rapid increase in %$C_{37:4}$ values (i.e., meltwater discharge) within a few decades. We name these events MW1 to MW4, with MW3 comprising two phases (a and b) that maybe occur around 150 years apart (MW1: 14.08-12.93 ka based on median age, 14.62-12.67 ka (95% confidence interval); MW2: 12.23-11.87 ka, 12.52-11.45 ka (95%); MW3a: 11.07-10.78 ka, 11.51-10.48 ka (95%); MW3b: 10.64-10.15 ka, 10.96-9.81 ka (95%); MW4: 8.74-8.33 ka, 9.05-8.01 ka (95%)) (Fig. 3.4c). The absence or low abundance of planktic foraminifera during meltwater events may also support low salinity in the upper ocean due to strong meltwater discharge (Figs. 3.3c, 3.4c). During the middle to late Holocene, i.e., the last about 8 ka, there is nearly no $C_{37:4}$ (meltwater input) due to the complete decay (absence) of the LIS. The absence of meltwater may explain the dominantly ice-free conditions in the eastern Labrador Sea during this time interval. At around 2 ka BP, a slight increase in %$C_{37:4}$ values are probably associated with the Neoglacial expansion of the GrIS (Lecavalier et al., 2014) which might have triggered some release of meltwater into the Labrador Sea.

There are probably two major sources of meltwater. One is from melted icebergs, which is characterized by increased ice-rafted debris (IRD) abundance. The other is meltwater plumes triggered by disintegration of ice sheets and characterised by high loading of fine-grained suspended matter (Rashid et al., 2011; Leng et al., 2018), as shown by increased %$C_{37:4}$ values, low percentage of coarse fraction (>63 μm/%), and low IRD abundance. During MW1, high %$C_{37:4}$ values and increased IRD abundance indicate increased iceberg discharge into the eastern Labrador Sea, a situation similar to the HS1. However, during MW2, MW3, and MW4, increased %$C_{37:4}$ values coinciding with extremely low coarse fraction content suggest freshwater/meltwater is released by meltwater plumes (Fig. 3.4i and 3.5c). The dominance of

laminated silty clay/clayey silt deposits and the absence of coarse-grained IRD during MW2 to MW4 (see X-ray photographs in Supplementary Fig. 3.3; "plumites") further demonstrate the importance of suspension-rich meltwater plumes controlling sedimentation at these times. Such pulses of suspended fine-grained detrital sediment input most likely contributed to high concentrations of the non-biogenic fraction and elevated sedimentation rates (Figs. 3.2, 3.4g). Increased silicon (Si) to strontium (Sr) ratios (an index for detrital silicate-rich minerals input (Hodell et al., 2008) and some dolomite deposition (Fig. 3.4g) suggest that these meltwater plumes are related to the LIS with transport via Hudson Strait, probably superimposed by input from the GrIS (Fig. 3.1).

3.3.4 Changes in the strength of bottom currents.

In addition to the surface water characteristics, some reconstruction of bottom currents has been conducted. Flow speed analysis was investigated via sortable silt mean size ($\overline{SS}$), a direct grain size proxy for the strength of bottom currents (McCave et al., 1995). $\overline{SS}$ values greatly decrease during the HS1 in agreement with increased meltwater discharge (Fig. 3.4c, j). During the Bølling warm period, $\overline{SS}$ values abruptly increase, accompanied by a peak in sedimentation rate (Fig. 3.4g) probably caused by increased advective supply, i.e., an increase in flow speed, which might reflect a strong DSOW. However, based on the increased accumulation rates (Fig. 3.3; Supplementary Fig. 3.2), the velocity is clearly not high enough for net winnowing since 14 ka BP.

Our $\overline{SS}$ values show a high-amplitude variability during the meltwater events that is difficult to interpret (Fig. 3.4j), possibly due to the very high detrital suspended matter supply and deposition related to meltwater plumes. However, $\overline{SS}$ from nearby Core 21GGC exhibits minimum values around 8.5 ka BP, corresponding to low Zr/Rb ratios (proxy for coarse versus fine-grained matter (Dypvik et al., 2001) (Fig. 3.5c; Supplementary Fig. 3.5), which suggests probably weakened bottom currents in the Eirik Drift area. $\overline{SS}$ values show a low-amplitude variability since the last about 8 ka indicate that the strength of bottom currents has been stable and vigorous.

Deglaciation

YD B/A HS1

a ice sheet volume (10^6 km^3)

July insolation (W/M^2 at 57.5°N)

sea level (m)

Northern Hemisphere

North America

Greenland

Eurasia

510 500 490 480 470

0 -30 -60 -90 -120

b NGRIP-δ^{18}O (‰)

Bølling

Allerød

MW1

c C_{37:4} (%)

MW4 MW3 b a MW2

d P_D IP_{25}

extended to permanent

??? ???

marginal

less

ice free

e SST-U^K_{37} (°C)

f GeoB18530-1 southern Labrador Sea

subSST_{Mg/Ca} (°C)

g Si/Sr

LSR (cm kyr^{-1})

Dolomite (%)

southwestern

southern GrIS exposure age

southeastern

h MD99-2236 Labrador Shelf

MD99-2227 Eirik Drift

Carbonate (%)

Ca-corrected Ti

i Vedde Ash?

tephra (n/g)

IRD (n/g)

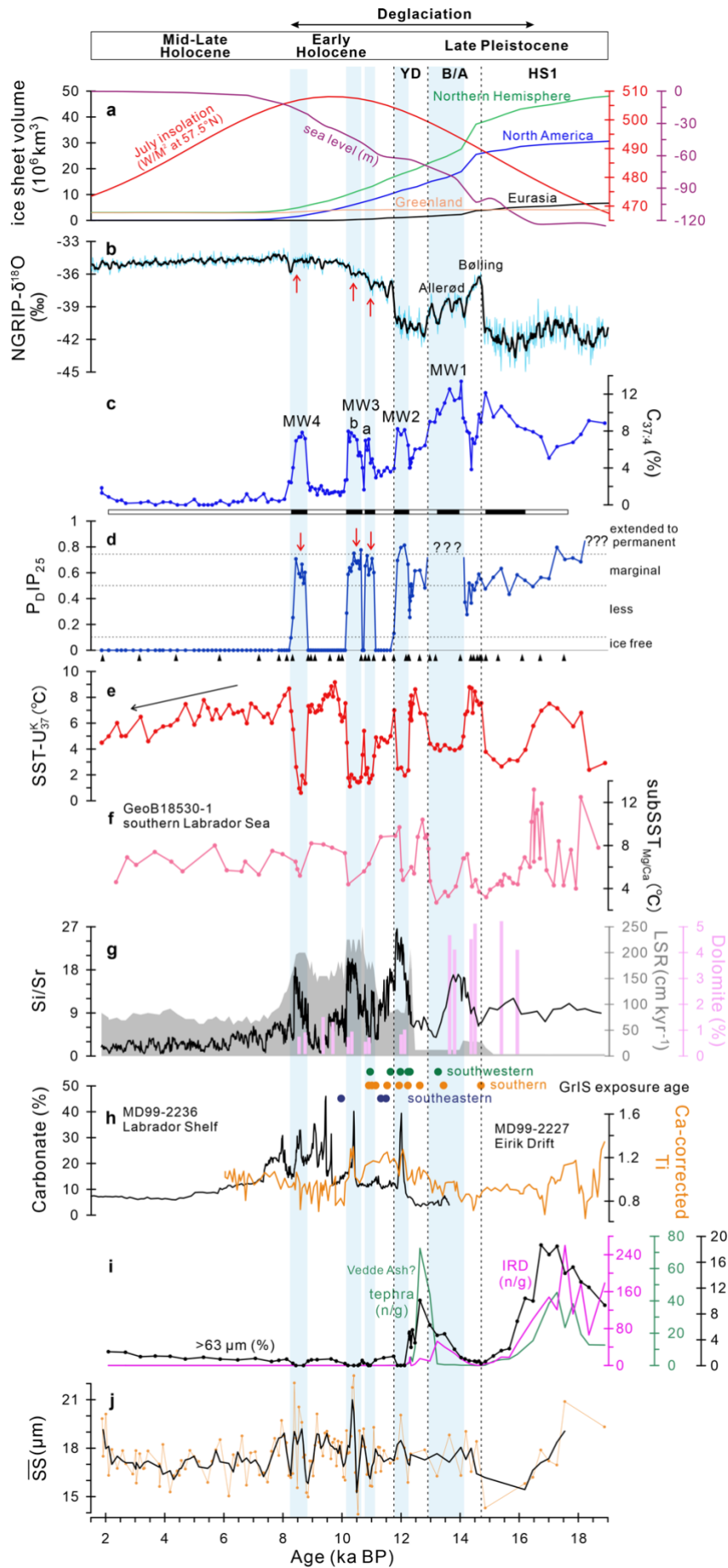>63 μm (%)

j SS (μm)

Age (ka BP)

Fig. 3.4 Proxy records of climate trends and abrupt climate changes during the last deglaciation.
(**a**) Changes in Northern Hemisphere ice sheet volumes (Peltier et al., 2015), global sea level (Lambeck et al., 2014), and July insolation at 57.5° N (Laskar et al., 2004); (**b**) Greenland NGRIP-δ^{18}O (Svensson et al., 2008). The age of ice core was calculated from GICC05 age to cal. ka BP; (**c** to **e**) Proxies for abrupt changes from Core MSM12/2-05-01: (**c**) Percentage of $C_{37:4}$ as proxy for meltwater discharge; black and white bar represents the abundance of planktic foraminifera, with black bars indicating intervals of absence or low abundance of planktic foraminifera; (**d**) P_DIP_{25} based on IP_{25} and dinosterol as proxy for sea ice extent (cf., Fig. 3.3b and Supplementary Fig. 3.4 for further explanation); red arrows indicate the intervals corresponding approximately to the cold phases in the ice core record during the early Holocene; (**e**) SST reconstruction based on U^K_{37}. Black arrow shows a decreasing trend following the decreasing insolation; (**f**) Subsurface temperature record based on Nps-Mg/Ca ratios from Core GeoB18530-1 (Max et al., 2022); (**g**) Si/Sr ratios as proxy for detrital silicate input, linear sedimentation rates (LSR; grey shading), and dolomite content from Core MSM12/2-05-01. (**h**) Exposure ages based on ^{10}Be indicating the decay of the GrIS (Levy et al., 2020; Funder et al., 2021); detrital carbonate content from Core MD99-2236 (Jennings et al., 2015); Ti record corrected against Ca from Core MD99-2227 indicating the runoff from the GrIS (Carlson et al., 2008); (**i**) Coarse fraction (>63 μm) content, IRD abundance, and tephra abundance from the Core MSM12/2-05-01; (**j**) Sortable silt mean size ($\overline{SS}$) record as proxy for flow speed of bottom currents from Core MSM12/2-05-01; black line shows 3 points running average of $\overline{SS}$ values. Age models of Core GeoB18530-1 and MD99-2236 have been recalculated based on Bacon program using "$\triangle R=0 \pm 200$" and "$\triangle R=50 \pm 50$", respectively. Light blue shadings highlight the intervals of strong meltwater discharge. Vertical stippled lines mark the intervals: Heinrich Stadial 1 (HS1), the Younger Dryas (YD), and the Bølling/Allerød (B/A). Black triangles mark available AMS^{14}C dates.

3.4 Discussion

The last deglaciation was characterized by abrupt shifts between cold and warm states in the context of gradually increasing insolation and the decay of the Northern Hemisphere ice sheets, especially the LIS (Fig. 3.4a). These abrupt events (MW1-MW4) were marked by strong meltwater discharge, rapidly increased sea ice concentration, decreased SSTs, reduced open-water productivity, and probably sluggish bottom currents. During the intervals without strong meltwater discharge, there was no or less sea ice cover, higher SSTs, increased open-water productivity, and stable bottom current intensity. Since the middle Holocene, more stable interglacial conditions characterized by the absence of sea ice, gradually decreasing SSTs, high open-water productivity, and stable and strong bottom currents, were predominant (Figs. 3.3, 3.4).

We propose that abrupt changes in sea surface characteristics during the last deglaciation can be attributed to meltwater pulses into the eastern Labrador Sea. During the meltwater events, the peaks in %$C_{37:4}$ (i.e., meltwater discharge) correlated with abrupt changes in sea ice cover and SSTs, i.e., low-salinity and low-temperature surface water promoted sea ice formation and decreased SSTs (Figs. 3.4c-e). These meltwater events exhibited millennial-scale climate fluctuations. Spectral analysis of %$C_{37:4}$ record showed high power on a 1560-year cycle (Supplementary Fig. 3.6), which was similar to 1500-year cycles in Holocene North-Atlantic records (cf., Bond et al., 1997; Bianchi and McCave, 1999) and prominent D-O cycles (every 1-2 kyr) during MIS 3 (Dokken et al., 2013). All these cycles showed alternating cold and warm

intervals with the cold intervals being related to huge freshwater discharge (this study; Dokken et al., 2013; Bond et al., 1997; Bianchi and McCave, 1999). However, D-O cycles were characterized by rapid warming followed by gradual cooling (NGRIP members, 2004; Dansgaard et al., 1993; Dokken et al., 2013) and were probably related to a rapid reduction in sea ice in the Nordic Seas (Sadatzki et al., 2020), whereas our four meltwater events were marked by abrupt cooling due to abrupt meltwater injection. The beginning and end of these events, i.e., the change from minima to maxima and vice versa, respectively, occurred within a 1-3 cm thick core section. Taken the high sedimentation rate of 100-200 cm/kyr (Fig. 3.2), this may suggest that the abrupt changes of these millennial-scale events may have occurred within a few decades or even less.

The meltwater pulses into the eastern Labrador Sea were controlled by meltwater discharge from mixed sources. The LIS discharge superimposed by the GrIS (more proximal to the Eirik Drift) was the main source of meltwater discharge. In addition, freshwater/meltwater from the Arctic Ocean might have also contributed to the surface freshening. High dolomite content and increased IRD abundance during MW1 suggest large volumes of meltwater coming from the LIS via iceberg discharge. High detrital carbonate input was also found in the southern Baffin Bay (Cores SL170 and SL174) (Jackson et al., 2017), supporting the statement that the LIS prominently collapsed around 14 ka BP. Additionally, increased detrital silicate input (high Si/Sr ratios) meanwhile indicates the GrIS may be also a major contributor to meltwater discharge during this time interval (see bedrock distribution in Fig. 3.1). During MW2, MW3, and MW4, high detrital silicate and some dolomite input corresponded to detrital carbonate peaks on the Labrador Shelf (Core MD99-2236) (Jennings et al., 2015), suggesting that such meltwater events were influenced by calving and meltwater plumes from the LIS, superimposed by the GrIS (Fig. 3.6b, c). No IRD deposition during these time intervals implies that the main route of icebergs transported into the Labrador Sea was probably south of our core location. Furthermore, based on increased continental titanium input between 14 to 10 ka BP from Core MD99-2227 (Carlson et al., 2008) and exposure ages of the southern/southwestern/southeastern GrIS (Funder et al., 2021; Levy et al., 2020) (Fig. 3.4h), the GrIS retreated significantly during the last deglaciation, resulting in increased local meltwater discharge towards Eirik Drift during MW1, MW2, and MW3. According to the drainage route and timing, the outburst of Lake Agassiz into the Labrador Sea contributed substantially to the development of MW4, whereas it may be not associated with the other three events (Teller et al., 2002; Süfke et al., 2022).

The four meltwater events MW1 to MW4 can be related approximately to cold episodes documented in the Greenland Ice Core record (Fig. 3.4b-d), suggesting that changes in sea surface characteristics in the Labrador Sea/subpolar regions may affect wider fluctuations in atmospheric temperature and closely relate to the classical cold events (e.g., YD, and 8.2 ka cold event). In general, and compared to extremely cold intervals (i.e., HS1 and YD), the Bølling/Allerød

interval is a relatively warm period shown in NGRIP record (Rasmussen et al., 2006; Svensson et al., 2008). However, the Allerød period is a relatively cold interval in contrast to the Bølling warm period (Rasmussen et al., 2006), including two major meltwater-related cold phases (the Older Dryas stadial and Intra-Allerød Cold period) (Thornalley et al., 2010). MW1 correlates with lighter $\delta^{18}O$ during the Allerød period in the NGRIP record (Fig. 3.4b), decreased (sub-)surface temperatures in the Labrador Sea (this study; Max et al., 2022) and the northeastern Atlantic (Peck et al., 2008; Benway et al., 2010), surface freshening and reduced ventilation in the North Atlantic (Thornalley et al., 2010, 2011) (Fig. 3.4e, f; Supplementary Fig. 3.7). These correlations/similarities indicate that meltwater discharge into the Labrador Sea/subpolar regions might have caused/contributed to the cooling in the high-latitude North Atlantic during the Allerød period. Surface freshening/sea ice expansion in the subpolar regions and following weakened ocean circulation (Moffa-Sánchez and Hall, 2017) (i.e., limited subpolar gyre and Atlantic Water inflow) could have restricted ocean-atmosphere heat exchange and heat transport northward, resulting in a decline in atmospheric temperatures (Sadatzki et al., 2020; Corella et al., 2022), which may also be applied to the other meltwater events (Fig. 3.6b). Recent work on the comparison between ice core record and sea ice changes in the Baffin Bay and the Labrador Sea (Core GS16-204-23CC) during the D-O events provides further evidence that sea ice expansion can greatly affect atmospheric temperatures (Scoto et al., 2022).

MW2 happened during the late YD, coinciding with the "Heinrich Event 0" (HE0) marked by high detrital carbonate input on the Labrador shelf (Jennings et al., 2015) and other North Atlantic areas (Andrews et al., 1995). Abrupt changes in (sub-)surface temperatures and reduced ocean ventilation in the North Atlantic support that MW2 might have a widespread impact on the subpolar regions (Supplementary Fig. 3.7). Furthermore, the timing of MW2 was in line with the second distinct weakening of the AMOC during the late YD (McManus et al., 2004), suggesting that the disintegration of the LIS and the GrIS might have caused/maintained the cold episode during the late YD, whereas the flooding event in the Arctic Ocean (Keigwin et al., 2018; Wu et al., 2020) might have induced the first phase of AMOC weakening. Therefore, the occurrence of MW2 (HE0 event) may explain why the catastrophic outburst of Lake Agassiz during the early YD lasted a few hundred years (Keigwin et al., 2018; Lippold et al., 2019) but resulted in a thousand-year cold episode. That means direct freshwater discharge from Lake Agassiz into the Arctic Ocean probably merely triggered the abrupt change during the early YD.

MW3 corresponded to relatively modest changes in the NRGIP record compared to other cold phases (Fig. 3.4b-d). On the one hand, this might be related to less volumes of meltwater discharge or limited distribution pattern. Thus, prominent changes in surface characteristics were most likely restricted to the proximal Labrador Sea as reflected in distinct decrease in (sub-)surface temperatures in the eastern and southern Labrador Sea (Fig. 3.4e, f) whereas only

modest changes occurred in the more distal northeastern Atlantic (Supplementary Fig. 3.7). More high-resolution and well-dated records are needed to constrain the distribution pattern. On the other hand, the impact of MW3 on climate may be influenced by the background climate condition. MW3 happened during the late transition phase towards a stable interglacial mode, accompanied by highest insolation and a gradual warming trend, which partially masked the short-term cooling trend caused by inferred meltwater discharge. In comparison to the unstable deglaciation, a larger magnitude and duration of freshwater influx may be required to generate a comparable impact under a relatively stable mode (Lippold et al., 2019; Barker et al., 2021). Alternatively, lower sea ice concentration in the Nordic Seas during the early Holocene (Xiao et al., 2017) may have contributed to heat release from the ocean and modest changes in the ice core record.
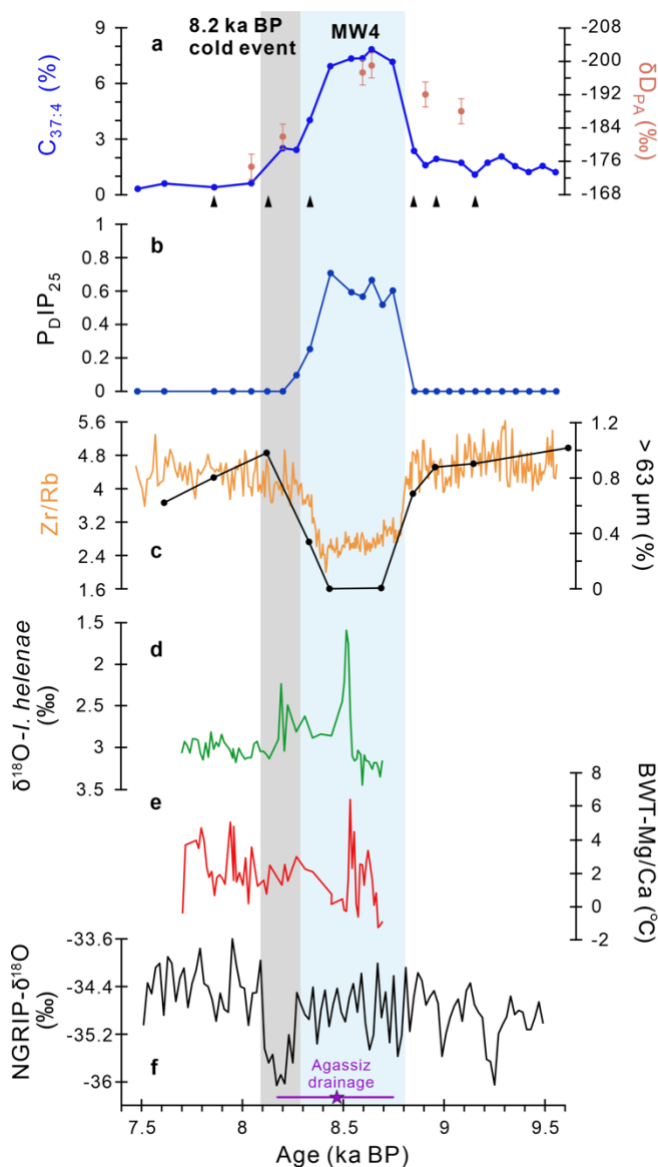
Fig. 3.5 Proxy records of MW4 versus the 8.2 ka BP cold event.
(**a-c**) Proxy records for abrupt change during MW4 from Core MSM12/2-05-01. (**a**) %$C_{37:4}$ and stable hydrogen isotope composition of palmitic acid (δD_{PA}) as proxies for meltwater discharge (with higher $C_{37:4}$ and lower δD_{PA} representing lower salinity). Vertical error bars represent the standard deviation of the δD_{PA} measurements (3 ‰); (**b**) $P_D IP_{25}$ as proxy for sea ice extent; (**c**) XRF-Zr/Rb ratios indicating coarse versus fine-grained matter; percentage of coarse fraction (>63 μm); (**d** and **e**) proxy records for abrupt change around 8.5 ka BP from Core MSM45-19-2 (Lochte et al., 2019). (**d**) $\delta^{18}O$ of benthic foraminifera *Islandiella helenae*; (**e**) Bottom water temperature estimates based on Mg/Ca ratios of *I. helenae*. (**f**) Greenland NGRIP-$\delta^{18}O$ (Svensson et al., 2008). The age of ice core record was calculated to cal. ka BP from GICC05 age. The purple star indicates the age for Lake Agassiz drainage event: 8.47 ka BP with 1σ uncertainties (purple line, 8.16-8.74 ka BP) (Barber et al., 1999). Light blue shading shows MW4, whereas grey shading indicates the 8.2 ka BP cold event shown in the Greenland Ice Core. Black triangles mark available AMS^{14}C dates.

MW4 that occurred between about 8.74 and 8.33 ka BP, was closely linked to the 8.2 ka BP cold event (Fig. 3.5). Unfortunately, the exact timing of the peak meltwater discharge cannot be determined in our record due to the limited number of AMS ^{14}C dates in this time interval. Nevertheless, surface freshening occurred in the Labrador Sea around 8.5 ka BP, consistent with the record from the Labrador Shelf (Hoffman et al., 2012; Lochte et al., 2019) and probably caused by the final Lake Agassiz outburst flood (Barber et al., 1999; Hoffman et al., 2012) and collapse of the Hudson Bay Saddle (Lochte et al., 2019). Based on the correlation between the δD$_{PA}$ values and surface water salinity obtained from Arctic Ocean surface sediments (Sachs et al., 2018), the δD$_{PA}$ minimum shown in Figure 3.5a may represent a salinity anomaly of about -4 for MW4, a tentative statement that has to be approved by further more detailed biomarker and isotope analyses. The onset of meltwater discharge during MW4 was prior to the widespread atmospheric cooling at the 8.2 ka BP cold event, which started about 200 years after the end of MW4. This time difference might be interpreted by the response time between changes in ocean circulation and climate (Muschitiello et al., 2019), e.g., such freshening might have perturbed the AMOC about 145-320 yr. and resulted in the 8.2 ka BP cold event (Lochte et al., 2019). If the Marine 20 calibration curve is used instead of the Marine 13 calibration curve, the 8.2 ka BP cold event occurred during the final stage of MW4 (see Methods and Supplementary Fig. 3.8). The abrupt changes in surface characteristics during MW4 (Fig. 3.5a and 3.5b) coincided with distinct minima in the Zr/Rb ratios and the coarse fraction of our Core MSM12/2-05-01 (Fig. 3.5c) and was consistent with an abrupt decrease in $\overline{SS}$ values from nearby Core 21GGC, suggesting weakened strength of bottom currents which may reflect a weak DSOW in the Eirik Drift (Henderson, 2009) (Supplementary Fig. 3.5). However, our $\overline{SS}$ record does not show a clear trend of bottom current variation during the MW4 as well as the other three meltwater events, despite some lowest $\overline{SS}$ values presence. To further understand bottom current variations and their correlations with changes in sea surface characteristics, a wider range of high-resolution bottom current records over the North Atlantic is needed.

The occurrence of meltwater events was triggered by (sub-)surface ocean warming in the Labrador Sea. Higher SSTs were found in the eastern Labrador Sea preceding high meltwater discharge (i.e., four meltwater events and late HS1) (Fig. 3.4c, e). *Neogloboquadrina pachyderma* (sin.) is calcifying at the base of the surface mixed layer (50 m depth) in the Eirik Drift region (Jonkers et al., 2010), and our reconstructed temperatures based on Nps-Mg/Ca ratios are quite similar to the U$^{K}_{37}$-based SST values (Fig. 3.3c). This suggests that the whole upper ocean (surface and subsurface water) was warmer during these periods, possibly caused by enhanced advection of the warm Irminger Current (cf., Seidenkrantz et al., 2021) (Fig. 3.6a). Recent research from the southern Labrador Sea (Max et al., 2022) shows highly comparable temperature estimates with our SST record and demonstrates that the subsurface warming preceded Heinrich

events. Additionally, ocean warming/enhanced Irminger Current has also been proven to be the trigger for surface freshening around 8.5 ka BP in the Labrador Sea (Core MSM45-19-12) (Lochte et al., 2019) (Fig. 3.5d, e). Our high-resolution records provide new evidence that millennial-scale meltwater events caused by extensive calving of the surrounding LIS and the GrIS were triggered by (sub-)surface ocean warming in the Labrador Sea. Furthermore, rapid sea level rise during the Bølling warm period (Lambeck et al., 2014) might also have contributed to basal melting/collapse of ice sheets during the last deglaciation.
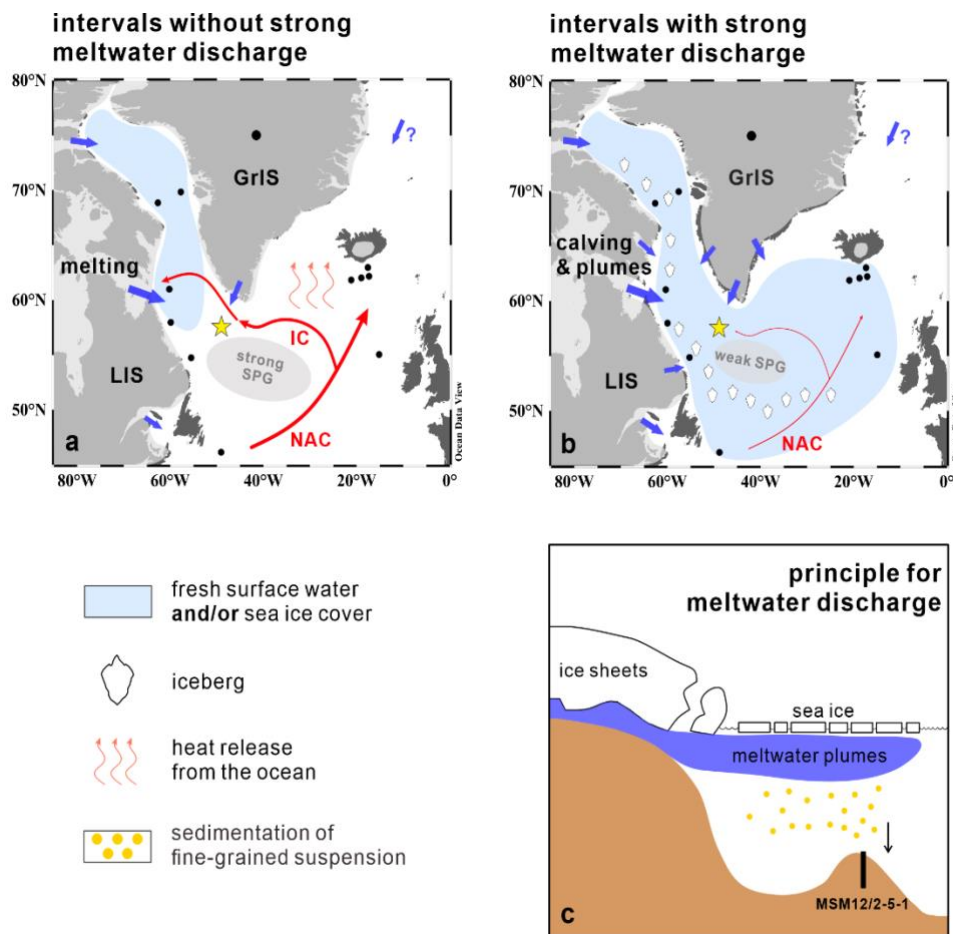
Fig. 3.6 Schematic illustration of intervals without/with strong meltwater discharge in the Labrador Sea during the last deglaciation.
(**a**) Intervals without strong meltwater discharge preceding the meltwater events: enhanced warm North Atlantic Current (NAC)/Irminger Current (IC) inflow; surface freshening in the Baffin Bay and the northwestern Labrador Sea; (**b**) Intervals with strong meltwater discharge: weakened NAC/IC inflow; surface freshening in extensive subpolar regions, probably resulting in increased sea ice extent and limited heat release from the ocean. Blue arrows show meltwater discharge: melting of the LIS and the GrIS and possible input from the Arctic Ocean (**a**); calving and meltwater plumes from the LIS and the GrIS and possible input from the Arctic Ocean (**b**). (**c**) Principal cartoon showing interactions among ice sheet (the LIS and the GrIS) dynamics/meltwater plumes, sea ice formation, and sedimentation of fine-grained suspension during the meltwater events. Yellow star: Core MSM12/2-05-01; black dots: other reference cores.

In conclusion, our study provides very well-dated and high-resolution proxy records from the eastern Labrador Sea, which could improve our understanding of the impact of meltwater injection into subpolar regions on abrupt climate changes during the last deglaciation. Our new data supports modelling results that higher frequency and amplitude of abrupt changes may occur during the transition states from background climates (Barker et al., 2021). We found that meltwater pulses following the collapse of the LIS and GrIS might have triggered millennial-scale abrupt changes in surface freshening and sea ice extent in the Labrador Sea, as well as cooling atmospheric temperatures. These abrupt changes might have occurred within a few decades, which need to be noted in the context of modern accelerating melting of the GrIS and Arctic sea ice due to anthropogenic climate change. Our findings may help to improve model simulations of abrupt changes and predictions of the impact of meltwater discharge on future ocean circulation and climate change.

3.5 Methods

Chronology

The age model of Core MSM12/2-05-01 was constrained by 38 Accelerator Mass Spectrometry (AMS) radiocarbon dates of planktic foraminifera *Neogloboquadrina pachyderma* (sinistral). All the AMS ^{14}C dates were calibrated to calendar years (cal. ka BP) based on the Marine 13 calibration curve (Reimer et al., 2013), with a global mean reservoir age ($\triangle R=0\pm200$) (see Supplementary Table 3.1 for details). We used the Marine 13 curve to keep consistency with other published records. We also tested the calibration with the Marine 20 curve (Heaton et al., 2020), and the results are similar (i.e., the whole records become around 200 years younger) and do not influence our interpretations (Figs. 3.5; Supplementary Fig. 3.8). The age-depth model was established on the Bayesian age-modelling (Bacon) approach (Blaauw and Christen, 2011). The tephra peak found in 1123 cm core depth and dated to around 12.6 ka BP (based on our current age model) might represent the Vedde Ash layer dated to 12.12 ka BP (Abbott and Davies, 2012) (Figs. 3.2 and 3.4i). However, without further geochemical analyses and possible impact from ice-rafted tephra, this tephra layer cannot be attributed to the Vedde Ash layer unambiguously. Furthermore, if this tephra layer is the Vedde Ash layer for sure, this would imply a local reservoir age correction of about 450 years ($\triangle R=450$) (cf., Austin et al., 1995). However, we cannot determine for which time interval this local reservoir age correction has to be considered. Thus, we have not used the Vedde Ash layer as an extra age control point to establish age model, but marked it in Figures 3.2 and 3.4.

Bulk parameters

For the measurement of bulk parameters, freeze-dried and homogenized sediments were used. Total organic carbon (TOC) contents were measured by Carbon-Sulfur Analyser (CS-125, Leco) after removing carbonate with hydrochloric acid. Total carbon (TC) contents were determined by Carbon-Nitrogen-Sulfur Analyser (Elementar III, Vario).

Biomarker analyses

For biomarker analysis, 5 g of freeze-dried and homogenized sediments were used for extraction by ultrasonication with dichloromethane/methanol (DCM/MeOH, 2:1 v/v). The internal standards 7-hexylnonadecane (7-HND, 0.076 μg), 9-octylheptadec-8-ene (9-OHD, 0.1 μg), 5α-androstan-3β-ol (androstanol, 10.8 μg), and squalane (3.2 μg) were added prior to the extraction. The extracts were concentrated and separated into hydrocarbon and sterol fraction by open silica gel column chromatography using 5 ml n-hexane and 9 ml ethylacetate/n-hexane, respectively. Furthermore, the sterol fraction was derivatized with 200 μl bis-trimethylsilyl-trifluoracet-amid (BSTFA) (60°C, 2h). Hydrocarbons were analysed by gas chromatography/mass spectrometry (GC/MS) (Agilent 7890GC-Agilent 5977 A). Sterols were analyses by GC/MS (Agilent 6850GC-Agilent 5975 A). Compound identification was based on comparison of GC retention times with reference compounds and published mass spectra for highly branched isoprenoids (HBIs) and sterols. HBIs were quantified based on their molecular ions (m/z 350 for IP_{25}, m/z 348 for HBI-II, and m/z 346 for HBI-III (Z)) in relation to the fragment ion m/z 266 (7-HND). Brassicasterol (24-methylcholesta-5,22E-dien-3β-ol), campesterol (24-methylcholest-5-en-3β-ol), sitosterol (24-ethylcholest-5-en-3β-ol), and dinosterol (4a-23,24-trimethyl-5a-cholest-22E-en-3β-ol) were quantified as trimethylsilyl ethers. Their molecular ions m/z 470, m/z 472, m/z 486, and m/z 500 were used in relation to the molecular ion m/z 348 of the internal standard androstanol. External calibration curves and specific response factors were applied for balancing the different responses of molecular ions of the analytes and the molecular/fragment ions of the internal standards. Biomarker concentrations were normalized based on TOC content of each sample. For analytical details and further references see Fahl and Stein, (2012).

Sea ice variations is indicated by the PIP_{25} value (equation 1), a semi-quantitative index for sea ice reconstruction (Müller et al., 2011; Belt et al., 2015). It is derived from the seasonal sea ice biomarker (IP_{25}) and open-water phytoplankton biomarker (e.g., dinosterol, brassicasterol, and HBI-III (Z)). In addition, the C_{37} alkenones were also used as phytoplankton marker for PIP_{25} calculation.

$$PIP_{25} = [IP_{25}] / ([IP_{25}] + [\text{Phytoplankton biomarker}] \times c) \tag{1}$$

The balance factor c corresponds to the ratio of mean concentration of IP_{25} and phytoplankton biomarker. In our study, all four PIP_{25} proxies based on dinosterol, brassicasterol, HBI-III (Z) and the C_{37} alkenones show very similar trends (see data online). Thus, we only used the IP_{25}-dinosterol-based P_DIP_{25} to reflect sea ice variations here (Fig. 3.3b).

As cleaning step for analysing alkenones were necessary, saponification was applied to sterol fraction (see above) using 1 ml 0.1 mol/L KOH (50°C, 12h) before determination of alkenones. Additionally, open silica gel column chromatography was performed using DCM. Internal standard *n*-hexatriacontane (C_{36}, 2.1435 μg) was added to each sample for quantification. Alkenones were analysed by GC (Agilent 6890 A) and identified by their retention times and the comparison with an external standard.

The SST reconstruction is based on long-chain C_{37} alkenones synthetized by haptophyte algae, using the alkenone unsaturation index (U_{37}^K) (Brassell et al., 1986; Prahl and Wakeham, 1987):

$$U_{37}^K = (C_{37:2} - C_{37:4})/(C_{37:2} + C_{37:3} + C_{37:4}) \tag{2}$$

For calibration of the U_{37}^K index to SST values we followed the most recent review study carried out by Filippova et al. (2016) for North Atlantic surface sediments, using

$$U_{37}^K = 0.021T + 0.243 \tag{3}$$

Despite U_{37}^K not only being affected by SSTs, the regional U_{37}^K values still show a high positive correlation with SSTs in the North Atlantic (Filippova et al., 2016). Furthermore, SST calibration based on $U_{37}^{K'}$ (i.e., excluding $C_{37:4}$ in the equation (2)) exhibits a significant warm bias and more unrealistic SSTs for the North Atlantic (Filippova et al., 2016; Wang et al., 2021). The often-used SST-alkenones reconstruction based on the global calibration of Müller et al. (1998) also displays a larger warm bias at cold temperatures/sea ice cover conditions. A comparison of SST values based on U_{37}^K and $U_{37}^{K'}$ indices as well as different calibration equations (Rosell-Mele et al., 1995; Müller et al., 1998; Filippova et al., 2016) are presented in online dataset (You et al., 2022). In the low-temperature range << 10 °C, the calibration equation becomes less precise (Filippova et al., 2016). Thus, the absolute SST values of the meltwater events should be interpreted more cautiously, and we focus more on the abrupt changes per se.

As a proxy for low temperature and low salinity water, we have used the percentage values of tetra-unsaturated alkenones (%$C_{37:4}$) to indicate meltwater input (cf., Bard et al., 2000) following equation:

$$\%C_{37:4} = C_{37:4} / (C_{37:2} + C_{37:3} + C_{37:4}) \times 100 \tag{4}$$

For the analysis of the stable hydrogen isotope composition of palmitic acid (δD_{PA}), 6g of freeze-dried and homogenized sediments were extracted by ultrasonication with dichloromethane/methanol (DCM/MeOH, 9:1 v/v). The internal standard C19:0 fatty acid (50.5 µg) was added prior to the extraction. The extracts were saponified using 0.1 M KOH in MeOH (50°C, 12h), yielding neutral and acid fractions after hexane extraction and after acidification, respectively. The acid fractions were methylated with MeOH of known isotopic composition (50°C, 12h), yielding the corresponding fatty acid methyl esters (FAMEs). The FAME fractions were cleaned by open pipet columns (4 cm silica gel with 0.5 cm Na_2SO_4) using DCM. δD_{PA} analyses were carried out on a Thermo Fisher Scientific MAT 253 Isotope Ratio Mass Spectrometer coupled via a GC IsoLink operated at 1420 °C to a Thermo Fisher Scientific TRACE GC equipped with a Rxi-5ms column (30 m x 0.25 mm x 0.5 µm). Isotope values were measured against calibrated H_2 gas and δD values are reported in permil against VSMOW. Measurement accuracy was controlled by *n*-alkane standards of known isotopic composition every six measurements. Long-term mean absolute deviation based on the external *n*-alkane standard mixture was 3.0‰. Daily determination of the H_3^+ factor using H_2 as reference gas gave 5.6-5.7, while the precision of the internal standard was 2‰. δD_{PA} values were corrected for the methyl group added during methylation. For analytical details and further reference see Häggi et al. (2015) and Sachs et al. (2018).

Accumulation rates

Accumulation rates of bulk parameters and biomarkers were calculated according to the following equations:

$$BAR = SR \times (WBD\text{-}1.026 \times PO/100) \qquad (5)$$
$$MAR = BAR \times BM \text{ (or TOC/100)} \qquad (6)$$

BAR: bulk sediment accumulation rate (g cm^{-2} kyr^{-1}); SR: sedimentation rate (cm kyr^{-1}); WBD: wet bulk density (g cm^{-3}); PO: porosity (%); MAR: mass accumulation rate (g cm^{-2} kyr^{-1} or µg cm^{-2} kyr^{-1}); BM: biomarker concentration (µg g^{-1}Sed).

Mg/Ca analysis

80 to 200 individuals of *N. pachyderma* (sin.) were picked from the size fraction 150 - 212 µm for Mg/Ca analysis. Samples were cleaned prior to the measurement. The majority of the Mg/Ca determinations were analysed on the ICP-MS at Cardiff University with an analytical precision for Mg/Ca of ± 2 % relative standard deviation (RSD) and the remaining samples on the ICP-OES at the Bjerknes Centre for Climate Research with an analytical precision of ±1.4 % RSD.

The precision for Mg/Ca standard measurements are similar on both the ICP-MS and ICP-OES (<0.9 % RSD for long term precision), thus the data from both instruments are interchangeable.

Temperatures were calculated using species-specific *N. pachyderma* (sin.) calibration equation (Elderfield et al., 2000):

$$Mg/Ca = 0.5 \exp (0.1\ T) \tag{7}$$

The analytical error of ± 2 % is equivalent to ± 0.2 °C using the calibration employed in this study. For analytical details and further references see Williams, (2015).

Core MSCL logging and XRF scanning

During Expedition MSM12/2, hole-core physical property measurements were carried out in the ship laboratory and included non-destructive, continuous determinations of core geometry (diameter), wet bulk density (WBD), P-wave velocity (Vp), and loop sensor magnetic susceptibility (MS) at 10 mm intervals. A standard Multi Sensor Core Logger (MSCL)-S track (GEOTEK Ltd., UK, Ser. No. 25) was used to measure temperature, core diameter, P-wave travel time, gamma-ray attenuation, and MS. The principle of logging cores is described in more detail in the GEOTEK manual "Multi-Sensor Core Logging", which can be downloaded from the web (*http://www.geotek.co.uk*). The orientation of the P-wave and gamma sensors was horizontal. For further details we refer to the Cruise Report (Uenzelmann-Neben, 2009).

The AWI Avaatech XRF (X-Ray Fluorescence) Core Scanner was used for rapid and non-destructive determination of the chemical composition of sediment sections of Core MSM12/2-05-01. Split core surfaces were scanned during a 10 kV, 30 kV, and 50 kV run, in order to obtain reliable intensities (counts per second) of specific major elements. Here we present data of K, Rb, Si, Sr, Ti, and Zr, plotted and interpreted as elemental ratios K/Ti, Si/Sr, and Zr/Rb. For documentation and analytical details, we refer to Avaatech Manual (Stein, 2015; *https://epic.awi.de/id/eprint/37355/4/XRFCore-Scanner_user-manualV2.pdf*).

Grainsize analysis: Sortable Silt

We analysed the mean size of the non-cohesive sortable silt ($\overline{SS}$) fraction (10-63 μm) of 118 samples as a proxy for the strength of bottom water currents (McCave et al., 1995; McCave and Hall, 2006). Particle sizes less than 10 μm are predominantly cohesive clay material deposited as aggregates and thus excluded, as they do not reflect hydrodynamic processes. The method of McCave et al. (1995) and McCave and Hall (2006) for sortable silt preparation of raw sediments was followed. Approximately 2-4 g of sediments were treated with 250 ml of 2 M acetic acid for carbonate removal and heated at 85 °C for 5 hours in 150 ml 2 M sodium carbonate for biogenic silica removal so as to remove biogenic influences on grain size. Samples were then suspended

in 0.2 % Calgon solution and placed on a rotating wheel for sediment disaggregation followed by 1-minute ultrasonic treatment just prior to analysis. Sample size was measured using a Beckman Coulter Multisizer III with a 200 μm aperture. $\overline{SS}$ mean size measurement errors are ±2 % at sortable silt concentrations >5 % (Bianchi et al., 1999).

Data availability

Acknowledgements

Author contributions

R.S. designed this study. D.Y. and M.C.W. prepared foraminifera samples for radiocarbon measurement. D.Y. and K.F. conducted biomarker analyses, evaluation, and quality control. D.Y. carried out bulk parameters and coarse fraction analyses. F.N. and G.K. performed MSCL logging and XRF scanning, respectively. M.C.W., D.N.S., I.N.M., and S.B. generated and evaluated sortable silt and Mg/Ca ratios of foraminifera. D.Y. carried out the extraction of palmitic acid. E.S. conducted hydrogen isotope measurements of palmitic acid and evaluation. D.Y. wrote the manuscript with strong input from R.S.. D.N.S., I.N.M., S.B., and L.N. contributed to the first version of this manuscript. All the co-authors contributed to the data interpretation and writing the final version of the paper.

3.6 Supplementary Information

This subchapter includes:

Supplementary Table 3.1: AMS ^{14}C dates of Core MSM12/2-05-01.

Supplementary Fig. 3.1: Modern hydrography of study area.

Supplementary Fig. 3.2: Records of lithology and bulk parameters (Core MSM12/2-05-01).

Supplementary Fig. 3.3: X-ray photographs of Core MSM12/2-05-01 (depth extent 500-1200 cm) showing internal structure of sediments.

Supplementary Fig. 3.4: P_DIP_{25} plot and scatter plot of concentrations of sea ice proxy IP_{25} versus open-water phytoplankton proxy dinosterol (Core MSM12/2-05-01).

Supplementary Fig. 3.5: Proxy records for sediment provenance and bottom current intensity (Core MSM12/2-05-01 and other cores referred to).

Supplementary Fig. 3.6: Spectral analysis record of meltwater proxy $\%C_{37:4}$ (Core MSM12/2-05-01).

Supplementary Fig. 3.7: Comparation between different proxy records from the North Atlantic during the last deglaciation.

Supplementary Fig. 3.8: Proxy records of MW4 (Core MSM12/2-05-01) versus the 8.2 ka BP cold event based on Marine 20 calibration curve.

Data availability:

All relevant data in this supplementary information is available at PANGAEA Data Publisher (*https://doi.org/10.1594/PANGAEA.952329*).

Supplementary Table 3.1   AMS ^{14}C dates of Core MSM12/2-05-01.

Lab ID	Depth/cm	Species	AMS ^{14}C Age (yr.)	△R	Calib. age median (yr. BP)	Model age median (yr. BP)
SUERC-45889*	4.75	*N. pachyderma ()*	2082±35	0±200	1669	1899
SUERC-47577	108.5	*N. pachyderma*	3450±38	0±200	3314	3281
SUERC-45890	200.5	*N. pachyderma*	4227±37	0±200	4319	4420
SUERC-47579	300.5	*N. pachyderma*	5473±39	0±200	5857	5875
SUERC-47579	390.5	*N. pachyderma*	6737±37	0±200	7236	7208
AWI-6946.1.1**	440.5	*N. pachyderma*	7520±85	0±200	7986	7860
AWI-6947.1.1	470.5	*N. pachyderma*	7933±86	0±200	8420	8123
AWI-6948.1.1	500.5	*N. pachyderma*	8115±84	0±200	8641	8334
AWI-6949.1.1	600.5	*N. pachyderma*	8134±84	0±200	8664	8852
AWI-6950.1.1	620.5	*N. pachyderma*	8298±83	0±200	8849	8962
SUERC-45891	650.5	*N. pachyderma*	8449±38	0±200	9038	9154
SUERC-47582	720.5	*N. pachyderma*	9049±40	0±200	9793	9625
AWI-5788.1.1	749.5	*N. pachyderma*	9096±122	0±200	9847	9802
AWI-5789.1.1	799.5	*N. pachyderma*	9585±117	0±200	10464	10099
AWI-5793.1.1	919.5	*N. pachyderma*	9831±127	0±200	10767	10680
AWI-5794.1.1	929.5	*N. pachyderma*	9606±120	0±200	10490	10729
AWI-5795.1.1	952.5	*N. pachyderma*	9641±119	0±200	10534	10855
AWI-5798.1.1	999.5	*N. pachyderma*	9860±119	0±200	10802	11131
AWI-5799.1.1	1029.5	*N. pachyderma*	10029±125	0±200	11008	11409
AWI-5800.1.1	1059.5	*N. pachyderma*	10428±128	0±200	11627	11744
AWI-5803.1.1	1108.5	*N. pachyderma*	10543±129	0±200	11788	12275
AWI-6484.1.1	1114.5	*N. pachyderma*	10621±100	0±200	11908	12308
AWI-6485.1.1	1118.5	*N. pachyderma*	11130±101	0±200	12611	12332
AWI-6486.1.1	1123.5	*N. pachyderma*	11141±94	0±200	12626	12635
AWI-6487.1.1	1127.5	*N. pachyderma*	11752±95	0±200	13213	12969
AWI-5952.1.1	1130.5	*N. pachyderma*	11854±131	0±200	13320	13217
SUERC-47583	1140.5	*N. pachyderma*	12379±43	0±200	13869	14027
SUERC-51888	1150.5	*N. pachyderma*	12975±44	0±200	14794	14374
AWI-6488.1.1	1153.5	*N. pachyderma*	12942±102	0±200	14742	14483
AWI-6489.1.1	1155.5	*N. pachyderma*	12671±102	0±200	14356	14555
AWI-6490.1.1	1157.5	*N. pachyderma*	12518±106	0±200	14086	14629
AWI-6491.1.1	1159.5	*N. pachyderma*	12721±106	0±200	14434	14699
AWI-5954.1.1	1160.5	*N. pachyderma*	12544±120	0±200	14135	14851
AWI-6492.1.1	1162.5	*N. pachyderma*	12972±105	0±200	14789	15387
AWI-5955.1.1	1165.5	*N. pachyderma*	13965±135	0±200	16361	16192
AWI-5956.1.1	1167.5	*N. pachyderma*	14937±147	0±200	17683	16731
SUERC-47584	1170.5	*N. pachyderma*	15386±51	0±200	18212	17542
SUERC-51887	1190.5	*N. pachyderma*	17007±57	0±200	20031	20358

* AMS ^{14}C dates have been carried out at the NERC Radiocarbon Laboratory at SUERC (Scottish Universities Environment Research Centre, the University of Glasgow). They were recalculated from the unpublished data of the PhD dissertation of Williams, (2015). ** AMS ^{14}C dates were measured at the Alfred Wegener Institute, Bremerhaven. A global mean reservoir age (R=405 years) was used for calibration to keep consistency with most of studies in the open North Atlantic regions (e.g., Ng et al., 2018; Zhao et al., 2019), and a △R of 0 ± 200 years was applied to account for the reservoir age variations, which is in line with other studies in the North Atlantic (cf., Toucanne et al., 2015; Oppo et al., 2015; Andrews et al., 2018).
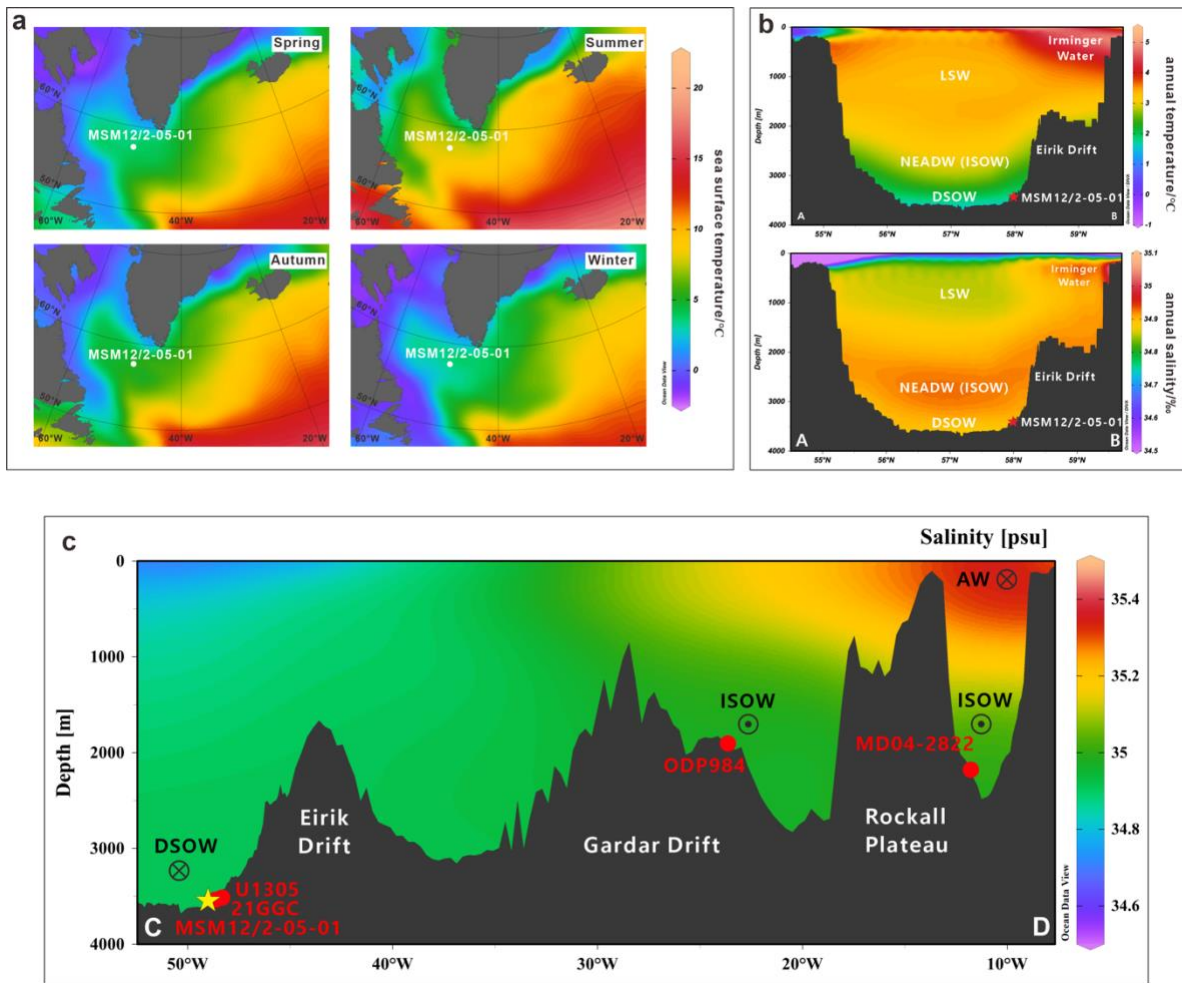
Supplementary Fig. 3.1 Modern hydrography of study area.

(**a**) Modern seasonal variability of SST in the subpolar western North Atlantic regions; (**b**) Vertical distribution of water masses in terms of temperature and salinity at profile A to B. northeastern Atlantic Deep Water (NEADW) in the Labrador Sea is derived from ISOW; (**c**) salinity profile in the North Atlantic from C to D. For location of profiles A to B and C to D see map of Figure 3.1. Data is from World Ocean Atlas 2018 (*https://odv.awi.de/data/ocean/*). Profiles were produced with Ocean Data View software (*https://odv.awi.de*).
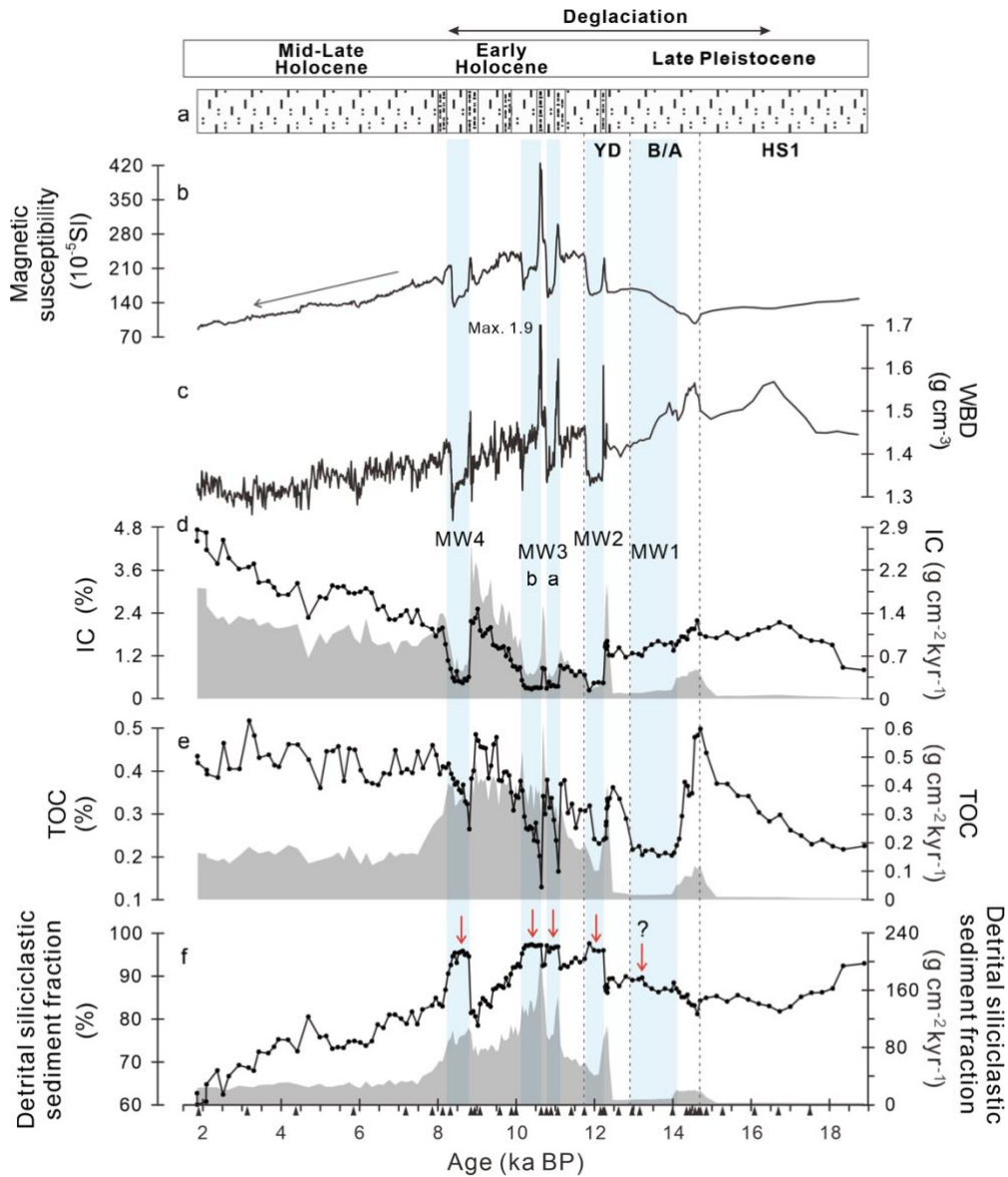
Supplementary Fig. 3.2 Records of lithology and bulk parameters (Core MSM12/2-05-01).
(**a**) Illustration of core lithology (Uenzelmann-Neben, 2009); (**b**) Magnetic susceptibility (MS); the decreasing trend of MS values since the middle to late Holocene are explained by increased input of carbonate and decreased input of siliciclastic material; (**c**) Wet bulk density (WBD); (**d**) Content (line) and accumulation rate (shading) of inorganic carbon (IC); (**e**) Content and accumulation rate of TOC; (**f**) Content and accumulation rate of detrital siliciclastic sediment fraction (bulk sediment without TOC and carbonate). Concentration and accumulation rate of carbonate were calculated assuming that calcite is the predominant carbonate phase (CaCO$_3$=(TC-TOC) × 8.333). As biogenic opal is insignificant in study area (Bohrmann and Stein, 1989), this predominantly represent the terrigenous/detrital siliciclastic sediment fraction. Red arrows indicate higher non-biogenic fraction input corresponding to peaks of sedimentation rate (Fig. 3.2). Black triangles mark available AMS[14]C dates.
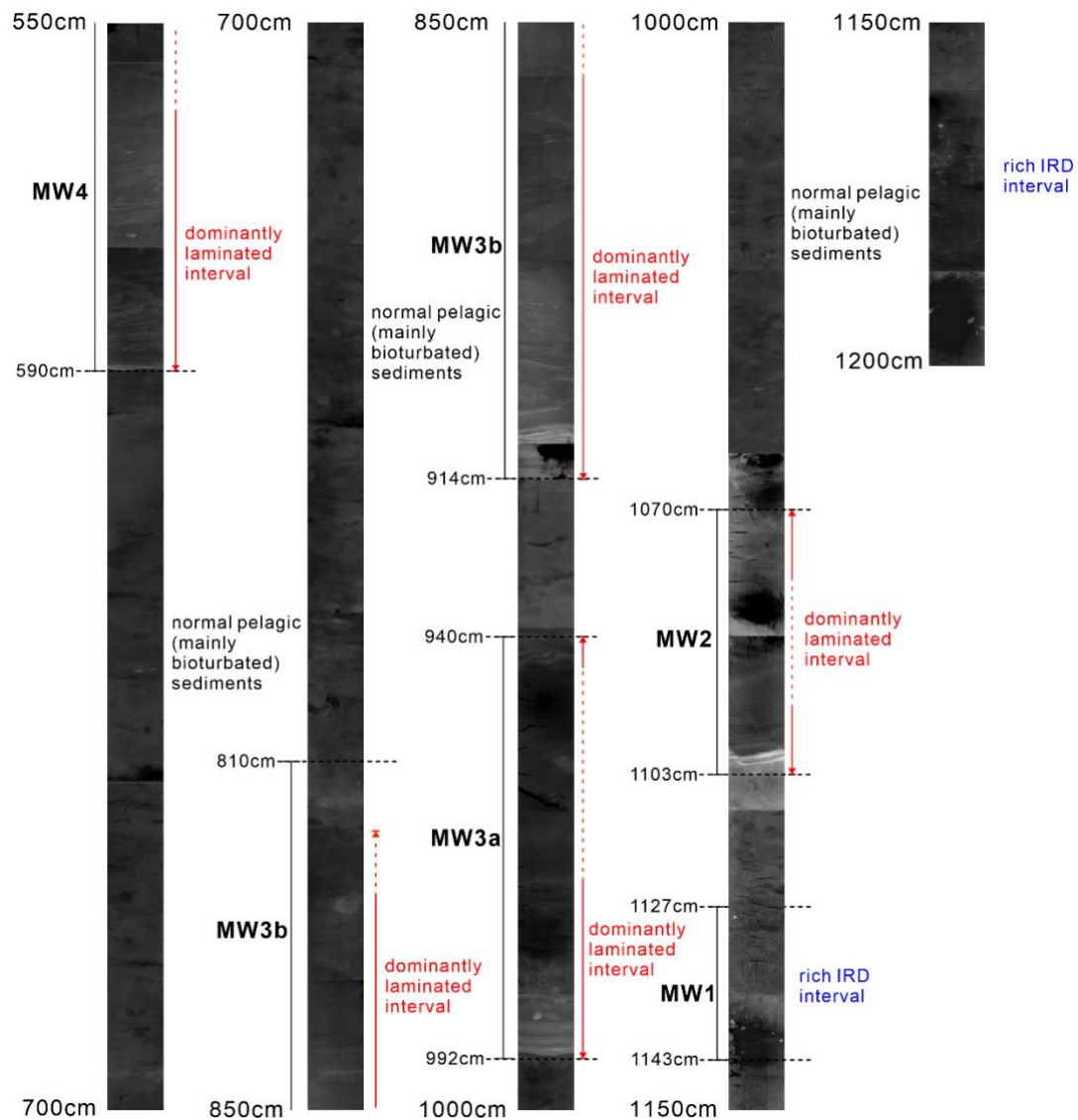
Supplementary Fig. 3.3 X-ray photographs of Core MSM12/2-05-01 (depth extent 500-1200 cm) showing internal structure of sediments.

MW1 to MW4 are characterised by silty clay/clayey silt laminations (interpreted as plumites) related to meltwater plumes as shown in the X-ray photographs. The dominant laminated intervals and IRD-rich intervals are highlighted. The bioturbated sediments are intercalated by dominant laminated intervals. For source of X-ray photographs of core MSM12/2-05-01 we refer to Stein, (2010).
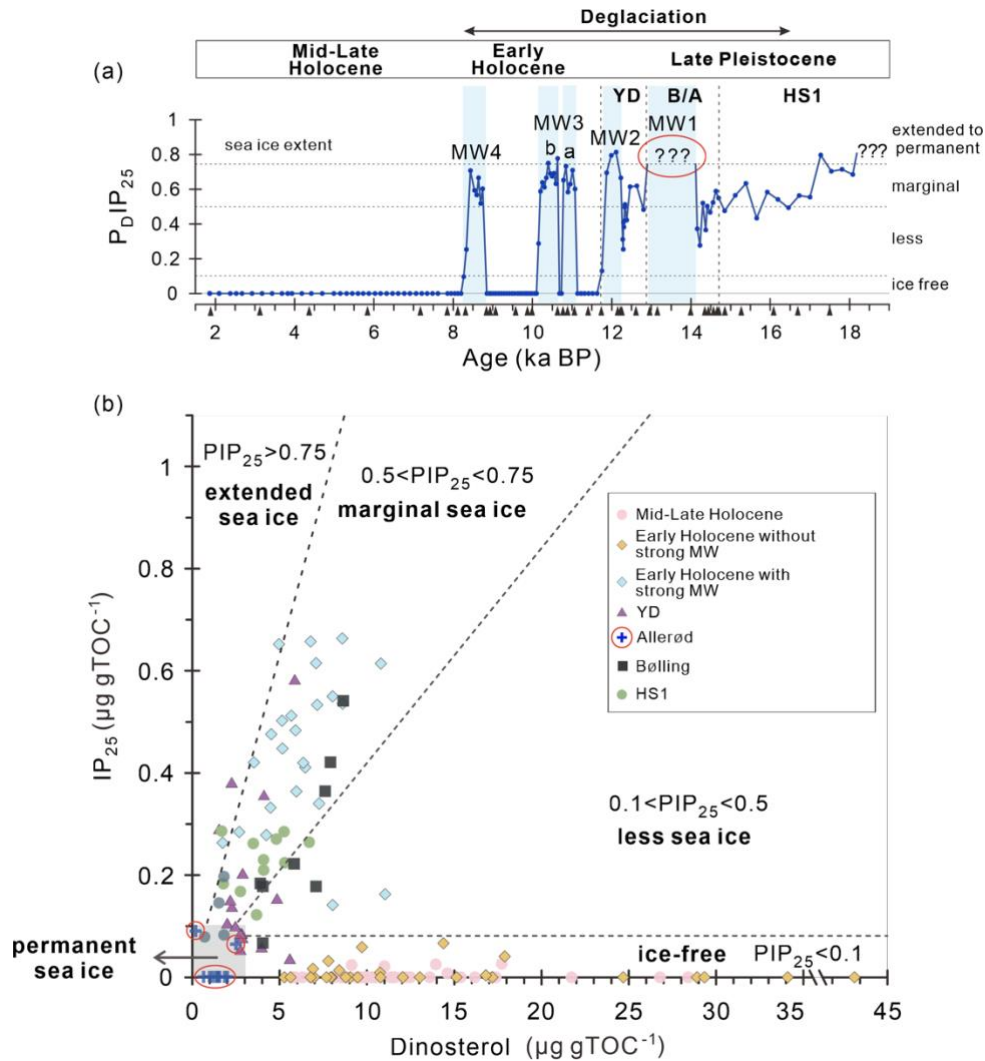
Supplementary Fig. 3.4 (a) P_DIP_{25} plot and (b) Scatter plot of concentrations of sea ice proxy IP_{25} versus open-water phytoplankton proxy dinosterol (Core MSM12/2-05-01).

Classification of sea ice cover according to Müller et al. (2011). For zero or minimum concentrations of IP_{25} and phytoplankton biomarkers, i.e., for the data points in the light grey background square close to the origin of the plot (**b**), reliable P_DIP_{25} cannot be calculated (highlighted by question marks in (**a**)) and set to "1" in the original work by Müller et al. (2011), assuming a permanent sea ice cover. Such interpretation is unrealistic in our case as SST values are well above 0 °C during these time intervals (for details see the text). Black triangles mark available AMS[14]C dates.
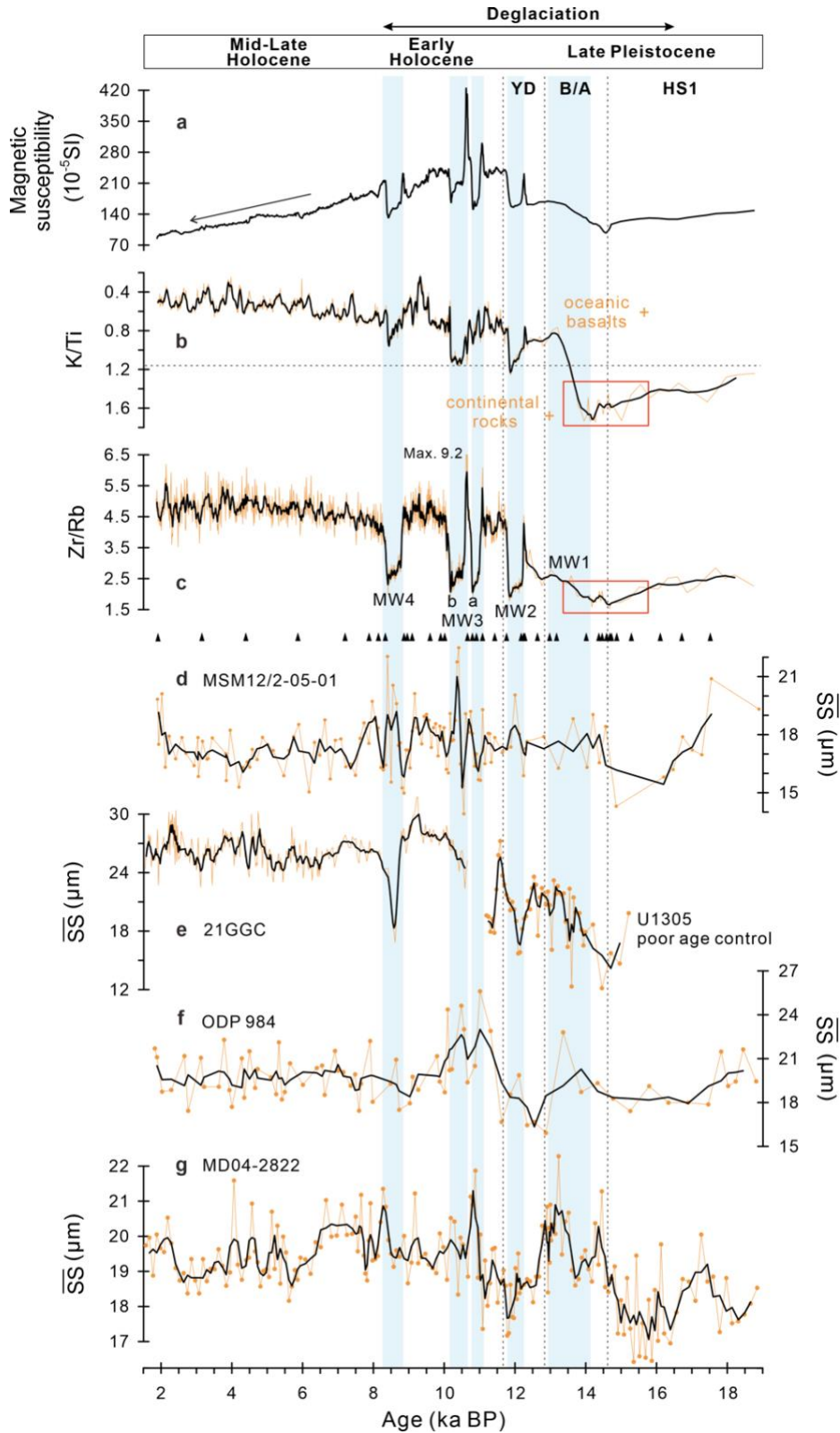
Supplementary Fig. 3.5 Proxy records for sediment provenance and bottom current intensity.
Records from Core MSM12/2-05-01 (**a-d**) and reference cores (**e-g**). (**a**) Magnetic susceptibility; the decreasing trend of MS values since the middle to late Holocene are explained by increased input of carbonate and decreased input of siliciclastic material (cf., Supplementary Fig. 3.2); (**b**) XRF-K/Ti ratios as proxy for sediment provenance. K might be indicative for input of weathering products of continental rocks (Grützner and Higgins, 2010) whereas Ti is more related to weathering products of basalts, e.g., from Iceland/eastern Greenland (Ballini

et al., 2006). Red box shows high input of continental rocks; (**c**) XRF-Zr/Rb ratios as proxy for coarse- versus fine-grained matter. The ratios during the late HS1 to Bølling periods could be highly influenced by increased input of continental sediments, causing high K but also high Rb values (Grützner and Higgins, 2010; Dypvik and Harris, 2001) and resulting in higher K/Ti and lower Zr/Rb ratios as shown in our records; (**d**) Sortable silt mean size ($\overline{\overline{SS}}$) record of Core MSM12/2-5-1; black line shows 3 points running average of $\overline{\overline{SS}}$ values; (**e**) $\overline{\overline{SS}}$ record of Core 21GGC and IODP Site 1305 from Eirik Drift (Henderson, 2009); (**f**) $\overline{\overline{SS}}$ record of ODP Site 984 from Gardar Drift (Praetorius et al., 2008); (**g**) $\overline{\overline{SS}}$ record of Core MD04-2822 from Rockall Plateau (Channell et al., 2016). Black triangles mark available AMS[14]C dates.
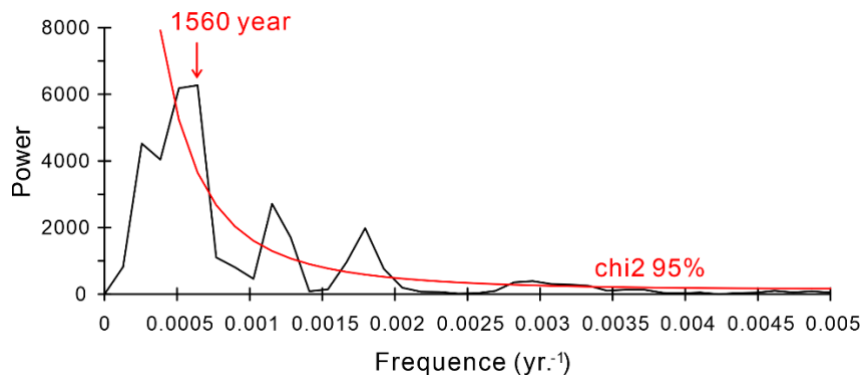
Supplementary Fig. 3.6 Spectral analysis record of meltwater proxy %C$_{37:4}$ (Core MSM12/2-05-01). %C$_{37:4}$ data during 14-8.2 ka BP was used for spectral analysis. The red line indicates 95% confidence level. The 1560-year cycle shows the highest power.
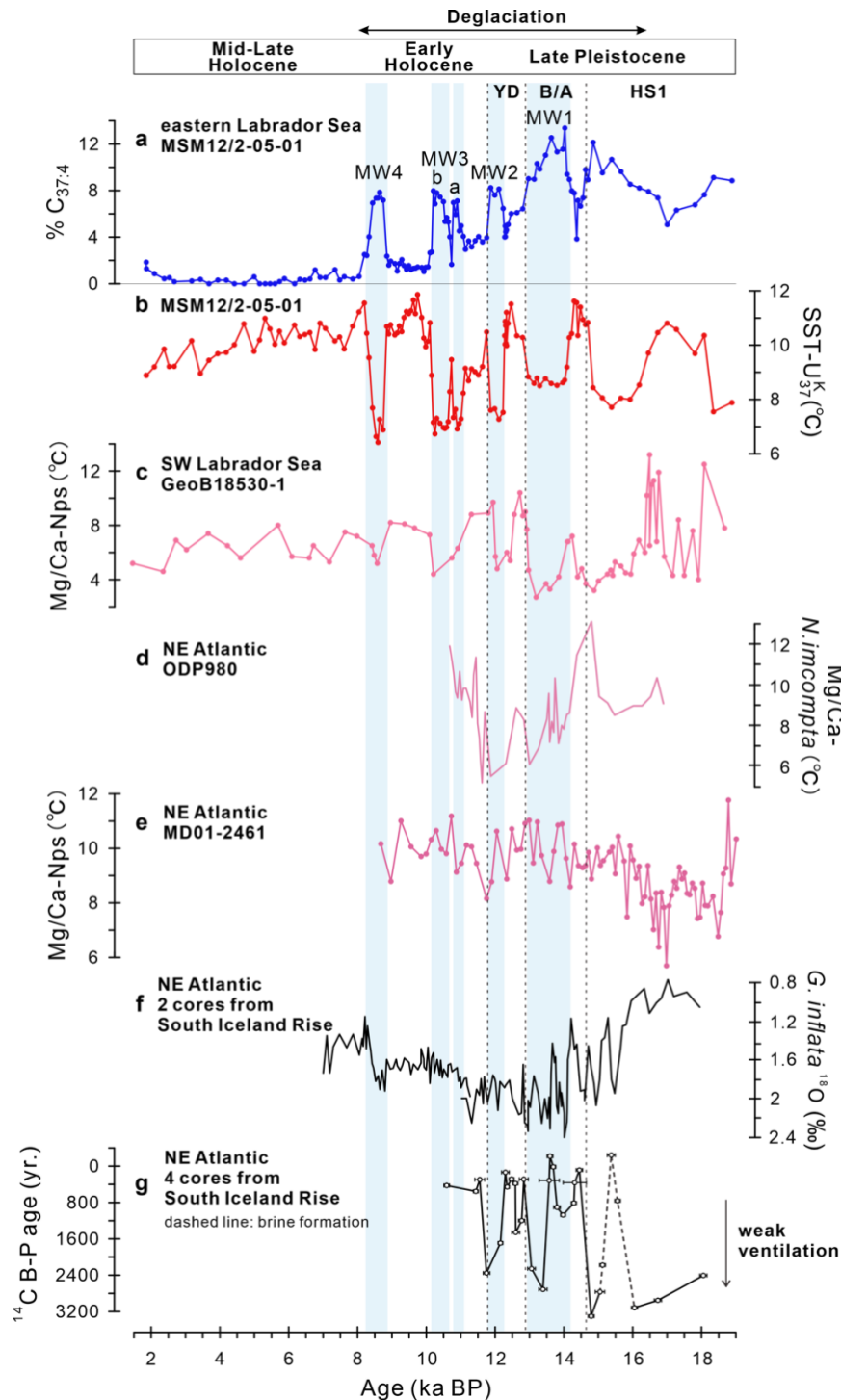
Supplementary Fig. 3.7 Comparation between different proxy records from the North Atlantic during the last deglaciation.

(**a**) Percentage of C$_{37:4}$ as proxy for meltwater discharge from Core MSM12/2-05-01; (**b**) SST reconstruction based on U$_{37}^{K}$ from Core MSM12/2-05-01; (**c**) Subsurface temperature record based on Nps-Mg/Ca ratios from Core GeoB18530-1 (Max et al., 2022); (**d**) Subsurface temperature estimates based on Ma/Ca ratios of *N. incompta* from ODP Site 980 (Benway et al., 2010); (**e**) Subsurface temperature record based on Nps-Mg/Ca ratios from Core MD01-2461 (Peck et al., 2008); (**f**) δ^{18}O record of *G. inflata* from South Iceland Rise (Thornalley et al., 2010); (**g**) Difference in ^{14}C between benthic and planktic foraminifera from South Iceland Rise, indicating the ventilation in the North Atlantic (Thornalley et al., 2011). The horizontal error bars represent the propagated uncertainties of ^{14}C measurement.
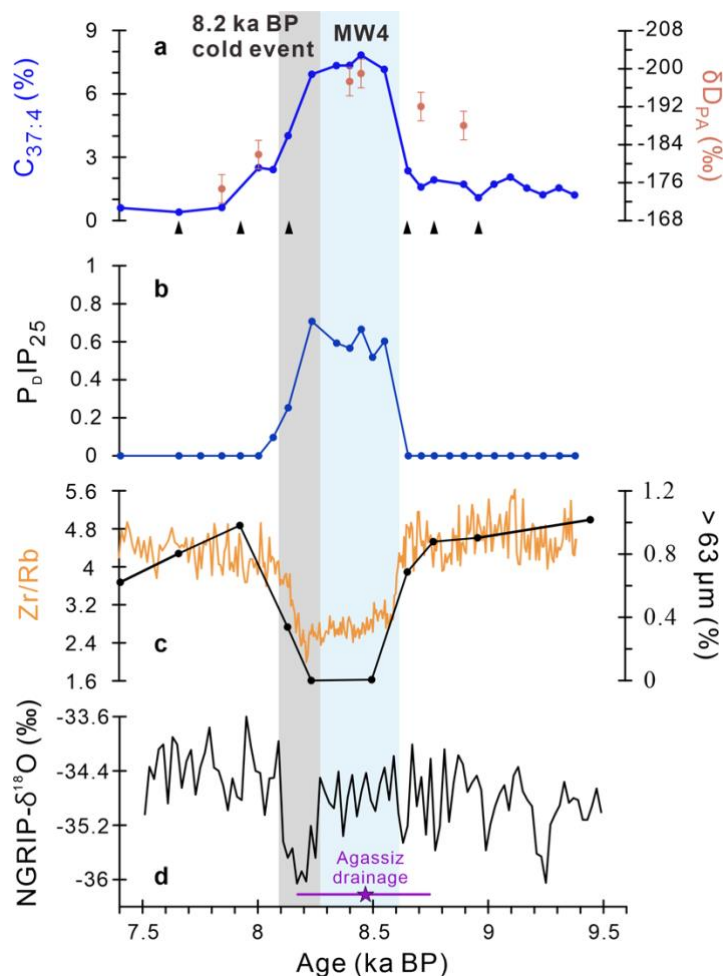
Supplementary Fig. 3.8 Proxy records of MW4 (Core MSM12/2-05-01) versus the 8.2 ka BP cold event based on Marine 20 calibration curve (Heaton et al., 2020).

(**a-c**) Proxy records for abrupt change in MW4 from Core MSM12/2-05-01. (**a**) %$C_{37:4}$ and stable hydrogen isotope composition of palmitic acid (δD_{PA}) as proxies for meltwater discharge (with higher %$C_{37:4}$ and lower δD_{PA} representing lower salinity). Vertical error bars represent the standard deviation of the δD_{PA} measurements (3 ‰); (**b**) $P_D IP_{25}$ as proxy for sea ice extent; (**c**) XRF-Zr/Rb ratios indicating coarse versus fine-grained matter; percentage of coarse fraction (>63 μm); (**d**) Greenland Ice Core record (Svensson et al., 2008). The age of ice core was calculated to cal. ka BP from GICC05 age. The purple star indicates the age for Lake Agassiz drainage event: 8.47 ka BP with 1σ uncertainties (purple line, 8.16-8.74 ka BP) (Barber et al., 1999). Light blue shading shows the meltwater event 4 (MW4), whereas grey shading indicates the 8.2 ka BP cold event shown in the Greenland Ice Core. Based on the Marine 20 calibration, the 8.2 ka BP cold event probably occurred at the end of MW4. That means, in comparison to the Marine 13 calibration, all three proxy records become around 200 years younger (see Fig. 3.5 in the main text). Black triangles mark available AMS[14]C dates.

4 Interaction between ice sheet instability and sea surface characteristics in the Labrador Sea during the last 50 ka

Defang You[1, *], Ruediger Stein[1,2,3,4], Kirsten Fahl[1], Audrey Limoges[5], Enno Schefuß[3]

[1]Alfred Wegener Institute Helmholtz Centre for Polar and Marine Research, Am Alten Hafen 26, Bremerhaven 27568, Germany

[2]Faculty of Geosciences, University of Bremen, Bremen 28359, Germany

[3]MARUM-Center for Marine Environmental Sciences, University of Bremen, Bremen 28359, Germany

[4]Frontiers Science Center for Deep Ocean Multispheres and Earth System, Key Laboratory of Marine Chemistry Theory and Technology, Ocean University of China, Qingdao 266100, China

[5]Department of Earth Sciences, University of New Brunswick, Fredericton NB E3B 5A3, Canada

*Corresponding author: defang.you@awi.de

4.1 Abstract

The study on the retreat of ice sheets in the past provides important insights into the interaction between ice sheet behaviours and ocean characteristics, especially under a sustained warming climate. The decay of ice sheets may affect the surrounding ocean environment, and changes in sea surface conditions can, in turn, affect the ice sheet stability. However, interactions between ice sheet dynamics and sea surface characteristics are still not fully understood. Here, we show sedimentary records from the eastern Labrador Sea, proximal to the Laurentide Ice Sheet (LIS) and the Greenland Ice Sheet (GrIS), and spanning the last 50 ka, i.e., the last glacial-deglacial-Holocene period. The XRF, biomarker, and planktic/benthic foraminifer data document the outstanding collapse of the LIS/iceberg discharge during Heinrich Events (i.e., HE5, HE4, HE2, and HE1) and the occurrence of meltwater plumes from the LIS and GrIS during the last deglaciation. Such meltwater discharges have caused surface freshening in the Labrador Sea and, consequently, decreased sea surface temperatures and phytoplankton production. Enhanced Irminger Current inflow might have caused (sub-)surface warming in the Labrador Sea and triggered the retreat of ice sheets/meltwater discharge. In contrast to relatively low open-water productivity during the glacial period, the Last Glacial Maximum (LGM) was characterized by increased sea ice algae and phytoplankton production, suggesting the presence of a polynya in front of the southern GrIS.

Key words: Labrador Sea, icebergs, meltwater plumes, sea surface characteristics, ice sheets, Irminger Current

Highlights:

1) Two different patterns of meltwater discharge into the eastern Labrador Sea: primarily iceberg discharge during the last glacial period versus meltwater plumes during the last deglaciation.

2) Enhanced warm Irminger Current inflow might have caused (sub-)surface warming in the Labrador Sea, subsequently contributing to the disintegration/retreat of the surrounding Laurentide Ice Sheet and Greenland Ice Sheet.

3) An offshore polynya probably occurred south of Greenland during the Last Glacial Maximum.

4.2 Introduction

Ice loss from the Greenland Ice Sheet (GrIS) and Antarctic Ice Sheet has accelerated over the past decade, leading to increased meltwater discharge and rising sea levels (Yang et al., 2016; Pattyn et al., 2018; Flowers, 2018; Hugonnet et al., 2021; Box et al., 2022). Greenland has lost 3.902 ± 342 billion tonnes of ice between 1992 and 2018, causing the mean sea level to rise by 10.8 ± 0.9 mm (Briner et al., 2020), while 2.720 ± 1.390 billion tonnes of ice was lost from the Antarctic Ice Sheet between 1992 and 2017, resulting in 7.6 ± 3.9 mm in mean sea-level rise (The IMBIE Team, 2018). In addition to sea-level rise, low-temperature and low-salinity meltwater discharge may affect sea surface characteristics in the surrounding areas and potentially prevent ocean ventilation/deep water formation in the sensitive regions. A recent study shows the Greenland runoff has caused salinity anomalies in the surface waters of the Labrador Sea at present, especially along the coastal regions (Böning et al., 2016). The accumulation of meltwater may become large enough to progressively prevent the deep winter convection/Labrador Sea Water formation in the coming years (Böning et al., 2016), which may have a significant impact on Atlantic Meridional Overturning Circulation (AMOC) (Hillaire-Marcel et al., 2001; Yang et al., 2016).

The Labrador Sea is a key area to study the impact of meltwater discharge on the ocean environment, due to its proximity to the GrIS and also the Laurentide Ice Sheet (LIS) during the last glacial period. Sedimentary records from the Labrador Sea dating back to the glacial/deglacial period with massive meltwater discharge can provide the long-term history of changes in surface characteristics in the subpolar regions (e.g., de Vernal and Hillaire-Marcel, 2000; Gibb et al., 2014; Moffa-Sanchez and Hall, 2017; You et al., 2023). During the last deglaciation, meltwater pulses from the LIS and GrIS into the Labrador Sea have caused a distinct decrease in surface salinity and sea surface temperature (SST), resulting in increased sea ice formation and possible perturbation of deep-water formation and atmosphere (Gibb et al., 2014; You et al., 2023). Depending on the magnitude of meltwater discharge, modest meltwater input

serves as a significant source of iron to surrounding coastal oceans, which might contribute to enhanced primary production (Bhatia et al., 2013). However, strong meltwater discharge may have caused significant stratification and increased sea ice cover, which would have restricted light penetration and delayed or impeded phytoplankton blooms, ultimately resulting in reduced productivity (Ardyna and Arrigo, 2020; Wassmann et al., 2020; You et al., 2023). As a direct sea ice proxy biosynthesized by sea ice diatoms (Belt et al., 2007), IP_{25} has been used in many studies in high-latitude regions (see reviews by Stein et al., 2012; Belt and Müller, 2013; Belt, 2018). However, paleo records of IP_{25} are scarce in the eastern Labrador Sea. Available studies only focus on specific Dansgaard-Oeschger cycle (34-42 ka BP) (Scoto et al., 2022), the last deglaciation to early Holocene (~19 ka BP) (You et al., 2023), and most recently the last interglacial (Steinsland et al., 2023). In order to enhance our comprehension of the effects of ice sheet instability/meltwater discharge on sea surface properties, additional high-resolution and continuous sedimentary records are necessary.

Surface ablation and retreat of marine-terminating glaciers are the main processes of mass loss of ice sheets observed today (Catania et al., 2019; Choi et al., 2021). Compared to inland ice sheet processes, increased glacier discharge is almost entirely related to the retreat of glacier fronts (King et al., 2020), which might contribute 50% or more to meltwater discharge at the end of this century (Choi et al., 2021). During the last glacial period, the decay of ice sheets was more easily influenced by ocean forcing due to the larger ice sheet extent on the continental shelves (Margold et al., 2018). Many studies have proposed that the retreat of marine-terminating glaciers was related to upper-ocean warming, which might have induced the retreat of the grounding line, melted the base of the ice sheet/shelf, and resulted in the disintegration and meltwater discharge (cf., DeConto and Pollard, 2016; Pattyn et al., 2018; Catania et al., 2019; Wood et al., 2021). Because extensive areas of polar ice sheets were grounded below sea level during the last glacial period (Clark et al., 2020), thus, this mechanism (i.e., ocean warming inducing the decay of ice sheets) has also been applied to the interpretation of paleo records, e.g., interpreting the occurrence of Heinrich Events (cf., Marcott et al., 2011; Menviel et al., 2020; Max et al., 2022). Evidence from proxy records indicates that subsurface warming in the Labrador Sea and North Atlantic preceded the occurrence of Heinrich Events (HEs), i.e., the collapse of the LIS accompanied by substantial detrital material and meltwater discharge into the Labrador Sea and adjacent subpolar regions may have been triggered by subsurface warming (Marcott et al., 2011; Max et al., 2022). In addition to HEs, evidence of subsurface warming has also been identified during other periods, such as 8.5 ka BP, prior to the decay of Hudson Bay Ice Saddle (Lochte et al., 2019). Furthermore, the warming of the upper ocean might have contributed to the retreat of the GrIS during the last deglaciation (Knutz et al., 2011; Rainsley et al., 2018). One prevalent hypothesis is that the subsurface warming in the North Atlantic has been caused by reduced

AMOC, which led to enhanced downward diffusive heat exchanges and deepening of the North Atlantic Current (Alvarez-Solas et al., 2010; Yasuhara et al., 2019; He et al., 2020; Larkin et al., 2022). However, the direct driving factor(s) behind subsurface warming in the Labrador Sea is still a topic of discussion.
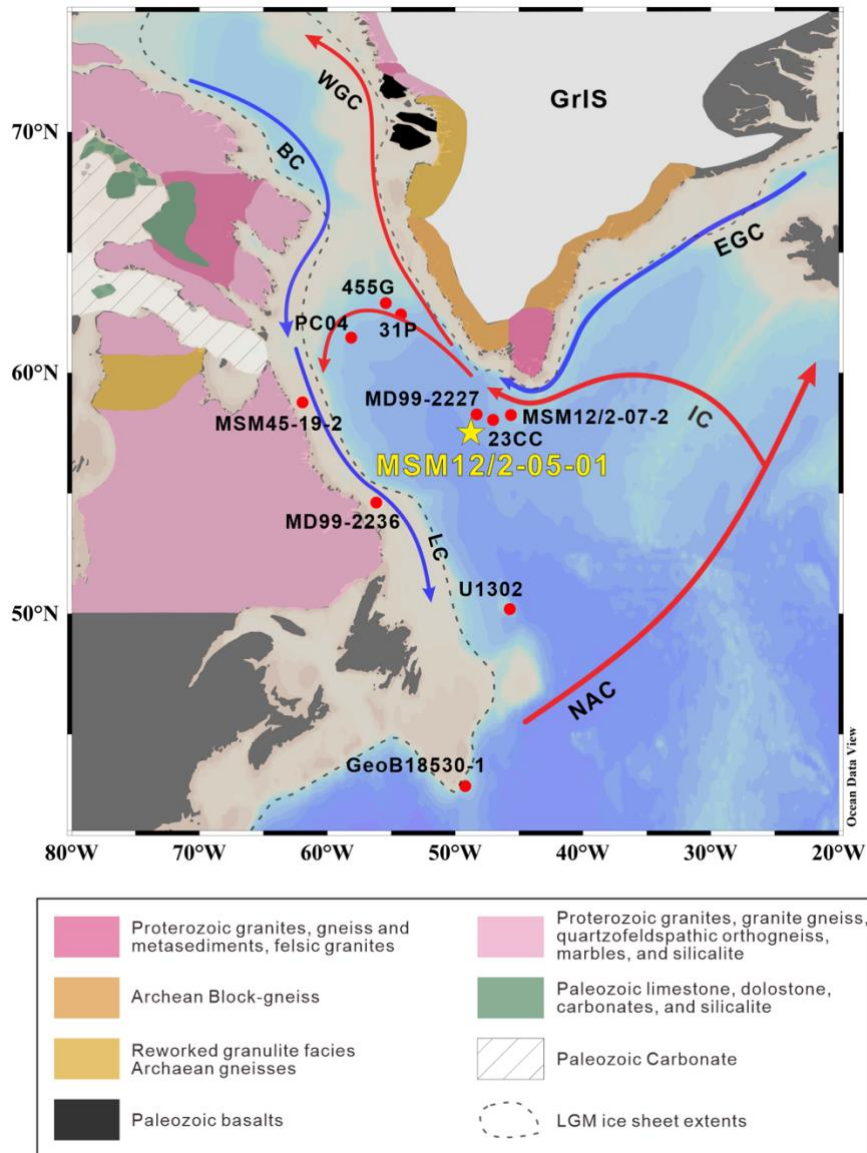
Fig. 4.1 Core sites, ocean circulation pattern, and general geology map.
Map with core sites, modern ocean circulation pattern, and surrounding geology (geology distribution below 50°N is not shown here). The location of Core MSM12/2-05-01 (this study) is shown by the yellow star, and other cores referred to are indicated by red dots. Red arrows: warm surface current; blue arrows: cold surface current. NAC North Atlantic Current, IC Irminger Current, WGC Western Greenland Current, EGC Eastern Greenland Current, BC Baffin Current, LC Labrador Current. Grey stippled lines show ice sheet extents during the LGM (Margold et al., 2018). Simplified bedrock geology is based on Simon et al. (2014) and bedrock geology map from *https://natural-resources.canada.ca*.

Here, we chose a sediment core from the eastern Labrador Sea to investigate the interaction between ice sheet instability and sea surface characteristics during the last 50 ka (Fig. 4.1). Ice sheets instability was reflected by detrital material input based on element ratios from X-ray fluorescence (XRF) scanning data and ice-rafted debris (IRD) abundance. Multiple biomarker indices were used to reconstruct meltwater discharge, sea ice cover, SST, and open-water phytoplankton productivity. Specific planktic/benthic foraminifer species were used to reflect warm Irminger Current inflow and primary production. Based on our records, we demonstrated that (1) massive detrital input during the HEs mainly occurred via iceberg discharge but was supplied by meltwater plumes during four other deglacial meltwater events (MWs), (2) meltwater discharge has caused surface freshening in the Labrador Sea resulting in decreased SSTs, probably increased sea ice formation, and reduced open-water phytoplankton productivity, (3) enhanced Irminger Current inflow might have induced the (sub-)surface warming in the Labrador Sea, leading to the collapse of the LIS and GrIS, and (4) a polynya was prevalent in the southern/southwestern Greenland area during the Last Glacial Maximum (LGM).

4.3 Regional setting

Eirik Drift is a sedimentation drift located off the southern tip of Greenland with sedimentation rates exceeding 30 cm/kyr (Hunter et al., 2007), which allows high-resolution palaeoceanography reconstruction in the Labrador Sea. In contrast to intense winnowing in the upstream regions by deep currents (Elliot et al., 2002; Evans et al., 2007), Eirik Drift may provide continuous sedimentary records of changes in surface characteristics and the retreat of the surrounding ice sheets. Deep-water circulation at Eirik Drift at present is dominated by the Western Boundary Undercurrent consisting of Denmark Strait Overflow Water, Northeastern Atlantic Deep Water (derived from Iceland-Scotland Overflow Water), and Labrador Sea Water (Hunter et al., 2007; Stanford et al., 2011). Our study core MSM12/2-05-1 is located at the foot of Eirik Drift (Fig. 4.1; see vertical water masses distribution in Supplementary Fig. 3.1, Chapter 3.8), bathed by Denmark Strait Overflow Water (Stanford et al., 2011). Surface circulation is dominated by the cold East Greenland Current (EGC) and the warm Irminger Current (IC), which mix south of Greenland and form the relatively warm West Greenland Current (WGC) that flows northward (Drinkwater et al., 1996; Cuny et al., 2005). Warm surface and subsurface water inflow along the west Greenland coast affects the present sea ice distribution. The eastern Labrador Sea is ice free throughout the whole year, whereas a seasonal sea ice cover is characteristic in the western Labrador Sea, influenced by the cold Labrador Current (LC) from Baffin Bay (Seidenkrantz, 2013).

4.4 Material and methods

4.4.1 Sediment core and chronology

The 15 m long sediment core MSM12/2-05-01 (MSM12/647-1) was retrieved from the Eirik Drift at 57° 32.31′ N, 48° 44.32′ W in a water depth of 3491 m during the *Maria S. Merian* cruise MSM12/2 (Uenzelmann-Neben, 2009) (Fig. 4.1). The age model of this core was established by 44 Accelerator Mass Spectrometry (AMS) radiocarbon dates of the planktic foraminifer species *Neogloboquadrina pachyderma* (sinistral) (Supplementary Table 4.1). 38 AMS dates were applied to the upper 12 m to constrain abrupt change events in our records during the last deglaciation (see more details in You et al. (2023)), whereas fewer age control points were only available in the lower part of this core. The global mean reservoir age (R=405 yr.) and the Marine 20 calibration curve were used to calculate calendar ages (Supplementary Table 4.1). The final age-depth model was established by the Bacon program (Blaauw and Christen, 2011). Based on the age model, the mean sedimentation rate is 107 cm/kyr in the upper 1118 cm, while it is assumed to be 10 cm/kyr in the lower 372 cm (Supplementary Fig. 4.1). The calibration based on the Marine 13 calibration curve was also evaluated, and the results were similar to those obtained using the Marine 20 calibration curve (i.e., the whole records became around 200 yr. older) and had no impact on our interpretation (Supplementary Fig. 4.2).

4.4.2 XRF and XRD

The AWI Avaatech X-Ray Fluorescence (XRF) Core Scanner was used for the determination of the chemical composition of the sediment. The split core surface was scanned during 10 kV, 30 kV, and 50 kV runs to obtain reliable intensities of specific major elements (for details see Stein, 2015)). Here, we present data of Ca, Sr, Si, Fe, and Ti and use the element ratios Ca/Sr, Si/Sr, and Fe/Sr to reflect terrigenous input.

For XRD measurements, a split of 1-2 gr of ground bulk sediment was measured continuously using a Phillips PW3020 diffractometer equipped with cobalt ka radiation, automatic divergence slit, graphite monochromator, and automatic sample changer, and measuring the spectrum from 20 to 40° 2Theta. Relative XRD intensities of quartz (4.26 Å), plagioclase (3.19 Å) and k-feldspar (3.23 Å), and dolomite (2.89 Å) were determined to be used as proxy for detrital input from surrounding continents by Sommerfeldt (2012). In addition, the relative intensity of calcite (3.04 Å) gives information about both detrital (terrigenous) and biogenic (foraminifers and coccoliths) carbonate input. In this study, we only use the intensities of calcite and dolomite to get a first-order estimate about the detrital carbonate (dolomite) input from the Laurentide Ice Sheet (cf., Stein et al., 2009b, 2010; Sommerfeldt, 2012). In this "screening approach", we simply divided the inorganic carbon (IC) (see subchapter 3.3) into its calcite and dolomite proportions using the relative intensity (r.i.) values of the calcite (3.04 Å) and dolomite (2.89 Å) XRD peaks and

assuming that calcite plus dolomite equals to the total carbonate content. This allows to calculate (estimate) the dolomite content (%):

$$\text{Dolomite (\%)} = \frac{\text{Dolomite 2.89 Å r.i.}}{\text{(Calcite 3.04 Å r.i. + Dolomite 2.89 Å r.i.)}} \quad \text{x IC} \quad \text{x 7.67}$$

For details and approach, we refer to Stein et al. (2009b, 2010).

4.4.3 Geochemical bulk parameters and biomarker analysis

Freeze-dried and homogenized sediments were used for geochemical bulk parameter measurement. Total organic carbon (TOC) contents were measured by Carbon-Sulfur Analyser (CS-125, Leco) after removing carbonate with hydrochloric acid. Total carbon (TC) contents were measured using the and Carbon-Nitrogen-Sulfur Analyser (Elementar III, Vario). Inorganic carbon content was calculated by subtracting TOC from TC values.

For biomarker analysis, 5 g of freeze-dried sediments were extracted by ultrasonication with dichloromethane/methanol (DCM/MeOH, 2:1 v/v). Hydrocarbon and sterol/alkenone fractions were separated by open silica gel column chromatography using 5 ml n-hexane and 9 ml ethylacetate/n-hexane, respectively. Hydrocarbon and sterols were measured by gas chromatography-mass spectrometry (GC-MS). Prior to GC-MS determination, the sterol fraction was silylated by BSTFA. After saponification for cleaning, alkenones were determined by GC. The internal standards 7-hexylnonadecane (7-HND, 0.076 µg), 5α-androstan-3β-ol (androstanol, 10.8 µg), and n-hexatriacontane (C36, 2,1435 µg) were added to quantify concentrations of IP$_{25}$, sterols, and alkenones. For further details about identification and quantification of specific biomarkers, please refer to Fahl and Stein (2012) and You et al. (2023). The SST reconstruction was based on equations U_{37}^{K}=(C$_{37:2}$-C$_{37:4}$)/(C$_{37:2}$+C$_{37:3}$+C$_{37:4}$) (Brassell et al., 1986) and U_{37}^{K} =0.021T+2.243 (Filippova et al., 2016). The percentage of tetra-unsaturated alkenones (%C$_{37:4}$) was used to estimate meltwater discharge (Bard et al., 2000; You et al., 2023).

In order to further support that %C$_{37:4}$ is related to meltwater discharge, the stable hydrogen isotope composition of palmitic acid (δD$_{PA}$) was measured at selected depths as a proxy for salinity changes (low δD$_{PA}$ indicating low salinity). Although palmitic acid is produced by most marine and terrestrial organisms, Sachs et al. (2018) presented multiple lines of evidence supporting that marine phytoplankton is the primary source to Arctic Ocean sediments. For the analysis of δD$_{PA}$, 6g of freeze-dried and homogenized sediments were used for extraction by ultrasonication with DCM/MeOH (9:1 v/v). The internal standard C19:0 fatty acid (50.5 µg) was added prior to the extraction. The extracts were saponified using 0.1 M KOH in MeOH, yielding neutral and acid fractions. The acid fractions were methylated with MeOH of known isotopic composition, yielding the corresponding fatty acid methyl esters (FAMEs). The FAME fractions

were cleaned by open pipet columns using DCM. δD_{PA} analyses were carried out by GC-IRMS. Isotope values were measured against calibrated H_2 gas and δD values were reported in permil against VSMOW. Long-term mean absolute deviation based on the external *n*-alkane standard mixture was 3.0‰. δD_{PA} values were corrected for the methyl group added during methylation. For analytical details and further references, see You et al. (2023). The δD_{PA} values were further corrected based on ice sheet volumes at different periods (Tierney et al., 2017). A good negative correlation between $\%C_{37:4}$ and δD_{PA} demonstrates that increased $\%C_{37:4}$ is linked to enhanced meltwater discharge (i.e., lower δD_{PA} correlating with lower salinity, see Sachs et al., 2018) (Fig. 4.2).
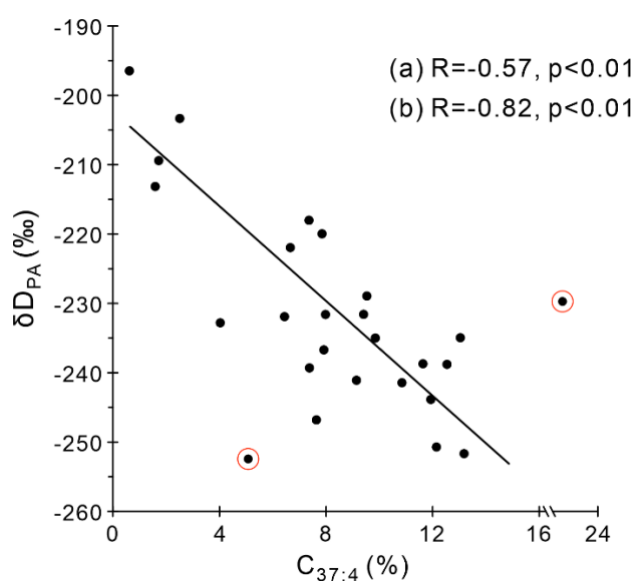
Fig. 4.2 Correlation between δD_{PA} and $\%C_{37:4}$ (Core MSM12/2-05-01).
δD_{PA} values at selected samples show a negative correlation with corresponding $\%C_{37:4}$ values (lower δD_{PA} corresponding to higher $\%C_{37:4}$). The correlation coefficient is -0.57 (p<0.01) if all the data points are included (black dots). If two very discrete points (probably outliers) are excluded (black dots with red circles), the correlation coefficient is -0.82 (p<0.01). Nevertheless, the negative correlation supports the use of $\%C_{37:4}$ as a proxy for meltwater discharge (lower δD_{PA} correlating with lower salinity, see Sachs et al., 2018).

4.4.4 Coarse fraction analysis: IRD and planktic/benthic foraminifer analysis

Bulk sediments were washed through a 63 μm sieve. Coarse fractions were dried and sieved through 125 μm and 250 μm meshes. IRD numbers were counted from the coarse fraction above 250 μm excluding tephra particles in each sample. Planktic/benthic foraminiferal assemblage analysis was carried out on the two fractions 125-250 μm and >250 μm, respectively, and the number of specimens per species from the two fractions were summed up. Only samples with more than 300 planktic specimens were used for relative abundance calculations. For the relative abundance of benthic foraminifera, it has been suggested that the total number of specimens

should be greater than 40 (Seidenkrantz et al., 2021). However, due to the low abundances of benthic foraminifera in our samples, we lowered the minimum limit of the total specimens, and samples with more than 30 specimens were used here. Therefore, we should interpret the percentage values of benthic foraminifera with caution. In order to better present changes in dominant species concentration, accumulation rates of specific planktic and benthic foraminifera have been calculated as well.

4.5 Results

4.5.1 Changes in physical and geochemical properties

Based on increased grain size and IRD deposition (Fig. 4.3h, i) and comparison with the North Atlantic IRD stack (Lisiecki and Stern, 2016) (Fig. 4.3a), four HEs (i.e., HE5, HE4, HE2, and HE1) have been identified in our records during the last glacial period (50-19 ka). HE5 was assumed due to weak age control in the lowest part of the records. Higher Ca/Sr ratios (a proxy for detrital carbonate input (Channell et al., 2012)) in line with higher percentages of dolomite and inorganic carbon further support the presence of HE4 and HE2 (Fig. 4.3c, d). However, Ca/Sr ratios showed minor peaks for HE5 and HE1 and no peak for HE3. In addition to Ca/Sr ratios, the elements Si, Fe, and Ti (terrigenous source) versus Sr (biogenic source) were also used as proxies for terrigenous material input. In contrast to increased IRD deposition, Si/Sr, Fe/Sr, and Ti/Sr ratios showed lower values during the HEs, whereas high ratios occurred during the LGM (Fig. 4.3f, g). Furthermore, four detrital input events, marked by abrupt increases in Si/Sr, Fe/Sr, and Ti/Sr ratios and low percentages of dolomite and inorganic carbon, have been identified during the last deglaciation. As outlined in You et al. (2023), we named these four detrital events as MW1 to 4 based on the abrupt increase in meltwater discharge (see below Fig. 4.5g). Additionally, MWs were characterized by low coarse fraction content (>63 μm/%) and a lack of IRD deposition (Fig. 4.3h, i). Increased coarse fraction contents with less IRD deposition occurred around 14 ka BP (MW1), consistent with increased abundance of planktic foraminifera (Fig. 4.4a). The last 8 ka were characterized by an absence of IRD deposition, very low coarse fraction content, decreased Si/Sr, Fe/Sr, and Ti/Sr ratios, whereas the inorganic carbon contents increased.
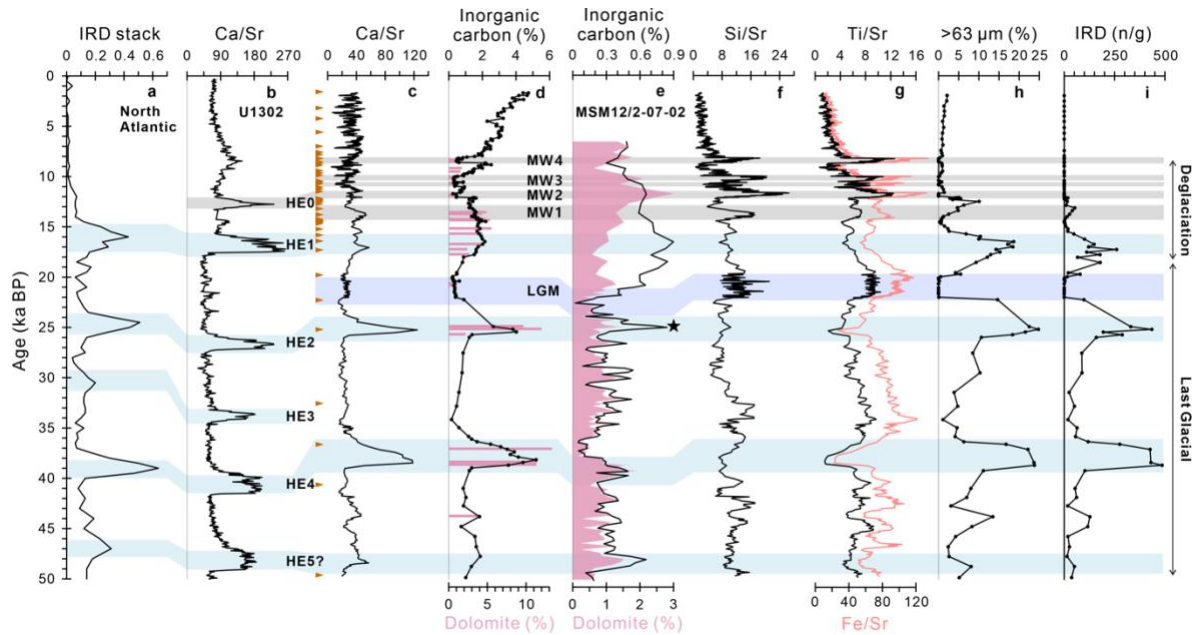
Fig. 4.3 Physical and geochemical properties (Core MSM12/2-05-01) and comparison with other records. **a** North Atlantic IRD stack for Henrich Events (HEs) (Lisiecki and Stern, 2016); **b** XRF-Ca/Sr ratios as proxy for detrital carbonate input from IODP Site U1302 (Channell et al., 2012); **c** Ca/Sr ratios from Core MSM12/2-05-01 (this study); **d** Percentages of inorganic carbon (line) and dolomite (bar) from Core MSM12/2-05-01 (this study); **e** Percentages of inorganic carbon (line) and dolomite (shading) from Core MSM12/2-07-02 (Sommerfeldt, 2012), the black star representing absolute maximum abundance in IRD ; (**f-i**) Proxy records from Core MSM12/2-05-01 (this study): **f** Si/Sr ratios as proxy for detrital silicate input; **g** Ti/Sr and Fe/Sr ratios as proxy for terrigenous Ti and Fe input; **h** Coarse fraction (>63 μm) contents; **i** IRD abundance. Brown triangles mark available AMS[14]C dates. Light blue, grey, and purple shadings highlight Heinrich Events (HEs), Meltwater Events (MWs), and Last Glacial Maximum (LGM), respectively. HE5 was given a question mark due to weak age control in the lowest part of the records.

4.5.2 Variation in planktic/benthic foraminiferal assemblages

A total of 30 calcareous and 3 agglutinated benthic foraminifer species were identified and counted in selected samples. The total number of counted benthic foraminifera in each sample was between 0 and 318, and the average value was 54. Due to their very low abundance (less than 1%), agglutinated foraminifera were not considered here. The percentages and accumulation rates of three dominant benthic species *Melonis barleeanus*, *Epistominella exigua*, and *Cibicidoides wuellerstorfi* are shown in Figure 4.4. The accumulation rates of benthic foraminifera were low during the last glacial period, whereas they showed higher values during the Holocene but these trends of higher values were interrupted by MWs (Fig. 4.4e, f, g). In this study, *M. barleeanus* was combined with *Epistominella exigua* due to similar ecological preferences, and the highest accumulation rates and percentages occurred during the early Holocene. Unlike the decreased percentage values in *M. barleeanus* and *E. exigua*, the percentage of *C. wuellerstorfi* showed a distinct increase during HE4, HE2, HE1, and MW1 (Fig. 4.4g).
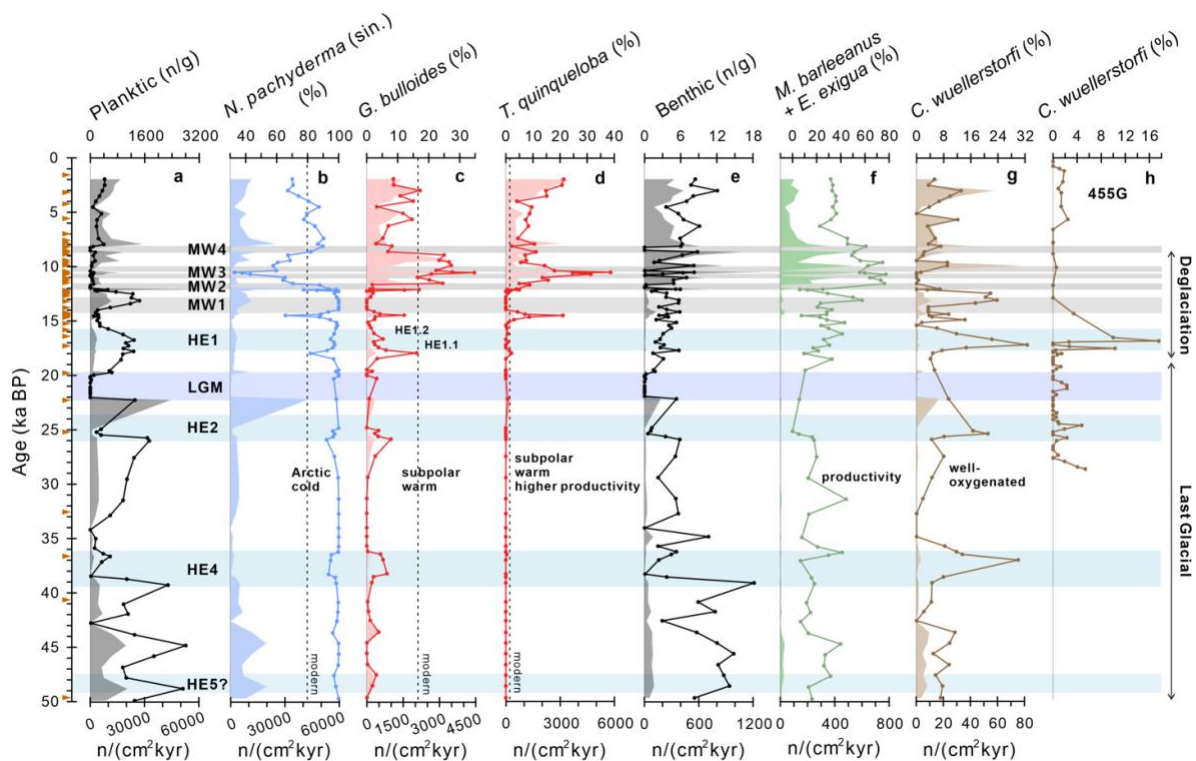
Fig. 4.4 Variation in specific planktic and benthic foraminifer species (Core MSM12/2-05-01).
(a-g) Planktic and benthic foraminifer records from Core MSM12/2-05-01 (this study): **a** Absolute abundances (specimens per gram, line) and accumulation rates (shading) of all planktic foraminifera; **b** Percentages (line) and accumulation rates (shading) of *N. pachyderma* (sin.); **c** Percentages and accumulation rates of *G. bulloides*; HE1 is divided into two phases (HE1.1 and HE1.2) (more details see discussion 5.1.1); **d** Percentages and accumulation rates of *T. quinqueloba*; **e** Absolute abundances and accumulation rates of all benthic foraminifera; **f** Percentages and accumulation rates of *M. barleeanus* and *E. exigua*; **g** Percentages and accumulation rates of *C. wuellerstorfi*; **h** Percentages of *C. wuellerstorfi* from Core 455G (northwestern Labrador Sea) (Seidenkrantz et al., 2021); the age-depth model was re-established based on the Marine 20 calibration curve and Bacon program. The vertical black stippled lines indicate modern percentages of *N. pachyderma* (sin.), *G. bulloides*, and *T. quinqueloba* in the Eirik Drift (**b-d**) based on the data from Kucera et al. (2005). Brown triangles mark available AMS[14]C dates. Light blue, grey, and purple shadings highlight HEs, MWs, and LGM, respectively.

A total of 7 calcareous planktic foraminifer species were identified and counted in selected samples. The total number of counted specimens were between 0 and 30300, and the average value was 5600. *Neogloboquadrina pachyderma* (sin.) (33% to 100%, mean value 88%), *Globigerina bulloides* (0 to 35%, mean value 6%), and *Turborotalita quinqueloba* (0 to 39%, mean value 4%) were the three dominant species in our samples (Fig. 4.4b, c, d). During the glacial period (50-20 ka BP), %*N. pachyderma* (sin.) were close to 100%, i.e., subpolar species %*G. bulloides* and %*T. quinqueloba* were extremely low. However, during the last deglaciation to Holocene (the last 20 ka), %*N. pachyderma* (sin.) showed a decreasing tendency with a significant decrease during the early Holocene (Fig. 4.4b). The percentages of *G. bulloides* showed abrupt and distinct increases prior to HE2, HE1, and MWs. Two pronounced peaks of %*T. quinqueloba* occurred around 14.5 ka BP and 10.5 ka BP, coeval with increased %*G. bulloides*

and decreased % *N. pachyderma* (sin.) (Fig. 4.4d). Additionally, accumulation rates of specific planktic foraminifera were low during HEs and MWs.

4.5.3 Changes in biomarkers

The concentrations and accumulation rates of IP_{25} and open-water phytoplankton biomarkers (brassicasterol, dinosterol, and alkenones) were very low during the last glacial period (50-25 ka BP) (Fig. 4.5b-e). However, maximum concentrations of IP_{25} occurred during the LGM, consistent with increased open-water phytoplankton indices and TOC contents. In contrast to the higher values of phytoplankton biomarkers since the last deglaciation, concentrations and accumulation rates of IP_{25} only showed abrupt and distinct increases during the MW3, MW2, and MW4, whereas no IP_{25} was found during MW1 (Fig. 4.5b). %$C_{37:4}$ values were relatively high
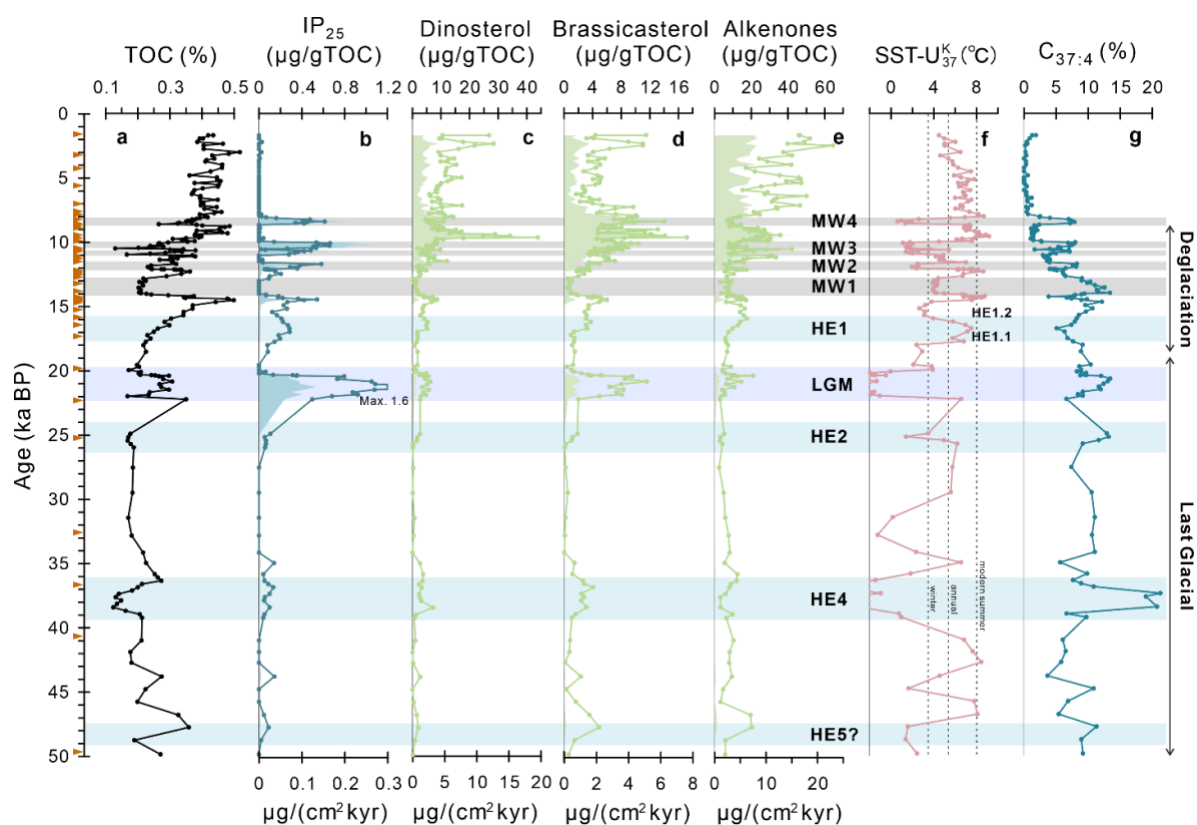
Fig. 4.5 Biomarker records for sea surface characteristics (Core MSM12/2-05-01).
(a-g) Geochemical and biomarker records from Core MSM12/2-05-01 (this study): **a** Percentages of total organic carbon (TOC); **b** Concentrations (line) and accumulation rates (shading) of IP_{25}; **c** Concentrations (line) and accumulation rates (shading) of dinosterol; **d** Concentrations and accumulation rates of brassicasterol; **e** Concentrations and accumulation rates of alkenones; **f** Sea surface temperature (SST) reconstruction based on U_{37}^K; The vertical black stippled lines show modern summer, annual, and winter temperatures around the study area, respectively (*https://odv.awi.de/data/ocean/*); **g** The percentages of tetra-unsaturated alkenones (%$C_{37:4}$). Brown triangles mark available AMS[14]C dates. Light blue, grey, and purple shadings highlight HEs, MWs, and LGM, respectively.

during the last glacial period compared with the interval from the last deglaciation to Holocene (Fig. 4.5g). Increased $\%C_{37:4}$ values were found during the HEs (except HE1.1) and MWs. Corresponding to increased $\%C_{37:4}$ and IP_{25}, SSTs showed abrupt decreases during these time intervals (Fig. 4.5f). Despite significant decreases in SSTs, SSTs were above 0 °C except during the HE4 and LGM. The highest SSTs occurred around the early Holocene, and were similar to modern summer temperatures, whereas abrupt decreases in SSTs occurred during the HEs and MWs with values generally below modern winter temperatures.

A scatter plot of IP_{25} against dinosterol is presented in Figure 4.6. It showed extremely low concentrations of IP_{25} and dinosterol during HE5, HE4, and HE2, which might be interpreted as a nearly permanent sea ice cover or oligotrophic conditions. However, a marginal sea ice cover was prevalent during HE1 and most MWs. In addition, the LGM was characterized by a marginal to extended sea ice cover.
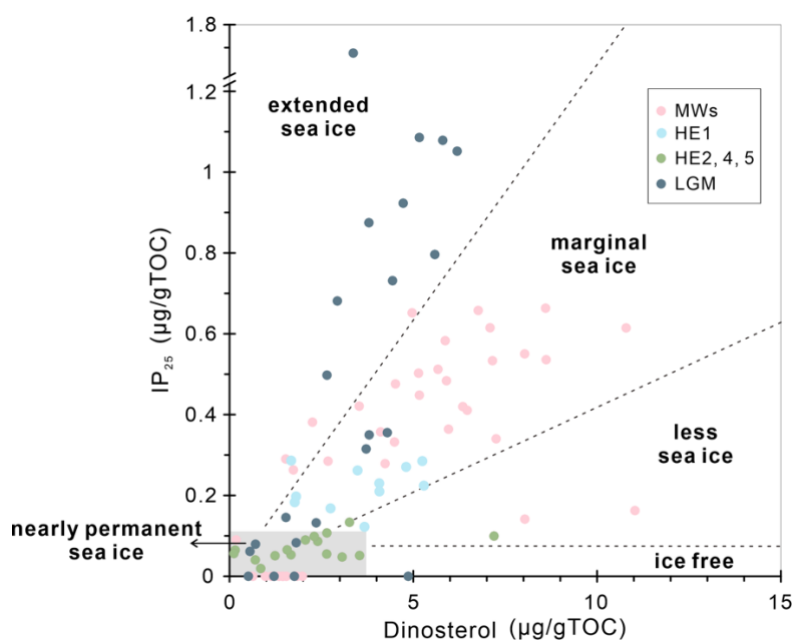
Fig. 4.6 Scatter plots of dinosterol versus IP_{25} (Core MSM12/2-05-01).
Sea ice concentration estimates at different cold periods based on the correlation between IP_{25} (proxy for seasonal sea ice cover) and dinosterol (proxy for open-water phytoplankton). The grey square indicates scenarios with extremely low concentrations of IP_{25} and dinosterol, suggesting a nearly permanent sea ice cover or highly oligotrophic condition in this study.

4.6 Discussion

4.6.1 Characteristics of Heinrich Events versus Meltwater Events in the Labrador Sea during the last 50 ka

Heinrich Events 1-5

HEs were significant cold events characterized by massive iceberg discharge mainly originating from the Hudson Strait Ice Stream (Andrews and Voelker, 2018). Following the melting of icebergs, large amounts of IRD were released into the North Atlantic, forming the IRD belt (Ruddiman, 1997; Hemming, 2004). Therefore, HEs can be identified in sediments by an increase in IRD deposition, particularly in detrital carbonate content (Hemming, 2004; Andrews and Voelker, 2018). Four HEs (i.e., HE5, HE4, HE2, and HE1) characterized by increased IRD deposition and higher dolomite content, were clearly represented in the studied core MSM12/2-05-1 (Fig. 4.3d, i). This indicates that massive icebergs have been transported into the eastern Labrador Sea during these HEs (Fig. 4.9c). Higher Ca/Sr ratios and dolomite contents during HE2 and HE4 imply that large amounts of detrital material originated from Hudson Strait (Channell et al., 2012; Simon et al., 2014). Ca/Sr ratios from Core U1302 (western Labrador Sea) also document the history of outstanding collapses of the LIS during the last 50 ka (Channell et al., 2012) (Fig. 4.3b). In contrast to high Ca/Sr ratios shown in each HEs from IODP Site U1302, no pronounced signals were identified for HE3 in our records. This suggests that icebergs with high loading of detrital carbonate were mostly floating into the western Labrador Sea, i.e., by a restricted distribution of iceberg discharge. Our findings are consistent with previous studies indicating that the LIS was probably not the major contributor to detrital material input in the subpolar regions/IRD belt during HE3 (e.g., Hemming, 2004; Naafs et al., 2013; Zhou et al., 2021). Surprisingly, despite increased IRD deposition and some dolomite input during HE1, Ca/Sr ratios did not show a distinct increase in our core (eastern Labrador Sea) in contrast to records from IODP Site U1302 and Core GeoB18530 (western Labrador Sea) (Figs. 4.3b, 4.7h). This may imply that the Hudson Strait was not the primary source of detrital material input into the eastern Labrador Sea during HE1. Si/Sr, Fe/Sr, and Ti/Sr ratios imply different sources of terrigenous input than Ca/Sr ratios (Jackson et al., 2023), probably the GrIS in the study area (cf., Carlson and Winsor, 2012; and Weiser et al., 2021). Lower Si/Sr, Fe/Sr, and Ti/Sr ratios during HEs suggest less detrital input from the GrIS, i.e., the GrIS had not experienced significant retreat during these periods.

HE1 probably consisted of two phases (HE1.1 and HE1.2), as evidenced by the presence of two separated detrital carbonate peaks in sediments from North Atlantic regions (Hodell et al., 2017). However, Ca/Sr ratios from our site did not show distinct detrital peaks around HE1, suggesting that icebergs with high loading of detrital carbonate mainly influenced sedimentation in the Labrador Sea south of our core site. Nevertheless, increased IRD abundance implies

iceberg discharge into the eastern Labrador Sea during the early HE1 (HE1.1) probably from the GrIS or other regions of the LIS where bedrock is not rich in carbonate (Evans et al., 2007; Rashid et al., 2019). During the late HE1 (HE1.2), coarse fraction contents were low (Fig. 4.3h), while %$C_{37:4}$ values and dolomite contents were high (Figs. 4.3d, 4.7d) suggesting the occurrence of meltwater plumes from the LIS during this interval (for more discussion about plumes, see section 4.6.1.2 below).

Iceberg discharge during HEs has caused enhanced surface freshening in the subpolar regions. %$C_{37:4}$ values were used as a proxy for low-temperature and low-salinity conditions (i.e., meltwater discharge) (Bard et al., 2000; You et al., 2023). This interpretation was supported by the good negative correlation between %$C_{37:4}$ and δD_{PA} (see Method 3.3), suggesting that %$C_{37:4}$ values were mainly influenced by meltwater discharge rather than sea ice formation (Wang et al., 2021). Increased %$C_{37:4}$ values occurred during HEs corresponding to increased IRD deposition, indicating that iceberg discharge has contributed to surface freshening in the eastern Labrador Sea (Fig. 4.7d, f). As a result, surface freshening might contribute to sea ice formation due to low salinity (Fig. 4.9c). According to Müller et al. (2011), low concentrations of both IP$_{25}$ and dinosterol/brassicasterol may reflect permanent sea ice conditions. In our case, we interpret this signal to reflect a nearly permanent sea ice cover or highly oligotrophic conditions rather than permanent sea ice cover during HE5, HE4, and HE2 (Fig. 4.6), because almost all SSTs values were above 0 °C except during HE4 (Fig. 4.7c). However, marginal sea ice cover was prevalent during HE1, probably related to lower volumes of meltwater discharge compared to HE5, HE4, and HE2 (Fig. 4.7d) or increased insolation (Laskar et al., 2004). Furthermore, increased meltwater discharge might have caused abrupt decreases in SSTs and low open-water phytoplankton productivity (Fig. 4.5c-e), similar to what we inferred to during HE5, HE4, HE2, and HE1.2. Surprisingly, HE1.1 was not characterized by a distinct increase in meltwater discharge and decrease in SSTs despite increased IRD deposition/iceberg discharge (Fig. 4.7b, d, f). This signal was different from the records from the western Labrador Sea that showed decreased subsurface temperatures and increased detrital carbonate input during HE1.1 (Max et al., 2022) (Fig. 4.7g, h). The discrepancy between western and eastern records is still under discussion.

The changes in planktic/benthic foraminiferal assemblages during HEs further support variations in primary production. The decreased accumulation rates of total benthic and planktic foraminifera during HEs, and decreased accumulation rates and concentrations of *M. barleeanus* and *E. exigua* (species indicating high food supply conditions (Rasmussen et al., 2003; Rasmussen and Thomsen, 2017; Consolaro et al., 2018)) indicates a decline in primary production (Fig. 4.4a, e, f). Furthermore, concentrations of *C. wuellerstorfi* were increased during HE4, HE2, and HE1, reflecting low to moderate food supply (Murray John W., 2006; Rasmussen

and Thomsen, 2017), well-oxygenated bottom water condition, and strong convection (Consolaro et al., 2018; Seidenkrantz et al., 2021), which was comparable to the record from the northwestern Labrador Sea (Core 455G) (Fig. 4.4g, h). The decrease in %Fe^{2+} values from Core 455G further indicates enhanced oxidizing conditions in the Labrador Sea during HE1 (Seidenkrantz et al., 2021). Such a well-oxygenated bottom environment might have been caused by brine rejections due to sea ice formation (Keigwin and Swift, 2017).
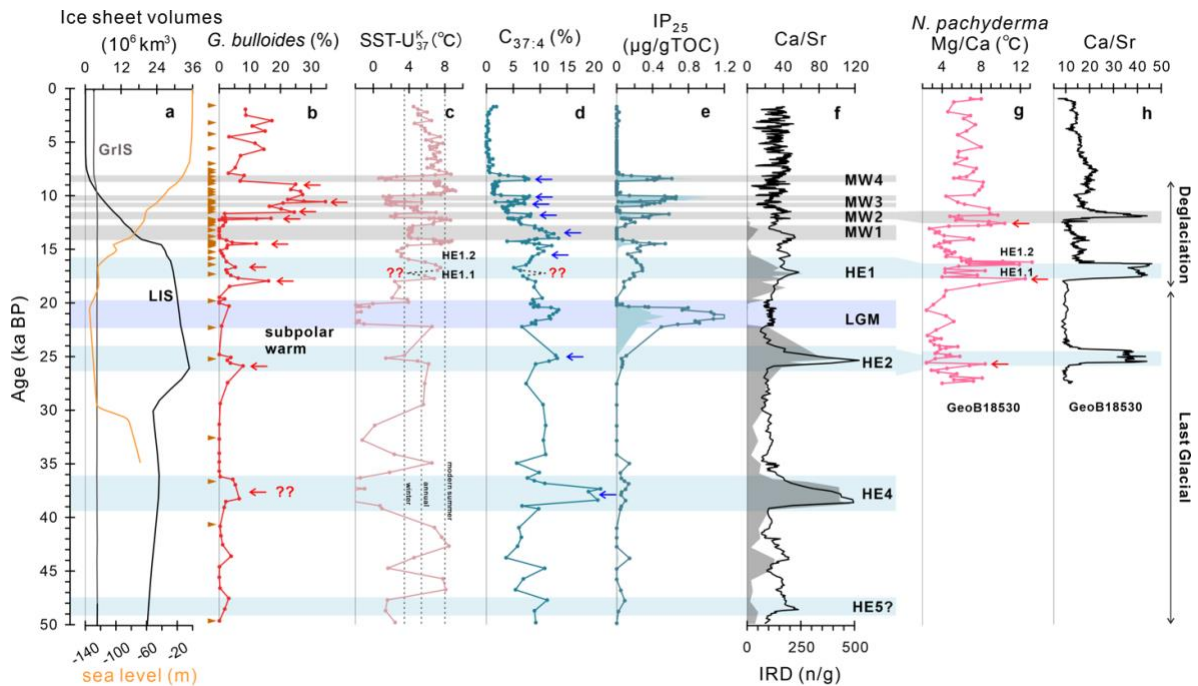
Fig. 4.7 Proxy records for changes in sea surface characteristics and detrital input (Core MSM12/2-05-01) and comparison with other records.
a Changes in the Laurentide Ice Sheet and Greenland Ice Sheet volumes (Peltier et al., 2015) and global sea level (Lambeck et al., 2014); (**b-f**) Proxy records from Core MSM12/2-05-01 (this study): **b** Percentages of *G. bulloides* as proxy for warm Irminger Current inflow, red arrows highlight spikes of abrupt increases in warm water inflow; **c** SST reconstruction based on U$^{K}_{37}$. HE1 is divided into two phases (HE1.1 and HE1.2); **d** %C$_{37:4}$ as proxy for meltwater discharge, blue arrows highlight significant increases in meltwater discharge; **e** Concentrations of IP$_{25}$ as proxy for seasonal sea ice cover; **f** Ca/Sr ratios as proxy for detrital carbonate input (line) and IRD abundance as proxy for iceberg discharge (shading); (**g and h**) Records from Core GeoB18530 (southern Labrador Sea) (Max et al., 2022); the age-depth model was re-established based on the Marine 20 calibration curve and Bacon program: **g** Subsurface temperature reconstruction based on Mg/Ca values of *N. pachyderma* (sin.), red arrows indicate abrupt increases in subsurface temperatures prior to the detrital input events; **h** Ca/Sr ratios. The question marks highlight the scenario during HE1.1 with reduced meltwater discharge (**d**) and no significant decreases in SSTs (**c**), which are different to what we expected (black dashed lines). Brown triangles mark available AMS^{14}C dates. Light blue, grey, and purple shadings highlight HEs, MWs, and LGM, respectively.

Meltwater Events 1-4

Four abrupt MWs have been identified during the last deglaciation, characterized by high-loading of fine-grained detrital input (in contrast to coarse detrital input during HEs), increased meltwater discharge, decreased SSTs, increased sea ice formation, and reduced open-water phytoplankton productivity (Figs. 4.3f-i, 4.5). Four MWs occurred at around 14.02-13.01 ka BP (MW1, Allerød period), 12.05-11.70 ka BP (MW2, late Younger Dryas (YD) correlating to H0 Event), 10.96-10.64 ka BP (MW3a), 10.49-9.98 ka BP (MW3b), and 8.55-8.13 ka BP (MW4), respectively (for more detailed description see You et al. (2023)). Increased fine-grained detrital deposition (Fig. 4.3f-i) along with increased meltwater discharge (Fig. 4.7d) suggests that sediment input by meltwater plumes rather than icebergs was predominant (Hesse et al., 1997; Knies and Stein, 1998; Leng et al., 2018; Rashid et al., 2019; You et al., 2023). The dominance of laminated silty clay/clayey silt deposits at our core location, i.e., a typical plumite deposition on Eirik Drift, further supports the occurrence of meltwater plumes during these MWs (see X-ray photography in Supplementary Fig. 3.3, Chapter 3.8). The occurrence of meltwater plumes might have been caused by the decay of ice sheets (Hesse et al., 1997; Lekens et al., 2005; Sachs et al., 2018; Keigwin et al., 2018), and the long-distance transportation of meltwater plumes might be attributed to strong katabatic winds (Hesse et al., 1997). The generation of fine-grained material in the plume was likely associated with the winnowing and resuspension of sediments from the base of ice sheets (cf., Knies and Stein, 1998; Leng et al., 2018). Thus, increased melting at the base of ice sheets due to the decline in ice sheet volume, the retreat of ice sheets landward, and the enhanced impact of warm water inflow might have contributed to the outburst of plumes (Fig. 4.9d, e). This may explain why the detrital input was mainly in the form of iceberg discharge during the last glacial period, whereas plumes occurred more during the last deglaciation due to more significant and much easier base melting. The absence of pronounced meltwater discharge during the last 8 ka might be attributed to the decreased Northern Hemisphere Ice Sheet volumes (Peltier et al., 2015), corresponding to the ice-free environment in the eastern Labrador Sea.

Increased Si/Sr, Fe/Sr, and Ti/Sr ratios with some dolomite input indicate that meltwater plumes came from the GrIS with contributions from the LIS (Fig. 4.3d, f, g). Increased Ti input during the last deglaciation from Core MD99-2227 supports our interpretation that meltwater discharge from the GrIS was enhanced during these MWs (Carlson and Winsor, 2012). In addition, increased dolomite contents from Core MSM12/2-07-2 on Eirik Drift (Sommerfeldt, 2012), along with the good correlation between detrital carbonate input on the Labrador Shelf (Core MD99-2236) (Jennings et al., 2015) and our Si/Sr, Fe/Sr, and Ti/Sr ratios, suggests that the LIS was also a major contributor to meltwater discharge to the eastern Labrador Sea.

Compared to the low level during the last glacial period, open-water phytoplankton productivity was increased since the last deglaciation as reflected in increased XRF-Sr (Supplementary Fig. 4.3), TOC contents (Fig. 4.5a), open-water phytoplankton biomarker

concentrations (Fig. 4.5 c-e), and accumulation rates of *M. barleeanus*, *E. exigua*, and *T. quinqueloba* (species indicating higher productivity (Rasmussen et al., 2008; Seidenkrantz et al., 2021)) (Fig. 4.4d, f). However, the increased open-water productivity trend was interrupted by MWs, corresponding to abrupt increases in meltwater discharge, sea ice formation, and decreases in SSTs (Fig. 4.7c, d, e). Low-temperature and low-salinity surface water, and limited light penetration due to sea ice cover might have limited the bloom of open-water phytoplankton (Wassmann et al., 2020). Furthermore, the significant differences in marine productivity between glacial and interglacial/deglacial conditions were likely influenced by the volumes of meltwater discharge from the surrounding ice sheets. As the size of the ice sheet gradually diminished and meltwater discharge reduced, the water-column stratification became weakened, leading to an increase in open-water productivity (Fig. 7a, d).
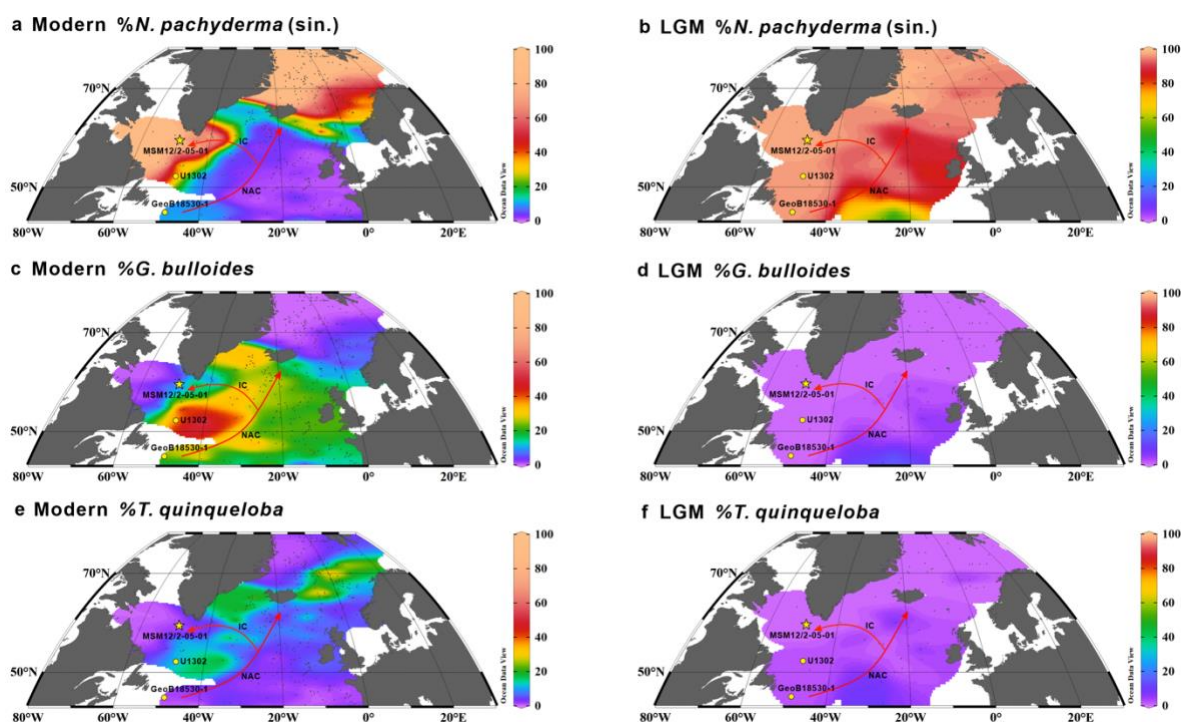
Fig. 4.8 Morden and LGM distribution of the dominant planktic foraminifera in the North Atlantic. (**a, b**) Distribution patterns of %*N. pachyderma* (sin.); (**c, d**) Distribution patterns of %*G. bulloides*; (**e, f**) Distribution patterns of %*T. quinqueloba*. Planktic foraminifer data from the MARGO dataset (Kucera et al., 2005). *N. pachyderma* (sin.) is the most dominant species in the study area in both the modern conditions and LGM, and concentrations of *G. bulloides* and *T. quinqueloba* are higher in the southern Labrador Sea during the modern environment, whereas no *G. bulloides* and *T. quinqueloba* were recorded during the LGM.

4.6.2 The causes of Heinrich Events and Meltwater Events in the Labrador Sea

Previous studies showed subsurface warming in the Labrador Sea and basin-wide warming in the North Atlantic preceding the occurrence of the HEs (Marcott et al., 2011; Max et al., 2022), probably related to the weakened AMOC (Max et al., 2022). However, the direct trigger for subsurface warming in the Labrador Sea is still under discussion. We propose that an enhanced Irminger Current inflow might have triggered/contributed to the (sub-)surface warming in the Labrador Sea, resulting in the occurrence of HEs and last deglacial MWs.

The planktic foraminifer *N. pachyderma* (sin.) is the characteristic species for Arctic and polar water, whereas *G. bulloides* and *T. quinqueloba* are abundant in warm subpolar water (cf., Consolaro et al., 2018). Based on the modern distribution of planktic species in the North Atlantic (Fig. 4.8a, c, e), cold water species *N. pachyderma* (sin.) is the dominant species in the Eirik Drift area, whereas concentrations of *G. bulloides* and *T. quinqueloba* are much higher in the south of our core site (e.g., southern Labrador Sea). Therefore, increased concentrations of warm subpolar species in the records suggest that the Eirik Drift region might have similar water mass characteristics (e.g., increased surface ocean temperatures) as the southern Labrador Sea. Such similar characteristics were probably caused by enhanced warm water inflow from the southern Labrador Sea (i.e., enhanced Irminger Current) (Fig. 4.9a). Several abrupt increases in concentrations of warm subpolar species (especially *G. bulloides*) occurred in our records, consistent with higher SST values but prior to increased meltwater discharge (i.e., HE2, HE1, and four MWs) (Fig. 4.7b, c, d). The close correlation between abrupt increases in %*G. bulloides* and SSTs further supports our argumentation that an enhanced Irminger Current caused or at least contributed to the surface warming in the Labrador Sea (Fig. 4.7b, c). Our interpretation is also supported by a study from the northwestern Labrador Sea (Core 455G), indicating that increased concentrations of subpolar species prior to HE1 and MW1 were attributed to enhanced Irminger Current inflow (Seidenkrantz et al., 2021). In addition, enhanced Irminger Current inflow/subsurface warming might have caused the collapse of the Hudson Bay Ice Saddle, accounting for the surface freshening in the Labrador Sea (Core MSM45-19-2) at around 8.5 ka BP (named as MW4 in our record) (Lochte et al., 2019). The similar temperature reconstructions from alkenones (surface) and Mg/Ca ratios of *N. pachyderma* (sin.) dwelling at 50 m in the Eirik Drift area (subsurface) imply that the whole upper ocean was warmer prior to HE2, HE1, and four MWs (You et al., 2023). The (sub-)surface ocean warming in the Labrador Sea might have accelerated the basal melting of the surrounding ice sheets and led to the collapse of the LIS and GrIS, resulting in massive iceberg/meltwater discharge into the Labrador Sea. Our finding is supported by subsurface temperature estimates from the southern Labrador Sea (Core GeoB18530), which demonstrates that warmer subsurface conditions preceded the distinct collapse of the LIS during HE2, HE1, and late YD (HE0) (Max et al., 2022) (Fig. 4.7g, h).

Here, we interpret our alkenone-based SST reconstruction as representing the surrounding environment (You et al., 2023) rather than signals from distant and warmer subpolar regions due to enhanced lateral advection of alkenones (Knutz et al., 2011). Despite temperature not being the only factor affecting alkenone concentrations (cf., Rosell-Mele,1998; Wang et al., 2021), U_{37}^{K} values show positive correlations with SSTs in high-latitude North Atlantic regions (Filippova et al., 2016). Furthermore, the SST reconstruction based on U_{37}^{K} might not exhibit significant warm bias and unrealistic SST values compared to those using $U_{37}^{K'}$ (without $C_{37:4}$) in subpolar regions (Filippova et al., 2016). Thus, warm SST bias during HE1 from the northwestern Labrador Sea (Core DA04-31P) might be related to temperature calibration excluding $C_{37:4}$. The similarity of temperature reconstruction based on alkenones and Mg/Ca ratios of *N. pachyderma* (sin.) (more likely to be in situ) further supports our argumentation. Therefore, two peaks of increased (sub-)surface temperatures during HE1 probably represent two warm episodes prior to HE1.1 and HE1.2 corresponding to the disintegration of the LIS (Fig. 4.7c) (Hodell et al., 2017; Max et al., 2022). Different to what we expected, iceberg discharge during HE1.1 has not caused a distinct increase in meltwater discharge and decline in SSTs based on our biomarker records, whereas significantly increased meltwater input and decreased SSTs were found during HE1.2 (Fig. 4.7c, e). This SST "anomaly" during HE1.1 might be related to sample resolution but is still under discussion.

Enhanced Irminger Current inflow prior to the HEs and MWs might be related to weakened AMOC. Modelled current patterns during the early YD and HE4 suggest that weakened AMOC might have caused enhanced Atlantic Water inflow into the Labrador Sea (Rainsley et al., 2018; Menviel et al., 2020) due to changes in density gradients (Rainsley et al., 2018; Fried and Jong, 2022). Furthermore, proxy records from the northeastern Atlantic and Labrador Sea indicate that the decline in AMOC happened before the HEs, i.e., massive iceberg/meltwater discharge from the LIS was not the trigger but a major contributor to pronounced decreases in AMOC/cold episodes in the Northern Hemisphere (Barker et al., 2015; Max et al., 2022). The initial decline in AMOC before detrital input/meltwater discharge might be associated with surface freshening in the Nordic Seas where deep-water convection happened (Hodell et al., 2017). For instance, the collapse of the Eurasian Ice Sheet during the Bølling warming period (Brendryen et al., 2020) and freshwater input from the Arctic Ocean during the early YD (Wu et al., 2020) may have caused the decline in AMOC prior to MW1 (Allerød period) and MW2 (late YD), respectively. Thus, weakened AMOC might have caused enhanced Irminger Current inflow and increased (sub-)surface temperatures in the Labrador Sea, leading to the disintegration of the surrounding ice sheets. The same mechanism may be applied to other HEs and MWs (Fig. 4.9).
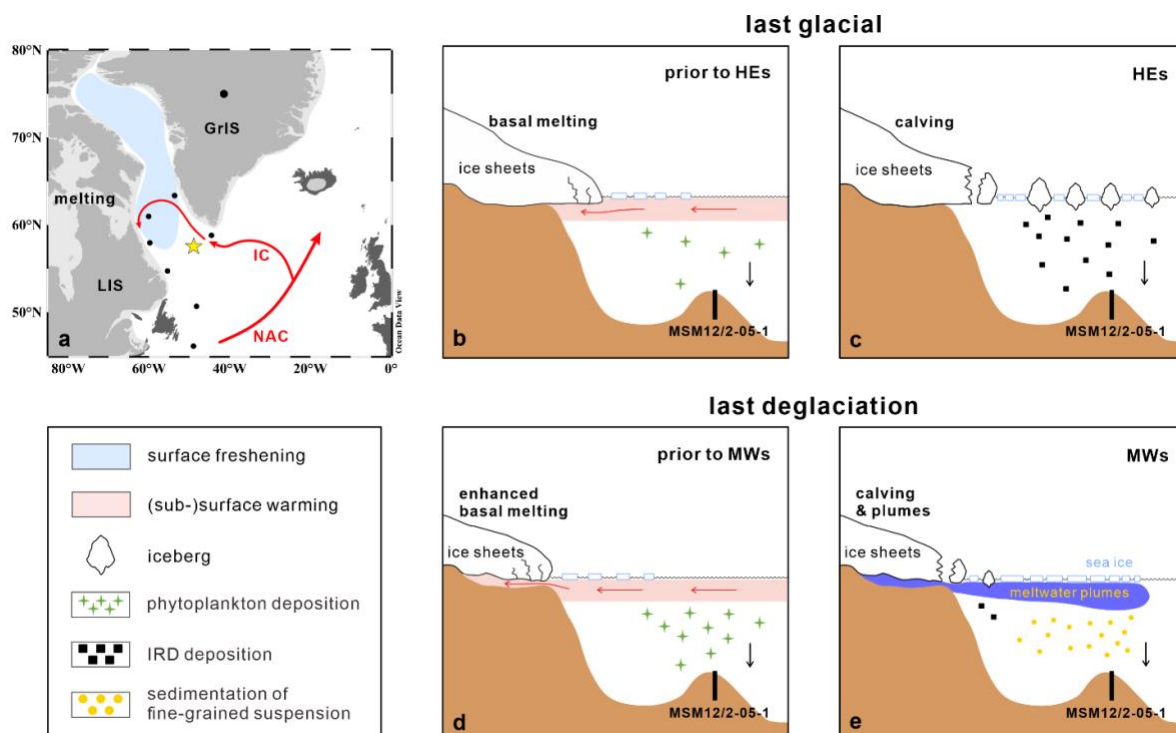
Fig. 4.9 Schematic illustration for processes of detrital input during the last glacial/deglaciation.
a Enhanced warm North Atlantic Current (NAC) and Irminger Current (IC) inflow into the Labrador Sea prior to the detrital events, the location of Core MSM12/2-05-01 (this study) is shown by the yellow star, and other cores referred to are indicated by black dots; **b** (Sub-)surface warming in the Labrador Sea during the last glacial caused by warm water inflow, leading to the basal melting of the surrounding ice sheets, increased phytoplankton productivity due to lower meltwater discharge; **c** The collapse of ice sheets/iceberg discharge during HEs resulting in increased IRD deposition, meltwater discharge, and sea ice formation; **d** (Sub-)surface warming in the Labrador Sea during the last deglaciation caused by warm water inflow, leading to enhanced basal melting of the surrounding ice sheets, increased phytoplankton productivity due to lower meltwater discharge; **e** Meltwater plumes injection during MWs with increased meltwater discharge, sea ice formation, and sedimentation of fine-grained suspension.

4.6.3 A special "Event": Polynya conditions during the LGM

The highest concentrations of IP_{25} were found during the LGM, indicating the highest production of seasonal sea ice algae (Fig. 4.7e). According to the scatter plot (IP_{25} versus dinosterol), marginal to extended sea ice conditions were predominant during this time interval (Fig. 4.6). However, increased open-water phytoplankton biomarkers indicate increased open-water productivity during the LGM (Fig. 4.5c, d, e) despite increased sea ice formation and low SSTs (Fig. 4.7c, e). These contemporaneous increases in sea ice cover and open-water productivity might be explained by the presence of an offshore polynya due to enhanced katabatic winds from the expanded GrIS (cf., Harning et al., 2023; Syring et al., 2020; Stein et al., 2017). Such offshore polynya condition in the southern/southwestern Greenland area was also supported by modelling reconstruction (Stärz et al., 2012).

Increased sea ice formation during the LGM might have been triggered by increased meltwater discharge, characterized by high-loading of fine-grained detrital input (Fig. 4.3f-i), suggesting that meltwater plumes probably also occurred during the LGM. Different to meltwater plumes that occurred during MWs, the meltwater plume during the LGM happened when the ice sheets expanded to their largest extents (Clark et al., 2009; Margold et al., 2018). Thus, increased meltwater discharge and terrigenous material input most likely indicate the disintegration/instability following the GrIS expansion rather than the decay of the ice sheet. Furthermore, enhanced katabatic winds from the expanded GrIS might have caused open water conditions that promoted the production of open-water phytoplankton. However, the absolute abundances of total planktic and benthic foraminifera were very low during the LGM despite increased open-water productivity (Fig. 4.4a, e), possibly reflecting strong carbonate dissolution due to brine rejection. Additionally, the absence of *G. bulloides* and *T. quinqueloba* suggests weak Irminger Current inflow during the LGM, whereas *N. pachyderma* (sin.) was the dominant species indicating cold surface conditions, consistent with SST reconstruction (Fig. 4.8b, d, f).

4.7 Conclusions

Continuous biomarker and foraminifer records from the eastern Labrador Sea, spanning the last 50 ka, allowed to reconstruct the history of changes in sea surface characteristics in sensitive subpolar regions. The XRF and coarse fraction records were used to infer information about the decay of the surrounding ice sheets. Furthermore, comparison between biogenic and terrigenous proxy records from the same sediment core allowed a detailed study of interactions between ice sheet dynamics and sea surface characteristics. Our study provided new important insight into processes involved in these interactions: enhanced warm Irminger Current inflow might have caused (sub-)surface warming in the Labrador Sea, followed by the disintegration/retreat of the surrounding LIS and GrIS. The patterns of meltwater discharge were distinct during different phases, possibly because of differential ice sheet volumes and extents. The release of meltwater and detrital materials were primarily caused by iceberg discharge during HEs (the last glacial), whereas it was dominated by meltwater plumes during MWs (the last deglaciation). No matter the pattern, increased meltwater discharge has resulted in increased sea ice formation, decreased SSTs, and reduced open-water productivity. In contrast to weakened ocean ventilation/AMOC in the northeastern Atlantic during HEs, the ventilation was enhanced in the Labrador Sea, indicating that the Labrador Sea may have been one of the major locations of North Atlantic Deep Water formation during HEs. Additionally, our study provided proxy evidence that an offshore polynya probably occurred south of Greenland during the LGM, supporting previous modelling results. Considering the contribution of enhanced warm water inflow/warmer (sub-)surface water temperatures to ice sheet instability, changes in sea surface characteristics and current behaviour

in the adjacent areas of the GrIS and Antarctic Ice Sheet should be given special attention, particularly in the context of a sustained warming climate.

Acknowledgements

Author contributions

Defang You: Conceptualization, Methodology, Formal analysis, Investigation, Visualization, Writing – original draft, Writing – review & editing. **Ruediger Stein**: Conceptualization, Methodology, Resources, Investigation, Visualization, Writing – review & editing, Supervision, Project administration, Funding acquisition. **Kirsten Fahl**: Methodology, Resources, Writing – review & editing. **Audrey Limoges**: Visualization, Resources, Writing – review & editing. **Enno Schefuß**: Methodology, Resources, Writing – review & editing.

4.8 Supplementary Information

This subchapter includes:

Supplementary Fig. 4.1: Age model of Core MSM12/2-05-01.

Supplementary Fig. 4.2: Comparison of proxy records from Core MSM12/2-05-01 based on Marine 20 and Marine 13 calibration curve.

Supplementary Fig. 4.3: Changes in primary production during the last 50 ka from Core MSM12/2-05-01.

Supplementary Table 4.1: AMS ^{14}C dates of Core MSM12/2-05-01
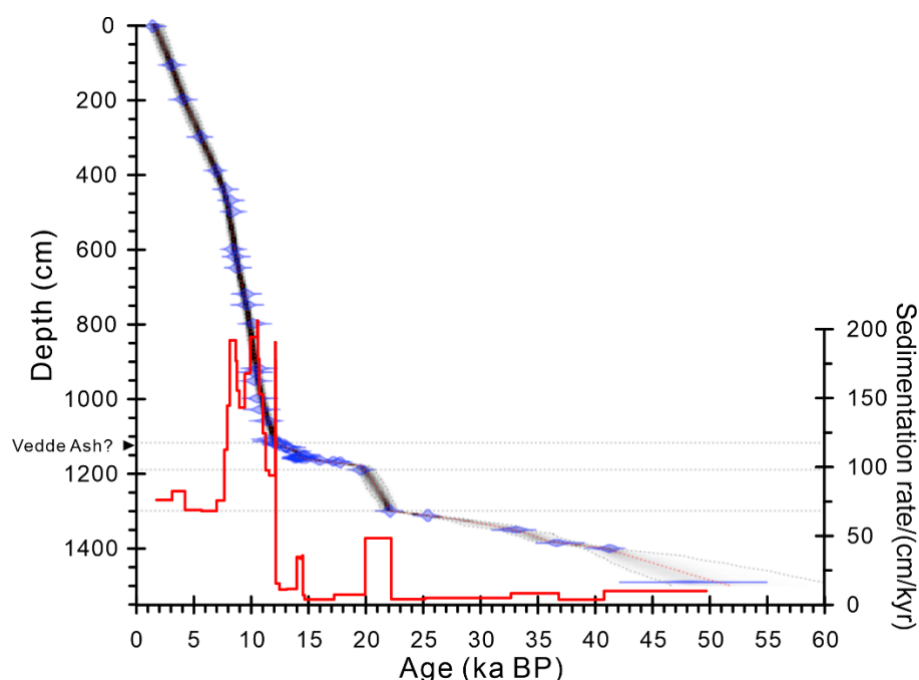
Supplementary Fig. 4.1 Age model of Core MSM12/2-05-01.
Bayesian age-depth model was established based on 44 radiocarbon dates using the Bacon program (Blaauw and Christen, 2011). The horizontal dashed lines indicate sediment depths where sedimentation rates significantly change. Grey stippled lines indicate 95% confidence intervals of calibration age. The red line shows linear sedimentation rates (LSR) based on the calibrated age control points. The black triangles mark the depth of a prominent tephra layer that probably represents the Vedde Ash layer (Abbott and Davies, 2012); for more details see You et al. (2023).
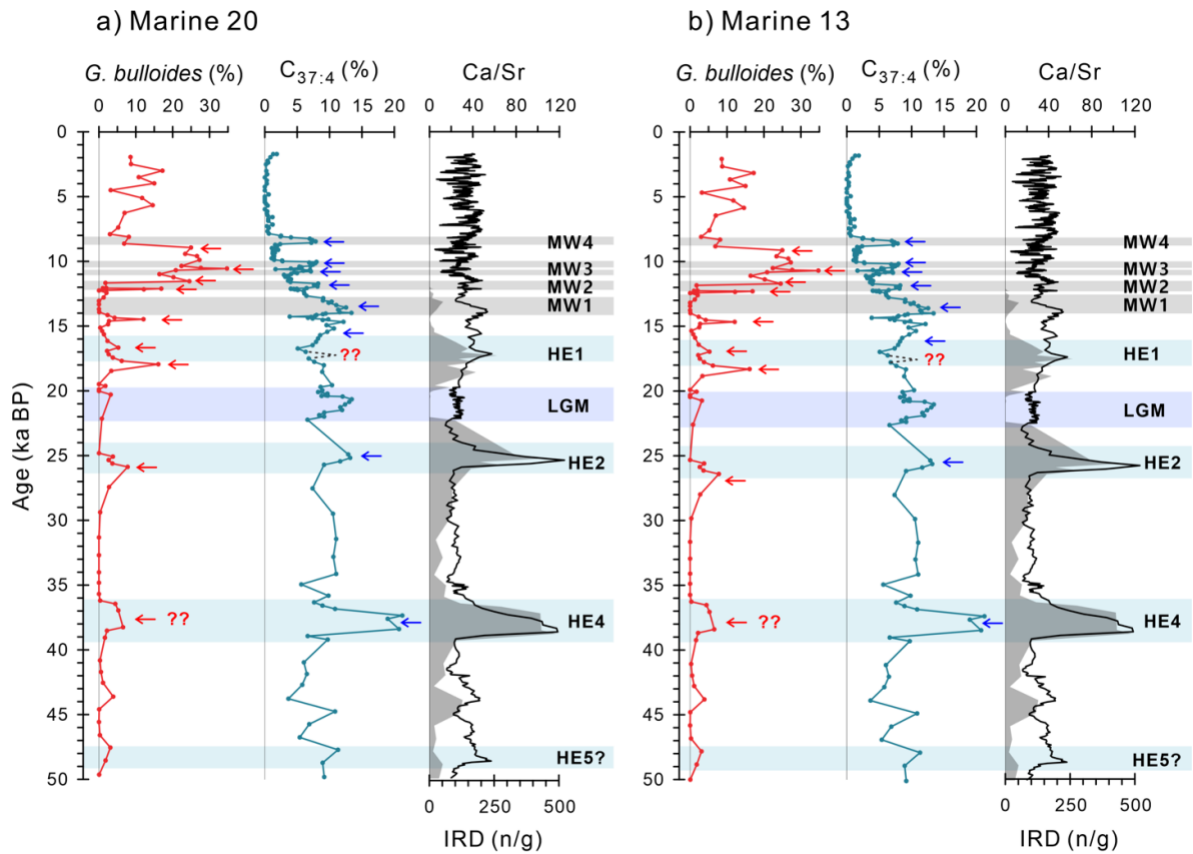
Supplementary Fig. 4.2 Comparison of proxy records from Core MSM12/2-05-01 based on Marine 20 and Marine 13 calibration curve.

a Proxy records based on Marine 20 calibration curve: percentages of *G. bulloides* as proxy for warm Irminger Current inflow, red arrows highlight spikes of abrupt increases in warm water inflow; %$C_{37:4}$ as proxy for meltwater discharge, blue arrows highlight significant increases in meltwater discharge; Ca/Sr ratios as proxy for detrital carbonate input (line) and IRD abundance as proxy for iceberg discharge (shading); **b** Proxy records based on Marine 20 calibration curve. The calibrated ages based on the Marine 13 calibration curve are around 200 years older than those calculated from the Marine 20 calibration curve.
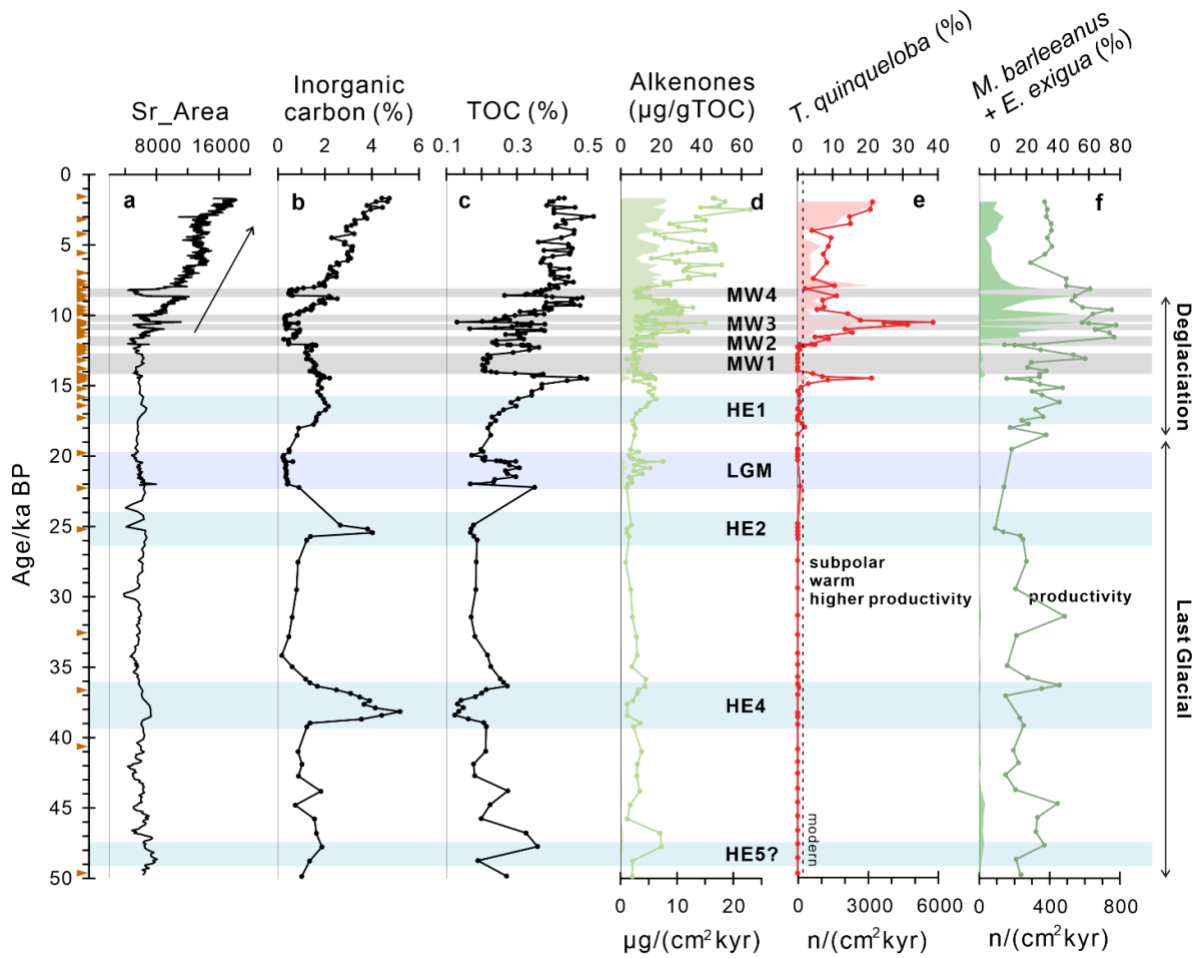
Supplementary Fig. 4.3 Changes in primary production during the last 50 ka from Core MSM12/2-05-01.

a XRF-Sr, black arrow indicating an increasing tendency of primary production since the last deglaciation; **b** Percentages of inorganic carbon; **c** Percentages of total organic carbon (TOC); **d** Concentrations (line) and accumulation rates (shading) of alkenones; **f** Percentages and accumulation rates of *T. quinqueloba*; **g** Percentages and accumulation rates of *M. barleeanus* and *E. exigua*. Brown triangles mark available AMS[14]C dates. Light blue, grey, and purple shadings highlight HEs, MWs, and LGM, respectively.

Supplementary Table 4.1 AMS ^{14}C dates of Core MSM12/2-05-01.

Lab ID	Depth (cm)	Species	AMS ^{14}C age (yr.)	$\triangle$R	Calib. age median (yr. BP)	Model age median (yr. BP)	Reference
SUERC-45889*	4.75	*N. pachyderma*	2082±35	0±200	1504	1745	You et al., 2023
SUERC-47577	108.5	*N. pachyderma*	3450±38	0±200	3148	3109	You et al., 2023
SUERC-45890	200.5	*N. pachyderma*	4227±37	0±200	4131	4225	You et al., 2023
SUERC-47579	300.5	*N. pachyderma*	5473±39	0±200	5660	5678	You et al., 2023
SUERC-47579	390.5	*N. pachyderma*	6737±37	0±200	7027	6999	You et al., 2023
AWI-6946.1.1**	440.5	*N. pachyderma*	7520±85	0±200	7806	7659	You et al., 2023
AWI-6947.1.1	470.5	*N. pachyderma*	7933±86	0±200	8231	7925	You et al., 2023
AWI-6948.1.1	500.5	*N. pachyderma*	8115±84	0±200	8445	8133	You et al., 2023
AWI-6949.1.1	600.5	*N. pachyderma*	8134±84	0±200	8468	8654	You et al., 2023
AWI-6950.1.1	620.5	*N. pachyderma*	8298±83	0±200	8666	8767	You et al., 2023
SUERC-45891	650.5	*N. pachyderma*	8449±38	0±200	8842	8960	You et al., 2023
SUERC-47582	720.5	*N. pachyderma*	9049±40	0±200	9609	9449	You et al., 2023
AWI-5788.1.1	749.5	*N. pachyderma*	9096±122	0±200	9671	9622	You et al., 2023
AWI-5789.1.1	799.5	*N. pachyderma*	9585±117	0±200	10305	9920	You et al., 2023
AWI-5793.1.1	919.5	*N. pachyderma*	9831±127	0±200	10644	10538	You et al., 2023
AWI-5794.1.1	929.5	*N. pachyderma*	9606±120	0±200	10335	10586	You et al., 2023
AWI-5795.1.1	952.5	*N. pachyderma*	9641±119	0±200	10384	10715	You et al., 2023
AWI-5798.1.1	999.5	*N. pachyderma*	9860±119	0±200	10683	11023	You et al., 2023
AWI-5799.1.1	1029.5	*N. pachyderma*	10029±125	0±200	10903	11264	You et al., 2023
AWI-5800.1.1	1059.5	*N. pachyderma*	10428±128	0±200	11492	11571	You et al., 2023
AWI-5803.1.1	1108.5	*N. pachyderma*	10543±129	0±200	11653	12093	You et al., 2023
AWI-6484.1.1	1114.5	*N. pachyderma*	10621±100	0±200	11764	12124	You et al., 2023
AWI-6485.1.1	1118.5	*N. pachyderma*	11130±101	0±200	12430	12147	You et al., 2023
AWI-6486.1.1	1123.5	*N. pachyderma*	11141±94	0±200	12445	12469	You et al., 2023
AWI-6487.1.1	1127.5	*N. pachyderma*	11752±95	0±200	13080	12829	You et al., 2023
AWI-5952.1.1	1130.5	*N. pachyderma*	11854±131	0±200	13186	13097	You et al., 2023
SUERC-47583	1140.5	*N. pachyderma*	12379±43	0±200	13777	13965	You et al., 2023
SUERC-51888	1150.5	*N. pachyderma*	12975±44	0±200	14650	14253	You et al., 2023
AWI-6488.1.1	1153.5	*N. pachyderma*	12942±102	0±200	14601	14342	You et al., 2023
AWI-6489.1.1	1155.5	*N. pachyderma*	12671±102	0±200	14212	14401	You et al., 2023
AWI-6490.1.1	1157.5	*N. pachyderma*	12518±106	0±200	13978	14459	You et al., 2023
AWI-6491.1.1	1159.5	*N. pachyderma*	12721±106	0±200	14288	14515	You et al., 2023
AWI-5954.1.1	1160.5	*N. pachyderma*	12544±120	0±200	14020	14656	You et al., 2023
AWI-6492.1.1	1162.5	*N. pachyderma*	12972±105	0±200	14643	15169	You et al., 2023
AWI-5955.1.1	1165.5	*N. pachyderma*	13965±135	0±200	16035	15943	You et al., 2023
AWI-5956.1.1	1167.5	*N. pachyderma*	14937±147	0±200	17265	16458	You et al., 2023
SUERC-47584	1170.5	*N. pachyderma*	15386±51	0±200	17797	17232	You et al., 2023
SUERC-51887	1190.5	*N. pachyderma*	17007±57	0±200	19631	19943	You et al., 2023
SUERC-47585	1300.5	*N. pachyderma*	19096±67	0±200	22171	22219	This study
SUERC-51889	1312.5	*N. pachyderma*	22063±90	0±200	25445	25163	This study
SUERC-45892	1350.5	*N. pachyderma*	29502±316	0±200	33064	32659	This study
SUERC-51890	1385.5	*N. pachyderma*	33049±305	0±200	36739	36828	This study
SUERC-47586	1400.5	*N. pachyderma*	37491±521	0±200	41254	40775	This study
SUERC-47587	1490.5	*N. pachyderma*	46458±1576	0±200	48401	49695	This study

* AMS ^{14}C dates have been carried out at the NERC Radiocarbon Laboratory at SUERC (Scottish Universities Environment Research Centre, the University of Glasgow). They were recalculated from the unpublished data of the PhD dissertation of Williams (Williams, 2015). ** AMS ^{14}C dates were measured at the Alfred Wegener Institute, Bremerhaven.

A global mean reservoir age (R=405 years) was used for calibration to keep consistency with most of studies in the open North Atlantic regions (e.g., Ng et al., 2018; Zhao et al., 2019), and a $\triangle$R of 0 ± 200 years was applied to account for the reservoir age variations, which is in line with other studies in the North Atlantic (cf., Toucanne et al., 2015; Oppo et al., 2015). The Marine 20 calibration curve was used to calibrated all AMS ^{14}C dates (Heaton et al., 2020). The model ages were calculated by Bacon Program (Blaauw and Christen, 2011).

5 Deglacial sea surface characteristics in the Labrador Sea-Baffin Bay and implication for abrupt transition during the mid-Younger Dryas

Defang You[1, *], Ruediger Stein[1,2,3], Kirsten Fahl[1], Rebecca Jackson[4]

[1]Alfred Wegener Institute Helmholtz Centre for Polar and Marine Research, Am Alten Hafen 26, Bremerhaven 27568, Germany

[2]Faculty of Geosciences and MARUM-Center for Marine Environmental Sciences, University of Bremen, Bremen 28359, Germany

[3]Frontiers Science Center for Deep Ocean Multispheres and Earth System, Key Laboratory of Marine Chemistry Theory and Technology, Ocean University of China, Qingdao 266100, China

[4]Globe Institute, Copenhagen University, Øster Voldgade 5 – 7, Copenhagen 1350, Denmark

*Corresponding author: defang.you@awi.de

5.1 Abstract

Variations in sea surface conditions in Baffin Bay and the Labrador Sea play an essential role in deglacial climate changes due to their impact on the stability of the Greenland and Laurentide Ice Sheet, whose retreat would induce meltwater discharge into the subpolar regions, subsequently disrupting the climate. The biomarker-based reconstruction exhibited six significant sea ice retreats in southeastern Baffin Bay and one prominent retreat in southwestern Baffin Bay, spanning the last 16-10 ka, which suggests strong Atlantic Water incursions. One of the abrupt transitions happened in Baffin Bay and also the Labrador Sea during the middle Younger Dryas (YD), coinciding with a slight recovery of the Atlantic Meridional Overturning Circulation (AMOC) but prior to the onset of Heinrich Event 0 (HE0). Enhanced Atlantic Water inflow might have triggered the occurrence of HE0, probably contributing to the second decline in the AMOC during the late YD, thereby the persistence of a cold episode of YD. These findings highlight the significance of oceanic processes in shaping deglacial climate changes and the complex interplay between sea ice, ice sheets, and ocean circulation in the polar/subpolar regions.

5.2 Introduction

Sea ice plays a critical role in the polar system and is highly responsive to changes in various factors such as atmospheric circulation, incoming radiation, atmospheric and oceanic heat transfer, and the hydrological cycle (Curry et al., 1995; Rudels et al., 1996; Thomas and Dieckmann, 2008). Over the past few decades, the loss of summer Arctic sea ice has accelerated, leading to increased solar radiation penetration into the polar regions and giving rise to a phenomenon known as Arctic Amplification (Serreze and Barry, 2011; Shukla et al., 2019). Climate model projections indicate that more warm Atlantic Water is expected to continue expanding into the Arctic Basin in a warming climate, further amplifying Arctic warming (i.e., Arctic Atlantification) (Shu et al., 2021). Furthermore, in the context of global warming, meltwater and iceberg discharge from the Greenland Ice Sheet (GrIS) has also increased due to the decay of ocean-terminating glaciers especially in the western GrIS, which is closely related to warm Atlantic Water inflow (cf., Yang et al., 2016; Wood et al., 2021; Choi et al., 2021; Box et al., 2022). The intensified meltwater discharge into the polar/subpolar regions from melted Arctic sea ice and the GrIS may have caused salinity anomaly in the Nordic Seas and Labrador Sea, leading to perturbations in deep-water formations and ocean circulation in recent years (Rahmstorf et al., 2015; Böning et al., 2016).

To enhance our understanding of the interactions between sea ice retreat or loss, ice sheet decay and ocean forcing, it is essential to investigate their interactions in the past within paleoclimate timescales. The western Greenland marginal seas, such as Baffin Bay and the Labrador Sea, are sensitive regions for climatical variations. Baffin Bay is connected to the Labrador Sea through the Davis Strait and to the Arctic Ocean through the Nares Strait, where warm Atlantic Water meets cold Arctic/Greenland-sourced water (Fig. 5.1). Changes in water masses in Baffin Bay have a direct impact on sea ice distribution and ice sheet activity (Oksman et al., 2017; Jennings et al., 2017; Wood et al., 2021). Baffin Bay is covered by sea ice in winter, with its maximum coverage typically occurring in March (Fig. 5.1). Despite some drift ice remaining in the central and western Baffin Bay, the eastern region experiences ice-free conditions during summer, primarily influenced by surface circulation patterns (Wang et al., 1994; Tang et al., 2004). Therefore, distinctive sea ice patterns make Baffin Bay an ideal location for investigating the correlations between ocean forcing and variations in sea ice and ice sheet activity.

The surface circulation in Baffin Bay is dominated by the advection of warm Atlantic water and cold polar water from the Arctic Ocean (Cuny et al., 2005). The relatively warm and saline West Greenland Current (WGC) flows northward along the Greenland coast, which is derived from both the warm and saline Irminger Current (IC) and the cold and fresh East Greenland Current (EGC) in the Labrador Sea. The convergence of the WGC with polar water from the Nares Strait forms the Baffin Current (BC), which then flows southward along the Baffin Island

and mixes with Atlantic Water, forming the Labrador Current (LC) (Fig. 5.1; Tang et al., 2004). In terms of the vertical distribution of temperature and salinity, three different water masses can be identified: Arctic/polar Water in the upper 300m, West Greenland Intermediate Water (i.e., Atlantic Water) between 300 and 800 m, and Deep Baffin Bay Water below 1200 m (Supplementary Fig. 5.1; Tang et al., 2004).

Abrupt climate changes occurred in the polar/subpolar North Atlantic during the last deglaciation characterized by pronounced variations in meltwater discharge, ocean circulation/ventilation patterns, atmospheric temperatures, etc. (McManus et al., 2004; Svensson et al., 2008; You et al., 2023). The activities of the Laurentide Ice Sheet (LIS) and GrIS surrounding the Labrador Sea and Baffin Bay have been proposed to be closely linked with these abrupt changes (cf., Hemming, 2004; Jennings et al., 2015; You et al., 2023). Moreover, these activities exhibited a strong correlation with ocean forcings/(sub-)surface warming in these regions (Oksman et al., 2017; Jennings et al., 2017; Lochte et al., 2019; Max et al., 2022). To reconstruct sea ice distribution, IP_{25} (a direct proxy for sea ice algae productivity) has been used in many studies around Baffin Bay and the Labrador Sea (e.g., Jennings et al., 2017; Kolling et al., 2020; Saini et al., 2022; You et al., 2023; Kolling et al., 2023). However, sea ice records based on IP_{25} during the last deglaciation in Baffin Bay are scarce, which may limit our insights into sea ice variation in this sensitive region and its role in deglacial abrupt climate changes.

Here, we investigated two sediment cores from southern Baffin Bay, representing the interval from the last deglaciation to early Holocene, i.e., the last 16.8 to 10 ka. Core SL170 is located in southeastern Baffin Bay with relatively high temporal-resolution, whereas Core SL174 is situated off the shelf of Baffin Island in the west of the bay. Multiple biomarker proxies were used to reconstruct changes in sea ice cover and open-water productivity during this time interval (i.e., IP_{25} and P_DIP_{25} for sea ice cover, specific sterols and HBI-III (Z) for open-water phytoplankton productivity, for details see Methods). Together with planktic foraminifera data from the Labrador Sea, specific benthic foraminifera records from Core SL170 were used to indicate warm Atlantic Water incursions. Overall, six abrupt decreases in sea ice cover were identified in southeastern Baffin Bay and one prominent sea ice retreat was observed in southwestern Baffin Bay. The significant sea ice retreat in both sides of the bay around 14.4 ka BP might have triggered/accelerated the following decay of the GrIS and LIS. Furthermore, another abrupt transition happened in both Baffin Bay and the Labrador Sea during the mid-Younger Dryas (mid-YD), coinciding with enhanced Atlantic Water inflow and a slight recovery of the Atlantic Meridional Overturning Circulation (AMOC), which might have triggered the occurrence of Henrich Event 0 (HE0).
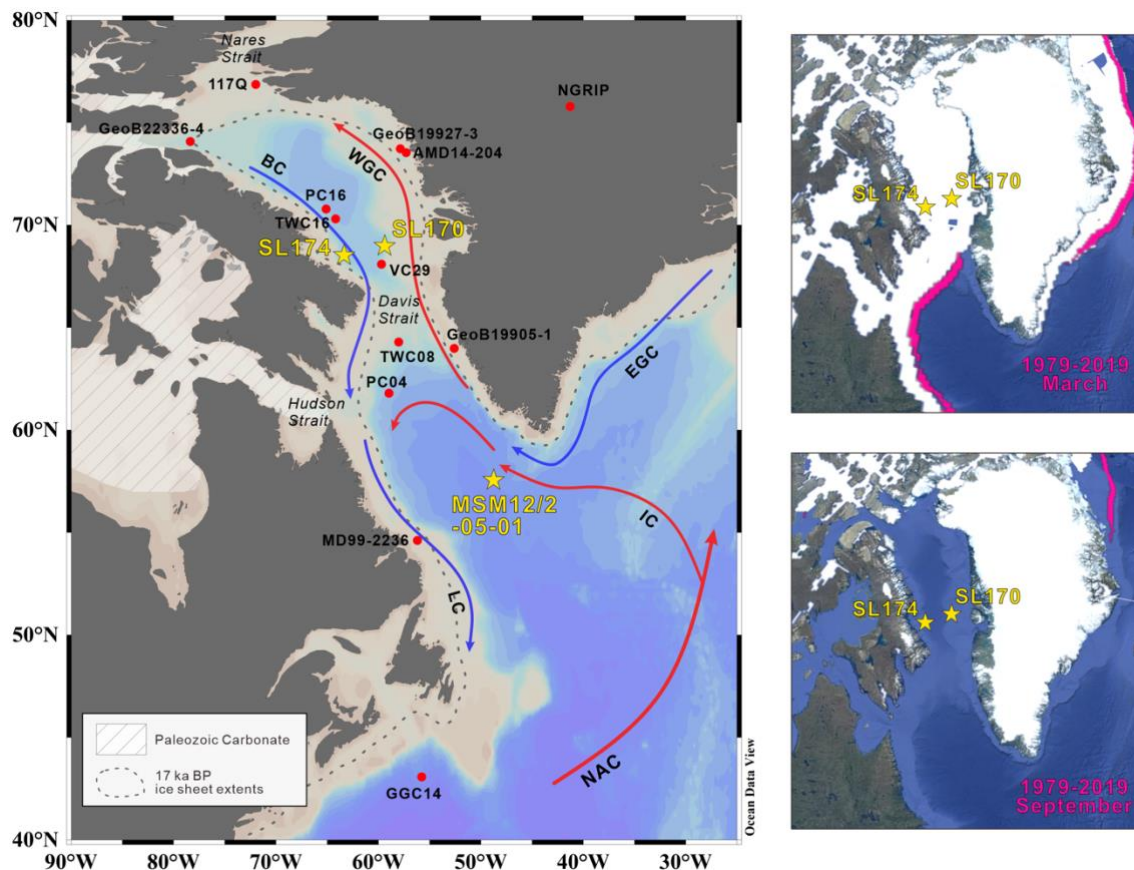
Fig. 5.1 Overview of Core locations, ocean circulation pattern, bedrock carbonate distribution, and modern sea ice distribution in Baffin Bay.

The left map shows core sites, modern ocean circulation patterns, and bedrock carbonate distribution. The location of Cores SL170, SL174, and MSM12/2-05-01 (this study) are shown by the yellow stars, and red dots indicate other cores referred to. Red arrows: warm surface current; blue arrows: cold surface current. NAC North Atlantic Current, IC Irminger Current, WGC Western Greenland Current, EGC Eastern Greenland Current, BC Baffin Current, LC Labrador Current. Grey stippled lines show ice sheet extents around 17 ka BP (Margold et al., 2018). Light grey with diagonal shading indicates simplified bedrock carbonate based on Simon et al. (2014). The right maps show modern sea ice distribution in the study area in 2021 March/September and the average sea ice extent of 1979–2019 March/September (image modified from Google Earth, data source: *https://nsidc.org/*).

5.3 Results

Only new biomarker results from Core SL170 and Core SL174 have been described in this section. The biomarker results of Core MSM12/2-05-01 from the Labrador Sea refer to You et al. (2023). The benthic foraminiferal data from Core SL170 refers to Jackson (2017).

5.3.1 Chronology and sedimentation rates

The 683 cm long sediment core SL170 (MSM09/02-0455/13, 68°58.15′ N, 59°23.58′ W) and the 777.5 cm long sediment core SL174 (MSM09/ 02-0467/3, 68°31.88′ N, 63°19.82′ W) were

retrieved from southern Baffin Bay during the *Maria S. Merian* cruise MSM09/02 (Kucera et al., 2014) (Fig. 5.1). The water depths at Core SL170 and Core SL174 is 1078 m and 1559 m, respectively. The age controls of these two cores were established based on Accelerator Mass Spectrometry (AMS) ^{14}C dates of foraminifera (Jackson et al., 2017). Local reservoir age ($\triangle$ R=140±35) and the Marine 20 calibration curve were used to recalculate the AMS ^{14}C dates (Supplementary Table 5.1, 5.2). The final age-depth models were established by the Bacon program (Blaauw and Christen, 2011) (Supplementary Fig. 5.2). In this study, we focus on the interval from the last deglaciation to the early Holocene, which is well dated in both cores (i.e., 0-677 cm of Core SL170; 95-296 cm of Core SL174). The time span covered is around 16.8 to 10 ka BP. The mean sedimentation rate of Core SL170 is 100 cm/kyr, and the highest sedimentation rates are ~130 cm/kyr between 13.1-11.7 ka BP. The mean sedimentation rate of Core SL174 is 28 cm/kyr, and the highest sedimentation rates are ~55 cm/kyr between 12.8-11.8 ka BP. The sedimentation rates of both cores began to increase around 14.2 ka BP.

5.3.2 Biomarkers of Core SL170

The concentrations of sea ice algae biomarker-IP_{25} were low during Heinrich Stadial 1 (HS1) with slight increases around 15.3 ka BP (Fig. 5.2b). At the onset of the Bølling/Allerød (B/A) period (~14.7 ka BP), the concentrations of IP_{25} showed abrupt increases, and its contents remained relatively higher until the early Holocene (~10.6 ka BP) with the highest values at the onset of the Holocene. During the mid-YD, significant decreases in IP_{25} contents were observed. Concentrations of open-water phytoplankton biomarkers, i.e., dinosterol, brassicasterol, and HBI-III (Z), were also low during HS1 with slight increases around 15.3 and 14.7 ka BP (Fig. 5.2c-e). Despite showing alternated increases and decreases, concentrations of open-water phytoplankton biomarkers were relatively higher during B/A to the early Holocene. The highest values appeared during the Bølling warm period (~14.2 ka BP), corresponding to higher TOC contents. However, the HBI-III (Z) concentrations were much lower than those of dinosterol and brassicasterol. Notably, HBI-III (Z) contents significantly decreased during the mid-YD, similar to changes in IP_{25}. The P_DIP_{25} values were set to "1" during most HS1 due to very low concentrations of both IP_{25} and open-water phytoplankton biomarkers (see Section 5.3.1 for more details). P_DIP_{25} values remained around 0.5 during B/A to the early Holocene. Six significant decreases in P_DIP_{25} values happened around 15.4 ka BP, 14.9 ka BP, 14.4 ka BP, 12.2 ka BP, 11.2 ka BP, and 10.6 ka BP (Fig. 5.2f).
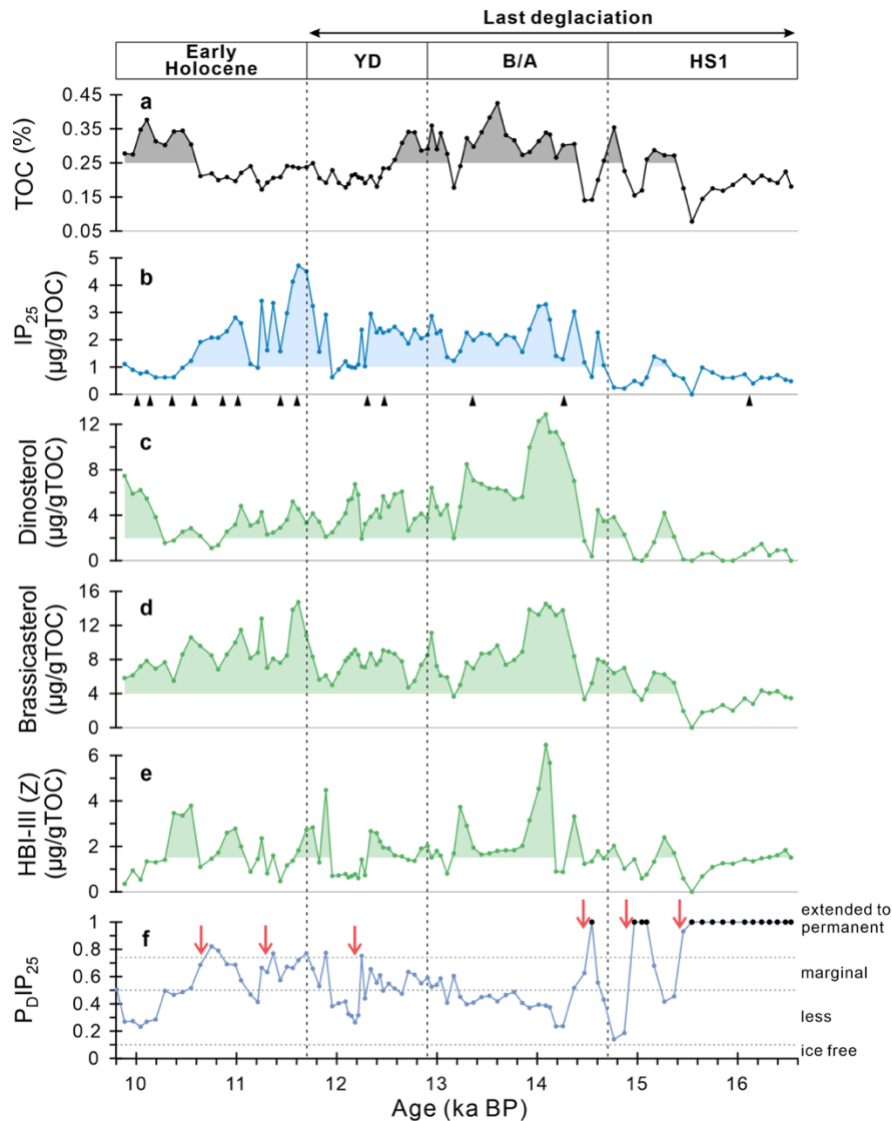
Fig. 5.2 Concentrations of total organic carbon and biomarkers of Core SL170
a Concentrations of total organic carbon (TOC); **b** Concentrations of IP_{25} as proxy for sea-ice algae; **(c-e)** Concentrations of open-water phytoplankton biomarkers as proxies for primary production: **c** dinosterol, **d** brassicasterol, **e** HBI-III (Z); **f** P_DIP_{25} values based on dinosterol as proxy for sea ice cover. For the intervals characterized by zero or minimum concentrations of IP_{25} and phytoplankton biomarkers, P_DIP_{25} values are indeterminable and are set to 1 (black circles), assuming permanent sea ice conditions (cf., Müller et al., 2011). Red arrows highlight abrupt decreases in P_DIP_{25} values. Concentrations of. Black triangles mark available AMS[14]C dates.

5.3.3 Biomarkers of Core SL174

The concentrations of IP_{25} were low during HS1 to the mid-YD (16.6-12 ka BP), followed by higher concentrations during the late YD to the early Holocene (Fig. 5.3a). Coinciding with IP_{25}, concentrations of dinosterol and brassicasterol remained low until 12.2 ka BP, whereas higher concentrations were observed during the following period (Fig. 5.3b, c). Different from low contents of dinosterol and brassicasterol, HBI-III (Z) concentrations showed significant increases

- 130 -

around 13.6 ka BP and 12.4 ka BP. Additionally, higher values of HBI-III (Z) concentrations were also observed during the late YD to the onset of the early Holocene (Fig. 5.3e). However, TOC contents were relatively higher before the late YD, with the highest values during the mid-YD. The P_DIP_{25} values were set to "1" during HS1 due to very low concentrations of both IP_{25} and open-water phytoplankton biomarkers (Fig. 5.3f). Abrupt decline in P_DIP_{25} values occurred around 15 ka BP, coeval with slight increases in the concentrations of open-water phytoplankton biomarkers. P_DIP_{25} values remained around 0.5 during B/A to the early Holocene.
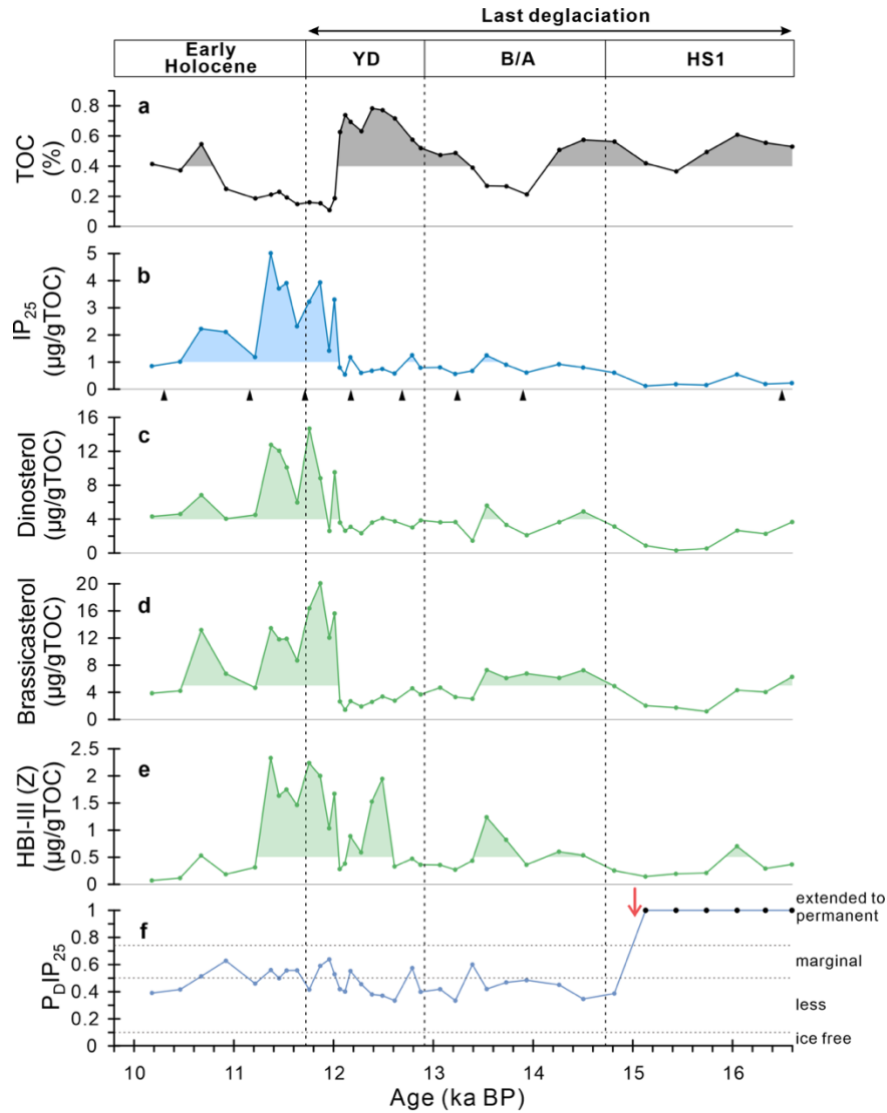
Fig. 5.3 Concentrations of total organic carbon and biomarkers of Core SL174.
a Concentrations of total organic carbon (TOC); **b** Concentrations of IP_{25} as proxy for sea-ice algae; **(c-e)** Concentrations of open-water phytoplankton biomarkers as proxies for primary production: **c** dinosterol, **d** brassicasterol, **e** HBI-III (Z); **f** P_DIP_{25} values based on dinosterol as proxy for sea ice cover. For the intervals characterized by zero or minimum concentrations of IP_{25} and phytoplankton biomarkers, P_DIP_{25} values are indeterminable and are set to 1 (black circles), assuming permanent sea ice conditions (cf., Müller et al., 2011). Red arrow highlights an abrupt decrease in P_DIP_{25} values. Concentrations of. Black triangles mark available AMS[14]C dates.

5.4 Discussion

5.4.1 Asynchronous sea ice variability in southern Baffin Bay during the last deglaciation

IP_{25} serves as a direct and reliable proxy for sea ice algae productivity, which has been used for sea ice reconstructions (cf., Belt et al., 2007; Müller et al., 2009; Brown et al., 2014). Due to the absence of sea ice algae (i.e., no IP_{25}), two extreme sea ice conditions (i.e., permanent sea ice cover and ice-free conditions) cannot be distinguished based only on IP_{25} records (Müller et al., 2011). To overcome this limitation, the combination of open-water phytoplankton biomarkers (e.g., dinosterol, brassicasterol, and HBI-III(Z)) with sea ice biomarker (IP_{25}) can help distinguish different sea ice scenarios (cf., Müller et al., 2011; Fahl and Stein, 2012). In the Core SL170, the highest values of P_DIP_{25} (representing the lowest concentrations of IP_{25} and open-water phytoplankton biomarkers) occurred at 16.8-15.4 ka BP, 15ka BP, and 14.5 ka BP, probably indicating permanent sea ice conditions in southeastern Baffin Bay (Fig. 5.4b). Subsequently, abrupt sea ice retreat occurred at 15.4 ka BP, 14.9 ka BP, and 14.4 ka BP. Given the high sedimentation rates of approximately 100 cm/kyr (Fig. 5.4c), these abrupt changes may have taken place within a few decades or even less. Another three abrupt decreases in sea ice cover were identified in southeastern Baffin Bay at 12.2 ka BP, 11.2 ka BP, and 10.6 ka BP, respectively. Similar variations in HBI-III (Z) and dinosterol/brassicasterol (e.g., highest concentrations appeared during the Bølling warming period) and synchronized rapid declines in concentrations of HBI-III (Z) and P_DIP_{25} values around 12.2 ka BP may support the hypothesis that HBI-III (Z) is an indicator of open-water productivity somehow linked with sea ice (marginal ice zone) (Belt et al., 2015). In contrast to Core SL170, the P_DIP_{25} values of Core SL174 in southwestern Baffin Bay indicates that permanent sea ice conditions remained until 15.1 ka BP (Fig. 5.4e). After an abrupt decrease around 15 ka BP, marginal sea ice conditions became prevalent in the western side of Baffin Bay without any further abrupt changes. The marginal sea ice reconstruction based on the diatom assemblage from Core SL170 showed a similar trend to our P_DIP_{25} record, particularly during the last 13 ka (Fig. 5.5b, Oksman et al., 2017). Notably, the increase (decrease) in sea ice formation in southern Baffin Bay did not correspond well with the decrease (increase) in atmospheric temperatures in the North Atlantic regions recorded by the Greenland Ice Core (Fig. 5.4a, b, e). This finding supports the conclusions from Jackson et al. (2017), indicating that icebergs and meltwater discharge associated with GrIS, LIS, and Innuitian Ice Sheet (IIS) were decoupled from the dominant North Atlantic climate mode.

The retreat of sea ice in southern Baffin Bay during the last deglaciation coincided with the decay of the surrounding ice sheets. The increased sedimentation rates observed in southern Baffin Bay have been interpreted as increased detrital input from the GrIS, LIS, and also IIS (Jackson et al., 2017; Oksman et al., 2017; Jackson et al., 2023). Both Core SL170 and Core

SL174 showed increased sedimentation rates since around 14.4 ka BP, coinciding with significant retreat of sea ice (Fig. 5.4b, c, e, f). Previous studies also indicate strong melting of icebergs from northern Baffin Bay and western Greenland margins around 14 ka BP (Sheldon et al., 2016; Jennings et al., 2017; Okuma et al., 2023) and during YD (Rinterknecht et al., 2014; Oksman et al., 2017). As a primary ice stream outlets of the GrIS, the western GrIS has been identified as a major source of terrigenous materials to southeastern Baffin Bay due to its proximity to Uummannaq Trough and Disko Bugt (Jennings et al., 2017). However, increased input of detrital carbonate, as evidenced by higher Ca/Sr ratios and dolomite contents after 14.4 ka BP, implies that the LIS and/or IIS were also contributors to the sedimentation (Fig. 5.4d, g) (Simon et al., 2014; Jackson et al., 2017; Okuma et al., 2023; Ownsworth et al., 2023). In contrast, southwestern Baffin Bay may be more subject to detrital input from the LIS with contribution from the western GrIS (cf., Core PC16, Simon et al., 2014).
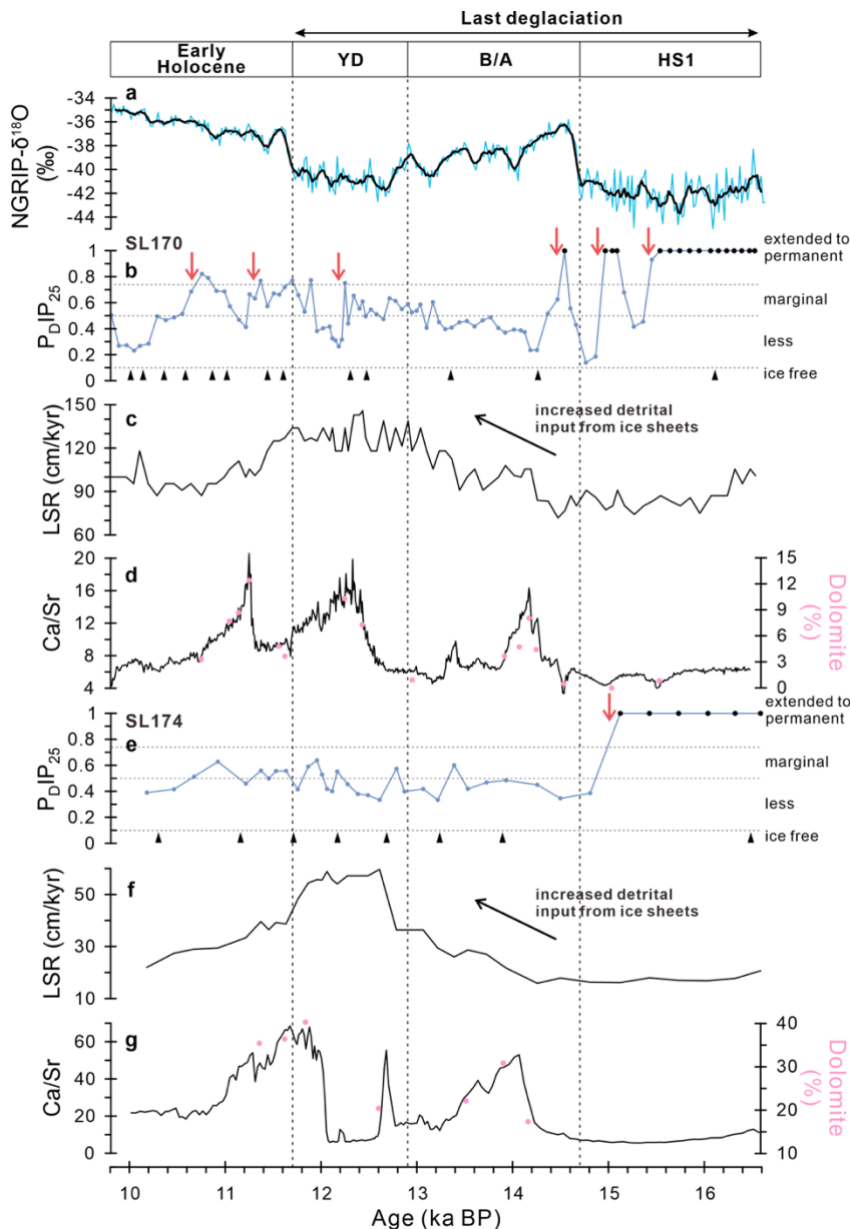
Fig. 5.4 Proxy records of sea ice cover, sedimentation rates, and detrital carbonate input of Core SL170 and Core SL174.

a Greenland Ice Core record (NGRIP)-δ^{18}O (Svensson et al., 2008); (**b-d**) Proxy records from Core SL170: **b** P_DIP_{25} values based on dinosterol as proxy for sea ice cover; **c** Linear sedimentation rates (LSR); **d** Ca/Sr ratios and dolomite contents indicating detrital carbonate input (Jackson et al., 2017); (**e-g**) Proxy records from Core SL174: **e** P_DIP_{25} values based on dinosterol as proxy for sea ice cover; **f** Linear sedimentation rates (LSR); **g** Ca/Sr ratios and dolomite contents indicating detrital carbonate input (Jackson et al., 2017). Red arrows highlight abrupt decreases in sea ice cover. Black arrows indicate the increasing tendency of sedimentation rates. Black triangles mark available AMS[14]C dates.
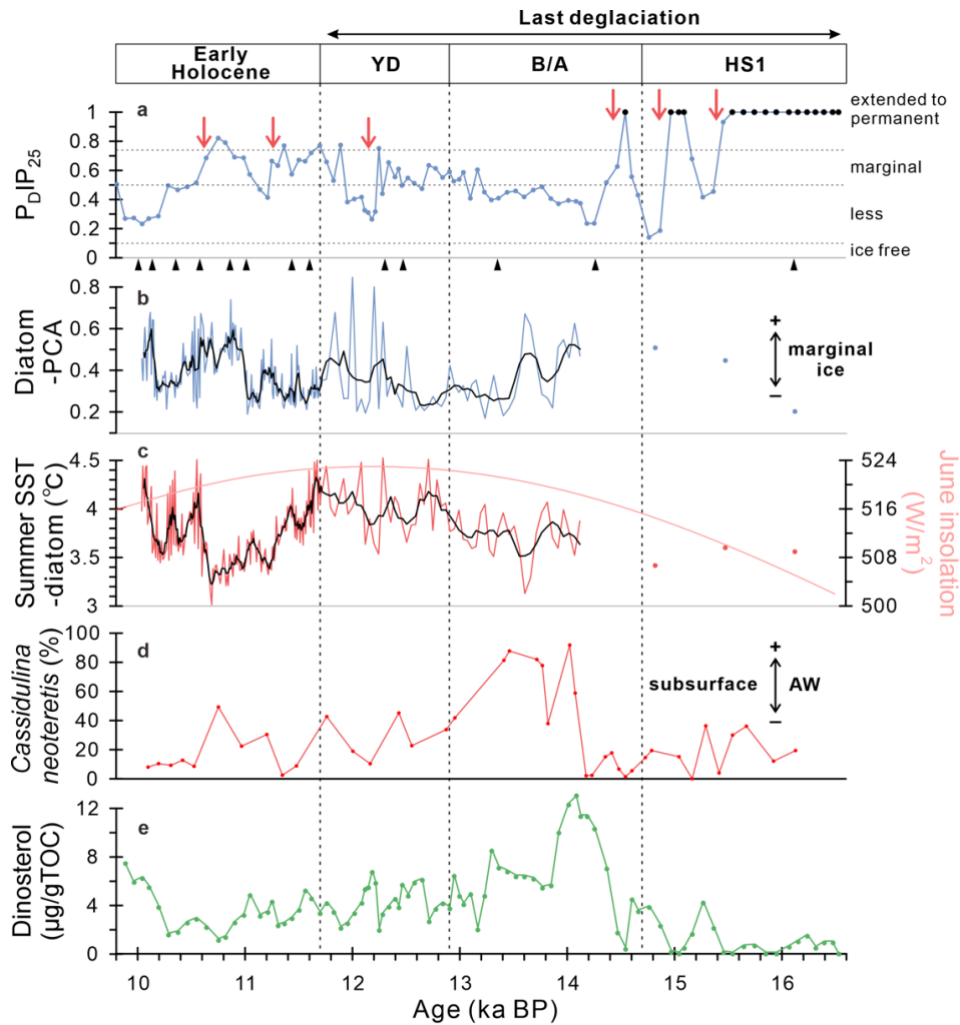
Fig. 5.5 Proxy records of sea ice cover and water mass characteristics of Core SL170.
a P_DIP_{25} values based on dinosterol as proxy for sea ice cover (this study); **b** Factor of diatom assemblage as proxy for marginal sea ice (Oksman et al., 2017); **c** Contents of diatom assemblage as proxy for summer sea surface temperature (SST) (Oksman et al., 2017) and summer insolation; **d** Contents of benthic foraminifera *Cassidulina neoteretis* as proxy for Atlantic Water inflow (subsurface, water depth 1078 m) (Jackson, 2017); **e** Dinosterol concentrations as proxy for open-water phytoplankton productivity (this study). Red arrows highlight abrupt decreases in sea ice cover. Black triangles mark available AMS[14]C dates.

The occurrence of abrupt retreats of sea ice in southeastern Baffin Bay was most likely influenced by the northward flow of warm WGC. It has been proposed that Atlantic-sourced water inflow combined with amplified seasonality has caused increased summer sea surface temperatures (SST) in this region during the last deglaciation (Oksman et al., 2017). The highest values of SSTs coincided with sea ice retreat and increased dinosterol concentrations in southeastern Baffin Bay during the Bølling warm period, the mid-YD, and the early Holocene. This may indicate that warm Atlantic Water inflow has triggered sea ice retreat and promoted open-water productivity (Fig. 5.5). Variations in the contents of benthic foraminifera *Cassidulina neoteretis* can also be used as a proxy for changes in Atlantic Water inflow at the intermediate

depths (Fig. 5.5d) (cf., Seidenkrantz, 1995; Jennings et al., 2017). During HS1 and B/A periods, the increased abundance of *C. neoteretis* along with decreased sea ice suggests that warm water incursion may have contributed to sea ice retreat (Fig. 5.5a, d). However, both *C. neoteretis* contents and sea ice cover was declined at the same time during the mid-YD and the early Holocene. In addition to the intensity of Atlantic Water inflow, variations in the depth of Atlantic Water inflow were also a factor influencing the presence of *C. neoteretis*, which were closely linked with the thickness of halocline (cf., Jakobsson et al., 2014; Weiser et al., 2021). During the mid-YD and the early Holocene, abrupt declines in sea ice cover indicate enhanced Atlantic Water inflow, while decreased contents of *C. neoteretis* suggest that the depth of Atlantic Water became shallower, probably due to a thinner halocline. Similar variations in *C. neoteretis* contents were also observed in Core VC29 to the south of Core SL170 (Supplementary Fig. 5.3). Increased Atlantic Water incursion and subsequent strong interactions between the ocean and ice sheets may have caused the retreat of ice sheet margins (Knutz et al., 2011; Straneo and Heimbach, 2013; Oksman et al., 2017; Jennings et al., 2017). The melting of sea ice along the ice sheet margins facilitated the warm water intrusion, leading to increased erosion and melting at the base and edges of the ice sheets, and consequently contributing to the potential collapse of the ice sheets. The comparable timing between abrupt sea ice retreat in Baffin Bay and the significant decay of the western GrIS further supports this interpretation (Jennings et al., 2017).

5.4.2 Deglacial sea ice variability in the Labrador Sea-Baffin Bay transect

Combined with previously published proxy-based sea ice reconstruction records, we have established a comprehensive picture of sea ice distribution along the Labrador Sea-Baffin Bay transect during the last deglaciation. The biomarker-based sea ice reconstruction was available from the eastern Labrador Sea (Core MSM12/2-05-01) (Fig. 5.6c, You et al., 2023). The marginal sea ice reconstruction was achieved by diatom assemblages from Core SL170, spanning the last 14-10 ka (Oksman et al., 2017) (Fig. 5.5b). Additionally, dinocyst assemblages were used to reconstruct the sea ice concentrations in the north Labrador Sea (Core PC04) (Gibb et al., 2014) (Fig. 5.6b).

The sea ice distribution in the Labrador Sea-Baffin Bay transect was distinctly variable during the last deglaciation. Permanent sea ice cover was predominant in southern Baffin Bay during most of HS1, interrupted by short periods with reduced sea ice cover around 15.4 ka BP and 14.9 ka BP (Figs. 5.4e, 5.6a). However, nearly continuous permanent sea ice cover was observed in the north Labrador Sea until around 12 ka BP, whereas the eastern Labrador Sea was characterised by marginal sea ice cover until 14 ka BP (Fig. 5.6b, c). Here, we chose the time slice at 16 ka BP to show sea ice distribution during this relatively stable period (Fig. 5.7a). Given less robust age controls of Core PC04, it is plausible that the abrupt retreat of sea ice in the northern Labrador Sea around 12 ka BP coincided with a similar retreat in the eastern Labrador

Sea, driven by decreased meltwater discharge and increased Atlantic Water inflow (You et al., 2023). An important transition occurred around 14.4 ka BP (the Bølling warm period), where sea ice retreat occurred along the southwestern Greenland margins caused by enhanced Irminger Current/AMOC conditions (Liu et al., 2009) (Fig. 5.7b). Subsequently, southern Baffin Bay was characterised by marginal sea ice conditions, though extended sea ice cover could still be found in the Davis Strait (Core TWC08, Gibb et al., 2015). Another abrupt retreat of sea ice in southern Baffin Bay and the eastern Labrador Sea happened during the mid-YD (around 12.2 ka BP) (Fig. 5.7c). Increased percentages of planktic foraminifera *Globigerina bulloides* during the mid-YD indicates enhanced Irminger Current inflow into the Labrador Sea (Fig. 5.8d). Furthermore, decreased concentrations of Arctic Water diatom assemblages provide additional support for the intensification of Atlantic Water influence during the mid-YD (Oksman et al., 2017), and such influence could reach to northernmost Baffin Bay based on benthic foraminifera data of Core 117Q (Jackson et al., 2021).
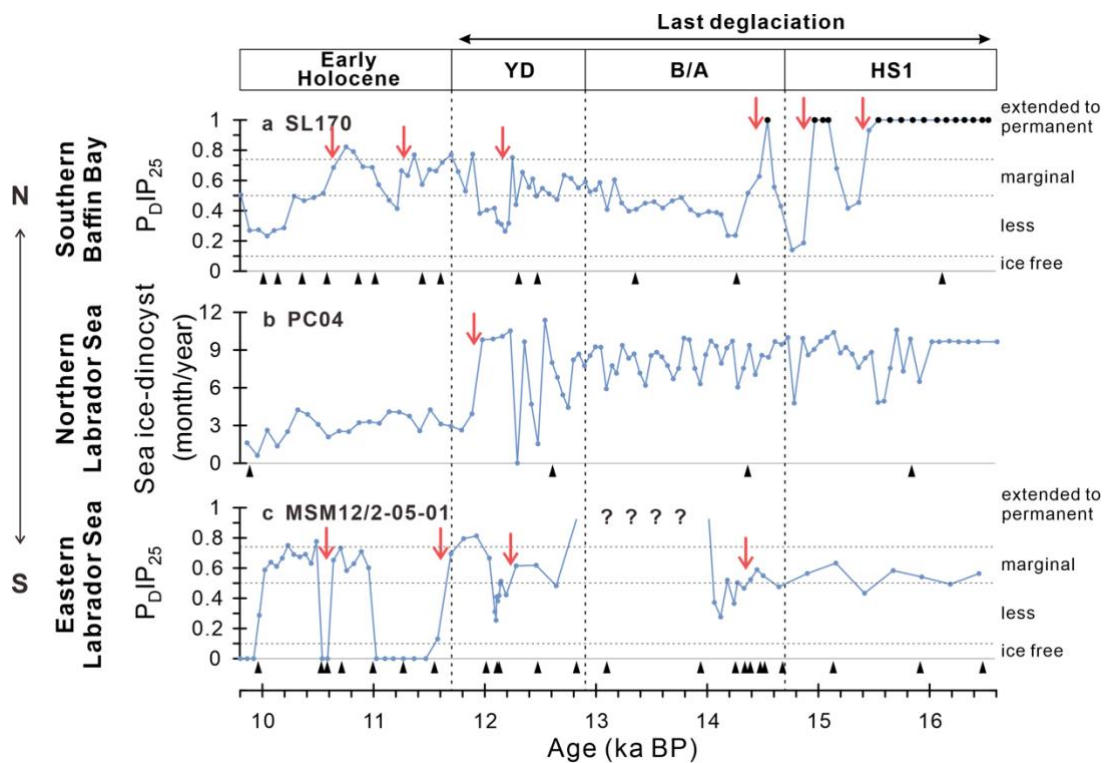
Fig. 5.6 Proxy records of sea ice cover in the Baffin Bay-Labrador Sea transect.
a P_DIP_{25} values based on dinosterol as proxy for sea ice cover (Core SL170) (this study); **b** Contents of dinocyst assemblage as proxy for sea ice concentration (Core PC04) (Gibb et al., 2014); **c** P_DIP_{25} values based on dinosterol as proxy for sea ice cover (Core MSM12/2-05-01) (You et al., 2023), question marks indicate the interval in which P_DIP_{25} values cannot be determined (for more details see You et al., 2023); Red arrows highlight significant decreases in sea ice cover. Black triangles mark available AMS[14]C dates.

In addition to warm water inflow causing sea ice retreat, meltwater discharge is another factor affecting sea ice distribution in Baffin Bay/the Labrador Sea (Saini et al., 2022; You et al., 2023). For instance, abrupt sea ice formation in the eastern Labrador Sea during the early Holocene has been attributed to increased meltwater discharge from the LIS and the GrIS (You et al., 2023). In contrast to reduced or absent sea ice cover in the southern Baffin Bay/Labrador Sea area during warm phases of the early Holocene (e.g., 10.6 ka BP), most northern Baffin Bay might have still been permanently covered by sea ice, according to Cores GeoB19905-1, TWC16, GeoB19927-3, AMD14-204 (Gibb et al., 2015; Caron et al., 2019; Saini et al., 2022) (Fig. 5.7d).
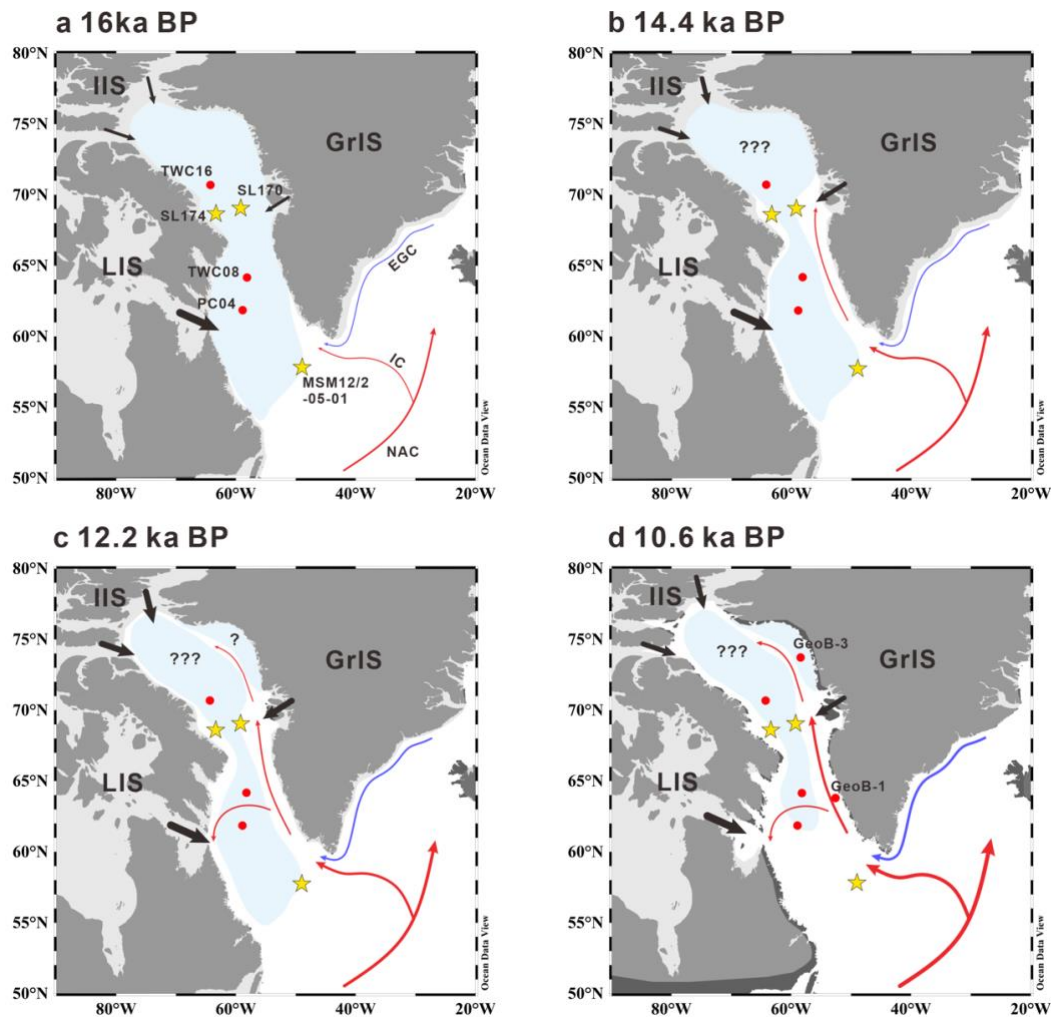
Fig. 5.7 Schematic illustrations of sea ice distribution in the Baffin Bay-Labrador Sea transect at four time slices.
The location of Cores SL170, SL174, and MSM12/2-05-01 (this study) are shown by the yellow stars, and red dots indicate other cores referred to. GeoB-1 refers to Core GeoB19905-1; GeoB-3 refers to Core GeoB19927-3. Red arrows indicate warm Atlantic Water inflow, blue arrow shows cold polar water inflow, and black arrows indicate detrital input from the Laurentide Ice Sheet (LIS), Greenland Ice Sheet (GrIS), and Innuitian Ice Sheet (IIS). Grey shadings indicate the ice sheet extents. NAC North Atlantic Current, IC Irminger Current, EGC Eastern Greenland Current.

5.4.3 Implication for abrupt transition in the Labrador Sea/Baffin Bay during the mid-Younger Dryas

Based on the reconstructions of sea ice and warm water inflow, an abrupt transition in surface characteristics occurred during the mid-YD in the subpolar North Atlantic, extending from the Labrador Sea into Baffin Bay. The YD, following the warm B/A period, was characterized by abrupt cooling in the North Hemisphere (Svensson et al., 2008). It has been proposed that the occurrence of the YD was caused by the catastrophic outburst of Lake Agassiz into the Arctic Ocean around 12.9 ka BP, resulting in surface freshening in the Nordic Seas and suppressing deep-water formation, ultimately leading to a reduced AMOC (Keigwin et al., 2018; Wu et al., 2020). However, the question remains as to whether a flooding event on the scale of a few centuries could sustain a thousand-year-long cold period. Modelling research provides an alternative perspective, suggesting that the export of Arctic sea ice into the Nordic Seas could have played a role in maintaining a weakened AMOC (Condron et al., 2020). Another notion proposes that the occurrence of HE0 during the late YD might have contributed to the cold episode during the late YD (cf., Andrews et al., 1995; You et al., 2023). The mid-YD shift (around 12.15 ka BP) has been proposed by Bakke et al. (2009): in contrast to the stable and colder conditions during the early YD, the influence of freshwater forcing was weakened during the late YD, causing alternating sea ice cover and Atlantic Water influx in the Nordic Seas. This study provides further evidence of an abrupt intensification of warm North Atlantic Current flowing into subpolar regions during the mid-YD, which preceded another surface freshening in the subpolar regions (i.e., the occurrence of HE0) possibly linked with the cold phase during the late YD.

Sea ice cover abruptly decreased around 12.2 ka BP in the eastern Labrador Sea, coinciding with abrupt increases in warm Irminger Current inflow (Fig. 5.8c, d). The rapid retreat of sea ice in southern Baffin Bay during this time interval further support for increased Atlantic Water incursion (Fig. 5.5). The enhanced Atlantic Water inflow was also evident in the record from the southern Labrador Sea (Core GGC14), which documented the transition from cold to warm water conditions (Fig. 5.8e; Gil et al., 2015). Furthermore, the recovery of the AMOC during the mid-YD corresponded to abrupt changes in the sea surface characteristics in the Labrador Sea and Baffin Bay, implying enhanced convection and deep-water formation in the North Atlantic (Fig. 5.8f). These findings align with the mid-YD shift proposed by Bakke et al. (2009).

Following enhanced Atlantic Water inflow during the mid-YD, a significant decay of the LIS and the IIS occurred, shown as the increased detrital carbonate input in the Labrador Sea and also Baffin Bay (Core MD99-2236, Jennings et al., 2015; this study) (Figs. 5.4d, g; 5.8g). This might have caused surface freshening in the Labrador Sea (Fig. 5.8g; You et al., 2023) and potentially broader areas of the North Atlantic, as indicated by reduced ocean ventilation in the south Iceland
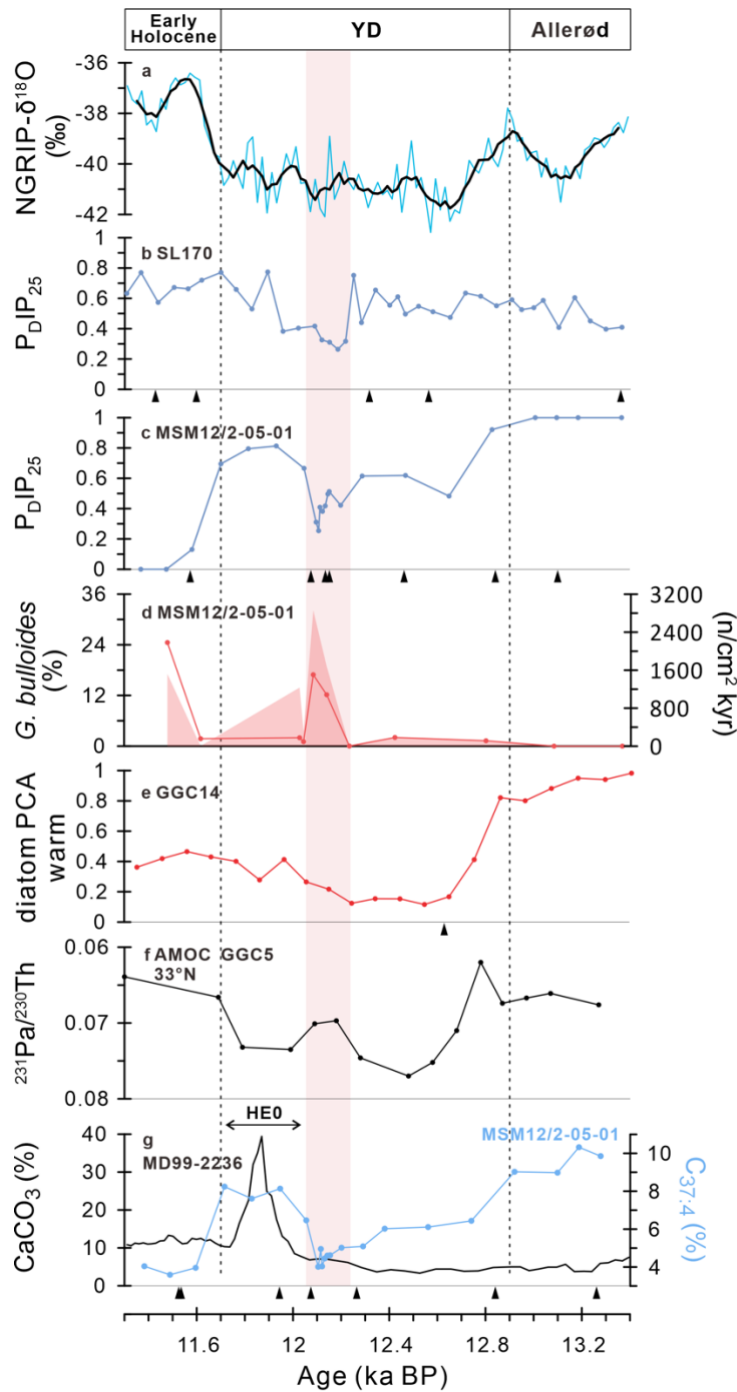
Fig. 5.8 Proxy records of abrupt transition during the mid-Younger Drays.
a Greenland Ice Core record (NGRIP)-δ^{18}O (Svensson et al., 2008); **b** $P_D IP_{25}$ values based on dinosterol indicating sea ice cover (Core SL170) (this study); **c** $P_D IP_{25}$ values based on dinosterol indicating sea ice cover (Core MSM12/2-05-01) (You et al., 2023; this study); **d** Contents and accumulation rates of planktic foraminifera *Globigerina bulloides* as proxy for Atlantic Water inflow (Core MSM12/2-05-01) (this study); **e** Factor of diatom assemblage indicating warm Atlantic Water inflow (Core GGC14) (Gil et al., 2015); **f** $^{231}Pa/^{230}Th$ ratios indicating the strength of AMOC at 33 °N (Core GGC5) (McManus et al., 2004); **g** Carbonate contents indicating the collapse of Laurentide Ice Sheet (Core MD99-2236) (Jennings et al., 2015), percentages of $C_{37:4}$ as proxy for meltwater discharge (Core MSM12/2-05-01) (You et al., 2023). Black triangles mark available AMS^{14}C dates based on the Marine 20 calibration curve. Black triangles in panel **g** indicating AMS^{14}C dates from Core MD99-2236.

Rise area (Thornalley et al., 2011), decreased sea surface/subsurface temperatures in the northeastern Atlantic and the southern Labrador Sea (Benway et al., 2010; Max et al., 2022) (Refer to Supplementary figure from You et al., 2023). Such surface freshening may have occurred within a few decades and contributed to weakened ocean convection/deep-water formation in the North Atlantic during the late YD, resulting in a second decrease in AMOC (Fig. 5.8f). This transition during the mid-YD was not only observed in the subpolar and polar regions of the North Atlantic (e.g., Bakke et al., 2009; Gil et al., 2015; You et al., 2023) but was also documented in many reconstruction records from European lakes and glaciers (cf., Isarin et al., 1998; Neugebauer et al., 2012; Hughes et al., 2012; Pawłowski, 2017; Sirocko et al., 2021). However, not all the proxy-based records demonstrated the occurrence of this transition during the mid-YD. The Greenland Ice Core record, for instance, did not show a distinct increase in atmospheric temperatures during the mid-YD (Fig. 5.8a; Svensson et al., 2008), suggesting the heat release from the ocean to the atmosphere in the North Atlantic remained restricted during this time interval. Furthermore, high-resolution records from Asian speleothems did not align with the patterns depicted in Figure 5.8 (Cheng et al., 2020). This suggests that this transition may be restricted to the North Atlantic regions whereas it played an essential role in deglacial abrupt climate changes.

5.5 Conclusions

Biomarker-based records allowed to reconstruct abrupt variations in sea ice cover and open-water phytoplankton productivity in southern Baffin Bay during the last deglaciation. Six significant sea ice retreats were identified in southeastern Baffin Bay, and one prominent retreat was observed in southwestern Baffin Bay, spanning the last 16-10 ka. These retreats have been proposed to be driven by enhanced Atlantic Water incursion. Notably, a major sea ice retreat occurred around 14.4 ka BP (the early Bølling warm period), coinciding with elevated detrital input from the GrIS and the LIS. Furthermore, a distinct sea ice retreat extended from the Labrador Sea to Baffin Bay during the mid-YD. This abrupt transition coincided with an intensified Atlantic Water inflow and a slight recovery of the AMOC. It is conceivable that this transition caused the occurrence of HE0, which might have contributed to the cold spell during the late YD. Oceanic forcings have not only shaped the historical retreat of sea ice and ice sheets, but they also are responsible for driving contemporary variations in the environment. As regions of highly sensitivity within the Earth's climate system, changes in oceanographic conditions and their implications for abrupt climate changes in the polar and subpolar North Atlantic regions deserve special attention, especially given the current accelerated melting of the GrIS and Arctic sea ice.

5.6 Methods

Geochemical bulk parameters

Freeze-dried and homogenized sediments were used for total organic carbon (TOC) and total carbon (TC) measurement. TOC contents were measured by Carbon-Sulfur Analyser (CS-125, Leco) after removing carbonate with hydrochloric acid. TC contents were determined by Carbon-Nitrogen-Sulfur Analyser (Elementar III, Vario). Inorganic carbon (IC) contents were calculated assuming that calcite was the predominant carbonate phase (IC=(TC-TOC)×8.333).

Biomarker analysis

5 g of freeze-dried and homogenized sediments were extracted by ultrasonication with dichloromethane/methanol (DCM/MeOH, 2:1 v/v). The internal standards 7-hexylnonadecane (7-HND, 0.076 μg) and 5α-androstan-3β-ol (androstanol, 10.8 μg) were added prior to the extraction. The concentrated extracts were separated into hydrocarbon and sterol fraction by open silica gel column chromatography using 5 ml *n*-hexane and 9 ml ethylacetate/*n*-hexane, respectively. The sterol fraction was derivatized with 200 μl bis-trimethylsilyl-trifluoracet-amid (BSTFA) (60°C, 2h) before measurement. Hydrocarbons and sterols were analysed by gas chromatography/mass spectrometry (GC/MS, Agilent 7890GC-Agilent 5977 A) and GC/MS (Agilent 6850GC-Agilent 5975 A), respectively. Highly-branched isoprenoid (HBIs) was quantified based on their molecular ions (m/z 350 for IP_{25}, m/z 348 for HBI-II, and m/z 346 for HBI-III (Z)) in relation to the fragment ion m/z 266 (7-HND). Brassicasterol (24-methylcholesta-5,22E-dien-3β-ol) and dinosterol (4a-23,24-trimethyl-5a-cholest-22E-en-3β-ol) were quantified as trimethylsilyl ethers. Their molecular ions (m/z 470 for brassicasterol and m/z 500 dinosterol) were used in relation to the molecular ion m/z 348 of the internal standard androstanol. External calibration curves and specific response factors were used to balance the different responses of molecular ions of the analytes and the molecular/fragment ions of the internal standards. Biomarker concentrations were normalized based on TOC content of each sample. For analytical details and further references see Fahl and Stein, (2012).

PIP_{25} values, a semi-quantitative index for sea ice reconstruction, were calculated based on equation 1 (Müller et al., 2011). It is derived from the seasonal sea ice biomarker (IP_{25}) and open-water phytoplankton biomarker (e.g., dinosterol, brassicasterol, and HBI-III (Z)).

$$PIP_{25} = [IP_{25}] / ([IP_{25}] + [\text{Phytoplankton biomarker}] \times c) \tag{1}$$

The balance factor c corresponds to the ratio of mean concentration of IP_{25} and phytoplankton biomarker. In our study, all three PIP_{25} proxies based on dinosterol, brassicasterol, and HBI-III (Z) show very similar trends (Supplementary Fig. 5.4). Thus, we only used the IP_{25}-dinosterol-based P_DIP_{25} to reflect sea ice variations here (Fig. 5.2f, 5.3f).

Acknowledgements

Author contributions

D. You and R. Stein designed this study. D. You carried out biomarker analyses and evaluations (i.e., HBIs and sterols). K. Fahl conducted evaluation and quality controls of biomarker data. R. Jackson provided benthic foraminifera data. D. You conducted bulk parameter measurements. D. You wrote the first version of the manuscript with input from R. Stein and some additional comments by R. Jackson. All the co-authors contributed to the data interpretation and the final version of the paper.

5.7 Supplementary Information

This subchapter includes:

Supplementary Table 5.1: AMS ^{14}C dates of Core SL170 from Jackson et al. (2017) and recalculated based on the Marine 20 calibration curve.

Supplementary Table 5.2: AMS ^{14}C dates of Core SL174 from Jackson et al. (2017) and recalculated based on the Marine 20 calibration curve.

Supplementary Fig. 5.1: Modern hydrography of study area.

Supplementary Fig. 5.2: Age models of Core SL70 and Core SL174.

Supplementary Fig. 5.3: Proxy records of Core SL170 using different local reservoir ages to establish age models.

Supplementary Fig. 5.4: Percentages of *Cassidulina neoteretis* of Core SL170 and Core VC29.

Supplementary Fig. 5.5: PIP_{25} values based on different phytoplankton biomarkers of Core SL70 and Core SL174.

Supplementary Table 5.1 AMS ^{14}C dates of Core SL170 from Jackson et al. (2017) and recalculated based on the Marine 20 calibration curve.

Lab ID	Depth (cm)	Species	AMS ^{14}C age (yr.)	$\triangle R$	Reference	Calib. age median (yr. BP)	Model age median (yr. BP)	Reference
ETH-55678	24-27	mixed benthic	9668±112	140±35	Jackson et al., 2017	10227	10055	This study
ETH-55679	35-37	mixed benthic	9460±80	140±35	Jackson et al., 2017	9945	10149	This study
ETH-55680	55-57	mixed benthic	9833±83	140±35	Jackson et al., 2017	10432	10371	This study
ETH-55681	74-76	planktic	9901±82	140±35	Jackson et al., 2017	10525	10578	This study
ETH-55683.1	98-100	mixed benthic	10243±80	140±35	Jackson et al., 2017	11014	10846	This study
ETH-55685	116-118	mixed benthic	10274±86	140±35	Jackson et al., 2017	11058	11033	This study
ETH-58351	159-160	mollusc fragments	10755±85	140±35	Jackson et al., 2017	11744	11430	This study
ETH-58353	180-181	mixed benthic	10671±85	140±35	Jackson et al., 2017	11809	11603	This study
ETH-55687	266-269	mixed benthic	11267±100	140±35	Jackson et al., 2017	12486	12305	This study
ETH-58354	288-290	mixed benthic	11150±75	140±35	Jackson et al., 2017	12345	12462	This study
ETH-55688	399-402	planktic	11597±104	140±35	Jackson et al., 2017	12799	13365	This study
KIA 40766	484-488	planktic	12730±60	140±35	Jackson et al., 2017	14024	14240	This study
ETH-58355	636-637	planktic	14640±130	140±35	Jackson et al., 2017	16722	16131	This study

All AMS[14]C dates were calculated based on the Marine 20 calibration curve (Heaton et al., 2020). The modelled ages were recalculated from Bacon program (Blaauw and Christen, 2011).

Supplementary Table 5.2 AMS ¹⁴C dates of Core SL174 from Jackson et al. (2017) and recalculated based on the Marine 20 calibration curve.

Lab ID	Depth (cm)	Species	AMS ¹⁴C age (yr.)	$\triangle$R	Reference	Calib. age median (yr. BP)	Model age median (yr. BP)	Reference
ETH-55690	97-100	planktic and mixed benthic	9793±120	140±35	Jackson et al., 2017	10390	10304	This study
Beta-344508	122-125	planktic and mixed benthic	10390±40	140±35	Jackson et al., 2017	11212	11184	This study
ETH-55691	142-145	mixed benthic	10997±110	140±35	Jackson et al., 2017	12129	11710	This study
ETH-58356	169-170	mixed benthic	11010±85	140±35	Jackson et al., 2017	12152	12187	This study
Beta - 344505	196-199	planktic	11410±50	140±35	Jackson et al., 2017	12630	12692	This study
KIA 40767	215-219	planktic	12000±80	140±35	Jackson et al., 2017	13184	13238	This study
Beta - 344507	233-236	planktic	12580±60	140±35	Jackson et al., 2017	13832	13888	This study
ETH-58357	278-279	planktic	14510±120	140±35	Jackson et al., 2017	16562	16489	This study
ETH-58358	294-295	planktic	15060±110	140±35	Jackson et al., 2017	17228	17228	This study

All AMS¹⁴C dates were calculated based on the Marine 20 calibration curve (Heaton et al., 2020). The modelled ages were recalculated from Bacon program (Blaauw and Christen, 2011).
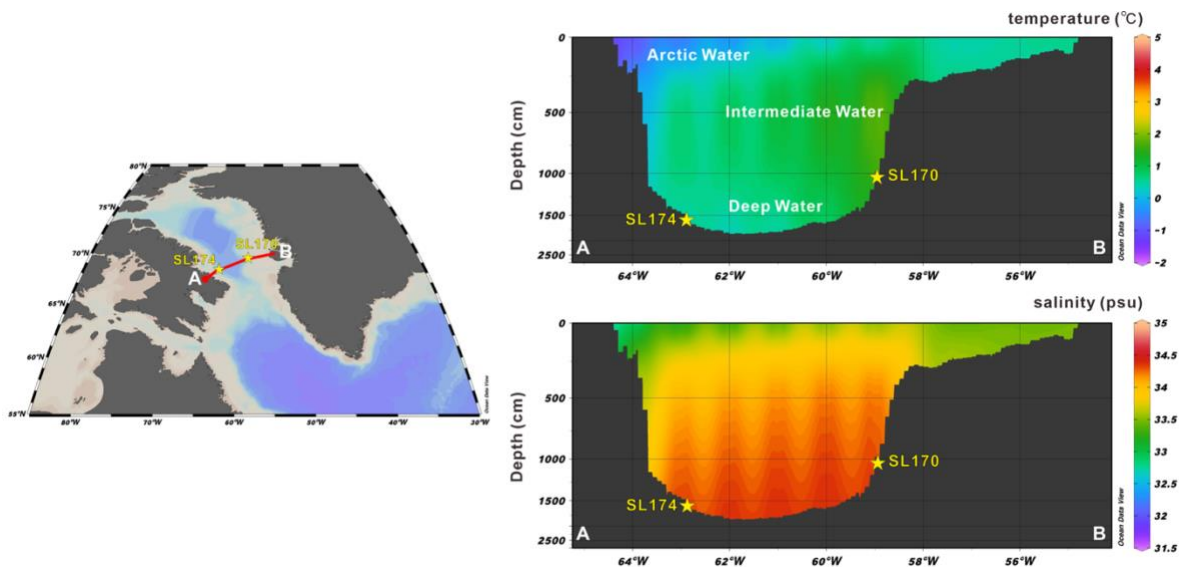
Supplementary Fig. 5.1 Modern hydrography of study area.
The left map shows location of hydrographic transect A to B. The right maps show vertical distribution of water masses in terms of temperature and salinity at profile A to B. Three water masses (i.e., Arctic Water, Atlantic Intermediate Water, and Baffin Bay Deep Water) can be identified. Data is from World Ocean Atlas 2018 (*https://odv.awi.de/data/ocean/*). Profiles were produced with Ocean Data View software (*https://odv.awi.de*).
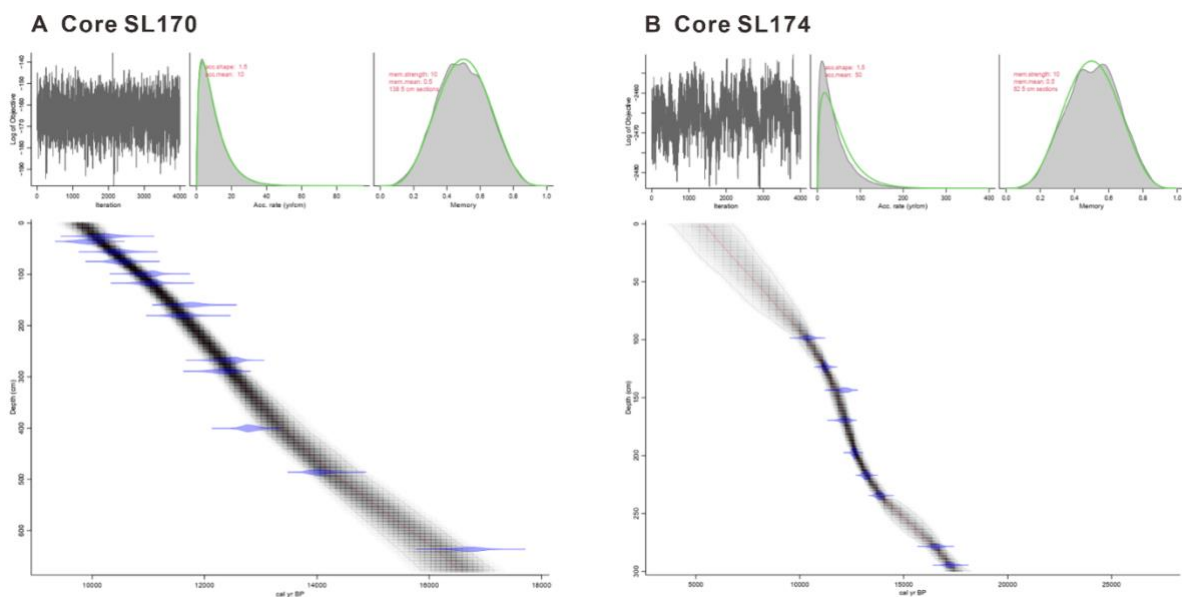
Supplementary Fig. 5.2 Age models of Core SL170 and Core SL174.
Bayesian age-depth model was established based on AMS[14]C dates from Jackson et al. (2017) using the Marine 20 calibration curve (Heaton et al., 2020) and Bacon program (Blaauw and Christen, 2011). The horizontal dashed lines indicate sediment depths where sedimentation rates change significantly. Grey stippled lines indicate 95% confidence intervals of calibration age.
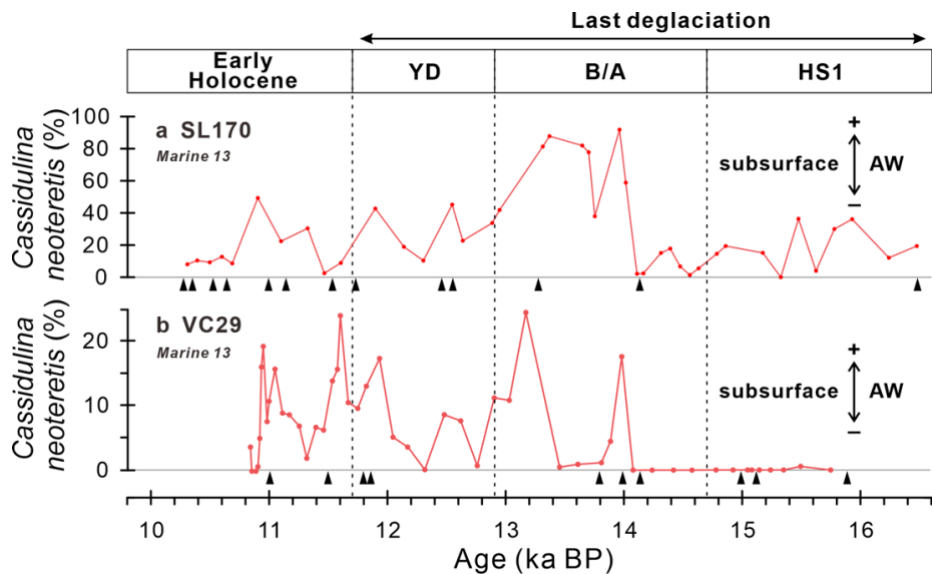
Supplementary Fig. 5.3 Percentages of *Cassidulina neoteretis* of Core SL170 and Core VC29.
a Percentages of *Cassidulina neoteretis* of Core SL170 based on the Marine 13 calibration curve (Jackson, 2017); **b** Percentages of *Cassidulina neoteretis* of Core VC29 based on the Marine 13 calibration curve (Jennings et al., 2017). Black triangles mark available AMS[14]C dates.
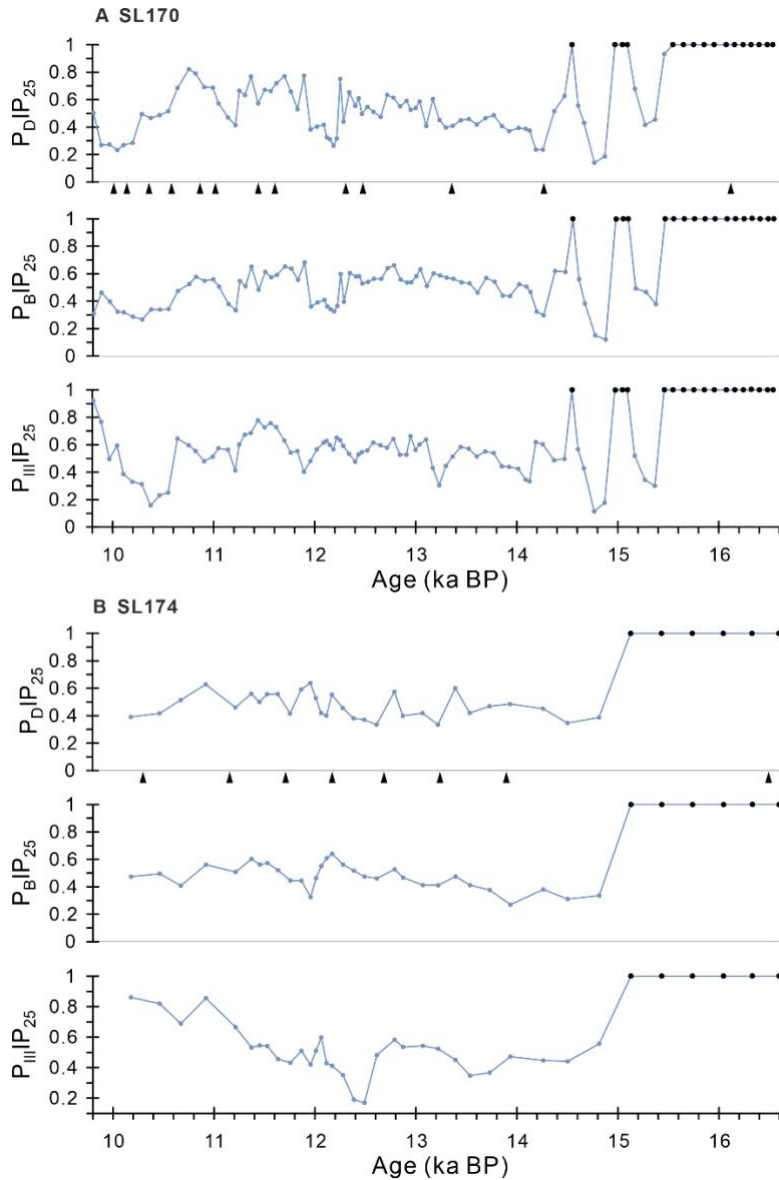
Supplementary Fig. 5.4 PIP$_{25}$ values based on different phytoplankton biomarkers of Core SL70 and Core SL174.

A PIP$_{25}$ values of Core SL170 based on dinosterol, brassicasterol, and HBI-III (Z), respectively. **B** PIP$_{25}$ values of Core SL174 based on dinosterol, brassicasterol, and HBI-III (Z), respectively. Black triangles mark available AMS[14]C dates. For the intervals characterized by zero or minimum concentrations of IP$_{25}$ and phytoplankton biomarkers, P$_D$IP$_{25}$ values are indeterminable and are set to 1 (black circles), assuming permanent sea ice conditions (cf., Müller et al., 2011).

6 Conclusions and outlook

6.1 Conclusions

The major objectives of this dissertation are to reconstruct changes in sea surface characteristics and the history of meltwater discharge in the Labrador Sea and to investigate correlations between ice sheet instability and sea surface characteristics during the last glacial-deglacial-Holocene period. In addition, our study also reconstructed deglacial variations in sea surface characteristics from southern Baffin Bay. To achieve these objectives, multiple biomarker proxies, foraminifera assemblages, and XRF scanning data, etc., were performed on one sediment core (MSM12/02-05-01) from the eastern Labrador Sea and two additional cores (SL170 and SL174) from southern Baffin Bay. Our sedimentary records provided valid information regarding the decay of the LIS and GrIS, meltwater discharge, variations in sea surface characteristics, and related abrupt climate changes. Notably, we used multiple and independent biomarker proxies to reconstruct sea surface characteristics: sea ice biomarker IP_{25} in combination with open-water phytoplankton biomarkers as a proxy for sea ice cover, concentrations of specific sterols and alkenones as proxies for primary production, U_{37}^{K}-based SST, $\%C_{37:4}$ coupled with δD_{PA} as proxies for meltwater discharge. In addition, changes in planktic and benthic foraminiferal assemblages were used to reflect variations in surface and bottom water mass characteristics. For reconstructing the history of ice sheet instability, specific element ratios from XRF scanning data, the quantification of detrital carbonate contents by XRD measurements, and IRD abundance were used to indicate detrital material input.

The history of meltwater discharge in the eastern Labrador Sea and its implications on abrupt changes in sea surface characteristics and climatic conditions during the last deglaciation have been described in Chapter 3. Based on well-dated and high-resolution sedimentary records representing the interval from the last deglaciation to Holocene (i.e., the last 19 ka), four millennial-scale meltwater events have been identified by abrupt changes in sea surface characteristics between 14 ka BP and 8.2 ka BP. These events were characterized by increased sea ice formation, decreased SSTs, and reduced primary production, which might have occurred within a few decades. We propose that these abrupt changes have been triggered by meltwater pulsing into the Labrador Sea periodically, resulting from the collapse of the LIS and GrIS caused by (sub-)surface ocean warming in the Labrador Sea. The increased meltwater discharges potentially increased sea ice formation and promoted stratification of the upper ocean column in the Labrador Sea/subpolar area, preventing Atlantic Water inflow, and consequently disrupting the deglacial climate.

A more comprehensive picture of interactions between ice sheet instability and sea surface characteristics in the Labrador Sea has been demonstrated in Chapter 4. As a continuation of

Chapter 3, the sedimentary records from the Labrador Sea have been extended 50 ka BP, in combination with further foraminiferal records. Enhanced warm Irminger Current inflow might have caused (sub-)surface warming in the Labrador Sea, leading to the disintegration of the surrounding LIS and GrIS, and subsequently increased meltwater discharge. The patterns of meltwater discharge were distinct during glacial and deglacial phases, possibly because of differential ice sheet volumes and extents. The release of meltwater and detrital materials were primarily caused by iceberg discharge during HEs (the last glacial period), whereas it was dominated by meltwater plumes during MWs (the last deglaciation). No matter the pattern, increased meltwater discharge has caused surface freshening in the Labrador Sea, resulting in decreased SSTs, increased sea ice formation, and reduced open-water phytoplankton productivity. Furthermore, our records provided proxy evidence that an offshore polynya probably occurred south of Greenland during the LGM.

Compared with those from the Labrador Sea, the deglacial changes in sea surface characteristics in southern Baffin Bay have been described in Chapter 5. Six significant sea ice retreats were identified in southeastern Baffin Bay, and one prominent retreat was observed in the southwestern Baffin Bay, spanning the last 16 to 10 ka. These retreats appear to be closely linked to enhanced Atlantic Water inflow. Notably, a major sea ice retreat occurred around 14.4 ka BP, coinciding with elevated detrital input from the GrIS and the LIS. Another distinct sea ice retreat extended from the Labrador Sea to Baffin Bay during the mid-YD, coinciding with intensified Atlantic Water inflow and a slight recovery of the AMOC but prior to the onset of HE0. It is conceivable that enhanced Atlantic Water inflow might have played a role in the occurrence of HE0, resulting in surface freshening in the subpolar regions, subsequently, the second decline in the AMOC during the late YD, thereby the persistence of a cold episode of YD.

In summary, our findings provide valuable insights into the interactions between ice sheet instability and sea surface characteristics in the Labrador Sea and Baffin Bay during the last glacial-deglacial-Holocene period. On the one hand, the decay of ice sheets has caused meltwater discharge, leading to abrupt changes in sea surface characteristics, which were closely related to deglacial abrupt climate changes. Our records provide more precise information about the impact of freshwater forcing on abrupt climate changes, which helps to improve simulations for past and future ocean circulation and climate changes. On the other hand, enhanced warm water inflow/(sub-)surface warming might have driven ice sheet instability. These findings highlight the significance of oceanic processes within the polar/subpolar regions not only in shaping glacial-deglacial-Holocene climate changes but also responsible for driving contemporary environmental variations. As regions of high sensitivity within the Earth's climate system, changes in oceanographic conditions and their implications for abrupt climate changes in the

polar and subpolar North Atlantic regions deserve more and special attentions, particularly given the current accelerated melting of the GrIS and Arctic sea ice under a sustained warm climate.

6.2 Outlook

Our study reconstructed the history of sea surface characteristics in the Labrador Sea during the last glacial-deglacial-Holocene period and those in Baffin Bay during the last deglaciation. Furthermore, our findings shed new light on that ocean forcings could play a pivotal role in driving ice sheet activities. In turn, the decay of ice sheets/meltwater discharge may trigger abrupt changes in sea surface characteristics and disrupt the climate. This work remains challenging in some aspects, but it also provides perspectives for future research.

$\%C_{37:4}$ has been used as a proxy for meltwater discharge due to its correlation with low-temperature and/or low-salinity sea surface conditions (cf., Bard et al., 2000). A recent study proposed that $C_{37:4}$ can also be produced by the newly found Isochrysidales lineage of sea ice algae (Wang et al., 2021), which challenges our interpretation. A good negative correlation between $\%C_{37:4}$ and δD_{PA} values in our study supports our interpretation that increased $\%C_{37:4}$ is somehow related to conditions with decreased salinity (i.e., meltwater discharge). Thus, to better and directly reconstruct changes in sea-surface salinity, it would be very necessary and useful to obtain more records of stable hydrogen isotope compositions of fatty acids and other specific phytoplankton biomarkers (e.g., dinosterol) for further research. Furthermore, the study of newly found Isochrysidales lineage needs to be carried on in terms of temporal and spatial distribution.

Most recently, non-correlation between δD_{PA} and sea-surface salinity has been observed in some surface sediments from the Labrador Sea and Baffin Bay (Allan et al., 2023). They suggest that the relative abundance of distinct organisms that employ different metabolisms, is the key in determining δD_{PA} values in modern conditions. However, these surface samples represent quite different environments, ranging from coastal to open ocean with very high to low terrigenous material input. Therefore, if we 'de-construct' the dataset by selecting specific groups of sub-samples, we may actually get a relation with salinity, which is overlain by other factors in the entire sample set. Additionally, the ages of these surface sediments need to be further determined. To figure out whether δD_{PA} could be used as a proxy for salinity in the Labrador Sea, particularly for paleo records, further investigations of the sources of palmitic acid and its stable hydrogen isotope compositions are needed. These studies should not only address surface sediments but also include sediment cores within different water depths and timescales.

Significant meltwater discharge into the Labrador Sea may affect LSW formation, subsequently influencing the AMOC. In this dissertation, we mainly focus on the changes in sea surface characteristics in the Labrador Sea during the last glacial-deglacial-Holocene period. The sparse

reconstructions of LSW formation during the last glacial-deglacial period limit our further discussion about the role of meltwater discharge in deep-water formation in the Labrador Sea. Furthermore, the evolutionary history of LSW is still controversial. Hillaire-Marcel et al. (2001) proposed that the LSW formation became active after 7 ka BP, whereas some studies suggest that the presence of deep-water formation in the Labrador Sea during the last glacial period/LGM (cf., Keigwin and Swift, 2017; Blaser et al., 2020). Therefore, more proxy-based reconstruction of deep-water formation in the Labrador Sea is needed, combined with variations in sea surface characteristics.

Our study firstly provides the continuous IP_{25} record and reconstructs the history of sea ice variation/meltwater discharge in the eastern Labrador Sea during the last 50 ka, which also reveals a high-resolution sea-ice record during the last deglaciation. Given a sensitive region in the Earth's system, sea ice cover/surface freshening in the subpolar North Atlantic is assumed to play an important role in disrupting the AMOC and triggering abrupt climate changes in the past (cf., Zhang et al., 2017). We note that our findings provide a glimpse solely into the history of surface conditions on the western side of the subpolar regions. For a comprehensive picture of sea ice distribution and better understanding of the mechanisms driving abrupt climate changes, further reconstructions of sea surface characteristics in wider subpolar regions are needed. These potential extensions could encompass the Irminger Sea and eastern subpolar regions (cf., Fig.1.28). Moreover, it would be of great interest to collaborate with modelers, applying our sea ice and meltwater records into oceanic and climatic simulations, which may provide some new insights into the dynamics of abrupt climate changes. In addition, more sedimentary records dating back to the glacial and deglacial periods from central or northern Baffin Bay are also necessary to get a more comprehensive reconstruction of sea ice variations, contributing to decipher interactions between ice sheet activities and sea surface characteristics in Baffin Bay.

The abrupt retreat of sea ice in the Labrador Sea and Baffin Bay during the mid-YD implicates enhanced warm Atlantic Water inflow, coinciding with a slight increase in the AMOC. These "anomaly" changes might have triggered the occurrence of HE0, probably contributing to the second decrease in the AMOC during the late YD and the persistence of a cold episode of YD. This finding is compelling but also challenging. More high-resolution sedimentary records and simulations are indispensable, offering more corroborative evidence. An in-depth discussion is further required to interpret why the mid-YD shift is primarily observed in some records from high-latitude North Atlantic regions and Europe, whereas it is missing in the Greenland Ice Core records and other records from low-middle latitude regions.

Besides the mid-YD, the enhanced warm water inflow/(sub-)surface warming has also been observed during other time intervals before the occurrence of abrupt meltwater events. Some studies suggest that enhanced warm water incursions into the Labrador Sea were related to the

decreased AMOC (e.g., Max et al., 2022). However, the specific mechanism is still not understood. In order to better understand such non-linear feedbacks and climatic thresholds in the Earth System (e.g., the presence of abrupt climate changes), it is essential to strengthen coupled studies between different climate components within different timescales (i.e., ocean-ice-atmosphere interactions) and enhance multidisciplinary collaboration.

We also notice that different age models significantly influence the final conclusions. The age models employed in this study were established on the ^{14}C dates calibrated using local reservoir ages (△R) referred to in previous studies (see Chapter 2.3 Chronology). For unpublished manuscripts, updated △R values should be considered to establish age models (cf., Pieńkowski et al., 2022; Pearce et al., 2023). Most recently, Heaton et al. (2023) recommended that modelled reservoir ages should be used for ^{14}C calibration in the polar regions when △R reconstruction is not available in study areas. This new method leads to significant changes in age models due to very large values of modelled reservoir age before the Holocene, challenging not only our findings but also most published sedimentary records from the high-latitude regions (Fig. 6.1). More discussion about the reliability of modelled reservoir ages is required for future study, and more proxy-based reservoir age reconstructions during the glacial period are also needed (cf., Bondevik et al., 2006; Cao et al., 2007).

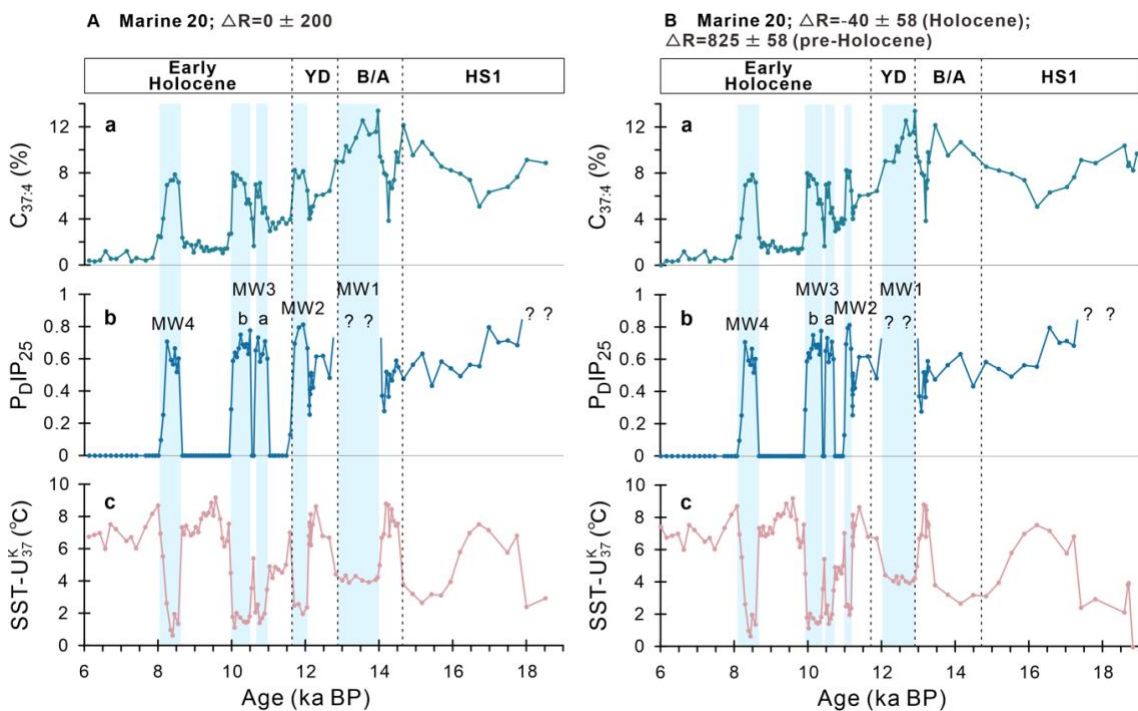**Fig. 6.1 Proxy records of Core MSS12/2-05-01 based on different reservoir ages.**
A proxy records based on the local reservoir age used in this study; **B** proxy records based on the local reservoir referred to Heaton et al., (2023).

7 References

Abbott P. M. and Davies S. M. (2012) Volcanism and the Greenland ice-cores: The tephra record. *Earth Sci Rev* 115, 173–191.

Alkire M. B., D'Asaro E., Lee C., Jane Perry M., Gray A., Cetinić I., Briggs N., Rehm E., Kallin E., Kaiser J. and González-Posada A. (2012) Estimates of net community production and export using high-resolution, Lagrangian measurements of O_2, NO^{3-}, and POC through the evolution of a spring diatom bloom in the North Atlantic. *Deep Sea Res 1 Oceanogr Res Pap* 64, 157–174.

Allan E., Douglas P. M. J., de Vernal A., Gélinas Y. and Mucci A. O. (2023) Palmitic Acid Is Not a Proper Salinity Proxy in Baffin Bay and the Labrador Sea but Reflects the Variability in Organic Matter Sources Modulated by Sea Ice Coverage. *Geochemistry, Geophysics, Geosystems* 24, 1–22.

Alley R. B., Andrews J. T., Brigham-Grette J., Clarke G. K. C., Cuffey K. M., Fitzpatrick J. J., Funder S., Marshall S. J., Miller G. H., Mitrovica J. X., Muhs D. R., Otto-Bliesner B. L., Polyak L. and White J. W. C. (2010) History of the Greenland Ice Sheet: paleoclimatic insights. *Quat Sci Rev* 29, 1728–1756.

Alley R. B. and MacAyeal D. R. (1994) Ice-rafted debris associated with binge/purge oscillation of the Laurentide Ice Sheet. *Paleoceonography* 9, 503–511.

Alvarez-Solas J., Charbit S., Ritz C., Paillard D., Ramstein G. and Dumas C. (2010) Links between ocean temperature and iceberg discharge during Heinrich events. *Nat Geosci* 3, 122–126.

Ambaum M. H. P., Hoskins B. J. and Stephenson D. B. (2001) Arctic Oscillation or North Atlantic Oscillation? *J Clim* 14, 3495–3507.

Anand P., Elderfield H. and Conte M. H. (2003) Calibration of Mg/Ca thermometry in planktonic foraminifera from a sediment trap time series. *Paleoceanography* 18.

Anderson J. B. and Andrews J. T. (1999) Radiocarbon constraints on ice sheet advance and retreat in the Weddell Sea, Antarctica. *Geology* 27, 179–182.

Andrews J. T., Cabedo-Sanz P., Jennings A. E., Ólafsdóttir S., Belt S. T. and Geirsdóttir (2018) Sea ice, ice-rafting, and ocean climate across Denmark Strait during rapid deglaciation (~16–12 cal ka BP) of the Iceland and East Greenland shelves. *J Quat Sci* 33, 112–130.

Andrews J. T., Dunhill G., Vogt C. and Voelker A. H. L. (2017) Denmark Strait during the Late Glacial Maximum and Marine Isotope Stage 3: Sediment sources and transport processes. *Mar Geol* 390, 181–198.

Andrews J. T., Jennings A. E., Kerwin M., Kirby M., Manley W. and Bond G. (1995) A Heinrich-like event, H-0 (DC-0): Source(s) for detrital carbonate in the North Atlantic during the Younger Dryas Chronozone. *Paleoceanography* 10, 943–952.

Andrews J. T. and Voelker A. H. L. (2018) "Heinrich events" (& sediments): A history of terminology and recommendations for future usage. *Quat Sci Rev* 187, 31–40.

Ardyna M. and Arrigo K. R. (2020) Phytoplankton dynamics in a changing Arctic Ocean. *Nat Clim Chang* 10, 892–903.

Austin W. E. N., Bard E., Hunt J. B., Kroon D. and Peacock J. D. (1995) The 14C age of the Icelandic Vedde Ash: implications for Younger Dryas marine reservoir age corrections. *Radiocarbon* 37, 53–62.

Badger M. P. S. (2021) Alkenone isotopes show evidence of active carbon concentrating mechanisms in coccolithophores as aqueous carbon dioxide concentrations fall below 7 μmolL-1. *Biogeosciences* 18, 1149–1160.

Bakke J., Lie O., Heegaard E., Dokken T., Haug G. H., Birks H. H., Dulski P. and Nilsen T. (2009) Rapid oceanic and atmospheric changes during the Younger Dryas cold period. *Nat Geosci* 2, 202–205.

Baldini J. U. L., Brown R. J. and Mawdsley N. (2018) Evaluating the link between the sulfur-rich Laacher See volcanic eruption and the Younger Dryas climate anomaly. *Climate of the Past* 14, 969–990.

Ballini M., Kissel C., Colin C. and Richter T. (2006) Deep-water mass source and dynamic associated with rapid climatic variations during the last glacial stage in the North Atlantic: A multiproxy investigation of the detrital fraction of deep-sea sediments. *Geochemistry, Geophysics, Geosystems* 7, Q02N01.

Barber D. C., Dyke A., Hillaire-Marcel C., Jennings A. E., Andrews J. T., Kerwin M. W., Bilodeau G., McNeely R., Southon J., Morehead M. D. and Gagnon J. M. (1999) Forcing of the cold event of 8,200 years ago by catastrophic drainage of Laurentide lakes. *Nature* 400, 344–348.

Bard E., Rostek F., Turon J. L. and Gendreau S. (2000) Hydrological impact of Heinrich events in the subtropical Northeast Atlantic. *Science* 289, 1321–1324.

Barker S., Chen J., Gong X., Jonkers L., Knorr G. and Thornalley D. (2015) Icebergs not the trigger for North Atlantic cold events. *Nature* 520, 333–336.

Barker S. and Knorr G. (2021) Millennial scale feedbacks determine the shape and rapidity of glacial termination. *Nat Commun* 12, 1–12.

Barker S., Zhang X., Jonkers L., Lordsmith S., Conn S. and Knorr G. (2021) Strengthening Atlantic Inflow Across the Mid-Pleistocene Transition. *Paleoceanogr Paleoclimatol* 36, 1–23.

Bartels M., Titschack J., Fahl K., Stein R., Seidenkrantz M. S., Hillaire-Marcel C. and Hebbeln D. (2017) Atlantic Water advection vs. glacier dynamics in northern Spitsbergen since early deglaciation. *Climate of the Past* 13, 1717–1749.

Batchelor C. L., Margold M., Krapp M., Murton D. K., Dalton A. S., Gibbard P. L., Stokes C. R., Murton J. B. and Manica A. (2019) The configuration of Northern Hemisphere ice sheets through the Quaternary. *Nat Commun* 10, 1–10.

Bellomo K., Angeloni M., Corti S. and von Hardenberg J. (2021) Future climate change shaped by inter-model differences in Atlantic meridional overturning circulation response. *Nat Commun* 12, 1–10.

Belt S. T. (2018) Source-specific biomarkers as proxies for Arctic and Antarctic sea ice. *Org Geochem* 125, 277–298.

Belt S. T., Cabedo-Sanz P., Smik L., Navarro-Rodriguez A., Berben S. M. P., Knies J. and Husum K. (2015) Identification of paleo Arctic winter sea ice limits and the marginal ice zone: Optimised biomarker-based reconstructions of late Quaternary Arctic sea ice. *Earth Planet Sci Lett* 431, 127–139.

Belt S. T., Massé G., Rowland S. J., Poulin M., Michel C. and LeBlanc B. (2007) A novel chemical fossil of palaeo sea ice: IP25. *Org Geochem* 38, 16–27.

Belt S. T. and Müller J. (2013) The Arctic sea ice biomarker IP$_{25}$: a review of current understanding, recommendations for future research and applications in palaeo sea ice reconstructions. *Quat Sci Rev* 79, 9–25.

Belt S. T., Smik L., Köseoğlu D., Knies J. and Husum K. (2019) A novel biomarker-based proxy for the spring phytoplankton bloom in Arctic and sub-arctic settings – HBI T25. *Earth Planet Sci Lett* 523, 115703.

Bendle J., Rosell-Melé A. and Ziveri P. (2005) Variability of unusual distributions of alkenones in the surface waters of the Nordic seas. *Paleoceanography* 20, PA2001.

Benway H. M., McManus J. F., Oppo D. W. and Cullen J. L. (2010) Hydrographic changes in the eastern subpolar North Atlantic during the last deglaciation. *Quat Sci Rev* 29, 3336–3345.

Berger W. H. (1990) The younger dryas cold spell-a quest for causes. *Palaeogeogr Palaeoclimatol Palaeoecol* 89, 219–237.

Bhatia M. P., Kujawinski E. B., Das S. B., Breier C. F., Henderson P. B. and Charette M. A. (2013) Greenland meltwater as a significant and potentially bioavailable source of iron to the ocean. *Nat Geosci* 6, 274–278.

Bianchi G. G., Hall I. R., McCave I. N. and Joseph L. (1999) Measurement of the sortable silt current speed proxy using the Sedigraph 5100 and Coulter Multisizer Ile: Precision and accuracy. *Sedimentology* 46, 1001–1014.

Bianchi G. G. and McCave I. N. (1999) Holocene periodicity in North Atlantic climate and deep-ocean flow south of Iceland. *Nature* 397, 515–517.

Blaauw M. and Christen J. A. (2011) Flexible paleoclimate age-depth models using an autoregressive gamma process. *Bayesian Anal* 6, 457–474.

Blaga C. I., Reichart G. J., Heiri O. and Sinninghe Damsté J. S. (2009) Tetraether membrane lipid distributions in water-column particulate matter and sediments: A study of 47 European lakes along a north-south transect. *J Paleolimnol* 41, 523–540.

Blaser P., Gutjahr M., Pöppelmeier F., Frank M., Kaboth-Bahr S. and Lippold J. (2020) Labrador Sea bottom water provenance and REE exchange during the past 35,000 years. *Earth Planet Sci Lett* 542, 116299.

Bohm E., Lippold J., Gutjahr M., Frank M., Blaser P., Antz B., Fohlmeister J., Frank N., Andersen M. B. and Deininger M. (2015) Strong and deep Atlantic meridional overturning circulation during the last glacial cycle. *Nature* 517, 73–76.

Bohrmann G. and Stein R. (1989) Biogenic silica at ODP Site 647 in the southern Labrador Sea: occurrence, diagenesis, and paleoceanographic implications. *Proceedings of the Ocean Drilling Program: Scientific Results* 105, 155–170.

Bond G. C. and Lotti R. (1995) Iceberg discharges into the North Atlantic on millennial time scales during the last glaciation. *Science* 267, 1005–1010.

Bond G., Kromer B., Beer J., Muscheler R., Evans M. N., Showers W., Hoffmann S., Lotti-Bond R., Hajdas I. and Bonani G. (2001) Persistent solar influence on north atlantic climate during the Holocene. *Science* 294, 2130–2136.

Bond G., Showers W., Cheseby M., Lotti R., Almasi P., DeMenocal P., Priore P., Cullen H., Hajdas I. and Bonani G. (1997) A pervasive millennial-scale cycle in North Atlantic Holocene and glacial climates. *Science* 278, 1257–1266.

Bondevik S., Mangerud J., Birks H. H., Gulliksen S. and Reimer P. (2006) Changes in North Atlantic Radiocarbon Reservoir Ages During the Allerød and Younger Dryas. *Science* 312, 1514–1517.

Böning C. W., Behrens E., Biastoch A., Getzlaff K. and Bamber J. L. (2016) Emerging impact of Greenland meltwater on deepwater formation in the North Atlantic Ocean. *Nat Geosci* 9, 523–527.

Box J. E., Hubbard A., Bahr D. B., Colgan W. T., Fettweis X., Mankoff K. D., Wehrlé A., Noël B., van den Broeke M. R., Wouters B., Bjørk A. A. and Fausto R. S. (2022) Greenland ice sheet climate disequilibrium and committed sea-level rise. *Nat Clim Chang* 12.

Brassell S. C., Eglinton G., Marlowe I. T., Pflaumann U. and Sarnthein M. (1986) Molecular stratigraphy: A new tool for climatic assessment. *Nature* 320, 129–133.

Brendryen J., Haflidason H., Yokoyama Y., Haaga K. A. and Hannisdal B. (2020) Eurasian Ice Sheet collapse was a major source of Meltwater Pulse 1A 14,600 years ago. *Nat Geosci* 13, 363–368.

Briner J. P., Cuzzone J. K., Badgeley J. S., Young N. E., Steig E. J., Morlighem M., Schlegel N.-J., Hakim G. J., Schaefer J., Johnson J. V., Lesnek A. J., Thomas E. K., Allan E., Bennike O., Cluett A. A., Csatho B., Vernal A. de., Downs J., Larour E. and Nowicki S. (2020) Rate of mass loss from the Greenland Ice Sheet will exceed Holocene values this century. *Nature* 586, 70–74.

Broecker, W., Bond, G., Klas, M., Clark, E., & McManus, J. (1992). Origin of the northern Atlantic's Heinrich events. *Clim Dyn*, 6, 265-273.

Broecker W. S. (2006) Was the Younger Dryas triggered by a flood? *Science* 312, 1146–1148.

Brown T. A., Belt S. T., Tatarek A. and Mundy C. J. (2014) Source identification of the Arctic sea ice proxy IP 25. *Nat Commun* 5, 4197.

Caesar L., McCarthy G. D., Thornalley D. J. R., Cahill N. and Rahmstorf S. (2021) Current Atlantic Meridional Overturning Circulation weakest in last millennium. *Nat Geosci* 14, 118–120.

Caesar L., Rahmstorf S., Robinson A., Feulner G. and Saba V. (2018) Observed fingerprint of a weakening Atlantic Ocean overturning circulation. *Nature* 556, 191–196.

Cage A. G., Pieńkowski A. J., Jennings A., Luise Knudsen K. and Seidenkrantz M. S. (2021) Comparative analysis of six common foraminiferal species of the genera *Cassidulina*, *Paracassidulina*, and *Islandiella* from the Arctic-North Atlantic domain. *J Micropalaeontol* 40, 37–60.

Cao L., Fairbanks R. G., Mortlock R. A. and Risk M. J. (2007) Radiocarbon reservoir age of high latitude North Atlantic surface water during the last deglacial. *Quat Sci Rev* 26, 732–742.

Carlson A. E., Stoner J. S., Donnelly J. P. and Hillaire-Marcel C. (2008) Response of the southern Greenland Ice Sheet during the last two deglaciations. *Geology* 36, 359–362.

Caron M., Rochon A., Montero-Serrano J. C. and St-Onge G. (2019) Evolution of sea-surface conditions on the northwestern Greenland margin during the Holocene. *J Quat Sci* 34, 569–580.

Carstens J., Hebbeln D. and Wefer G. (1997) Distribution of planktic foraminifera at the ice margin in the Arctic (Fram Strait). *Mar Micropaleontol* 29, 257–269.

Cartapanis O., Jonkers L., Moffa-Sanchez P., Jaccard S. L. and de Vernal A. (2022) Complex spatio-temporal structure of the Holocene Thermal Maximum. *Nat Commun* 13.

Catania G. A., Stearns L. A., Moon T. A., Enderlin E. M. and Jackson R. H. (2019) Future Evolution of Greenland's Marine-Terminating Outlet Glaciers. *J Geophys Res Earth Surf* 125, 1–28.

Chalk T. B., Hain M. P., Foster G. L., Rohling E. J., Sexton P. F., Badger M. P. S., Cherry S. G., Hasenfratz A. P., Haug G. H., Jaccard S. L., Martínez-García A., Pälike H., Pancost R. D. and Wilson P. A. (2017) Causes of ice age intensification across the mid-pleistocene transition. *Proc Natl Acad Sci U S A* 114, 13114–13119.

Chan P., Halfar J., Adey W., Hetzinger S., Zack T., Moore G. W. K., Wortmann U. G., Williams B. and Hou A. (2017) Multicentennial record of Labrador Sea primary productivity and sea-ice variability archived in coralline algal barium. *Nat Commun* 8, 1–10.

Channell J. E. T., Harrison R. J., Lascu I., McCave I. N., Hibbert F. D. and Ausin W. E. N. (2016) Magnetic record of deglaciation using FORC-PCA, sortable-silt grain size, and magnetic excursion at 26 ka, from the Rockall Trough (NE Atlantic). *Geochemistry Geophysics Geosystems* 17, 1823–1841.

Channell J. E. T., Hodell D. A., Romero O., Hillaire-Marcel C., de Vernal A., Stoner J. S., Mazaud A. and Röhl U. (2012) A 750-kyr detrital-layer stratigraphy for the North Atlantic (IODP Sites U1302-U1303, Orphan Knoll, Labrador Sea). *Earth Planet Sci Lett* 317–318, 218–230.

Cheng H., Zhang H., Spötl C., Baker J., Sinha A., Li H., Bartolomé M., Moreno A., Kathayat G., Zhao J., Dong X., Li Y., Ning Y., Jia X., Zong B., Brahim Y. A., Pérez-Mejiás C., Cai Y., Novello V. F., Cruz F. W., Severinghaus J. P., An Z. and Edwards R. L. (2020) Timing and structure of the Younger Dryas event and its underlying climate dynamics. *Proc Natl Acad Sci U S A* 117, 23408–23417.

Choi Y., Morlighem M., Rignot E. and Wood M. (2021) Ice dynamics will remain a primary driver of Greenland ice sheet mass loss over the next century. *Commun Earth Environ* 2, 1–9.

Clark D. L. and Hanson A. (1983) Central Arctic Ocean Sediment Texture: A Key to Ice Transport Mechanisms. In *Glacial-Marine Sedimentation* pp. 301–330.

Clark P. U., Archer D., Pollard D., Blum J. D., Rial J. A., Brovkin V., Mix A. C., Pisias N. G. and Roy M. (2006) The middle Pleistocene transition: characteristics, mechanisms, and implications for long-term changes in atmospheric pCO2. *Quat Sci Rev* 25, 3150–3184.

Clark P. U., Dyke A. S., Shakun J. D., Carlson A. E., Clark J., Wohlfarth B., Mitrovica J. X., Hostetler S. W. and McCabe A. M. (2009) The Last Glacial Maximum. *Science* 325, 710–714.

Clark P. U., He F., Golledge N. R., Mitrovica J. X., Dutton A., Hoffman J. S. and Dendy S. (2020) Oceanic forcing of penultimate deglacial and last interglacial sea-level rise. *Nature* 577, 660–664.

Colville E. J., Carlson A. E., Beard B. L., Hatfield R. G., Stoner J. S., Reyes A. V. and Ullman D. J. (2011) Sr-Nd-Pb isotope evidence for ice-sheet presence on southern Greenland during the Last Interglacial. *Science* 333, 620–623.

Condron A., Joyce A. J. and Bradley R. S. (2020) Arctic sea ice export as a driver of deglacial climate. *Geology* 48, 395–399.

Condron A. and Winsor P. (2012) Meltwater routing and the Younger Dryas. *Proc Natl Acad Sci U S A* 109, 19928–19933.

Consolaro C., Rasmussen T. L. and Panieri G. (2018) Palaeoceanographic and environmental changes in the eastern Fram Strait during the last 14,000 years based on benthic and planktonic foraminifera. *Mar Micropaleontol* 139, 84–101.

Corella J. P., Maffezzoli N., Spolaor A., Vallelonga P., Cuevas C. A., Scoto F., Müller J., Vinther B., Kjær H. A., Cozzi G., Edwards R., Barbante C. and Saiz-Lopez A. (2022) Climate changes modulated the history of Arctic iodine during the Last Glacial Cycle. *Nat Commun* 13, 1–9.

Crivellari S., Chiessi C. M., Kuhnert H., Häggi C., da Costa Portilho-Ramos R., Zeng J. Y., Zhang Y., Schefuß E., Mollenhauer G., Hefter J., Alexandre F., Sampaio G. and Mulitza S. (2018) Increased Amazon freshwater discharge during late Heinrich Stadial 1. *Quat Sci Rev* 181, 144–155.

Cronin T. M., Deninno L. H., Polyak L., Caverly E. K., Poore R. Z., Brenner A., Rodriguez-Lazaro J. and Marzen R. E. (2014) Quaternary ostracode and foraminiferal biostratigraphy and paleoceanography in the western Arctic Ocean. *Mar Micropaleontol* 111, 118–133.

Cronin T. M., Gemery L., Briggs W. M., Jakobsson M., Polyak L. and Brouwers E. M. (2010) Quaternary Sea-ice history in the Arctic Ocean based on a new Ostracode sea-ice proxy. *Quat Sci Rev* 29, 3415–3429.

Cronin T. M., Smith S. A., Eynaud F., Regan M. O.' and King J. (2008) Quaternary paleoceanography of the central Arctic based on Integrated Ocean Drilling Program Arctic Coring Expedition 302 foraminiferal assemblages. *Paleoceanography* 23, PA1S18.

Crosta X. and Koç N. (2007) Chapter Eight Diatoms: From Micropaleontology to Isotope Geochemistry. *Developments in Marine Geology* 1, 327–369.

Crosta X., Pichon J.-J. and Burckle L. H. (1998) Application of modern analog technique to marine Antarctic and to reconstruct the modem We then use this approach to reconstruct presence in number of months per year during the last glacial maximum presence was greater than north of its the of modem sea. *Paleoceanography* 13, 284–297.

Cuny J., Rhines P. B. and Kwok R. (2005) Davis Strait volume, freshwater and heat fluxes. *Deep Sea Res 1 Oceanogr Res Pap* 52, 519–542.

Curry J. A., Schramm J. L. and Ebert E. E. (1995) Sea I ce-Albedo Climate Feedback Mechanism. *J Clim* 8, 240–247.

Dahl-Jensen D., Mosegaard K., Gundestrup N., Clow G. D., Johnsen S. J., Hansen A. W. and Balling N. (1998) Past temperatures directly from the Greenland Ice Sheet. *Science* 282, 268–271.

Dai A., Luo D., Song M. and Liu J. (2019) Arctic amplification is caused by sea-ice loss under increasing CO 2. *Nat Commun* 10, 1–13.

Dansgaard W., Johnsen S. J., Clausen H. B., Dahl-Jensen D., Gundestrup N. S., Hammer C. U., Hvidberg.C.S., Steffensen J. P., Sveinbjörnsdóttir Á. E., Jouzel J. and Bond G. (1993) Evidence for general instability of past climate from a 250-kyr ice-core record. *Nature* 364, 218–220.

Darby D. A., Ortiz J. D., Grosch C. E. and Lund S. P. (2012) 1,500-year cycle in the Arctic Oscillation identified in Holocene Arctic sea-ice drift. *Nat Geosci* 5, 897–900.

DeConto R. M. and Pollard D. (2016) Contribution of Antarctica to past and future sea-level rise. *Nature* 531, 591–597.

Denton G. H., Anderson R. F., Toggweiler J. R., Edwards R. L., Schaefer J. M. and Putnam A. E. (2010) The last glacial termination. *Science* 328, 1652–1656.

Deschamps P., Durand N., Bard E., Hamelin B., Camoin G., Thomas A. L., Henderson G. M., Okuno J. and Yokoyama Y. (2012) Ice-sheet collapse and sea-level rise at the Bølling warming 14,600 years ago. *Nature* 483, 559–564.

Dethleff D. (2005) Entrainment and export of Laptev Sea ice sediments, Siberian Arctic. *J Geophys Res Oceans* 110, 1–17.

Devillers R. and De Vernal A. (2000) Distribution of dinoflagellate cysts in surface sediments of the northern North Atlantic in relation to nutrient content and productivity in surface waters. *Mar Geol* 166, 103–124.

Ditlevsen P. D. and Ditlevsen S. (2023) Warning of a forthcoming collapse of the Atlantic meridional overturning circulation. *Nat Commun*, 1–12.

Dokken T. M., Nisancioglu K. H., Li C., Battisti D. S. and Kissel C. (2013) Dansgaard-Oeschger cycles: Interactions between ocean and sea ice intrinsic to the Nordic seas. *Paleoceanography* 28, 491–502.

Drinkwater K. F. (1996) Atmospheric and oceanic variability in the northwest Atlantic during the 1980s and early 1990s. *Journal of Northwest Atlantic Fishery Science* 18, 77–97.

Duplessy L. Labeyrie, M. Arnold, M. Paterne, J. Duprat, and T.C.E. Vanweering J. C., Duplessy J. C., Labeyrie L., Arnold M., Paterne M., Duprat J. and van Weering (1992) Changes in surface salinity of the North Atlantic Ocean during the last deglaciation. *Nature* 358, 485–488.

Dypvik H. and Harris N. B. (2001) Geochemical facies analysis of fine-grained siliciclastics using Th/U, Zr/Rb and (Zr + Rb)/Sr ratios. *Chem Geol* 181, 131–146.

Elderfield H. and Ganssen G. (2000) Past temperature and δ18O of surface ocean waters inferred from foraminiferal Mg/Ca ratios. *Nature* 405, 442–445.

Elliot M., Labeyrie L., Bond G., Cortijo E., Turon J. L., Tisnerat N. and Duplessy J. C. (1998) Millennial-scale iceberg discharges in the Irminger Basin during the last glacial period: Relationship with the Heinrich events and environmental settings. *Paleoceanography* 13, 433–446.

Elliot M., Labeyrie L. and Duplessy J. C. (2002) Changes in North Atlantic deep-water formation associated with the Dansgaard - Oeschger temperature oscillations (60-10 ka). *Quat Sci Rev* 21, 1153–1165.

Elmore A. C., Wright J. D. and Chalk T. B. (2015) Precession-driven changes in Iceland-Scotland Overflow Water penetration and bottom water circulation on Gardar Drift since ~200ka. *Palaeogeogr Palaeoclimatol Palaeoecol* 440, 551–563.

Elverhøi A., Dowdeswell J. A., Funder S., Mangerud J. and Stein R. (1998) Glacial and oceanic history of the polar north atlantic margins: An overview. *Quat Sci Rev* 17, 1–10.

Evans H. F., Channell J. E. T., Stoner J. S., Hillaire-Marcel C., Wright J. D., Neitzke L. C. and Mountain G. S. (2007) Paleointensity-assisted chronostratigraphy of detrital layers on the Eirik Drift (North Atlantic) since marine isotope stage 11. *Geochemistry, Geophysics, Geosystems* 8.

Evans J., Dowdeswell J. A., Grobe H., Niessen F., Stein R., Hubberten H. W. and Whittington R. J. (2002) Late Quaternary sedimentation in Kejser Franz Joseph Fjord and the continental margin of East Greenland. *Geol Soc Spec Publ* 203, 149–179.

Ezat M. M., Rasmussen T. L., Hönisch B., Groeneveld J. and Demenocal P. (2017) Episodic release of CO 2 from the high-latitude North Atlantic Ocean during the last 135 kyr. *Nat Commun* 8.

Fagel N., Robert C. and Hillaire-Marcel C. (1996) Clay mineral signature of the NW Atlantic Boundary Undercurrent. *Mar Geol* 130, 19–28.

Fahl K. and Stein R. (1999) Biomarkers as organic-carbon-source and environmental indicators in the late quaternary Arctic Ocean: Problems and perspectives. *Mar Chem* 63, 293–309.

Fahl K. and Stein R. (2012) Modern seasonal variability and deglacial/Holocene change of central Arctic Ocean sea-ice cover: New insights from biomarker proxy records. *Earth Planet Sci Lett* 351–352, 123–133.

Filippova A., Kienast M., Frank M. and Schneider R. R. (2016) Alkenone paleothermometry in the North Atlantic: A review and synthesis of surface sediment data and calibrations. *Geochemistry Geophysics Geosystems* 17, 1370–1382.

Flower B. P., Hastings D. W., Hill H. W. and Quinn T. M. (2004) Phasing of deglacial warming and Laurentide Ice Sheet meltwater in the Gulf of Mexico. *Geology* 32, 597–600.

Flowers G. E. (2018) Hydrology and the future of the Greenland Ice Sheet. *Nat Commun* 9, 1–4.

Frajka-Williams E. and Rhines P. B. (2010) Physical controls and interannual variability of the Labrador Sea spring phytoplankton bloom in distinct regions. *Deep Sea Res 1 Oceanogr Res Pap* 57, 541–552.

Frey K. E., Moore G. W. K., Cooper L. W. and Grebmeier J. M. (2015) Divergent patterns of recent sea ice cover across the Bering, Chukchi, and Beaufort seas of the Pacific Arctic Region. *Prog Oceanogr* 136, 32–49.

Fried N. and de Jong M. F. (2022) The Role of the Irminger Current in the Irminger Sea Northward Transport Variability. *J Geophys Res Oceans* 127, 1–16.

Funder S., Sørensen A. H. L., Larsen N. K., Bjørk A. A., Briner J. P., Olsen J., Schomacker A., Levy L. B. and Kjær K. H. (2021) Younger Dryas ice margin retreat in Greenland: New evidence from southwestern Greenland. *Climate of the Past* 17, 587–601.

Ganopolski A. and Rahmstorf S. (2001) Rapid changes of glacial climate simulated in a coupled climate model. *Nature* 409, 153–158.

Gemery L., Cronin T. M., Poirier R. K., Pearce C., Barrientos N., O'Regan M., Johansson C., Koshurnikov A. and Jakobsson M. (2017) Central Arctic Ocean paleoceanography from∼ 50 ka to present, on the basis of ostracode faunal assemblages from the SWERUS 2014 expedition. *Climate of the Past* 13, 1473–1489.

Gersonde R. and Zielinski U. (2000) The reconstruction of late Quaternary Antarctic sea-ice distribution - The use of diatoms as a proxy for sea-ice. *Palaeogeogr Palaeoclimatol Palaeoecol* 162, 263–286.

Gibb O. T., Hillaire-Marcel C. and de Vernal A. (2014) Oceanographic regimes in the northwest Labrador Sea since Marine Isotope Stage 3 based on dinocyst and stable isotope proxy records. *Quat Sci Rev* 92, 269–279.

Gibb O. T., Steinhauer S., Fréchette B., de Vernal A. and Hillaire-Marcel C. (2015) Diachronous evolution of sea surface conditions in the labrador sea and baffin bay since the last deglaciation. *Holocene* 25, 1882–1897.

Gil I. M., Keigwin L. D. and Abrantes F. (2015) The deglaciation over Laurentian Fan: History of diatoms, IRD, ice and fresh water. *Quat Sci Rev* 129, 57–67.

Gregoire L. J., Otto-Bliesner B., Valdes P. J. and Ivanovic R. (2016) Abrupt Bølling warming and ice saddle collapse contributions to the Meltwater Pulse 1a rapid sea level rise. *Geophys Res Lett* 43, 9130–9137.

Griem L., Voelker A. H. L., Berben S. M. P., Dokken T. M. and Jansen E. (2019) Insolation and Glacial Meltwater Influence on Sea-Ice and Circulation Variability in the Northeastern Labrador Sea During the Last Glacial Period. *Paleoceanogr Paleoclimatol* 34, 1689–1709.

Grobe H. (1987) A Simple Method for the Determination of Ice-Rafted Debris in Sediment Cores. *Polarforschung* 57, 123–126.

Grootes P. M., Stuiver M., White J. W. C., Johnsen S. and Jouzel J. (1993) Comparison of oxygen isotope records from the GISP2 and GRIP Greenland ice cores. *Nature* 366, 552–554.

Grousset F. E., Labeyrie L., Sinko J. a, Bond G., Duprat J. and Cortijo E. (1993) Patterns of ice-rafted detritus in the glacial North Atlantic (40–55° N). *Atlantic* 8, 175–192.

Grützner J. and Higgins S. M. (2010) Threshold behavior of millennial scale variability in deep water hydrography inferred from a 1.1 Ma long record of sediment provenance at the southern Gardar Drift. *Paleoceanography* 25, PA4204.

Häggi C., Chiessi C. M. and Schefuß E. (2015) Testing the D/H ratio of alkenones and palmitic acid as salinity proxies in the Amazon Plume. *Biogeosciences* 12, 7239–7249.

Harning D. J., Holman B., Woelders L., Jennings A. E. and Sepúlveda J. (2023) Biomarker characterization of the North Water Polynya, Baffin Bay: Implications for local sea ice and temperature proxies. *Biogeosciences* 20, 229–249.

He C., Liu Z., Zhu J., Zhang J., Gu S., Otto-Bliesner B. L., Brady E., Zhu C., Jin Y. and Sun J. (2020) North Atlantic subsurface temperature response controlled by effective freshwater input in "Heinrich" events. *Earth Planet Sci Lett* 539, 116247.

Heaton T. J., Butzin M., Bard É., Ramsey C. B., Hughen K. A., Köhler P. and Reimer P. J. (2023) Marine Radiocarbon Calibration in Polar Regions: A Simple Approximate Approach using Marine20. *Radiocarbon* 00, 1–28.

Heaton T. J., Köhler P., Butzin M., Bard E., Reimer R. W., Austin W. E. N., Bronk Ramsey C., Grootes P. M., Hughen K. A., Kromer B., Reimer P. J., Adkins J., Burke A., Cook M. S., Olsen J. and Skinner L. C. (2020) Marine20 - the marine radiocarbon age calibration curve (0-55,000 cal BP). *Radiocarbon* 62, 779–820.

Hebbeln D., Henrich R. and Baumann K. H. (1998) Paleoceanography of the last interglacial/glacial cycle in the Polar North Atlantic. *Quat Sci Rev* 17, 125–153.

Hefter J., Naafs B. D. A. and Zhang S. (2017) Tracing the source of ancient reworked organic matter delivered to the North Atlantic Ocean during Heinrich Events. *Geochim Cosmochim Acta* 205, 211–225.

Heinrich H. (1988) Origin and consequences of cyclic ice rafting in the Northeast Atlantic Ocean during the past 130,000 years. *Quat Res* 29, 142–152.

Hemming S. R. (2004) Heinrich events: Massive late Pleistocene detritus layers of the North Atlantic and their global climate imprint. *Reviews of Geophysics* 42, RG1005.

Hemming S. R. and Hajdas I. (2003) Ice-rafted detritus evidence from 40Ar/39Ar ages of individual hornblende grains for evolution of the eastern margin of the Laurentide ice sheet since 43 14C ky. *Quaternary International* 99–100, 29–43.

Henderson S. S. (2009) Tracking Deep-Water Flow On Eirik Drift Over The Past 160 Kyr: Linking Deep-Water Changes To Freshwater Fluxes. Doctoral dissertation, Rutgers The State University of New Jersey.

Henry L. G., McManus J. F., Curry W. B., Roberts N. L., Piotrowski A. M. and Keigwin L. D. (2016) North Atlantic ocean circulation and abrupt climate change during the last glaciation. *Science* 353, 470–474.

Hesse R., Khodabakhsh S., Klaucke I. and Ryan W. B. F. (1997) Asymmetrical turbid surface-plume deposition near ice-outlets of the Pleistocene Laurentide ice sheet in the Labrador Sea. *Geo-Marine Letters* 17, 179–187.

Hillaire-Marcel C., De Vernal A., Bilodeau G. and Weaver A. J. (2001) Absence of deep-water formation in the Labrador Sea during the last interglacial period. *Nature* 410, 1073–1077.

Hodell D. A., Channeil J. E. T., Curtis J. H., Romero O. E. and Röhl U. (2008) Onset of "Hudson Strait" Heinrich events in the eastern North Atlantic at the end of the middle Pleistocene transition (~640 ka)? *Paleoceanography* 23, PA4218.

Hodell D. A., Nicholl J. A., Bontognali T. R. R., Danino S., Dorador J., Dowdeswell J. A., Einsle J., Kuhlmann H., Martrat B., Mleneck-Vautravers M. J., Rodríguez-Tovar F. J. and Röhl U. (2017) Anatomy of Heinrich Layer 1 and its role in the last deglaciation. *Paleoceanography* 32, 284–303.

Hoff U., Rasmussen T. L., Stein R., Ezat M. M. and Fahl K. (2016) Sea ice and millennial-scale climate variability in the Nordic seas 90 kyr ago to present. *Nat Commun* 7.

Hoffman J. S., Carlson A. E., Winsor K., Klinkhammer G. P., LeGrande A. N., Andrews J. T. and Strasser J. C. (2012) Linking the 8.2 ka event and its freshwater forcing in the Labrador Sea. *Geophys Res Lett* 39, 2005–2009.

Hoffmann S. S., Dalsing R. E. and Murphy S. C. (2019) Sortable silt records of intermediate-depth circulation and sedimentation in the Southwest Labrador Sea since the Last Glacial Maximum. *Quat Sci Rev* 206, 99–110.

Hörhold M., Münch T., Weißbach S., Kipfstuhl S., Freitag J., Sasgen I., Lohmann G., Vinther B. and Laepple T. (2023) Modern temperatures in central–north Greenland warmest in past millennium. *Nature* 613, 503–507.

Hughes P. D., Braithwaite R. J., Fenton C. R. and Schnabel C. (2012) Two Younger Dryas glacier phases in the English Lake District: geomorphological evidence and preliminary 10Be exposure ages. *North West Geography* 12, 10–19.

Hugonnet R., McNabb R., Berthier E., Menounos B., Nuth C., Girod L., Farinotti D., Huss M., Dussaillant I., Brun F. and Kääb A. (2021) Accelerated global glacier mass loss in the early twenty-first century. *Nature* 592, 726–731.

Hunter S., Wilkinson D., Louarn E., McCave I. N., Rohling E., Stow D. A. V. and Bacon S. (2007) Deep western boundary current dynamics and associated sedimentation on the Eirik Drift, Southern Greenland Margin. *Deep Sea Res 1 Oceanogr Res Pap* 54, 2036–2066.

Hurrell J. W. (1995) Decadal trends in the North Atlantic oscillation: Regional temperatures and precipitation. *Science* 269, 676–679.

Imbrie J., Boyle E. a, Clemens S. C., Duffy A., Howard W. R., Kukla G., Kutzbach J., Martinson D. G., Mcintyre A., Pisias N. G., Prell W. L., Raytoo M. E. and Shackleton N. J. (1992) On the Structure and Origin of Major Glaciation Cycles 1. Linear Responses to Milankovitch Forcing. *Paleoceanography* 7, 701–738.

Imbrie J. and Kipp N. G. (1971) A new micropaleontological method for quantitative paleoclimatology: Application to a Late Pleistocene Caribbean core, in The Late Cenozoic Glacial Ages. In *The Late Cenozoic Glacial Ages* pp. 71–181.

Inglis G. N., Bhattacharya T., Hemingway J. D., Hollingsworth E. H., Feakins S. J. and Tierney J. E. (2022) Biomarker Approaches for Reconstructing Terrestrial Environmental Change. *Annu Rev Earth Planet Sci* 50, 369–394.

Isarin R. F. B., Renssen H. and Vandenberghe J. (1998) The impact of the North Atlantic Ocean on the Younger Dryas climate in northwestern and central Europe. *J Quat Sci* 13, 447–453.

Ivanovic R. F., Gregoire L. J., Wickert A. D., Valdes P. J. and Burke A. (2017) Collapse of the North American ice saddle 14,500 years ago caused widespread cooling and reduced ocean overturning circulation. *Geophys Res Lett* 44, 383–392.

Jackson L. C., Biastoch A., Buckley M. W., Desbruyères D. G., Frajka-Williams E., Moat B. and Robson J. (2022) The evolution of the North Atlantic Meridional Overturning Circulation since 1980. *Nat Rev Earth Environ* 3, 241–254.

Jackson R. (2017) History of ice sheets surrounding Baffin Bay and its link with oceanic conditions since MIS3. Doctoral dissertation, University of Bremen.

Jackson R., Carlson A. E., Hillaire-Marcel C., Wacker L., Vogt C. and Kucera M. (2017) Asynchronous instability of the North American-Arctic and Greenland ice sheets during the last deglaciation. *Quat Sci Rev* 164, 140–153.

Jackson R., Frederichs T., Schulz H. and Kucera M. (2023) Chronology of detrital carbonate events in Baffin Bay reveals different timing but similar average recurrence time of North American-Arctic and Laurentide ice sheet collapse events during MIS 3. *Earth Planet Sci Lett* 613, 118191.

Jackson R., Kvorning A. B., Limoges A., Georgiadis E., Olsen S. M., Tallberg P., Andersen T. J., Mikkelsen N., Giraudeau J., Massé G., Wacker L. and Ribeiro S. (2021) Holocene polynya dynamics and their interaction with oceanic heat transport in northernmost Baffin Bay. *Sci Rep* 11.

Jakobsson M., Andreassen K., Bjarnadóttir L. R., Dove D., Dowdeswell J. A., England J. H., Funder S., Hogan K., Ingólfsson Ó. and Jennings A. (2014) Arctic Ocean glacial history. *Quat Sci Rev* 92, 40–67.

James A C. and T.C.R. P. (2001) Development of the continental margins of the Labrador Sea: a review. *Geological Society, London, Special Publications* 187, 77–105.

Jennings A., Andrews J., Pearce C., Wilson L. and Ólfasdótttir S. (2015) Detrital carbonate peaks on the Labrador shelf, a 13-7ka template for freshwater forcing from the Hudson Strait outlet of the Laurentide Ice Sheet into the subpolar gyre. *Quat Sci Rev* 107, 62–80.

Jennings A. E., Andrews J. T., Ó Cofaigh C., Onge G. S., Sheldon C., Belt S. T., Cabedo-Sanz P. and Hillaire-Marcel C. (2017) Ocean forcing of Ice Sheet retreat in central west Greenland from LGM to the early Holocene. *Earth Planet Sci Lett* 472, 1–13.

Jennings A. E. and Helgadottir G. (1994) Foraminiferal assemblages from the fjords and shelf of eastern Greenland. *J Foraminifer Res* 24, 123–144.

Jensen M. F., Nilsson J. and Nisancioglu K. H. (2016) The interaction between sea ice and salinity-dominated ocean circulation: implications for halocline stability and rapid changes of sea ice cover. *Clim Dyn* 47, 3301–3317.

Johannessen T., Jansen E., Flatøy A. and Ravelo A. C. (1994) The Relationship between Surface Water Masses, Oceanographic Fronts and Paleoclimatic Proxies in Surface Sediments of the Greenland, Iceland, Norwegian Seas. In *Carbon Cycling in the Glacial Ocean: Constraints on the Ocean's Role*

in Global Change: Quantitative Approaches in Paleoceanography Springer Berlin Heidelberg. pp. 61–85.

Jones P. D. and Mann M. E. (2004) Climate over past millennia. *Reviews of Geophysics* 42.

Jonkers L., Brummer G. J. A., Peeters F. J. C., Van Aken H. M. and De Jong M. F. (2010) Seasonal stratification, shell flux, and oxygen isotope dynamics of leftcoiling N. pachyderma and T. quinqueloba in the western subpolar North Atlantic. *Paleoceanography* 25, PA2204.

Jorissen F. J., Fontanier C. and Thomas E. (2007) Chapter Seven Paleoceanographical Proxies Based on Deep-Sea Benthic Foraminiferal Assemblage Characteristics. *Developments in Marine Geology* 1, 263–325.

Jorissen F. J., Stigter H. C. De and Widmark J. G. V (1995) A conceptual model explaining benthic foraminiferal microhabitats. *Marine Micropaleontogy* 26, 3–15.

Kaufman D. S. and Broadman E. (2023) Revisiting the Holocene global temperature conundrum. *Nature* 614, 425–435.

Keigwin L. D., Klotsko S., Zhao N., Reilly B., Giosan L. and Driscoll N. W. (2018) Deglacial floods in the Beaufort Sea preceded Younger Dryas cooling. *Nat Geosci* 11, 599–604.

Keigwin L. D., Sachs J. P., Rosenthal Y. and Boyle E. A. (2005) The 8200 year B.P. event in the slope water system, western subpolar North Atlantic. *Paleoceanography* 20, 1–14.

Keigwin L. D. and Swift S. A. (2017) Carbon isotope evidence for a northern source of deep water in the glacial western North Atlantic. *Proc Natl Acad Sci U S A* 114, 2831–2835.

Kieke D. and Yashayaev I. (2015) Studies of Labrador Sea Water formation and variability in the subpolar North Atlantic in the light of international partnership and collaboration. *Prog Oceanogr* 132, 220–232.

Kim J. H., van der Meer J., Schouten S., Helmke P., Willmott V., Sangiorgi F., Koç N., Hopmans E. C. and Damsté J. S. S. (2010) New indices and calibrations derived from the distribution of crenarchaeal isoprenoid tetraether lipids: Implications for past sea surface temperature reconstructions. *Geochim Cosmochim Acta* 74, 4639–4654.

King M. D., Howat I. M., Candela S. G., Noh M. J., Jeong S., Noël B. P. Y., van den Broeke M. R., Wouters B. and Negrete A. (2020) Dynamic ice loss from the Greenland Ice Sheet driven by sustained glacier retreat. *Commun Earth Environ* 1, 1–7.

Kireenko L., Tikhonova A., Kozina N. and Matul A. (2022) Image dataset of benthic foraminifera in multicorer and gravity corer sediments from north-western Scotland shelf (North Atlantic Ocean). *Biodivers Data J* 10.

Kissel C., Laj C., Labeyrie L., Dokken T., Voelker A. and Blamart D. (1999) Rapid climatic variations during marine isotopic stage 3: Magnetic analysis of sediments from Nordic Seas and North Atlantic. *Earth Planet Sci Lett* 171, 489–502.

Kleiven H. F., Kissel C., Laj C., Ninnemann U. S., Richter T. O. and Cortijo E. (2008) Reduced North Atlantic deep water coeval with the glacial lake agassiz freshwater outburst. *Science* 319, 60–64.

Knies J., Köseoğlu D., Rise L., Baeten N., Bellec V. K., Bøe R., Klug M., Panieri G., Jernas P. E. and Belt S. T. (2018) Nordic Seas polynyas and their role in preconditioning marine productivity during the Last Glacial Maximum. *Nat Commun* 9, 1–10.

Knies J. and Stein R. (1998) New aspects of organic carbon deposition and its paleoceanographic implications along the Northern Barents Sea Margin during the last 30,000 years. *Paleoceanography* 13, 384–394.

Knutz P. C., Sicre M. A., Ebbesen H., Christiansen S. and Kuijpers A. (2011) Multiple-stage deglacial retreat of the southern Greenland Ice Sheet linked with Irminger Current warm water transport. *Paleoceanography* 26, 1–18.

Kolling H. (2017) Decadal to centennial variability of (sub-) Arctic sea ice distribution and its paleoenvironmental significance. Doctoral dissertation, University of Bremen.

Kolling H. M., Stein R., Fahl K., Sadatzki H., de Vernal A. and Xiao X. (2020) Biomarker Distributions in (Sub)-Arctic Surface Sediments and Their Potential for Sea Ice Reconstructions. *Geochemistry, Geophysics, Geosystems* 21, e2019GC008629.

Kolling H., Schneider R., Gross F., Hamann C., Kienast M., Kienast S., Doering K., Fahl K. and Stein R. (2023) Biomarker Records of Environmental Shifts on the Labrador Shelf During the Holocene. *Paleoceanogr Paleoclimatol* 38, e2022PA004578.

Kostov Y., Johnson H. L., Marshall D. P., Heimbach P., Forget G., Holliday N. P., Lozier M. S., Li F., Pillar H. R. and Smith T. (2021) Distinct sources of interannual subtropical and subpolar Atlantic overturning variability. *Nat Geosci* 14, 491–495.

K.S. M. and D.B. C. (1973) *Geologic Structure of Baffin Bay and Davis Strait as Determined by Geophysical Techniques: Evolution of Arctic Ocean Basin*.,

Kucera M. (2007) Chapter Six Planktonic Foraminifera as Tracers of Past Oceanic Environments. *Developments in Marine Geology* 1, 213–262.

Kucera M., Rhein M. and Gohl K. (2014) *Oceanography and geodynamics in the NW Atlantic and the Baffin Bay-Cruise No. MSM09-July 23-October 29, 2008-Bremen (Germany)-Ponta Delgada (Azores)*.,

Kucera M., Weinelt Mara, Kiefer T., Pflaumann U., Hayes A., Weinelt Martin, Chen M.-T., Mix A. C., Barrows T. T. and Cortijo E. (2005) Reconstruction of sea-surface temperatures from assemblages of planktonic foraminifera: multi-technique approach based on geographically constrained calibration data sets and its application to glacial Atlantic and Pacific Oceans. *Quat Sci Rev* 24, 951–998.

Kurzweil F., Gutjahr M., Vance D. and Keigwin L. (2010) Authigenic Pb isotopes from the Laurentian Fan: Changes in chemical weathering and patterns of North American freshwater runoff during the last deglaciation. *Earth Planet Sci Lett* 299, 458–465.

Labeyrie L., Leclaire H., Waelbroeck C., Cortijo E., Duplessy J. C., Vidal L., Elliot M. and Coat B. Le (1999) Labeyrie, Laurent, et al. "Temporal variability of the surface and deep waters of the North West Atlantic Ocean at orbital and millennial scales. *GEOPHYSICAL MONOGRAPH-AMERICAN GEOPHYSICAL UNION* 112, 77–98.

Lam A. R. and Mark Leckie R. (2020) Late neogene and quaternary diversity and taxonomy of subtropical to temperate planktic foraminifera across the kuroshio current extension, northwest Pacific Ocean. *Micropaleontology* 66, 177–268.

Lambeck K., Rouby H., Purcell A., Sun Y. and Sambridge M. (2014) Sea level and global ice volumes from the Last Glacial Maximum to the Holocene. *Proc Natl Acad Sci U S A* 111, 15296–15303.

Larkin C. S., Ezat M. M., Roberts N. L., Bauch H. A., Spielhagen R. F., Noormets R., Polyak L., Moreton S. G., Rasmussen T. L., Sarnthein M., Tipper E. T. and Piotrowski A. M. (2022) Active Nordic Seas deep-water formation during the last glacial maximum. *Nat Geosci* 15, 925–931.

Laskar J., Robutel P., Joutel F., Gastineau M., Correia A. C. M. and Levrard B. (2004) A long-term numerical solution for the insolation quantities of the Earth. *Astron Astrophys* 428, 261–285.

Lazar K. B. and Polyak L. (2016) Pleistocene benthic foraminifers in the Arctic Ocean: Implications for sea-ice and circulation history. *Mar Micropaleontol* 126, 19–30.

Lecavalier B. S., Milne G. A., Simpson M. J. R., Wake L., Huybrechts P., Tarasov L., Kjeldsen K. K., Funder S., Long A. J., Woodroffe S., Dyke A. S. and Larsen N. K. (2014) A model of Greenland ice sheet deglaciation constrained by observations of relative sea level and ice extent. *Quat Sci Rev* 102, 54–84.

Lekens W. A. H., Sejrup H. P., Haflidason H., Petersen G., Hjelstuen B. and Knorr G. (2005) Laminated sediments preceding Heinrich event 1 in the Northern North Sea and Southern Norwegian Sea: Origin, processes and regional linkage. *Mar Geol* 216, 27–50.

Lemieux-Dudon B., Blayo E., Petit J. R., Waelbroeck C., Svensson A., Ritz C., Barnola J. M., Narcisi B. M. and Parrenin F. (2010) Consistent dating for Antarctic and Greenland ice cores. *Quat Sci Rev* 29, 8–20.

Leng W., von Dobeneck T., Bergmann F., Just J., Mulitza S., Chiessi C. M., St-Onge G. and Piper D. J. W. (2018) Sedimentary and rock magnetic signatures and event scenarios of deglacial outburst floods from the Laurentian Channel Ice Stream. *Quat Sci Rev* 186, 27–46.

Leventer A., Williams D. F. and Kennett J. P. (1982) Dynamics of the Laurentide ice sheet during the last deglaciation: evidence from the Gulf of Mexico. *Earth Planet Sci Lett* 59, 11–17.

Levy L. B., Larsen N. K., Davidson T. A., Strunk A., Olsen J. and Jeppesen E. (2017) Contrasting evidence of Holocene ice margin retreat, south-western Greenland. *J Quat Sci* 32, 604–616.

Levy L. B., Larsen N. K., Knudsen M. F., Egholm D. L., Bjørk A. A., Kjeldsen K. K., Kelly M. A., Howley J. A., Olsen J., Tikhomirov D., Zimmerman S. R. H. and Kjær K. H. (2020) Multi-phased deglaciation of south and southeast Greenland controlled by climate and topographic setting. *Quat Sci Rev* 242, 106454.

Li C. and Born A. (2019) Coupled atmosphere-ice-ocean dynamics in Dansgaard-Oeschger events. *Quat Sci Rev* 203, 1–20.

Lin Y., Hibbert F. D., Whitehouse P. L., Woodroffe S. A., Purcell A., Shennan I. and Bradley S. L. (2021) A reconciled solution of Meltwater Pulse 1A sources using sea-level fingerprinting. *Nat Commun* 12.

Lippold J., Luo Y., Francois R., Allen S. E., Gherardi J., Pichat S., Hickey B. and Schulz H. (2012) Strength and geometry of the glacial Atlantic Meridional Overturning Circulation. *Nat Geosci* 5, 813–816.

Lippold J., Pöppelmeier F., Süfke F., Gutjahr M., Goepfert T. J., Blaser P., Friedrich O., Link J. M., Wacker L., Rheinberger S. and Jaccard S. L. (2019) Constraining the Variability of the Atlantic Meridional Overturning Circulation During the Holocene. *Geophys Res Lett* 46, 11338–11346.

Lisiecki L. E. and Raymo M. E. (2005) A Pliocene-Pleistocene stack of 57 globally distributed benthic δ 18O records. *Paleoceanography* 20, 1–17.

Lisiecki L. E. and Stern J. V (2016) Regional and global benthic δ^{18}O stacks for the last glacial cycle. *Paleoceanography* 31, 1368–1394.

Liu J., Song M., Zhu Z., Horton R. M., Hu Y. and Xie S. P. (2022) Arctic sea-ice loss is projected to lead to more frequent strong El Niño events. *Nat Commun* 13, 1–11.

Liu Y. and He S. (2020) Strengthened linkage between November/December North Atlantic Oscillation and subsequent January european precipitation after the late 1980s. *J Clim* 33, 8281–8300.

Liu Z., Otto-Bliesner B. L., He F., Brady E. C., Tomas R., Clark P. U., Carlson A. E., Lynch-Stieglitz J., Curry W., Brook E., Erickson D., Jacob R., Kutzbach J. and Cheng J. (2009) Transient simulation of last deglaciation with a new mechanism for bølling-allerød warming. *Science* 325, 310–314.

Liu Z., Zhu J., Rosenthal Y., Zhang X., Otto-Bliesner B. L., Timmermann A., Smith R. S., Lohmann G., Zheng W. and Timm O. E. (2014) The Holocene temperature conundrum. *Proc Natl Acad Sci U S A* 111.

Lloyd J., Moros M., Perner K., Telford R. J., Kuijpers A., Jansen E. and McCarthy D. (2011) A 100 yr record of ocean temperature control on the stability of Jakobshavn Isbrae, West Greenland. *Geology* 39, 867–870.

Lochte A. A., Repschläger J., Kienast M., Garbe-Schönberg D., Andersen N., Hamann C. and Schneider R. (2019) Labrador Sea freshening at 8.5 ka BP caused by Hudson Bay Ice Saddle collapse. *Nat Commun* 10, 1–9.

Lochte A., Schneider R., Repschläger J., Kienast M., Blanz T., Garbe-Schönberg D. and Andersen N. (2020) Surface and subsurface Labrador Shelf water mass conditions during the last 6,000 years. *Climate of The Past* 16, 1127–1143.

Lohmann G., Butzin M., Eissner N., Shi X. and Stepanek C. (2020) Abrupt Climate and Weather Changes Across Time Scales. *Paleoceanogr Paleoclimatol* 35, e2019PA003782.

Maffezzoli N., Vallelonga P., Edwards R., Saiz-Lopez A., Turetta C., Astrid Kjær H., Barbante C., Vinther B. and Spolaor A. (2019) A 120 000-year record of sea ice in the North Atlantic? *Climate of the Past* 15, 2031–2051.

Marcott S. A., Clark P. U., Padman L., Klinkhammer G. P., Springer S. R., Liu Z., Otto-Bliesner B. L., Carlson A. E., Ungerer A., Padman J., He F., Cheng J. and Schmittner A. (2011) Ice-shelf collapse from subsurface warming as a trigger for Heinrich events. *Proc Natl Acad Sci U S A* 108, 13415–13419.

Marcott S. a., Shakun J. D., Clark P. U. and Mix A. C. (2013) A Reconstruction of Regional and Global Temperature for the Past 11,300 Years. *Science* 339, 1198–1201.

Margold M., Stokes C. R. and Clark C. D. (2018) Reconciling records of ice streaming and ice margin retreat to produce a palaeogeographic reconstruction of the deglaciation of the Laurentide Ice Sheet. *Quat Sci Rev* 189, 1–30.

Marlowe I. T., Brassell S. C., Eglinton G. and Green J. C. (1984) Long chain unsaturated ketones and esters in living algae and marine sediments. *Org Geochem* 6, 1–7.

Martrat B., Grimalt J. O., Shackleton N. J., Abreu L. de, Hutterli M. A. and Stocker T. F. (2007) Four Climate Cycles of Recurring Deep and Surface Water Destabilizations on the Iberian Margin. *Science* 317, 502–507.

Masson-Delmotte V. P., Zhai P., Pirani S. L., Connors C., Péan S., Berger N., Caud Y., Chen L., Goldfarb M. I., Monteiro S. and M P. (2021) IPCC, 2021: Summary for policymakers. in: Climate change 2021: The physical science basis. contribution of working group i to the sixth assessment report of the intergovernmental panel on climate change.

Matthiessen J., Vernal A., Head M., Okolodkov Y., Zonneveld K. and Harland R. (2005) Modem organic-walled dinoflagellate cysts in arctic marine environments and their (paleo-) environmental significance. *Palaontol Z* 79, 3–51.

Max L., Nürnberg D., Chiessi C. M., Lenz M. M. and Mulitza S. (2022) Subsurface ocean warming preceded Heinrich Events. *Nat Commun* 13, 1–8.

McCarthy G. D., Smeed D. A., Johns W. E., Frajka-Williams E., Moat B. I., Rayner D., Baringer M. O., Meinen C. S., Collins J. and Bryden H. L. (2015) Measuring the Atlantic Meridional Overturning Circulation at 26°N. *Prog Oceanogr* 130, 91–111.

McCave I. N. and Hall I. R. (2006) Size sorting in marine muds: Processes, pitfalls, and prospects for paleoflow-speed proxies. *Geochemistry, Geophysics, Geosystems* 7, Q10N05.

McCave I. N., Manighetti B. and Robinson S. G. (1995) Sortable silt and fine sediment size/composition slicing: Parameters for palaeocurrent speed and palaeoceanography. *Paleoceanography* 10, 593–610.

McClymont E. L., Mackay H., Stevenson M. A., Damm-Johnsen T., Honan E. M., Penny C. E. and Cole Y. A. (2023) Biomarker proxies for reconstructing Quaternary climate and environmental change. *J Quat Sci*, 1–34.

McClymont E. L., Sosdian S. M., Rosell-Melé A. and Rosenthal Y. (2013) Pleistocene sea-surface temperature evolution: Early cooling, delayed glacial intensification, and implications for the mid-Pleistocene climate transition. *Earth Sci Rev* 123, 173–193.

McManus J. F., Francois R., Gherardi J.-M., Keigwin L. D. and Brown-Leger S. (2004) Collapse and rapid resumption of Atlantic meridional circualtion linked to deglacial climate changes. *Nature* 428, 834–837.

Menviel L. C., Skinner L. C., Tarasov L. and Tzedakis P. C. (2020) An ice–climate oscillatory framework for Dansgaard–Oeschger cycles. *Nat Rev Earth Environ* 1, 677–693.

Milankovitch M. (1941) Kanon der Erdbestrahlung und seine Anwendung auf das Eiszeitenproblem. *Royal Serbian Academy Special Publication* 133, 1–633.

Moffa-Sánchez P. and Hall I. R. (2017) North Atlantic variability and its links to European climate over the last 3000 years. *Nat Commun* 8, 1–9.

Mollenhauer G., McManus J. F., Wagner T., McCave I. N. and Eglinton T. I. (2011) Radiocarbon and 230Th data reveal rapid redistribution and temporal changes in sediment focussing at a North Atlantic drift. *Earth Planet Sci Lett* 301, 373–381.

Monnin E., Indermühle A., Dällenbach A., Flückiger J., Stauffer B., Stocker T. F., Raynaud D. and Barnola J. M. (2001) Atmospheric CO2 concentrations over the last glacial termination. *Science* 291, 112–114.

Moossen H. M. (2012) Palaeoclimate reconstructions from Arctic and Nordic Shelf seas: development and application of multiple proxies. Doctoral dissertation, University of Glasgow.

Morey A. E., Mix A. C. and Pisias N. G. (2005) Planktonic foraminiferal assemblages preserved in surface sediments correspond to multiple environment variables. *Quat Sci Rev* 24, 925–950.

Müller J., Massé G., Stein R. and Belt S. T. (2009) Variability of sea-ice conditions in the Fram Strait over the past 30,000 years. *Nat Geosci* 2, 772.

Müller J. and Stein R. (2014) High-resolution record of late glacial and deglacial sea ice changes in Fram Strait corroborates ice-ocean interactions during abrupt climate shifts. *Earth Planet Sci Lett* 403, 446–455.

Müller J., Wagner A., Fahl K., Stein R., Prange M. and Lohmann G. (2011) Towards quantitative sea ice reconstructions in the northern North Atlantic: A combined biomarker and numerical modelling approach. *Earth Planet Sci Lett* 306, 137–148.

Müller P. J., Kirst G., Ruhland G., Von Storch I. and Rosell-Melé A. (1998) Calibration of the alkenone paleotemperature index U37K based on core-tops from the eastern South Atlantic and the global ocean (60°N-60°S). *Geochim Cosmochim Acta* 62, 1757–1772.

Murray John W. (2006) *Ecology and applications of benthic foraminifera.*, Cambridge University Press.

Murton J. B., Bateman M. D., Dallimore S. R., Teller J. T. and Yang Z. (2010) Identification of Younger Dryas outburst flood path from Lake Agassiz to the Arctic Ocean. *Nature* 464, 740–743.

Muschitiello F., D'Andrea W. J., Schmittner A., Heaton T. J., Balascio N. L., DeRoberts N., Caffee M. W., Woodruff T. E., Welten K. C., Skinner L. C., Simon M. H. and Dokken T. M. (2019) Deep-water circulation changes lead North Atlantic climate during deglaciation. *Nat Commun* 10, 1–10.

Naafs B. D. A., Hefter J. and Stein R. (2013) Millennial-scale ice rafting events and Hudson Strait Heinrich(-like) Events during the late Pliocene and Pleistocene: A review. *Quat Sci Rev* 80, 1–28.

Nakamura T., Yamazaki K., Iwamoto K., Honda M., Miyoshi Y., Ogawa Y. and Ukita J. (2015) A negative phase shift of the winter AO/NAO due to the recent Arctic sea-ice reduction in late autumn. *Journal of Geophysical Research: Atmospheres* 120, 3209–3227.

Nelson D. M., Tréguer P., Brzezinski M. A., Leynaert A. and Quéguiner B. (1995) Production and dissolution of biogenic silica in the ocean: Revised global estimates, comparison with regional data and relationship to biogenic sedimentation. *Global Biogeochem Cycles* 9, 359–372.

Nesje A. (2009) Latest Pleistocene and Holocene alpine glacier fluctuations in Scandinavia. *Quat Sci Rev* 28, 2119–2136.

Nesje A. and Dahl S. O. (2003) The "Little Ice Age" - Only temperature? *Holocene* 13, 139–145.

Nesje A., Matthews J. A., Dahl S. O., Berrisford M. S. and Andersson C. (2001) Holocene glacier fluctuations of Flatebreen and winter-precipitation changes in the Jostedalsbreen region, western Norway, based on glaciolacustrine sediment records. *Holocene* 11, 267–280.

Neugebauer I., Brauer A., Dräger N., Dulski P., Wulf S., Plessen B., Mingram J., Herzschuh U. and Brande A. (2012) A Younger Dryas varve chronology from the Rehwiese palaeolake record in NE-Germany. *Quat Sci Rev* 36, 91–102.

Ng H. C., Robinson L. F., McManus J. F., Mohamed K. J., Jacobel A. W., Ivanovic R. F., Gregoire L. J. and Chen T. (2018) Coherent deglacial changes in western Atlantic Ocean circulation. *Nat Commun* 9, 1–10.

NGRIP members (2004) High-resolution record of Northern Hemisphere climate extending into the last interglacial period. *Nature* 431, 147–151.

Nurnberg D. (1995) Magnesium in tests of Neogloboquadrina pachyderma sinistral from high northern and southern latitudes. *J Foraminifer Res* 25, 350–368.

Oksman M., Weckström K., Miettinen A., Juggins S., Divine D. V., Jackson R., Telford R., Korsgaard N. J. and Kucera M. (2017) Younger Dryas ice margin retreat triggered by ocean surface warming in central-eastern Baffin Bay. *Nat Commun* 8, 1–8.

Okuma E., Hingst J., Weiser J., Madaj L., Titschack J., Vogt C., Kienast M., Hillaire-Marcel C., Hebbeln D. and Kasemann S. A. (2023) Deglacial and Holocene sediment dynamics and provenances off Lancaster Sound: Implications for paleoenvironmental conditions in northern Baffin Bay. *Quat Sci Rev* 309, 108101.

Oppo D. W., Curry W. B. and McManus J. F. (2015) What do benthic δ13C and δ18O data tell us about Atlantic circulation during Heinrich Stadial 1? *Paleoceanography* 30, 353–368.

Osman M. B., Das S. B., Trusel L. D., Evans M. J., Fischer H., Grieman M. M., Kipfstuhl S., McConnell J. R. and Saltzman E. S. (2019) Industrial-era decline in subarctic Atlantic productivity. *Nature* 569, 551–555.

Ownsworth E., Selby D., Lloyd J., Knutz P., Szidat S., Andrews J. and Ó Cofaigh C. (2023) Tracking sediment delivery to central Baffin Bay during the past 40 kyrs: Insights from a multiproxy approach and new age model. *Quat Sci Rev* 308, 108082.

Patton H., Hubbard A., Andreassen K., Winsborrow M. and Stroeven A. P. (2016) The build-up, configuration, and dynamical sensitivity of the Eurasian ice-sheet complex to Late Weichselian climatic and oceanic forcing. *Quat Sci Rev* 153, 97–121.

Pattyn F., Ritz C., Hanna E., Asay-Davis X., DeConto R., Durand G., Favier L., Fettweis X., Goelzer H., Golledge N. R., Kuipers Munneke P., Lenaerts J. T. M., Nowicki S., Payne A. J., Robinson A., Seroussi H., Trusel L. D. and van den Broeke M. (2018) The Greenland and Antarctic ice sheets under 1.5 °C global warming. *Nat Clim Chang* 8, 1053–1061.

Pawłowski D. (2017) The usefulness of subfossil Cladocera remains in Younger Dryas climatic reconstructions in central Poland. *Acta Geologica Polonica* 67, 567–584.

Pearce C., Søby Özdemir K., Forchhammer R., Detlef H. and Olsen J. (2023) The marine reservoir age of Greenland coastal waters. *Geochronology* Preprint, 1–26.

Peck V. L., Hall I. R., Zahn R. and Elderfield H. (2008) Millennial-scale surface and subsurface paleothermometry from the northeast Atlantic, 55-8 ka BP. *Paleoceanography* 23, PA3221.

Peltier W. R., Argus D. F. and Drummond R. (2015) Space geodesy constrains ice age terminal deglaciation: The global ICE-6G_C (VM5a) model. *J Geophys Res Solid Earth* 120, 450–487.

Peltier W. R., Vettoretti G. and Stastna M. (2006) Atlantic meridional overturning and climate response to Arctic Ocean freshening. *Geophys Res Lett* 33, 2–5.

Perovich D. K., Light B., Eicken H., Jones K. F., Runciman K. and Nghiem S. V. (2007) Increasing solar heating of the Arctic Ocean and adjacent seas, 1979-2005: Attribution and role in the ice-albedo feedback. *Geophys Res Lett* 34, 1–5.

Pflaumann U., Sarnthein M., Chapman M., D'Abreu L., Funnell B., Huels M., Kiefer T., Maslin M., Schulz H., Swallow J., van Kreveld S., Vautravers M., Vogelsang E. and Weinelt M. (2003) Glacial North Atlantic: Sea-surface conditions reconstructed by GLAMAP 2000. *Paleoceanography* 18, 1065.

Pieńkowski A. J., Coulthard R. D. and Furze M. F. A. (2022) Revised marine reservoir offset (ΔR) values for molluscs and marine mammals from Arctic North America. *Boreas* 52, 145–167.

Polyak L., Best K. M., Crawford K. A., Council E. A. and St-Onge G. (2013) Quaternary history of sea ice in the western Arctic Ocean based on foraminifera. *Quat Sci Rev* 79, 145–156.

Pöppelmeier F., Jeltsch-Thömmes A., Lippold J., Joos F. and Stocker T. F. (2023) Multi-proxy constraints on Atlantic circulation dynamics since the last ice age. *Nat Geosci* 16, 349–356.

Praetorius S. K., McManus J. F., Oppo D. W. and Curry W. B. (2008) Episodic reductions in bottom-water currents since the last ice age. *Nat Geosci* 1, 449–452.

Prahl F. G., Muehlhausen L. A. and Zahnle D. L. (1988) Further evaluation of long-chain alkenones as indicators of paleoceanographic conditions. *Geochim Cosmochim Acta* 52, 2303–2310.

Prahl F. G. and Wakeham S. G. (1987) Calibration of unsaturation patterns in long-chain ketone compositions for palaeotemperature assessment. *Nature* 330, 367–369.

Rahmstorf S. (2002) Ocean circulation and climate during the past 120,000 years. *Nature* 419, 207–214.

Rahmstorf S., Box J. E., Feulner G., Mann M. E., Robinson A., Rutherford S. and Schaffernicht E. J. (2015) Exceptional twentieth-century slowdown in Atlantic Ocean overturning circulation. *Nat Clim Chang* 5, 475–480.

Rainsley E., Menviel L., Fogwill C. J., Turney C. S. M., Hughes A. L. C. and Rood D. H. (2018) Greenland ice mass loss during the Younger Dryas driven by Atlantic Meridional Overturning Circulation feedbacks. *Sci Rep* 8, 1–9.

Rampen S. W., Abbas B. A., Schouten S. and Damsté J. S. S. (2010) A comprehensive study of sterols in marine diatoms (Bacillariophyta): Implications for their use as tracers for diatom productivity. *Limnol Oceanogr* 55, 91–105.

Rashid H., Piper D. J., Drapeau J., Marin C. and Smith M. E. (2019) Sedimentology and history of sediment sources to the NW Labrador Sea during the past glacial cycle. *Quat Sci Rev* 221, 105880.

Rashid H., Piper D. J. W. and Flower B. P. (2011) The Role of Hudson Strait Outlet in Younger Dryas Sedimentation in the Labrador Sea. *Geophysical Monograph Series* 193, 93–110.

Rasmussen S. O., Andersen K. K., Svensson A. M., Steffensen J. P., Vinther B. M., Clausen H. B., Siggaard-Andersen M. L., Johnsen S. J., Larsen L. B., Dahl-Jensen D., Bigler M., Röthlisberger R., Fischer H., Goto-Azuma K., Hansson M. E. and Ruth U. (2006) A new Greenland ice core chronology for the last glacial termination. *Journal of Geophysical Research Atmospheres* 111, D06102.

Rasmussen T. L., Oppo D. W., Thomsen E. and Lehman S. J. (2003) Deep sea records from the southeast Labrador Sea: Ocean circulation changes and ice-rafting events during the last 160,000 years. *Paleoceanography* 18, n/a-n/a.

Rasmussen T. L. and Thomsen E. (2017) Ecology of deep-sea benthic foraminifera in the North Atlantic during the last glaciation: Food or temperature control. *Palaeogeogr Palaeoclimatol Palaeoecol* 472, 15–32.

Rasmussen T. L. and Thomsen E. (2008) Warm Atlantic surface water inflow to the Nordic seas 34-10 calibrated ka B.P. *Paleoceanography* 23, 1–13.

Ravelo A. C. and Hillaire-Marcel C. (2007) Chapter Eighteen The Use of Oxygen and Carbon Isotopes of Foraminifera in Paleoceanography. *Developments in Marine Geology* 1, 735–764.

Reimer P. J., Bard E., Bayliss A., Beck J. W., Blackwell P. G., Ramsey C. B., Buck C. E., Cheng H., Edwards R. L. and Friedrich M. (2013) IntCal13 and Marine13 radiocarbon age calibration curves 0–50,000 years cal BP. *Radiocarbon* 55, 1869–1887.

Reinig F., Wacker L., Jöris O., Oppenheimer C., Guidobaldi G., Nievergelt D., Adolphi F., Cherubini P., Engels S., Esper J., Land A., Lane C., Pfanz H., Remmele S., Sigl M., Sookdeo A. and Büntgen U. (2021) Precise date for the Laacher See eruption synchronizes the Younger Dryas. *Nature* 595, 66–69.

Ren J., Gersonde R., Esper O. and Sancetta C. (2014) Diatom distributions in northern North Pacific surface sediments and their relationship to modern environmental variables. Palaeogeogr Palaeoclimatol Palaeoecol 402, 81–103.

Ren J., Chen J., Bai Y., Sicre M. A., Yao Z., Lin L., Zhang J., Li H., Wu B., Jin H., Ji Z., Zhuang Y. and Li Y. (2020) Diatom composition and fluxes over the Northwind Ridge, western Arctic Ocean: Impacts of marine surface circulation and sea ice distribution. *Prog Oceanogr* 186, 102377.

Ren J., Chen J., Li H., Wiesner M. G., Bai Y., Sicre M. A., Yao Z., Jin H., Zhuang Y. and Li Y. (2021) Siliceous micro- and nanoplankton fluxes over the Northwind Ridge and their relationship to environmental conditions in the western Arctic Ocean. *Deep Sea Res 1 Oceanogr Res Pap* 174, 103568.

Renssen H., Mairesse A., Goosse H., Mathiot P., Heiri O., Roche D. M., Nisancioglu K. H. and Valdes P. J. (2015) Multiple causes of the Younger Dryas cold period. *Nat Geosci* 8, 946–949.

Rinterknecht V., Jomelli V., Brunstein D., Favier V., Masson-Delmotte V., Bourlès D., Leanni L. and Schläppy R. (2014) Unstable ice stream in Greenland during the Younger Dryas cold event. *Geology* 42, 759–762.

Rodrigues A. R., Pivel M. A. G., Schmitt P., de Almeida F. K. and Bonetti C. (2018) Infaunal and epifaunal benthic foraminifera species as proxies of organic matter paleofluxes in the Pelotas Basin, south-western Atlantic Ocean. *Mar Micropaleontol* 144, 38–49.

Rosell-Melé A. (1998) Interhemispheric appraisal of the value of alkenone indices as temperature and salinity proxies in high-latitude locations. *Paleoceanography* 13, 694–703.

Rosell-Melé A., Eglinton G., Pflaumann U. and Sarnthein M. (1995) Atlantic core-top calibration of the U37K index as a sea-surface palaeotemperature indicator. *Geochim Cosmochim Acta* 59, 3099–3107.

Ruddiman W. F. (1977) Late Quaternary deposition of ice-rafted sand in the subpolar North Atlantic (lat 40° to 65°N). *Bulletin of the Geological Society of America* 88, 1813–1827.

Rudels B., Anderson L. G. and Jones E. P. (1996) Formation and evolution of the surface mixed layer and halocline of the Arctic Ocean. *J Geophys Res Oceans* 101, 8807–8821.

Sachs J. P., Stein R., Maloney A. E., Wolhowe M., Fahl K. and Nam S. il (2018) An Arctic Ocean paleosalinity proxy from δ2H of palmitic acid provides evidence for deglacial Mackenzie River flood events. *Quat Sci Rev* 198, 76–90.

Sadatzki H., Dokken T. M., Berben S. M. P., Muschitiello F., Stein R., Fahl K., Menviel L., Timmermann A. and Jansen E. (2019) Sea ice variability in the southern norwegian sea during glacial dansgaard-oeschger climate cycles. *Sci Adv* 5, 1–11.

Sadatzki H., Maffezzoli N., Dokken T. M., Simon M. H., Berben S. M. P., Fahl K., Kjær H. A., Spolaor A., Stein R., Vallelonga P., Vinther B. M. and Jansen E. (2020) Rapid reductions and millennial-

scale variability in Nordic Seas sea ice cover during abrupt glacial climate changes. *Proc Natl Acad Sci U S A* 117, 29478–29486.

Sahoo N., Saalim S. M., Matul A., Mohan R., Tikhonova A. and Kozina N. (2022) Planktic Foraminiferal Assemblages in Surface Sediments from the Subpolar North Atlantic Ocean. *Front Mar Sci* 8, 1–19.

Saini J., Stein R., Fahl K., Weiser J., Hebbeln D. and Madaj L. (2022) Holocene variability in sea-ice conditions in the eastern Baffin Bay-Labrador Sea – A north–south biomarker transect study. *Boreas* 51, 553–572.

Sakshaug E. (2004) Primary and Secondary Production in the Arctic Seas. In *The Organic Carbon Cycle in the Arctic Ocean* Springer Berlin Heidelberg. pp. 57–81.

Schepper S. D., Ray J. L., Skaar K. S., Sadatzki H., Ijaz U. Z., Stein R. and Larsen A. (2019) The potential of sedimentary ancient DNA for reconstructing past sea ice evolution. *ISME Journal* 13, 2566–2577.

Schmitt J., Schneider R., Elsig J., Leuenberger D., Lourantou A., Chappellaz J., Köhler P., Joos F., Stocker T. F., Leuenberger M. and Fischer H. (2012) Carbon isotope constraints on the deglacial CO2 rise from ice cores. *Science* 336, 711–714.

Schouten S., Hopmans E. C., Schefuß E. and Sinninghe Damsté J. S. (2003) Corrigendum to "Distributional variations in marine crenarchaeotal membrane lipids: a new tool for reconstructing ancient sea water temperatures?" *Earth Planet Sci Lett* 211, 205–206.

Schouten S., Hopmans E. C. and Sinninghe Damsté J. S. (2013) The organic geochemistry of glycerol dialkyl glycerol tetraether lipids: A review. *Org Geochem* 54, 19–61.

Scoto F., Sadatzki H., Maffezzoli N., Barbante C., Gagliardi A., Varin C., Vallelonga P., Gkinis V., Dahl-Jensen D., Kjær H. A., Burgay F., Saiz-Lopez A., Stein R. and Spolaor A. (2022) Sea ice fluctuations in the Baffin Bay and the Labrador Sea during glacial abrupt climate changes. *Proc Natl Acad Sci U S A* 119, 1–9.

Scott D. B., Schell T., St-Onge G., Rochon A. and Blasco S. (2009) Foraminiferal assemblage changes over the last 15,000 years on the Mackenzie-Beaufort Sea Slope and Amundsen Gulf, Canada: Implications for past sea ice conditions. *Paleoceanography* 24, 1–20.

Seager R., Haibo L. I. U., Kushnir Y., Osborn T. J., Simpson I. R., Kelley C. R. and Nakamura J. (2020) Mechanisms of winter precipitation variability in the european-mediterranean region associated with the north atlantic oscillation. *J Clim* 33, 7179–7196.

Seidenkrantz M. (1995) *Cassidulina teretis* Tappan and Cassidulina neoteretis new species (Foraminifera): stratigraphic markers for deep sea and outer shelf areas. *J Micropalaeontol* 14, 145–157.

Seidenkrantz M. S. (2013) Benthic foraminifera as palaeo sea-ice indicators in the subarctic realm - examples from the Labrador Sea-Baffin Bay region. *Quat Sci Rev* 79, 135–144.

Seidenkrantz M. S., Ebbesen H., Aagaard-Sørensen S., Moros M., Lloyd J. M., Olsen J., Knudsen M. F. and Kuijpers A. (2013) Early Holocene large-scale meltwater discharge from Greenland documented by foraminifera and sediment parameters. *Palaeogeogr Palaeoclimatol Palaeoecol* 391, 71–81.

Seidenkrantz M. S., Kuijpers A., Aagaard-Sørensen S., Lindgreen H., Olsen J. and Pearce C. (2021) Evidence for influx of Atlantic water masses to the Labrador Sea during the Last Glacial Maximum. *Sci Rep* 11, 1–14.

Serreze M. C. and Barry R. G. (2011) Processes and impacts of Arctic amplification: A research synthesis. *Glob Planet Change* 77, 85–96.

Serreze M. C., Holland M. M. and Stroeve J. (2007) Perspectives on the Arctic's Shrinking Sea-Ice Cover. *Science* 315, 1533–1536.

Sessions A. L., Burgoyne T. W., Schimmelmann A. and Hayes J. M. (1999) Fractionation of hydrogen isotopes in lipid biosynthesis. *Org Geochem* 30, 1193–1200.

De Sève M. A. (1999) Transfer function between surface sediment diatom assemblages and sea-surface temperature and salinity of the Labrador Sea. *Mar Micropaleontol* 36, 249–267.

Sévellec F., Fedorov A. V. and Liu W. (2017) Arctic sea-ice decline weakens the Atlantic Meridional Overturning Circulation. *Nat Clim Chang* 7, 604–610.

Sheldon C., Jennings A., Andrews J. T., Ó Cofaigh C., Hogan K., Dowdeswell J. A. and Seidenkrantz M. S. (2016) Ice stream retreat following the LGM and onset of the west Greenland current in Uummannaq Trough, west Greenland. *Quat Sci Rev* 147, 27–46.

Shu Q., Wang Q., Song Z. and Qiao F. (2021) The poleward enhanced Arctic Ocean cooling machine in a warming climate. *Nat Commun* 12, 1–9.

Shukla P. R., Skea J., Calvo Buendia E., Masson-Delmotte V., Pörtner H. O., Roberts D. C., Zhai P., Slade R., Connors S. and Van Diemen R. (2019) IPCC, 2019: Climate Change and Land: an IPCC special report on climate change, desertification, land degradation, sustainable land management, food security, and greenhouse gas fluxes in terrestrial ecosystems.

Simon Q., Hillaire-Marcel C., St-Onge G. and Andrews J. T. (2014) North-eastern Laurentide, western Greenland and southern Innuitian ice stream dynamics during the last glacial cycle. *J Quat Sci* 29, 14–26.

Simon Q., Thouveny N., Bourlès D. L., Nuttin L., Hillaire-Marcel C. and St-Onge G. (2016) Authigenic 10Be/9Be ratios and 10Be-fluxes (230Thxs-normalized) in central Baffin Bay sediments during the last glacial cycle: Paleoenvironmental implications. *Quat Sci Rev* 140, 142–162.

Sirocko F., Martínez-García A., Mudelsee M., Albert J., Britzius S., Christl M., Diehl D., Diensberg B., Friedrich R., Fuhrmann F., Muscheler R., Hamann Y., Schneider R., Schwibus K. and Haug G. H. (2021) Muted multidecadal climate variability in central Europe during cold stadial periods. *Nat Geosci* 14, 651–658.

Smik L., Cabedo-Sanz P. and Belt S. T. (2016) Semi-quantitative estimates of paleo Arctic sea ice concentration based on source-specific highly branched isoprenoid alkenes: A further development of the PIP25 index. *Org Geochem* 92, 63–69.

Solignac S., De Vernal A. and Hillaire-Marcel C. (2004) Holocene sea-surface conditions in the North Atlantic - Contrasted trends and regimes in the western and eastern sectors (Labrador Sea vs. Iceland Basin). *Quat Sci Rev* 23, 319–334.

Sommerfeldt R. (2012) Palaeoenvironmental conditions and sediment inputs in the Late Quaternary North Atlantic/Labrador Sea: reconstruction based on sedimentological studies of a sediment core from the Eirik Ridge. Master thesis, University of Potsdam.

Spielhagen R. F., Baumann K. H., Erlenkeuser H., Nowaczyk N. R., Nørgaard-Pedersen N., Vogt C. and Weiel D. (2004) Arctic Ocean deep-sea record of northern Eurasian ice sheet history. *Quat Sci Rev* 23, 1455–1483.

Srokosz M. A. and Bryden H. L. (2015) Observing the Atlantic Meridional Overturning Circulation yields a decade of inevitable surprises. *Science* 348.

Stanford J. D., Rohling E. J., Bacon S. and Holliday N. P. (2011) A review of the deep and surface currents around Eirik Drift, south of Greenland: Comparison of the past with the present. *Glob Planet Change* 79, 244–254.

Stanford J. D., Rohling E. J., Hunter S. E., Roberts A. P., Rasmussen S. O., Bard E., McManus J. and Fairbanks R. G. (2006) Timing of meltwater pulse 1a and climate responses to meltwater injections. *Paleoceanography* 21, 1–9.

Stärz M., Gong X., Stein R., Darby D. A., Kauker F. and Lohmann G. (2012) Glacial shortcut of Arctic sea-ice transport. *Earth Planet Sci Lett* 357–358, 257–267.

Stein R. (2008) *Arctic Ocean Sediments: Processes, Proxies, and Paleoenvironment*., Elsevier, UK.

Stein R., Niessen F., Schmidt D., Naafs D., Peters C., Saukel C. and Sommerfeldt R. (2009a) The Expedition of the Research Vessel "Maria S. Merian" to the Labrador Sea in 2009 (MSM12/2), 68-86.

Stein R., Hefter J., Grützner J., Voelker A. and David A Naafs B. (2009b) Variability of surface water characteristics and heinrich-iike events in the pleistocene midlatitude North Atlantic Ocean: biomarker and XRD records from iodp site U1313 (MIS 16-9). *Paleoceanography* 24, 1–13.

Stein R. (2010) Documentation of sediment core MSM12:647-1 (MSM12/2-05-01). Alfred Wegener Institute, Helmholtz Centre for Polar and Marine Research, Bremerhaven. *PANGAEA*.

Stein R., Matthiessen J., Niessen F., Krylov A., S-I N. and Bazhenova E. (2010) Towards a better (litho-) stratigraphy and reconstruction of Quaternary Paleoenvironment in the Amerasian Basin (Arctic Ocean). *Polarforschung* 79, 97–121.

Stein R., Fahl K. and Müller J. (2012) Proxy reconstruction of Cenozoic Arctic Ocean sea ice history– from IRD to IP$_{25}$. *Polarforschung* 82, 37–71.

Stein R. (2015) X-ray fluorescence on sediment core MSM12/647-1 (raw data from XRF-core scanner). Alfred Wegener Institute, Helmholtz Centre for Polar and Marine Research, Bremerhaven. PANGAEA.

Stein R., Fahl K., Gierz P., Niessen F. and Lohmann G. (2017) Arctic Ocean sea ice cover during the penultimate glacial and the last interglacial. *Nat Commun* 8, 373.

Stein R. (2019) The late Mesozoic-Cenozoic Arctic Ocean climate and sea ice history: A challenge for past and future scientific ocean drilling. *Paleoceanogr Paleoclimatol* 34, PA003433.

Steinsland K., Grant D. M., Ninnemann U. S., Fahl K., Stein R. and Schepper S. De (2023) Sea ice variability in the North Atlantic subpolar gyre throughout the last interglacial. *Quat Sci Rev* 313, 108198.

de Steur L., Sumata H., Divine D. V., Granskog M. A. and Pavlova O. (2023) Upper ocean warming and sea ice reduction in the East Greenland Current from 2003 to 2019. *Commun Earth Environ* 4, 1–11.

Stocker T., Dahe Q., Plattner G. -K., Tignor M. M. B., Allen S. K., Boschung, J. E. . . . and Midgley P. M. (2013) IPCC,2013: the physical science basis: Working Group I contribution to the Fifth assessment report of the Intergovernmental Panel on Climate Change., Cambridge university press.

Straneo F. and Heimbach P. (2013) North Atlantic warming and the retreat of Greenland's outlet glaciers. *Nature* 504, 36–43.

Stroeve J. C., Markus T., Boisvert L., Miller J. and Barrett A. (2014) Changes in Arctic melt season and implications for sea ice loss. *Geophys Res Lett* 41, 1216–1225.

Stroeve J. C., Maslanik J., Serreze M. C., Rigor I., Meier W. and Fowler C. (2011) Sea ice response to an extreme negative phase of the Arctic Oscillation during winter 2009/2010. *Geophys Res Lett* 38, 1–6.

Stroeve J. C., Serreze M. C., Holland M. M., Kay J. E., Malanik J. and Barrett A. P. (2012) The Arctic's rapidly shrinking sea ice cover: a research synthesis. *Clim Change* 110, 1005–1027.

Stroeve J., Holland M. M., Meier W., Scambos T. and Serreze M. (2007) Arctic sea ice decline: Faster than forecast. *Geophys Res Lett* 34, 1–5.

Süfke F., Gutjahr M., Keigwin L. D., Reilly B., Giosan L. and Lippold J. (2022) Arctic drainage of Laurentide Ice Sheet meltwater throughout the past 14,700 years. *Commun Earth Environ* 3, 1–11.

Sumata H., de Steur L., Divine D. V., Granskog M. A. and Gerland S. (2023) Regime shift in Arctic Ocean sea ice thickness. *Nature* 615, 443–449.

Sun Y., Knorr G., Zhang X., Tarasov L., Barker S., Werner M. and Lohmann G. (2022) Ice sheet decline and rising atmospheric CO2 control AMOC sensitivity to deglacial meltwater discharge. *Glob Planet Change* 210, 103755.

Svendsen J. I. and Mangerud J. (1997) Holocene glacial and climatic variations on Spitsbergen, Svalbard. *Holocene* 7, 45–57.

Svensson A., Andersen K. K., Bigler M., Clausen H. B., Davies S. M. and Johnsen S. J. (2008) A 60 000 year Greenland stratigraphic ice core chronology. *Climate of the Past* 4, 47–57.

Syring N., Stein R., Fahl K., Vahlenkamp M., Zehnich M., Spielhagen R. F. and Niessen F. (2020) Holocene changes in sea-ice cover and polynya formation along the eastern North Greenland shelf : New insights from biomarker records. *Quat Sci Rev* 231, 106173.

Tang C. C. L., Ross C. K., Yao T., Petrie B., DeTracey B. M. and Dunlap E. (2004) The circulation, water masses and sea-ice of Baffin Bay. *Prog Oceanogr* 63, 183–228.

Telesiński M. M., Spielhagen R. F. and Bauch H. A. (2014) Water mass evolution of the Greenland sea since late glacial times. *Climate of the Past* 10, 123–136.

Teller J. T., Leverington D. W. and Mann J. D. (2002) Freshwater outbursts to the oceans from glacial Lake Agassiz and their role in climate change during the last deglaciation. *Quat Sci Rev* 21, 879–887.

The IMBIE Team (2018) Mass balance of the Antarctic ice sheet from 1992 to 2017. *Nature* 558, 219–222.

Thomas D. N. and Dieckmann G. S. (2008) *Sea ice: an introduction to its physics, chemistry, biology and geology.*, Blackwell Science.

Thornalley D. J. R., Barker S., Broecker W. S., Elderfield H. and McCave I. N. (2011) The deglacial evolution of north atlantic deep convection. *Science* 331, 202–205.

Thornalley D. J. R., Bauch H. A., Gebbie G., Guo W., Ziegler M., Bernasconi S. M., Barker S., Skinner L. C. and Yu J. (2015) A warm and poorly ventilated deep Arctic Mediterranean during the last glacial period. *Science* 349, 706–710.

Thornalley D. J. R., Elderfield H. and McCave I. N. (2009) Holocene oscillations in temperature and salinity of the surface subpolar North Atlantic. *Nature* 457, 711–714.

Thornalley D. J. R., McCave I. N. and Elderfield H. (2010) Freshwater input and abrupt deglacial climate change in the North Atlantic. *Paleoceanography* 25, PA1201.

Tierney J. E., Pausata F. S. R. and De Menocal P. B. (2017) Rainfall regimes of the Green Sahara. *Sci Adv* 3, 1–10.

Tilstone G. H., Miller P. I., Brewin R. J. W. and Priede I. G. (2014) Enhancement of primary production in the North Atlantic outside of the spring bloom, identified by remote sensing of ocean colour and temperature. *Remote Sens Environ* 146, 77–86.

Toucanne S., Soulet G., Freslon N., Silva Jacinto R., Dennielou B., Zaragosi S., Eynaud F., Bourillet J. F. and Bayon G. (2015) Millennial-scale fluctuations of the European Ice Sheet at the end of the last glacial, and their potential impact on global climate. *Quat Sci Rev* 123, 113–133.

Uenzelmann-Neben G. (2009) *The expedition of the research vessel" Maria S. Merian" to the Labrador Sea in 2009 (MSM 12/2) Reykjavik-Reykjavik 17. June-13. July 2009.*,

Vaks A., Mason A. J., Breitenbach S. F. M., Kononov A. M., Osinzev A. V., Rosensaft M., Borshevsky A., Gutareva O. S. and Henderson G. M. (2020) Palaeoclimate evidence of vulnerable permafrost during times of low sea ice. *Nature* 577, 221–225.

Vallelonga P., Maffezzoli N., Saiz-Lopez A., Scoto F., Kjær H. A. and Spolaor A. (2021) Sea-ice reconstructions from bromine and iodine in ice cores. *Quat Sci Rev* 269.

de Vernal A., Gersonde R., Goosse H., Seidenkrantz M.-S. and Wolff E. W. (2013) Sea ice in the paleoclimate system: the challenge of reconstructing sea ice from proxies–an introduction. *Quat Sci Rev* 79, 1–8.

de Vernal A., Henry M., Matthiessen J., Mudie P. J., Rochon A., Boessenkool K. P., Eynaud F., Grøsfjeld K., Guiot J., Hamel D., Harland R., Head M. J., Kunz-Pirrung M., Levac E., Loucheur V., Peyron O., Pospelova V., Radi T., Turon J. L. and Voronina E. (2001) Dinoflagellate cyst assemblages as tracers of sea-surface conditions in the Northern North Atlantic, Arctic and sub-Arctic seas: The new "n = 677" data base and its application for quantitative palaeoceanographic reconstruction. *J Quat Sci* 16, 681–698.

de Vernal A. and Hillaire-Marcel C. (2000) Sea-ice cover, sea-surface salinity and halo-/thermocline structure of the northwest North Atlantic: Modern versus full glacial conditions. *Quat Sci Rev* 19, 65–85.

de Vernal A., Rosell-Melé A., Kucera M., Hillaire-Marcel C., Eynaud F., Weinelt M., Dokken T. and Kageyama M. (2006) Comparing proxies for the reconstruction of LGM sea-surface conditions in the northern North Atlantic. Quat Sci Rev 25, 2820–2834.

de Vernal A. and Marret F. (2007) Chapter Nine Organic-Walled Dinoflagellate Cysts: Tracers of Sea-Surface Conditions. *Developments in Marine Geology* 1, 371–408.

Vettoretti G. and Peltier W. R. (2016) Thermohaline instability and the formation of glacial North Atlantic super polynyas at the onset of Dansgaard-Oeschger warming events. *Geophys Res Lett* 43, 5336–5344.

Volkman J. K. (1986) A review of sterol markers for marine and terrigenous organic matter. *Org Geochem* 9, 83–99.

Wang J., Mysak L. A. and Grant Ingram R. (1994) Interannual variability of sea-ice cover in Hudson bay, Baffin bay and the Labrador Sea. *Atmosphere - Ocean* 32, 421–447.

Wang K. J., Huang Y., Majaneva M., Belt S. T., Liao S., Novak J., Kartzinel T. R., Herbert T. D., Richter N. and Cabedo-Sanz P. (2021) Group 2i Isochrysidales produce characteristic alkenones reflecting sea ice distribution. *Nat Commun* 12, 1–10.

Wanner H., Beer J., Bütikofer J., Crowley T. J., Cubasch U., Flückiger J., Goosse H., Grosjean M., Joos F., Kaplan J. O., Küttel M., Müller S. A., Prentice I. C., Solomina O., Stocker T. F., Tarasov P., Wagner M. and Widmann M. (2008) Mid- to Late Holocene climate change: an overview. *Quat Sci Rev* 27, 1791–1828.

Wassmann P., Carmack E. C., Bluhm B. A., Duarte C. M., Berge J., Brown K., Grebmeier J. M., Holding J., Kosobokova K., Kwok R., Matrai P., Agusti S., Babin M., Bhatt U., Eicken H., Polyakov I., Rysgaard S. and Huntington H. P. (2020) Towards a unifying pan-arctic perspective: A conceptual modelling toolkit. *Prog Oceanogr* 189, 102455.

Weiser J., Titschack J., McCave I. N., Lochte A. A., Saini J., Stein R. and Hebbeln D. (2021) Atlantic water inflow to Labrador Sea and its interaction with ice sheet dynamics during the Holocene. *Quat Sci Rev* 256, 106833.

Werner A. (1993) Holocene moraine chronology, Spitsbergen, Svalbard: lichenometric evidence for multiple Neoglacial advances in the Arctic. *Holocene* 3, 128–137.

Williams M. C. (2015) The Pelagic Record of Ocean Acidification. Doctoral dissertation, University of Bristol.

Winsor K., Carlson A. E., Welke B. M. and Reilly B. (2015a) Early deglacial onset of southwestern Greenland ice-sheet retreat on the continental shelf. *Quat Sci Rev* 128, 117–126.

Winsor K., Carlson A. E., Caffee M. W. and Rood D. H. (2015b) Rapid last-deglacial thinning and retreat of the marine-terminating southwestern Greenland ice sheet. *Earth Planet Sci Lett* 426, 1–12.

Wood M., Rignot E., Fenty I., An L., Bjørk A., van den Broeke M., Cai C., Kane E., Menemenlis D., Millan R., Morlighem M., Mouginot J., Noël B., Scheuchl B., Velicogna I., Willis J. K. and Zhang H. (2021) Ocean forcing drives glacier retreat in Greenland. *Sci Adv* 7, 1–11.

Wu J., Stein R., Fahl K., Syring N., Nam S., Hefter J., Mollenhauer G. and Geibert W. (2020) Deglacial to Holocene variability in surface water characteristics and major floods in the Beaufort Sea. *Commun Earth Environ* 1, 1–12.

Xiao X., Fahl K., Müller J. and Stein R. (2015) Sea-ice distribution in the modern Arctic Ocean: Biomarker records from trans-Arctic Ocean surface sediments. *Geochim Cosmochim Acta* 155, 16–29.

Xiao X., Zhao M., Knudsen K. L., Sha L., Eiríksson J., Gudmundsdóttir E., Jiang H. and Guo Z. (2017) Deglacial and Holocene sea–ice variability north of Iceland and response to ocean circulation changes. *Earth Planet Sci Lett* 472, 14–24.

Yang Q., Dixon T. H., Myers P. G., Bonin J., Chambers D. and Van Den Broeke M. R. (2016) Recent increases in Arctic freshwater flux affects Labrador Sea convection and Atlantic overturning circulation. *Nat Commun* 7.

Yasuhara M., deMenocal P. B., Dwyer G. S., Cronin T. M., Okahashi H. and Huang H. H. M. (2019) North Atlantic intermediate water variability over the past 20,000 years. *Geology* 47, 659–663.

You D. (2019) Foraminiferal Assemblages and Their Paleoceanographic Research in the Arctic Modern and Late Quaternary Sediments. Master thesis, Tongji University.

You D., Stein R., Fahl K., Williams M. C., Schmidt D. N., Mccave I. N., Barker S., Schefuß E., Niu L., Kuhn G. and Niessen F. (2023) Last deglacial abrupt climate changes caused by meltwater pulses in the Labrador Sea. *Commun Earth Environ* 4, 1–12.

Yu J., Menviel L., Jin Z. D., Thornalley D. J. R., Foster G. L., Rohling E. J., McCave I. N., McManus J. F., Dai Y., Ren H., He F., Zhang F., Chen P. J. and Roberts A. P. (2019) More efficient North Atlantic carbon pump during the Last Glacial Maximum. *Nat Commun* 10, 1–11.

Yu Z. and Eicher U. (1998) Abrupt climate oscillations during the last deglaciation in central North America. *Science* 282, 2235–2238.

Zhang W., Wu H., Cheng J., Geng J., Li Q., Sun Y., Yu Y., Lu H. and Guo Z. (2022) Holocene seasonal temperature evolution and spatial variability over the Northern Hemisphere landmass. *Nat Commun* 13.

Zhang X., Barker S., Knorr G., Lohmann G., Drysdale R., Sun Y., Hodell D. and Chen F. (2021) Direct astronomical influence on abrupt climate variability. *Nat Geosci* 14, 819–826.

Zhang X., Knorr G., Lohmann G. and Barker S. (2017) Abrupt North Atlantic circulation changes in response to gradual CO 2 forcing in a glacial climate state. *Nat Geosci* 10, 518–523.

Zhang X., Lohmann G., Knorr G. and Purcell C. (2014) Abrupt glacial climate shifts controlled by ice sheet changes. *Nature* 512, 290–294.

Zhao N., Oppo D. W., Huang K. F., Howe J. N. W., Blusztajn J. and Keigwin L. D. (2019) Glacial–interglacial Nd isotope variability of North Atlantic Deep Water modulated by North American ice sheet. *Nat Commun* 10, 1–10.

Zhou Y., McManus J. F., Jacobel A. W., Costa K. M., Wang S. and Alvarez Caraveo B. (2021) Enhanced iceberg discharge in the western North Atlantic during all Heinrich events of the last glaciation. *Earth Planet Sci Lett* 564, 116910.

Zimmermann H. H., Stoof-Leichsenring K. R., Dinkel V., Harms L., Schulte L., Hütt M. T., Nürnberg D., Tiedemann R. and Herzschuh U. (2023) Marine ecosystem shifts with deglacial sea-ice loss inferred from ancient DNA shotgun sequencing. *Nat Commun* 14, 1650.

Appendix

Appendix A

Table A.1 AMS ¹⁴C dates of Core MSM12/2-05-01 based on modelled reservoir age during the glacial period.

Lab ID	Depth (cm)	AMS ^{14}C age (yr.)	$\triangle$R***	Calib. age (yr. BP) ****	Model age (yr. BP) ****
SUERC-45889*	4.75	2082±35	-40±58	1529	1672
SUERC-47577	108.5	3450±38	-40±58	3202	3163
SUERC-45890	200.5	4227±37	-40±58	4186	4238
SUERC-47579	300.5	5473±39	-40±58	5700	5702
SUERC-47579	390.5	6737±37	-40±58	7085	7069
AWI-6946.1.1**	440.5	7520±85	-40±58	7835	7740
AWI-6947.1.1	470.5	7933±86	-40±58	8262	8018
AWI-6948.1.1	500.5	8115±84	-40±58	8468	8205
AWI-6949.1.1	600.5	8134±84	-40±58	8490	8679
AWI-6950.1.1	620.5	8298±83	-40±58	8699	8792
SUERC-45891	650.5	8449±38	-40±58	8892	8971
SUERC-47582	720.5	9049±40	-40±58	9623	9490
AWI-5788.1.1	749.5	9096±122	-40±58	9706	9636
AWI-5789.1.1	799.5	9585±117	-40±58	10356	9887
AWI-5793.1.1	919.5	9831±127	-40±58	10698	10405
AWI-5794.1.1	929.5	9606±120	-40±58	10383	10444
AWI-5795.1.1	952.5	9641±119	-40±58	10427	10535
AWI-5798.1.1	999.5	9860±119	-40±58	10740	10737
AWI-5799.1.1	1029.5	10029±125	-40±58	10956	10867
AWI-5800.1.1	1059.5	10428±128	785±58	10380	10991
AWI-5803.1.1	1108.5	10543±129	785±58	10533	11213
AWI-6484.1.1	1114.5	10621±100	785±58	10643	11221
AWI-6485.1.1	1118.5	11130±101	785±58	11359	11223
AWI-6486.1.1	1123.5	11141±94	785±58	11372	11635
AWI-6487.1.1	1127.5	11752±95	785±58	12277	12101
AWI-5952.1.1	1130.5	11854±131	785±58	12393	12410
SUERC-47583	1140.5	12379±43	785±58	12917	12904
SUERC-51888	1150.5	12975±44	785±58	13528	13198
AWI-6488.1.1	1153.5	12942±102	785±58	13495	13224
AWI-6489.1.1	1155.5	12671±102	785±58	13210	13242
AWI-6490.1.1	1157.5	12518±106	785±58	13051	13260
AWI-6491.1.1	1159.5	12721±106	785±58	13260	13278
AWI-5954.1.1	1160.5	12544±120	785±58	13079	13455
AWI-6492.1.1	1162.5	12972±105	785±58	13529	14147
AWI-5955.1.1	1165.5	13965±135	785±58	14994	15185
AWI-5956.1.1	1167.5	14937±147	785±58	16282	15876
SUERC-47584	1170.5	15386±51	785±58	16850	16837
SUERC-51887	1190.5	17007±57	785±58	18727	18711
SUERC-47585	1300.5	19096±67	785±58	21205	21225
SUERC-51889	1312.5	22063±90	785±58	24576	24553
SUERC-45892	1350.5	29502±316	785±58	32046	31926
SUERC-51890	1385.5	33049±305	785±58	35873	36049
SUERC-47586	1400.5	37491±521	785±58	40668	40207
SUERC-47587	1490.5	46458±1576	785±58	47478	49572

* AMS ^{14}C dates were carried out at the NERC Radiocarbon Laboratory at SUERC (Scottish Universities Environment Research Centre, the University of Glasgow). They were recalculated from the unpublished data of Williams, (2015). ** AMS ^{14}C dates were measured at the Alfred Wegener Institute, Bremerhaven. *** The reservoir age during the Holocene is based on modern-day reservoir age from nearby locations (*http://calib.org/marine/*). The reservoir age during the glacial period is based on the modelling results from Heaton et al. (2023). **** Calibrations based on the Marine 20 calibration curve (Heaton et al., 2020).